Vehicle Dynamics Virtual Sensing and Advanced Motion Control for Highly Skilled Autonomous Vehicles

Dissertation

zur Erlangung des akademischen Grades

Doktoringenieur
(Dr.-Ing.)

vorgelegt der
Fakultät für Maschinenbau der
Technischen Universität Ilmenau

von Herrn

Msc. Manuel Acosta Reche

1. Gutachter: PD Dr.-Ing. habil. Valentin Ivanov
2. Gutachter: Univ. -Prof. Dr. Yuri Shardt
3. Gutachter: Univ. -Prof. Dipl. -Ing. Dr. rechn. Daniel Watzenig

Tag der Einreichung: 18/06/2019
Tag der wissenschaftlichen Aussprache: 26/11/2019

urn:nbn:de:gbv:ilm1-2019000541

Abstract

This dissertation is aimed at elucidating the path towards the development of a future generation of highly-skilled autonomous vehicles (HSAV). In brief, it is envisaged that future HSAVs will be able to exhibit advanced driving skills to maintain the vehicle within stable limits in spite of the driving conditions (limits of handling) or environmental adversities (e.g. low manoeuvrability surfaces). Current research lines on intelligent systems indicate that such advanced driving behaviour may be realised by means of expert systems capable of monitoring the current vehicle states, learning the road friction conditions, and adapting their behaviour depending on the identified situation. Such adaptation skills are often exhibited by professional motorsport drivers, who fine-tune their driving behaviour depending on the road geometry or tyre-friction characteristics. On this basis, expert systems incorporating advanced driving functions inspired by the techniques seen on highly-skilled drivers (e.g. high body slip control) are proposed to extend the operating region of autonomous vehicles and achieve high-level automation (e.g. manoeuvrability enhancement on low-adherence surfaces). Specifically, two major research topics are covered in detail in this dissertation to conceive these expert systems: vehicle dynamics virtual sensing and advanced motion control. With regards to the former, a comprehensive research is undertaken to propose virtual sensors able to estimate the vehicle planar motion states and learn the road friction characteristics from readily available measurements. In what concerns motion control, systems to mimic advanced driving skills and achieve robust path-following ability are pursued. An optimal coordinated action of different chassis subsystems (e.g. steering and individual torque control) is sought by the adoption of a centralised multi-actuated system framework. The virtual sensors developed in this work are validated experimentally with the Vehicle-Based Objective Tyre Testing (VBOTT) research testbed of JAGUAR LAND ROVER and the advanced motion control functions with the Multi-Actuated Ground Vehicle “DevBot” of ARRIVAL and ROBORACE.

Abstrakt

Diese Dissertation soll den Weg zur Entwicklung einer zukünftigen Generation hochqualifizierter autonomer Fahrzeuge (HSAV) aufzeigen. Kurz gesagt, es ist beabsichtigt, dass zukünftige HSAVs fortgeschrittene Fahrfähigkeiten aufweisen können, um das Fahrzeug trotz der Fahrbedingungen (Grenzen des Fahrverhaltens) oder Umgebungsbedingungen (z. B. Oberflächen mit geringer Manövrierfähigkeit) in stabilen Grenzen zu halten. Aktuelle Forschungslinien zu intelligenten Systemen weisen darauf hin, dass ein solches fortschrittliches Fahrverhalten mit Hilfe von Expertensystemen realisiert werden kann, die in der Lage sind, die aktuellen Fahrzeugzustände zu überwachen, die Straßenreibungsbedingungen kennenzulernen und ihr Verhalten in Abhängigkeit von der ermittelten Situation anzupassen. Solche Anpassungsfähigkeiten werden häufig von professionellen Motorsportfahrern gezeigt, die ihr Fahrverhalten in Abhängigkeit von der Straßengeometrie oder den Reifenreibungsmerkmalen abstimmen. Auf dieser Grundlage werden Expertensysteme mit fortschrittlichen Fahrfunktionen vorgeschlagen, die auf den Techniken hochqualifizierter Fahrer basieren (z. B. hohe Schlupfregelung), um den Betriebsbereich autonomer Fahrzeuge zu erweitern und eine Automatisierung auf hohem Niveau zu erreichen (z. B. Verbesserung der Manövrierfähigkeit auf niedrigem Niveau) -haftende Oberflächen). Um diese Expertensysteme zu konzipieren, werden zwei große Forschungsthemen in dieser Dissertation ausführlich behandelt: Fahrdynamik-virtuelle Wahrnehmung und fortschrittliche Bewegungssteuerung. In Bezug auf erstere wird eine umfassende Forschung durchgeführt, um virtuelle Sensoren vorzuschlagen, die in der Lage sind, die Bewegungszustände der Fahrzeugebenen abzuschätzen und die Straßenreibungseigenschaften aus leicht verfügbaren Messungen kennenzulernen. In Bezug auf die Bewegungssteuerung werden Systeme zur Nachahmung fortgeschrittener Fahrfähigkeiten und zum Erzielen einer robusten Wegfolgefähigkeit angestrebt. Eine optimale koordinierte Wirkung verschiedener Fahrgestellsubsysteme (z. B. Lenkung und individuelle Drehmomentsteuerung) wird durch die Annahme eines zentralisierten, mehrfach betätigten Systemrahmens angestrebt. Die in dieser Arbeit entwickelten virtuellen Sensoren wurden experimentell mit dem Vehicle-Based Objective Tyre Testing (VBOTT) -Prüfstand von JAGUAR LAND ROVER und den fortschrittlichen Bewegungssteuerungsfunktionen mit dem mehrfach betätigten Bodenfahrzeug "DevBot" von ARRIVAL und ROBORACE validiert.

Acknowledgements

First of all, I would like to thanks the Marie-Curie Sklodowska Actions, the European Commission, and Coventry University, for making possible starting this adventure and funding my research during the first years. Special thanks to my ITEAM colleagues, whose dedication and professionalism have been a constant source of motivation for me.

I would like to express my most sincere gratitude to Prof. Valentin Ivanov for his help, advice and dedication as ITEAM project coordinator and thesis supervisor. I am very grateful to Mr Savitsky as well for helping me to keep on track.

The virtual sensing work described in this thesis was possible thanks to the Tyre-CAE modelling department of Jaguar Land Rover. I would like to thank Mr Jan Prins and Mr Mateo Gladstone for giving me the opportunity to work with their team. I am very grateful to Jaguar Land Rover for all the help during my research.

The work on advanced motion control presented in this thesis was possible thanks to ARRIVAL Software. I want to thank Mr Sergey Malygin for supporting this research. Thanks to Mr Max Kumskoy for his continuous attention. I also really appreciate the support provided by ROBORACE during the “drifting” project. Thank you all for the hard work and dedication to make the tests successful.

Last but not least, thanks to my family and my beautiful wife, Maria, to whom I dedicate my work.

”To achieve anything, you must be prepared
to dabble on the boundary of disaster”

-Sir Stirling Moss.

Contents

Chapter 1

Introduction

1.1 Highly-Skilled Autonomous Vehicles (HSAV)

In spite of the on-going investment on autonomous vehicle technology [96], Autonomous Vehicles (AV) are still experiencing low acceptance rates [90]. The reduction of the safety perceived by the users with the increase of the autonomy level [65] and the loss of driving enjoyment traditionally offered by premium luxury brands are major factors that contribute to this effect. It is expected, therefore, that in order to increase the popularity of self-driving cars, it will be of vital importance to develop more advanced systems capable of exhibiting unparalleled driving features only seen on professional highly-skilled drivers.

Professional rally drivers are considered the most talented drivers of all the motorsport disciplines. They exploit the full chassis potential remarkably well, exciting the yaw transient dynamics to change the vehicle attitude fast and, immediately after that, stabilising the vehicle around a large body slip angle in an impressive drifting motion. They hit the throttle forcefully and apply fast steering corrections based on their reflexes, co-pilot notes, and a limited preview horizon. Furthermore, they adapt their driving style depending on the road geometry or the road friction characteristics. For instance, on tarmac roads they keep a “racing-line” driving style and limit the maximum body slip angle, thus taking advantage of the full vehicle responsiveness and controllability. Conversely, they drift aggressively on gravel surfaces to maximise the lateral friction and increase the centripetal acceleration during prolonged turns.

Following an analogy with chassis control systems, rally drivers may be seen as extremely robust controllers, which can operate the vehicle safely in a wide range of limit situations, and adapt their internal parameters and references to cope with changing friction characteristics. Moreover, this adaptation is carried out without having any particular vehicle or tyre model in mind, but based on the driver's experience and sensory feedback. Ideally, future chassis control systems should incorporate these adaptation and robustness characteristics, Fig. 1.1.

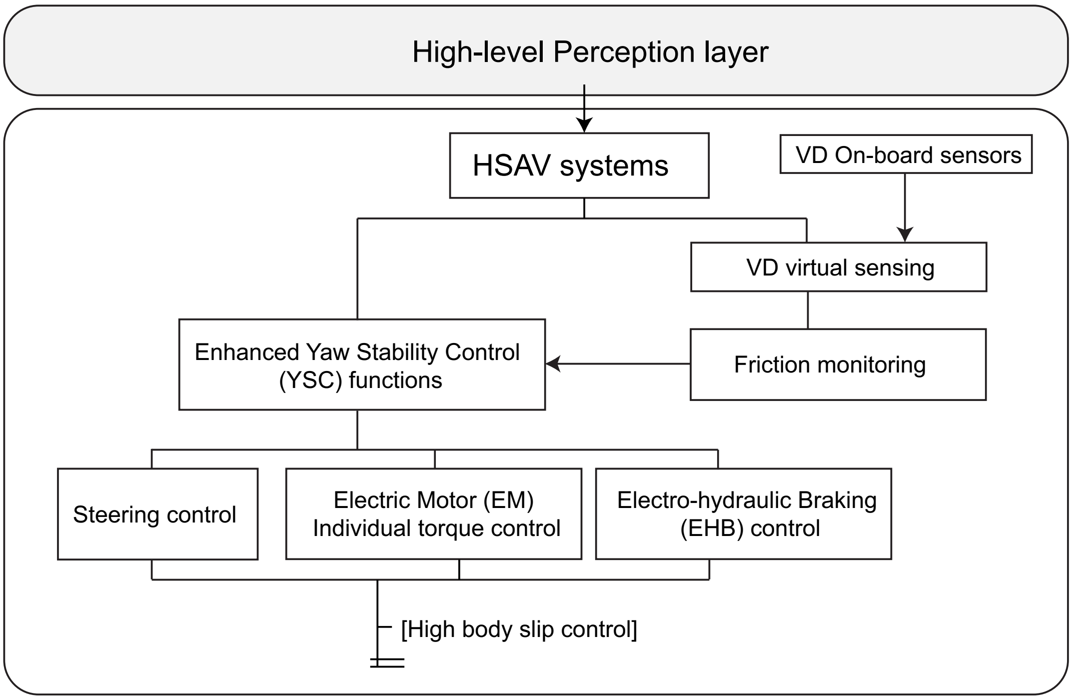

Figure 1.1: Conceptual scheme illustrating the high body slip Highly-skilled Autonomous (HSA) function. The centralised Yaw Stability Control (YSC) coordinates different chassis systems in a wise manner depending on the sensed friction characteristics.

In this way, future envisaged Advanced Driver Assistance Systems (ADAS) or Unmanned Ground Vehicles (UGV) might behave as "expert" drivers to maintain the vehicle stability in certain critical situations (e.g. at the limits of handling) or to drive safely and efficiently over low-manoeuvrability surfaces (e.g. gravel, deep snow, Fig. 1.2). Unfortunately, rallying has always been a complex and not fully understood discipline for vehicle dynamics researchers. Instead, other motorsport variants such as Formula One have been studied in greater detail. Research in this field has contributed to the elaboration of relevant "racing-line" driver models [40]. Despite the fact that these models have been commonly applied in path-following scenarios and have significantly contributed to the development of ADAS functions such as the Lane Keeping Assistance System (LKAS), their suitability under critical conditions that might arise while driving on off-road scenarios (e.g. loose surfaces) or tight road segments (e.g. country roads) has not been addressed in the literature. In these demanding conditions, more advanced driver models able of reproducing expert rally driving skills might perform better [133].

Figure 1.2: Ari Vatanen, Peugeot 405 T16, Pikes Peak 1988. [*supercars.net*]

In what concerns active safety, the vast majority of development efforts on current Yaw Stability Control (YSC) systems have been restricted to the classic controllability principle described by Shibahata et al. [120] and Van Zanten [130], which states that the maximum body slip angle must be kept within low limits to guarantee the vehicle steerability. Although YSC systems based on this principle (e.g. Electronic Stability Program, ESP [130]) have shown a remarkable performance on regular asphalt roads, their function in more demanding road conditions and scenarios might be compromised. Based on empirical evidence, one may think that expert rally driving techniques such as active drifting could be advantageous for exploiting the full chassis potential on extreme off-road surfaces, where the tyre cornering stiffness is drastically reduced and large body slip angles are necessary to build up sufficient lateral friction levels [128]. This reasoning is contrary to the well-established controllability principle introduced previously and leads to the conclusion that drifting-based strategies could help to increase the vehicle safety on loose surfaces during limit lane departure situations (e.g. approaching a turn at excessive speed).

In this line of thought, a reduced number of researchers have started recently approaching new concepts such as vehicle agile manoeuvring [133], autonomous drift control [134, 131], or minimum-time cornering on loose surfaces [128]. These investigations are aimed at providing a better understanding of the vehicle dynamics principles involved in the driving patterns exhibited by expert drivers in the previous critical scenarios. A comprehensive and rigorous analysis of this advanced driving behaviour can elucidate the path towards the development of safer and more sophisticated "intelligent" chassis systems and, in the long term, to the conception of a new generation of Highly-Skilled

Autonomous Vehicles (HSAVs) capable of undergoing any critical scenario and drive safely on any road surface (full level autonomy [114]).

1.2 Current research needs

Nevertheless, there is still a long way to go before the first pieces of evidence for such a generation of autonomous vehicles will be seen. Specifically, an intensive research effort on different areas such as chassis control systems, vehicle dynamics virtual sensing, driving behaviour characterisation, and road geometry recognition will be necessary.

To start with, modern Multi-Actuated Ground Vehicles (MAGV) incorporating individual Electric Motors (EM) and Active Front Steering (AFS) among other systems can significantly enhance the vehicle responsiveness and stability. Individual wheel torque allocation to achieve the desired vehicle response and power expenditure minimisation to prolong the vehicle autonomy are still challenging problems. Of particular importance will be the application of control techniques to coordinate the simultaneous intervention of multiple chassis systems in the presence of actuator constraints (e.g. maximum steering wheel rate) in an optimal manner.

For these systems to execute satisfactory advanced driving skills such as active drift control, stricter requirements regarding vehicle state estimation are foreseen. Some vehicle planar motion states like the body slip angle are still difficult to measure [70], and require the use of dedicated expensive instrumentation (e.g. Differential Global Positioning System, DGPS). The development of virtual sensing tools to infer these motion states from signals already available on the CAN bus of modern vehicles must be pursued to facilitate the implementation of these solutions at a production level. Apart from this, future autonomous vehicles should be able to sense the environment (e.g. road friction characteristics) and adapt their function accordingly, as professional drivers do. Road friction virtual sensing is not a trivial task [19], particularly in the absence of high longitudinal or lateral excitation levels [98], or when driving over non-uniform loose surfaces. Therefore, significant efforts are still needed to develop virtual sensing tools capable of detecting changes in the available road friction, identifying and classifying different surfaces, and learning unknown terrains in real time.

The performance of the previous control systems and virtual sensing tools could be largely enhanced with the aid of Artificial Intelligence (AI). In brief, new artificially intelligent systems could perform advanced virtual sensing tasks such as learning the road friction characteristics directly from the sensory feedback, thus avoiding the necessity of employing a complex analytical tyre model. The adoption of this data-based (e.g.

Artificial Neural Networks, ANN) modelling techniques can be especially attractive in scenarios where analytical models are difficult and expensive to obtain by conventional means. Regarding chassis control systems, the same data-based approaches could be employed to train artificially intelligent systems to reproduce certain driving patterns directly from field tests. As an example, ANN could be used to capture the operating points around which expert drivers stabilise the vehicle during drifting motion on surfaces of unknown friction characteristics. This methodology can substitute the complex feedforward control input generation process, which requires the resolution of quasi-static driving events employing accurate analytical models [134, 50]. The uncertainties derived from imperfect analytical vehicle and tyre models can contribute to decreasing the performance of virtual sensing tools and chassis control systems. The introduction of artificially intelligent data-based and self-learning methods can not only help to curve the errors derived from purely model-based approaches but to reduce the costs related to model characterisation activities.

Finally, apart from the previous control and virtual sensing requirements, there is still an inherent research need for tools and methods to access the road geometry from the fusion of camera-based information, GPS, and inertial on-board measurements. The ability of the future envisaged systems to determine the road curvature at different preview distance points, the path width, and the lateral distance with respect to the path boundaries in adverse environments will be critical to achieving the HSAVs introduced in this section.

1.3 Thesis outline

The rest of the work carried out in this research is structured in the following manner:

Chapter Two: Motivation and state of the art

The motivation behind this research is introduced and a comprehensive overview of the current state-of-the-art of the research topics addressed in this thesis is given.

Chapter Three: Vehicle Dynamics Virtual Sensing

The vehicle dynamics virtual sensors are derived in this section. Relevant solutions to estimate the vehicle planar motion states and the tyre forces adopting Kalman filtering techniques and machine learning-based approaches are described in detail and assessed in IPG-CarMaker following a software-in-the-loop (SiL) validation procedure.

Chapter Four: Advanced Vehicle Motion Control

The controllers and driver models for MAGVs are derived in this section. Controllers for high body slip stabilisation are presented first, followed by a description of the highly-skilled driver model. The proposed solutions are tested in IPG-CarMaker (SiL) and the hardware-in-the-loop (HiL) platform of ARRIVAL and ROBORACE under a wide range of scenarios.

Chapter Five: Experiments

The virtual sensing and motion control concepts introduced in the previous chapters are validated experimentally in this section. Specifically, virtual tyre force sensors are benchmarked against the measurements provided by a fully instrumented vehicle (JLR VBOTT research testbed) in a comprehensive tyre characterisation program carried out in dry tarmac and snow. In the second part of the chapter, the motion controllers are implemented in the DeVBOT driver-less MAGV of ARRIVAL and ROBORACE. Driver-less experiments are carried out in Millbrook proving ground (UK) in dry and wet tarmac conditions.

Chapter Six: Conclusions and future work

Summarises the progress made with this thesis and highlights the potential applications of the presented virtual sensing tools and advanced motion control functions. Relevant guidelines for future investigations on these topics are provided.

Chapter 2

Motivation and State of the art

2.1 How skilled are current Advanced Driver Assistance Systems?

Advanced Driver Assistance Systems (ADAS) are often catalogued as a subset of Driving Assistance Systems (DAS) [149]. In brief, the development of DAS dates back to the eighties decade, when the earliest braking-based chassis systems relying on proprioceptive sensors (i.e. sensors measuring the internal status of the vehicle) were introduced [31]. The Anti-lock Braking System (ABS) and Traction Control System (TCS) were designed first, followed by the Electronic Stability Control (ESC) system [78]. After that, the adoption of new exteroceptive sensors on vehicle systems (e.g. Light Detection And Ranging (LIDAR) and Global Positioning System (GPS)) originated the second generation of DAS, Figure 2.1. This second generation of DAS, often referred to as ADAS, was conceived with the aim to improve the comfort and safety of the driver by sensing, analysing, predicting, and reacting to the road environment [106]. Lane Departure Warning (LDW), Adaptive Cruise Control (ACC) and early Navigation Systems belong to this generation of ADAS.

In spite of the on-going development of DAS, these started to be massively introduced in the market quite recently. This was in part due to the aggressive promotion of DAS technologies carried out by EURO NCAP, making several features mandatory for any new car pursuing the five-star safety rating [97]. Such promotion of DAS attempts to reduce drastically the number of fatal accidents caused by human factors (which accounts for approximately 90% of the total accidents that occur in roads across the EU [129]). Recent studies have shown that every year approximately 26.000 road fatalities occur in the EU [129] and almost 33.000 people lose their lives in road accidents in the United

States [97]. The target of the EU is to reduce the number of traffic fatalities by 50% between 2010 and 2020 [129].

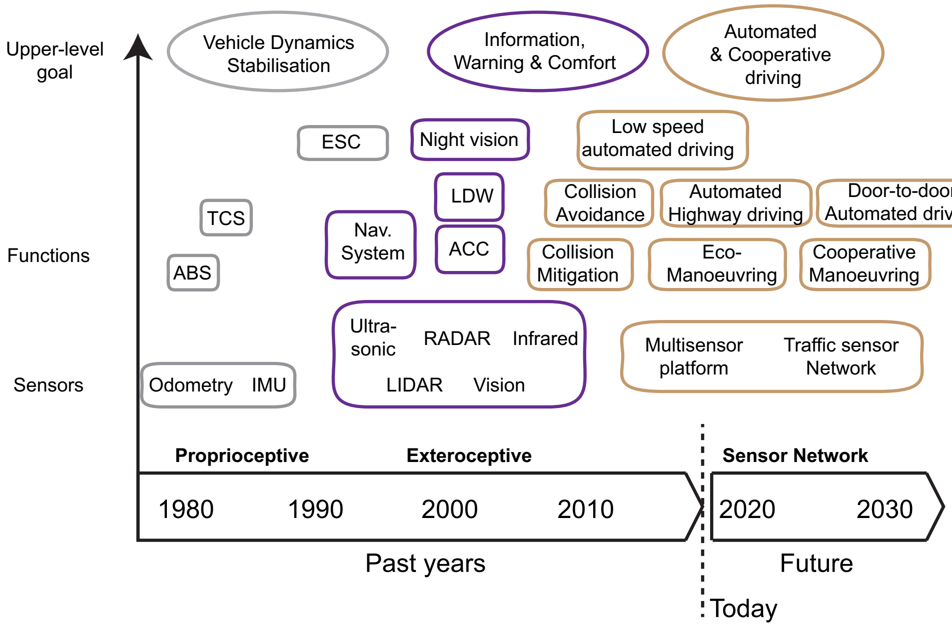

FIGURE 2.1: Past and future potential evolution of DAS systems according to Bengler et al. [31]. Figure reproduced by the author from [31].

The progressive market acceptance of ADAS motivated intensive research and development efforts from Original Equipment Manufacturers (OEMs) and Tier 1 suppliers in cost-effective vision-based and free-space detection technology. These enhanced sensing and recognition technology led to more sophisticated ADAS. Thus, while early ACC systems were able to maintain a predefined speed set by the driver, current Intelligent Speed Assistance (ISA) systems are able to adjust the speed thresholds depending on the current road segment or the traffic surrounding the ego vehicle. In what concerns vehicle safety, several systems under the “collision avoidance” umbrella have been developed to this end. It is expected that the degree of sophistication of these functions will increase significantly during the following years with the refinement of vehicle-2-vehicle (V2V) and vehicle-2-infrastructure (V2I) technologies [31].

From a chassis control perspective, ADAS can be grouped into longitudinal dynamics control, lateral dynamics control and coupled dynamics control. Regarding the first group, ACC, Autonomous Emergency Braking (AEB) and ISA functions have been extensively studied in the literature [79, 105, 80, 59, 142, 69] and implemented in passenger cars (e.g. *BMW Pedestrian Warning with City Brake Activation*). In brief, these functions modulate the braking and driving commands with the aim to diminish the risk of a potentially hazardous situation. The distance with respect to a frontal obstacle or the road speed limits are continuously monitored to assess the probability of these situations to happen, and warn the driver or trigger the system intervention when necessary. In what regards the second group, Lane Departure Warning (LDW), Lane Keeping Assistance Systems (LKAS) and steering-based Rear-end Collision Avoidance Systems (RCAS) have been treated in detail in the literature [35, 63, 41, 32, 93, 77]. Commercially available solutions such as the *Skoda Lane Assist* provide gentle steering corrections and warn the driver through steering-wheel vibrations when lane-departure situations are prone to occur. These partial interventions can be easily overridden by the driver's inputs. Following the SAE automation-level classification [114], the previous systems form part of the level 1 automation (Driver Assistance), Figure 2.2. Early stage DAS (ABS, TCS, ESC) also belong to this autonomy level.

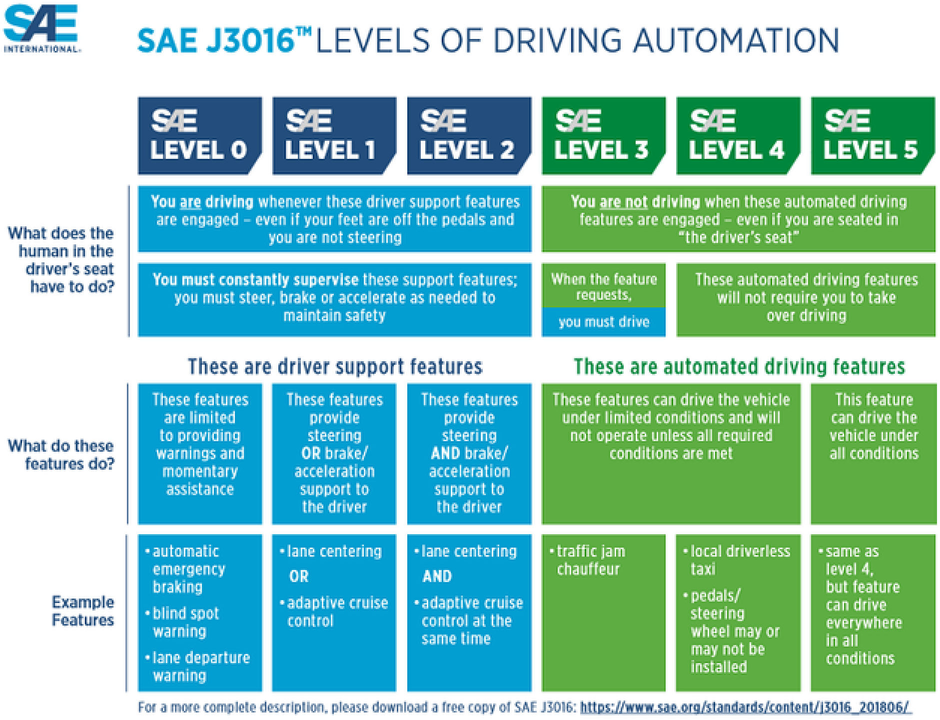

SAE J3016™ LEVELS OF DRIVING AUTOMATION

	SAE LEVEL 0	SAE LEVEL 1	SAE LEVEL 2	SAE LEVEL 3	SAE LEVEL 4	SAE LEVEL 5
What does the human in the driver's seat have to do?	**You are driving** whenever these driver support features are engaged – even if your feet are off the pedals and you are not steering			**You are not driving** when these automated driving features are engaged – even if you are seated in "the driver's seat"		
	You must constantly supervise these support features; you must steer, brake or accelerate as needed to maintain safety			When the feature requests, you must drive	These automated driving features will not require you to take over driving	
	These are driver support features			These are automated driving features		
What do these features do?	These features are limited to providing warnings and momentary assistance	These features provide steering **OR** brake/ acceleration support to the driver	These features provide steering **AND** brake/ acceleration support to the driver	These features can drive the vehicle under limited conditions and will not operate unless all required conditions are met		This feature can drive the vehicle under all conditions
Example Features	• automatic emergency braking • blind spot warning • lane departure warning	• lane centering **OR** • adaptive cruise control	• lane centering **AND** • adaptive cruise control at the same time	• traffic jam chauffeur	• local driverless taxi • pedals/ steering wheel may or may not be installed	• same as level 4, but feature can drive everywhere in all conditions

For a more complete description, please download a free copy of SAE J3016: https://www.sae.org/standards/content/j3016_201806/

Figure 2.2: Automation levels defined by SAE J3016 Standard [114].

Up to now, the complexity of the driving tasks executed by the previous systems is reduced (from a vehicle dynamics point of view). Kinematic models [51] or simplified single-track vehicle dynamics models [147] are often employed to perform the obstacle avoidance or lane-following tasks. In addition, constant cornering stiffness tyre models are normally assumed [147], as the vehicle rarely exceeds the linear region limits during regular driving conditions [94].

Regarding the longitudinal dynamics, Single-Input Single-Output (SISO) control formulations are sufficient to regulate the vehicle speed. With respect to coupled-dynamics control ADAS, these correspond to the second SAE level (Partial automation). Luxury vehicles like the *Tesla S* or the *Mercedes Benz E-Class* incorporate this partial automation and are able to maintain the vehicle longitudinal and lateral control under the driver's supervision. The operating envelope of these functions is limited to regular motorway driving conditions in which the longitudinal and lateral dynamics are not fully excited simultaneously. For instance, in an automated overtaking lane change manoeuvre, the vehicle will normally change to the adjacent line and then accelerate [100]. Therefore, the traditional approach found in the literature is to develop the longitudinal and lateral controllers individually, using the above-mentioned vehicle models, and then coordinate the controller actuation in a conservative way so as to maintain the vehicle stability [147, 51, 27, 28].

In what concerns the third autonomy level (conditional automation), Audi announced recently the first vehicle (new Audi A8, commercially available in 2019) that will officially belong to this group. Specifically, the difference with respect to other existing vehicles lies in the incorporation of a fully automated driving function (*Audi AI traffic jam pilot*), which will be available during traffic jams or congested traffic environments (for driving speeds below 60 kph). This technical solution correlates well with the evolution towards fully automated vehicles predicted by Bengler et al. [31], Figure 2.1. According to the authors, low-speed automated driving is expected to be achieved first and implemented in certain operating environments under the level-4 autonomy label (e.g. fully automated urban city driving). In these low-demanding vehicle dynamic conditions, it is expected that further refinements with respect to the vehicle models and chassis control systems employed in the previous ADAS will not be required.

Overall, the technical evolution observed during recent years in areas such as image processing and vision-based artificial intelligence for automated driving contrasts with the lack of advancement and research in other areas relevant to vehicle dynamics and chassis control systems. The necessity of broadening the knowledge in subjects like advanced driving skills, vehicle dynamics virtual sensing or vehicle behaviour at the limits of handling is twofold. First, there is still a significant research gap in what concerns vehicle safety. Current Yaw Stability Control (YSC) systems are aimed at maintaining the vehicle stability in conventional road scenarios (e.g. aggressive lane change on a motorway). Despite the fact that different control formulations have been proposed to increase the robustness of these systems, their function principle has been maintained during the last decades (yaw-controllability principle presented by Van Zanten [130]), and their performance on more demanding road conditions (e.g. on loose surfaces) has not been fully evaluated yet. Second, current ADAS are precursors of the future envisaged autonomous vehicles. As remarked by Bengler et al. [31], the ultimate goal of the driverless-future concept is to have vehicles with the ability to drive autonomously at a safety level **significantly superior** to that of average human drivers in the presence of other traffic agents. Leaving aside the developments still needed in areas such as car-to-X communications, the previous statement will not be realisable if future autonomous vehicles do not incorporate advanced driving skills. Otherwise, future autonomous vehicles will demonstrate average skills for conventional driving tasks and will rely on the intervention of current YSC systems when things go wrong (e.g. in a road junction during snowy conditions), as “average” drivers do. Therefore, at this point, it is of vital importance for vehicle dynamics and chassis systems engineers to investigate the major requirements to produce AVs incorporating **significantly superior** safety levels. Some of these requirements might be better understood if the following research questions were answered:

- *What is behind some well-known advanced driving skills? What motivate expert drivers to execute these tasks?*
- *Would it be possible to develop controllers capable of performing these tasks autonomously or semi-autonomously?*
- *Which set of vehicle states or environmental factors need to be monitored to develop these advanced systems?*
- *Are these tasks realisable with current chassis architectures? Are more complex chassis architectures (MAGV) necessary for these tasks?*

This thesis is motivated by the necessity of addressing the previous questions and is the consequence of an intensive academic and professional research activity in the areas of *advanced driving skills, vehicle dynamics virtual sensing*, and *multi-actuated chassis control systems.*

2.2 Advanced driving skills

A first rough distinction between a “regular” road driver and a highly-skilled driver can be established based on the vehicle inputs exhibited by each. According to Blundell and Harty [36], the behaviour exhibited by skilled rally drivers is characterised by a rapid and high-frequency steering content. While an average road driver will often operate within a 1 Hz frequency bandwidth, a professional rally driver can exhibit a significant spectral content for frequencies up to 5 Hz in an off-road rally stage. Apart from this, skilled drivers combine their steering inputs with the longitudinal vehicle control (throttle / braking modulation) in order to extract the maximum chassis potential operating along the tyre friction boundaries (commonly represented by the G-G diagram or adherence ellipsoid) [119]. Conversely, "regular" road drivers are unable to operate safely at the limits of handling during combined-slip situations (e.g. trail braking) and work well inside the tyre friction limits, Fig. 2.3.

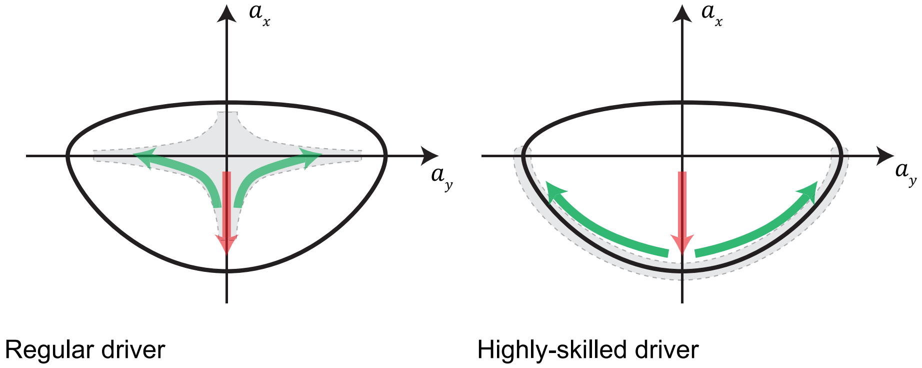

FIGURE 2.3: a_x: Longitudinal acceleration, a_y: Lateral acceleration. Left: Regular driver operating well inside the adherence ellipsoid boundaries. Right: Highly-skilled driver operating along the boundaries of the adherence ellipsoid.

The first pieces of evidence of the interest of automotive researchers on modelling the driving behaviour exhibited by professional drivers can be found in the works carried out by Velenis et al. [135, 136]. The authors studied numerically typical rally manoeuvres characteristic of loose surface stages like trail-braking or pendulum turn. The vehicle planar dynamics were approximated using a single-track (ST) vehicle modelisation and the tyre planar forces using a simplified isotropic *Magic Formula* tyre model [104]. The influence of the suspension dynamics on the vehicle planar behaviour was disregarded and the driver's steering and throttle inputs were parameterised. A minimum-time cornering Optimal Control (OC) problem was solved and the optimum steering and throttle commands were compared to those obtained empirically in the vehicle dynamics simulation software CARSIM [121] using a static driving simulator. Overall, a close similarity between the optimal and empirical driving commands was observed.

Following a similar OC formulation, Berntorp et al. [33] approached the minimum-time-cornering problem of a hairpin turn. In this case, the authors focused on a high-mu rigid surface and calculated the optimal vehicle responses for different tyre modelisations. Specifically, the authors computed the tyre forces under pure tyre slip conditions using a *Magic Formula* formulation and calculated the forces under combined slip conditions using two different methods: the friction ellipse (FE) and weighting functions

(WF). Moreover, the authors performed this analysis assuming isotropic and anisotropic tyre characteristics. A single-track vehicle model was considered and the suspension dynamics and weight transfer were disregarded, assuming static vertical forces on the front and rear axles. Overall, the authors remarked that the qualitative behaviour was similar for all the models considered. Nevertheless, some dissimilarities were observed during braking events. The authors explained that this might have an impact on model choice, particularly if braking-based active safety systems are considered. This study was extended in [34], where three different vehicle modelisations (two-track with suspension dynamics, single-track with pitch dynamics (ST-pitch), and single-track with static loads) were combined with the previous FE and WF tyre models (dry asphalt conditions). The authors provided a detailed discussion regarding the minimum-time-cornering results obtained for a ninety-degree turn and a hairpin turn. In brief, it was pointed out by the authors that important differences were observed between different combinations of chassis and tyre models. Thus, the authors stated that the choice of different models can potentially lead to fundamentally different control strategies. For instance, the use of the FE or WF tyre models on the two-track chassis model seems crucial due to the influence of the weight transfer and suspension dynamics on the tyre forces under coupled-slip conditions. Apart from this, the authors remarked that the results obtained with the ST-pitch model may be too unrealistic, presenting high body slip angles that do not correlate well with the racing-line driving style seen on high-mu rigid surfaces. Last but not least, the authors mentioned that the differences seen on low-order models could be alleviated employing an online control implementation with feedback. Following this research line, Lundhal et al. [91] complemented the previous study taking into account the influence of the friction coefficient of rigid surfaces on the minimum-time cornering problem. In this case, a more complex *Magic Formula* WF tyre model was adopted to approximate the tyre friction forces in dry asphalt, wet asphalt, and smooth ice conditions. These tyre models were generated following the scaling parameter extraction study presented by Braghin et al. [37].

The influence of the road surface on the vehicle cornering performance was also evaluated by Tavernini et al. [128]. The authors synthesised the vehicle responses using a single-track planar dynamics model and approached the minimum-time cornering problem of a ten-metre radius hairpin turn. Different rigid and loose surfaces (dry asphalt, wet asphalt, dirty off-road, and gravel) were reproduced using an isotropic *Magic Formula* tyre model. The pitch suspension dynamics were also considered assuming a first order like response. This problem was solved adopting an OC formulation. The authors demonstrated that in off-road terrains (Fig. 2.5-b) high body slip solutions are associated to minimum-time cornering manoeuvres whereas a racing-line driving style (low body slip) is desirable in rigid surfaces (dry and wet asphalt). These results correlate well with the behaviour seen in rallying. As can be noticed in Fig. 2.4, professional rally drivers often maintain a high body slip angle along curved segments when driving over snow (c) or gravel (b) terrains. These cases contrast with the driving style seen on tarmac segments, which resembles the racing-line style adopted in other *motorsport* disciplines (e.g. formula).

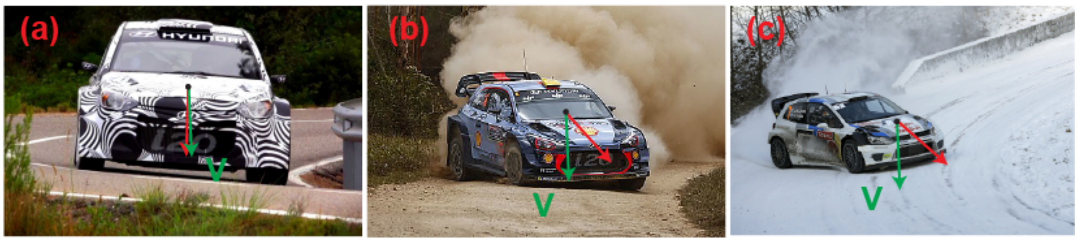

Figure 2.4: (a) Turning on tarmac (low body slip), (b) Turning on gravel (High body slip), (c) Turning on snow (High body slip).

This particular behaviour motivated the elaboration of relevant works [50, 134] to address the high body slip stabilisation problem. To start with, Edelmann and Plöchl [50] performed a numerical analysis of the steady-state drifting motion employing a two-track vehicle planar dynamics model and a quasi-static weight transfer model based on the roll stiffness distribution. Wet asphalt conditions were approximated using a nonlinear steady-state tyre model (the reader is referred to [81] for additional details). Steady-state conditions were imposed on the vehicle dynamics equations and drift equilibrium solutions were obtained for a fifty-metre circular trajectory. The authors performed several drifting field tests and demonstrated that the numerical solutions match reasonably well the real vehicle states. Authors concluded that the powerslide motion is unstable regardless of the vehicle speed, as two eigenvalues lie on the positive semi-plane of the complex plane for all the velocities. The quick steering corrections (up to 1100 degrees/s [36]) and "pedal dance" (see Walter Röhrl [53]) exhibited by professional rally drivers is an empirical evidence of this unstable behaviour where the driver acts as a multi-actuated system that stabilises the plant (chassis) around an unstable high body slip equilibrium point.

In [134], Velenis et al. followed a similar approach than [50] and computed the high body slip equilibrium points using a two-track vehicle planar dynamics model. A Rear-Wheel-Drive (RWD) powertrain layout and a viscous Limited Slip Differential (LSD) were considered during this analysis. The friction forces developed on a typical loose surface were approximated using an isotropic *Magic Formula* tyre model. This numerical analysis evidenced that high body slip equilibrium solutions (i.e. drifting) increase the centripetal acceleration generated while the vehicle is in cornering motion. The main explanation for this behaviour resides on the abrupt reduction in the tyre cornering stiffness caused by the interaction of the tyre's carcass with the particles present on the upper layer of these surfaces. Some authors have named this phenomenon as the "equivalent tyre-road stiffness" [47, 19]. In relation to this, field tests [20] have demonstrated that these surfaces exhibit a monotonic friction versus slip curve 2.5. This monotonic shape has been labelled by some authors as the *bulldozing* effect [22, 88]. In few words, this principle states that in surfaces like snow or gravel the friction is maximised when large tyre slips are present and the tyre sinks on the surface.

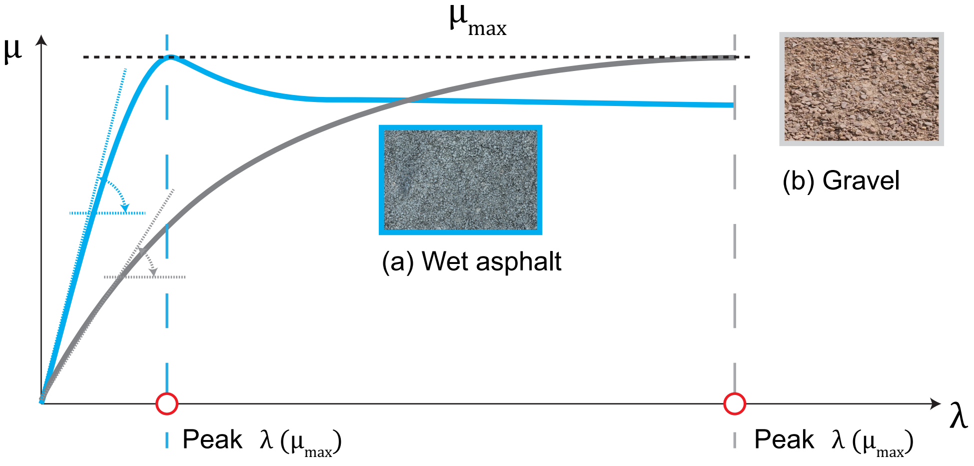

FIGURE 2.5: Typical friction (μ) versus slip (λ) shape of (a) rigid surface and (b) loose surface. Friction curves reproduced from the tyre parameters detailed in [128].

In addition to the previous works on high body slip stabilisation, Li et al. [85] and Yi et al. [144] studied the ability of professional drivers to control the vehicle outside the chassis stable limits. In a first study, Li et al. [85] modelled the vehicle planar behaviour with a two-track model and the tyre forces with the Burckhardt tyre model [78]. The tyre vertical loads at each axle were computed using a quasi-static weight transfer approach and the yaw moment components derived from uneven longitudinal forces were disregarded (i.e. no differential braking action). The authors linearised the system dynamics ($\dot{x} = Ax$) under different combinations of the front and rear longitudinal slips and computed a stability region based on the stability properties of the system matrix A. Some interesting results obtained by the authors are (a) rear wheel lock leads to severe instability and (b) positive longitudinal slips on the front and rear axles help to maintain the vehicle stability. An example of the former statement can be found during the hand-brake inputs previous to a tight turn, where it is pursued to induce a large yaw instability to maximise the yaw acceleration. The latter conclusion seems reasonable since All-Wheel-Drive (AWD) vehicles are easily controllable during positive accelerations due to the even lateral grip reduction experienced by the front and rear axles. This analysis was completed by Yi et al. in [144] were the authors computed a wide range of stability regions using a more sophisticated hybrid physical/dynamic tyre friction modelisation based on the *LuGre* dynamic friction model [143].

The previous analyses on vehicle stability at the limits of handling led to the elaboration of the first high body slip stability control systems. In [132, 133], the authors introduced a preliminary "drift" control system adopting a torque control formulation based on Sliding Mode Control (SMC). A single-track vehicle model was employed and the tyre forces were approximated using an isotropic *Magic Formula* tyre model. Initially, the authors developed a synthesised control system based on the same vehicle model used during the simulations. After that, the vehicle model complexity was increased (considering the pitch dynamics) and the robustness of the synthesised controller to changes in the road friction characteristics was studied. An important conclusion provided by the authors is that the system performance is affected if the tyre parameters embedded in the controller do not match the real friction characteristics. These results evidenced the importance of monitoring on real-time the tyre friction characteristics to enhance the controller performance. This research evolved into a new drift control system using steering and drive torque control inputs [134]. Moreover, a new RWD chassis configuration equipped with an LSD differential was considered in a two-track vehicle model. Once again, the tyre friction forces were calculated using an isotropic *Magic Formula* modelisation. A Linear Quadratic Regulator (LQR) backstepping controller was implemented in CARSIM and drift control was verified for different open loop constant-radius circular manoeuvres.

Furthermore, the closed-loop solutions obtained in the software CARSIM were compared to experimental measurements obtained from field drifting tests. Overall, a good correlation between the simulations and experimental signals was observed. The drift stabilisation problem has been revisited intermittently since Velenis works [56, 66, 55, 46]. Thus, Gray et al. [56] proposed a semi-agile automated vehicle capable of performing drifting manoeuvres. Nevertheless, detailed information regarding the drift control system was not revealed. Hindiyeh [66] carried out a detailed investigation regarding the drift equilibrium solutions and proposed different longitudinal and lateral control strategies to stabilise the vehicle at high body slip angles. These controllers were implemented and assessed experimentally in the P1 testbed of Stanford University. Gonzales et al. [55] employed an LQR formulation to achieve the drift stabilisation and substitute the full-state feedback assumption by means of vision-based state estimation. Finally, Cutler and How [46] used Reinforcement Learning (RL) to stabilise a radio control prototype car in a circular drifting motion without prior knowledge of the tyre friction characteristics.

2.2.1 Summary and research gaps

To sum up, the research carried out up to now in the advanced driving skills topic is still insufficient and not very mature. The most relevant aspects of the current state-of-the-art, as well as the major research gaps existing in this field, can be summarised in the following points:

- **Chassis and tyre model complexity**: Overall, low-complexity chassis models (single track and two track) have been employed in OC problems and model-based controller design. In these cases, the suspension dynamics are often disregarded or approximated using a second order roll-pitch suspension model. More complex formulations incorporating the suspension kinematics have not been found in the literature. The controller robustness to unmodelled suspension dynamics and kinematics has been evaluated in several works with successful results. Regarding the tyre modelisation, the isotropic *Magic Formula* tyre model has been widely used in drift stabilisation on loose surfaces. In some cases, the full-vehicle-level responses from the simulation model have been compared to the responses measured in a real vehicle during field tests on off-road surfaces. The usage of synthesised chassis and tyre models during the design of model-based controllers has been derived from the necessity of achieving a real-time control operation in state-of-the-art on-board controllers. Finally, the predominant trend is to consider known tyre parameters during the design of the controller for a fixed road surface condition. In this sense, a significant research gap exists in what concerns the development of high body slip control systems with the ability to adapt to different road surfaces.
- **High-fidelity simulation environment**: As mentioned previously, the vehicle behaviour has been approximated using simplified chassis models in optimal control problems. These models are sufficient to provide a high-level idea of the vehicle behaviour and give some hints regarding the vehicle dynamics principles behind some manoeuvres (e.g. why drifting on loose surfaces if minimum-time cornering is pursued). Nevertheless, during controller validation and verification, high-fidelity vehicle dynamics simulation software is desirable to approximate with higher accuracy the real vehicle responses. Among the cases studied in this section, real-time simulation software (e.g. Carsim [121], Ipg-CarMaker [29]) seem most suitable for controller implementation (due to their SiL and HiL capabilities) and have been widely employed in the literature. Pieces of evidence regarding the use of other multibody software often employed in the automotive industry (like Simpack [127] or Msc Adams [124]) have not been found in the literature. The latter programs require higher computational resources and are more oriented towards

the detailed analysis of subsystem forces and suspension kinematics (e.g. ride analysis). Finally, the validation of the control systems discussed in this section has been achieved predominantly in a SiL stage.

- **Applicability to AVs**: At this point, the current research in advanced driving skills has shown some interesting and promising results. Nevertheless, there is still little light regarding how these driving skills should be implemented to increase vehicle safety. The majority of the results presented in this section have been obtained adopting an optimal control approach, and therefore real-time closed-loop control policies to reproduce this behaviour are still to be designed. Furthermore, in those cases in which closed-loop controllers based on advanced driving skills (e.g. drift stabilisation) have been developed, the vehicle safety benefits derived from this actuation have not been fully explored. Aspects such as the path-following ability of these systems need to be addressed before these control systems could be considered as novel ADAS functions.

- **Full-state feedback and MAGV architectures**: In the vast majority of the works analysed in this section it is assumed that vehicle states like the body slip angle can be easily measured. There is still an important research need in what regards the development of virtual sensing techniques. The possibility of adopting tyre-model-less approaches in the virtual sensor construction seems very attractive since the uncertainties associated with different tyre models could be eliminated. Furthermore, this seems the only valid alternative when drastically different surfaces are considered. As pointed out in [91], applying a friction scaling approach in a tyre model parameterised on high mu may be insufficient to provide accurate tyre force estimates in some particular surfaces (e.g. non-rigid surfaces). With respect to MAGV architectures, their ability to reproduce advanced driving skills has not been evaluated yet. The combination of Active Front Steering (AFS) and vehicle longitudinal control has been successfully accomplished in some works on drift stabilisation. Nevertheless, the potential agility or cornering improvement that could be achieved with the exploitation of chassis architectures incorporating in-wheel EM is still to be addressed. Moreover, as the final system performance might be compromised by the real actuator limitations, the consideration of chassis actuator constraints in the design of the highly-skilled control system is an important aspect that should not be overlooked.

The previous points, especially the virtual sensing requirements expected to accomplish the envisaged HSAVs (e.g. friction learning) motivated the elaboration of a comprehensive literature review on virtual tyre force sensors [11] and road friction monitoring

[10]. Due to space limitations, only a brief overview of these works is presented in the following.

2.3 Vehicle Dynamics Virtual Sensing

The real-time measurement of the tyre forces is of vital importance to extract information regarding the road friction conditions. Unfortunately, direct measurement techniques are still restricted to automotive testing or research, and not suitable for mass implementation. Wheel force transducers (WFT) are still too costly to be mounted in production vehicles [49] and their use is reduced to testing activities during vehicle development stages [89]. The *Smart Tyre* technology is still under development [44, 43] and current results indicate that further investigations are required before this technology can be implemented in regular tyres. Finally, despite *SKF*® or *NSK*® have developed different designs of Load Sensing Bearings (LSB), these are still not commercially available. Aspects such as the elastic deformation of the knuckle affect the measurement accuracy and are currently being investigated [76]. These limitations justify the necessity of evaluating different virtual sensing alternatives.

According to a recent literature survey elaborated by the author of this thesis, two trends can be clearly differentiated regarding tyre force virtual sensing: *tyre-model-based* and *tyre-model-less* approaches, Fig 2.6. In the former group, Antonov et al. used an empirical *Magic Formula* tyre model in [25] to compute the tyre forces from a set of tyre states (tyre longitudinal slip, lateral slip, vertical force and wheel inclination angle). The states required by the tyre model were computed adopting an Unscented Kalman Filter (UKF). In a similar line of thought, Doumiati et al. employed a *Dugoff* tyre model formulation in [48, 49] and described the vehicle planar dynamics adopting Extended Kalman Filter (EKF) and UKF observers. Overall, the major limitation of these model-based approaches is that the tyre model parameters need to be known *a priori* for fixed road friction conditions. Depending on the model complexity and the mismatches between the tyre characterisation testbed and the real tyre operating conditions, the force estimation will be subjected to a certain degree of uncertainty.

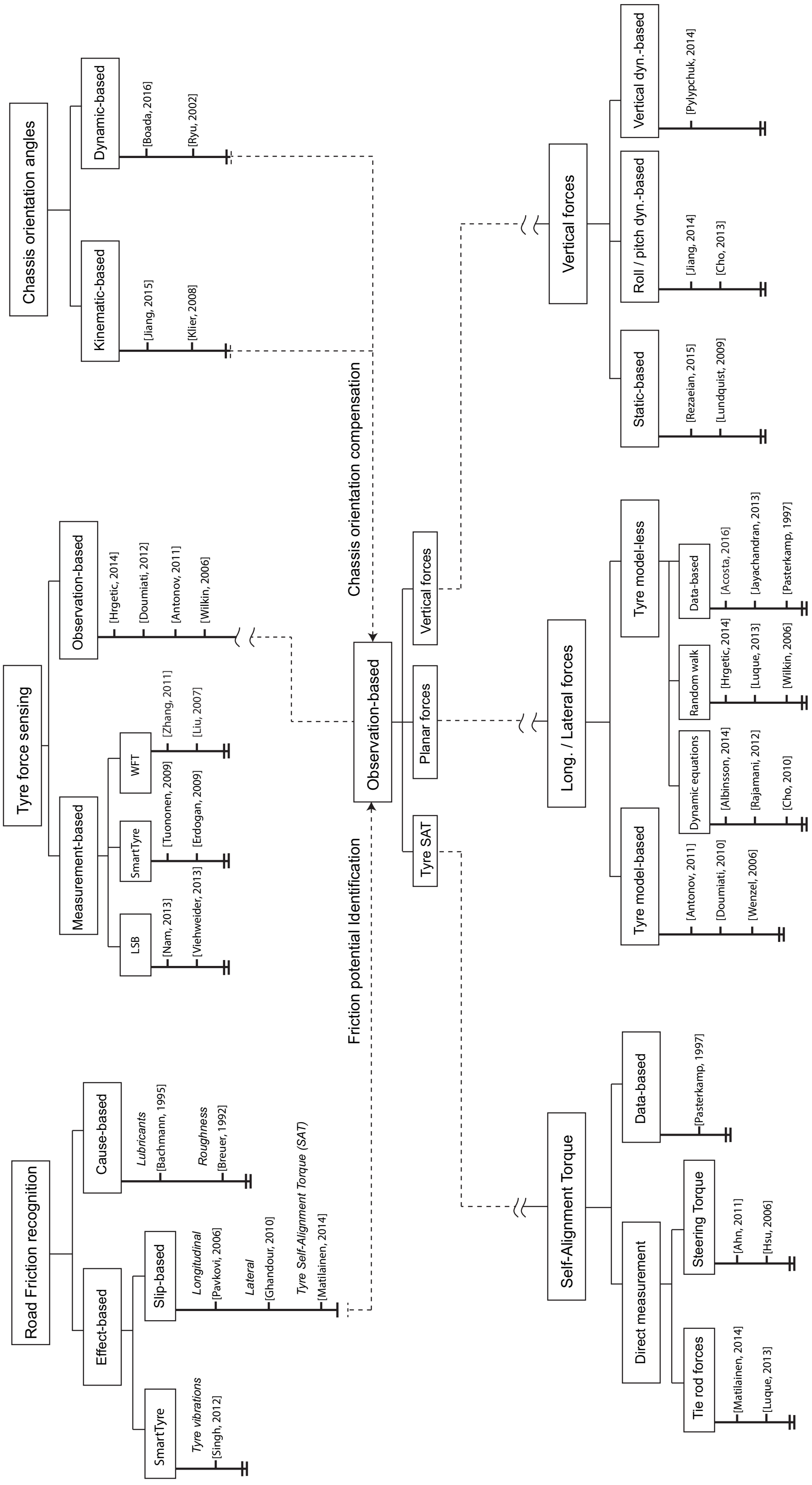

FIGURE 2.6: Overall picture of the tyre force virtual sensing problem found during the literature survey prepared by the author of this thesis [11].

Such uncertainties might be caused by pressure and temperature variations, wear, suspension kinematics and compliances or a limited wheel slip characterisation range. In addition, if the friction characteristics of the road change, it is necessary to scale the tyre forces with a suitable friction scaling factor. In this sense, the necessity of computing a timely and accurate estimation of the maximum friction coefficient complicates significantly the tyre-model-based virtual sensing problem.

Concerning *tyre-model-less* approaches, a tyre model is not necessary to build the virtual sensor. In this case, stochastic-based approaches are predominantly adopted. Examples of this virtual sensing technique can be found in the works elaborated by Ray [108] and Wilkin et al. [141]. In brief, the authors modelled the tyre forces as random-walk variables and integrated these into a model-based state estimator representing the vehicle planar dynamics (often in the form of an EKF or UKF observer). The estimation of the tyre forces is achieved by correcting the states predicted by the model in the *measurement update stage* of the Kalman filter [48]. The major advantage derived from this approach is that an estimation of a friction scaling factor is not required to correct the estimated tyre forces. This makes this approach very attractive for applications in which uncertain road friction characteristics are expected. On the other hand, a complex and time-consuming calibration of the state estimator is necessary in order to achieve sufficient dynamic response while maintaining low noise levels on the random-walk observer states.

Additional information regarding other less common virtual tyre force sensing approaches as well as direct tyre force measurement techniques can be found in the literature review prepared during the course of this research [11].

2.3.1 Road friction monitoring

To this end, several approaches have been discussed in the literature to estimate the road friction potential. A first classification provided by Müller et al. in [98] established a distinction between *cause-based* and *effect-based* approaches. While *cause-based* approaches focus on estimating the road friction potential from aspects such as the lubricant present at the road surface [38], *effect-based* approaches infer the road friction from the tyre responses (e.g. lateral or longitudinal slip [57]), Figure 2.7. A general trend exhibited by slip-based solutions is that a significant excitation level (up to 80-90% on low-mu conditions [122]) is required to provide an accurate estimation of the maximum available road friction [24, 78, 19, 126]. This may not be a major problem for current DAS systems like ABS, TCS, or ESC, which intervene when significant lateral or longitudinal excitation occurs [26, 148, 107] (e.g., during an emergency braking manoeuvre).

In these cases, the road friction potential can be inferred during the system intervention and the DAS thresholds can be adjusted in parallel [60, 87].

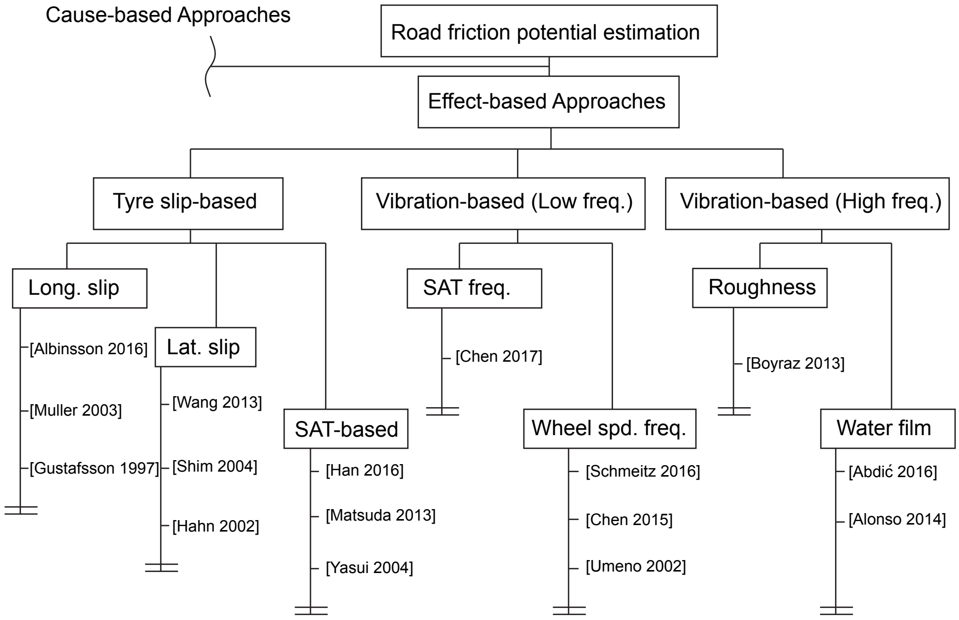

Figure 2.7: Overall picture of the effect-based road friction recognition approaches found during the literature survey prepared by the author of this thesis [10].

Nevertheless, with the development of new ADAS functions and the growing interest in the advanced-driving-skill functions presented in previous sections, new stricter requirements regarding the road friction estimation have arisen [86, 82, 134]. Specifically, it is expected that the realisation of functions such as high body slip control on non-rigid surfaces will not only require an estimation of the maximum road friction, but also a more detailed characterisation of the road surface (e.g. force versus slip curve [134, 128]). Apart from this, functions such as ACC [95] or AEB [80] require an accurate and timely estimation of the maximum road friction before system intervention. Thus, the road friction potential should be continuously monitored during free-rolling, coast-down, gentle acceleration or gentle steering events to correct critical variables such as the minimum separation between vehicles.

Despite the fact that *cause-based* approaches can potentially facilitate the estimation of the maximum available road friction during free-rolling or low-excitation driving conditions, an important handicap of these is that a large database is required in order to achieve an accurate correlation between the monitored tyre-road property (e.g. noise emitted by the tyre) and the road friction potential [98]. Therefore, such approaches might present insufficient correlation [23] or extrapolation issues when situations not included in the training dataset are faced. A friction-fusion approach employing both *effect-based* and *cause-based* approaches could help to overcome the drawbacks derived from each estimation technique. Thus, an initial "rough" road friction estimation or "road label" (e.g. wet road) obtained from a cause-based approach could serve to initialise the system during low excitation driving. This initial estimate would be then adapted on real-time during high dynamic excitation by means of an effect-based approach. For a comprehensive discussion on road friction monitoring the reader may consult the literature survey prepared by the author of this thesis [10].

2.3.2 Summary and research gaps

The most relevant conclusions, as well as the research gaps identified during the elaboration of the literature surveys [11, 10] are summarised in the following.

- **Tyre modelling resources:** Parameterising a tyre model in a wide range of friction conditions is not straightforward and therefore limits the applicability of tyre-model-based virtual sensors. This task may be alleviated with the aid of artificial intelligence (e.g. using Artificial Neural Networks) or random-walk tyre force modelling. If the former approach is employed, it is necessary to construct a suitable training dataset from experimental tests. An important aspect of data-based approaches is the lack of extrapolation ability to handle driving events not included in the training dataset. If the virtual sensor is aimed at estimating the tyre forces during non-conventional manoeuvres in which extreme tyre slips can be achieved (e.g. high body slip stabilisation), a stochastic approach without boundary constraints might be preferred, as the construction of a suitable training dataset for this operating envelope would be extremely costly.
- **Road friction characteristics:** If it is aimed to estimate the tyre forces while the vehicle is driven on conventional rigid surfaces (i.e. tarmac roads), tyre model-based or data-based approaches employing a suitable maximum friction scaling approach [104] may be sufficient. On the other hand, if large excursions into off-road segments are expected, a stochastic approach robust to road friction uncertainties is preferred. As the tyre force versus slip curve is abruptly distorted in loose surfaces, a model-based friction scaling approach can lead to inaccurate results. According to the well-established tyre modelling theory impulsed by Pacejka [104], a single friction scaling factor (commonly known as the maximum road friction factor or the road grip potential) might be sufficient to represent the tyre behaviour in a wide range of rigid road surfaces using a single tyre model characterised on dry conditions. This concept is true as long as the road surface can be considered infinitely rigid compared to the tyre's carcass [19]. Unfortunately, little information exists in what concerns the characterisation of loose surfaces like

snow or gravel, where the *bulldozing* effect contributes drastically to the generation of the tyre friction. In these cases, a single variable is not enough to represent accurately the road friction characteristics, as the friction versus slip shape varies abruptly depending on the agents present in the tyre-surface interface.

- **Self-learning structures**: Following the previous point, it is worth remarking the importance of developing structures capable of learning the current friction characteristics to provide with friction-based "adaptation" skills the envisaged HSAVs. The introduction of artificially intelligent structures may facilitate the extraction of a richer surface feature vector, instead of a single maximum friction factor as current *slip-based* friction monitoring approaches do. AI-based solutions may be implemented on this basis by means of ANNs or Adaptive Neuro-Fuzzy Inference Systems (ANFIS). These could be trained regularly to approximate a cloud of friction versus slip points extracted from on-board measurements during the vehicle operation. As mentioned previously, this will be critical to recognise surfaces in which peak friction values are achieved at high slip values and that can not be explained by the classical tyre modelling theory (for a comparison of different friction versus slip curves the reader may consult the works carried out by Tavernini et al. [128] and Albinsson et al. [20]).

2.4 Advanced Motion Control

The discussion on advanced driving skills presented in Section 2.2 evidenced the necessity of coordinating inputs from different system domains (e.g. steering, powertrain, brakes) to mimic certain professional driving tasks (e.g. trail braking, high body slip stabilisation). Therefore, using single standalone braking-based (ESC) [83] or steering-based (AFS) [45] systems may be insufficient to produce the envisaged HSAVs. In order to gain some insight into the different methodologies existent in the literature to coordinate systems from different domains in a MAGV framework (Fig. 2.8), this chapter is completed with a discussion on Integrated Chassis Control (ICC) architectures. For additional details on this topic relevant works carried out by the Fakultät für Maschinenbau of the Technische Universität of Ilmenau can be consulted [74, 115, 73].

2.4.1 Integrated Chassis Control

According to Chen et al. [45], the coordinated intervention of different chassis subsystems in an ICC framework can offer superior performance levels than the independent actuation of different standalone subsystems. The authors defined three major chassis

Figure 2.8: "DevBOT", first autonomous race car developed by ARRIVAL and ROBORACE. This Multi-Actuated Ground Vehicle is equipped with four independent electric motors, independent front and rear brake-pressure lines and steering control. LiDARS, cameras, and a high-accuracy two-antenna GPS system complete the vehicle perception and positioning features.

integration strategies as de-centralised, centralised and multi-layer. This classification was also adopted by Vivas et al. in [137]. These integration strategies are depicted schematically in Fig. 2.9, and can be explained in the following manner:

- **De-centralised control**: In this case, each subsystem tries to fulfil its own particular goals, which difficulties the achievement of a full-vehicle optimal performance. Moreover, some stability problems may arise if the individual goals obey contradictory control objectives (E.g., rear Active Roll Control System (ARCS) trying to mitigate rollover but causing severe unstable behaviour during ESC interventions due to an increase in the rear axle roll stiffness [145]). The major advantage of this integration strategy relies on its implementation easiness and the lack of information exchange between different suppliers and OEMs. Specifically, each active subsystem can be treated as a "black box" and integrated into the chassis platform independently from the rest of vehicle components, thus avoiding the disclosure of confidential information or intellectual property.
- **Centralised Control**: When this integration strategy is applied, all the vehicle states to be controlled are embedded in a central controller. For instance, if an ICC system to coordinate the suspension and vehicle planar dynamics were to be designed, the controller vector of states might be composed of vehicle planar states like the chassis velocities and yaw rate, as well as vehicle suspension states like the roll, pitch, or suspension deflection rates. Incorporating several

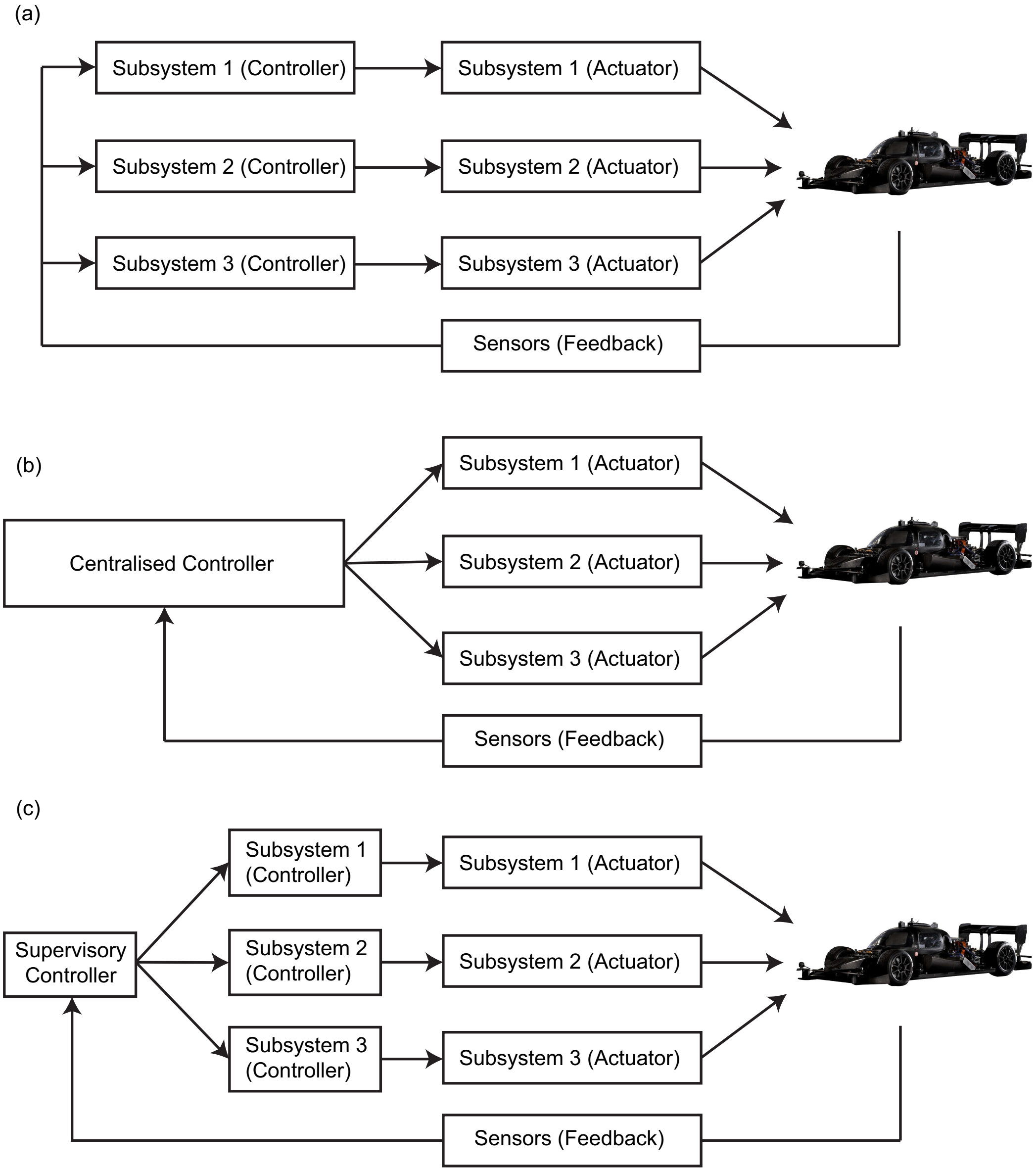

FIGURE 2.9: ICC strategies. (a) De-centralised ICC, (b) Centralised ICC and (c) Multi-level ICC. Figure adapted by the author from Vivas et al. [137].

vehicle domains into the central controller may lead to a significantly large vector of states. This can complicate the design procedure and implementation of an optimal Multi-Input Multi-Output (MIMO) control formulation (e.g., non-trivial and time-consuming tuning procedure). In addition, the large computational resources required by such central controller may prevent its implementation in a commercial ECU. Apart from the previous technical considerations, implementing this control architecture requires having access to all the chassis subsystem signals (e.g., Continuous Damping Control (CDC)+Electronic Stability Control (ESC)).

As these subsystems can be developed by different suppliers it is expected that some information exchange between suppliers and OEMs will be necessary. Finally, the central controller needs to be re-designed if different equipment options (e.g., ESC only, ESC+CDC) are offered in the same vehicle platform. On the other hand, a centralised control approach (adopting an optimal control solution like Linear Quadratic Regulator or Model Predictive Control) may offer the highest performance levels and most systematic and straight-forward design procedure. This can alleviate the necessity of developing complex rule-based or decision-tree algorithms when a close interaction between two subsystems (e.g. AFS and vehicle torque control) is required.

- **Multi-layer**: This integration strategy has been promoted recently as an intermediate approach between purely centralised and de-centralised strategies. Specifically, the key idea of this concept lies in the adoption of an upper-level "intelligent" layer that monitors the vehicle states, driver's intentions and environmental conditions to coordinate the actuation of different subsystems in a wise manner. This coordination can be carried out adopting different approaches such as discrete modding-based [99] or linear interpolation Fuzzy-logic [83]. Taking as a reference the "modding" concept introduced by Narula et al. in [99], the major advantage derived from this integration strategy is that each supplier can design its subsystem with different operating modes (e.g., CDC mode: 0 stability - 1 ride) and the upper-level coordinator only needs to select the driving mode to be realised based on the current driving situation. This avoids the information exchange required by centralised approaches and facilitates the orientation of all the chassis subsystems towards a common full-vehicle goal. Expectedly, the major difficulties associated with this strategy reside in the design of the upper-level coordinator and driving event classifier. In addition, studying the stability and performance enhancement obtained from these hybrid systems in a wide range of operating conditions might be a non-trivial task.

With regards to multi-layer systems, Hattori proposed a Hierarchical Vehicle Dynamics Management (HVDM) algorithm in [61]. In this ICC, an upper-level Vehicle Dynamics Control (VDC) system determines the tyre force and yaw moment components to achieve the desired vehicle motion. A nonlinear optimisation routine based on Sequential Quadratic Programming (SQP) is employed to determine an optimised tyre force balance. In a similar line of thought, Kou et al. proposed in [83] an ICC system to coordinate the actuation of ESC and CDC systems. Specifically, the CDC system provides a suspension damping torque proportional to the vehicle lateral acceleration and the ESC system computes the wheel slip values necessary to avoid the yaw rate, body slip or roll rate states passing a set of “stable” thresholds. A rule-based ICC master decides the contribution of each subsystem based on a set of prioritised control objectives.

Following a more centralised design methodology, Yim et al. proposed in [145] a two-level ICC system to coordinate the actuation of ESC, AFS, and a four-wheel-drive (4WD) system in a hybrid four-wheel-drive (H4V) vehicle configuration. In the first layer, the authors adopted an SMC formulation to calculate the yaw moment required to track the desired yaw rate and maintain a reduced body slip angle. A Weighted Least Square (WLS) optimisation routine based on Quadratic Programming (QP) was proposed in the second layer to calculate an optimised tyre force vector and generate the requested upper-level yaw moment. The tyre vertical forces were taken into account to solve the previous vector of forces. Similarly, Hirano proposed an ICC system to combine AFS and Torque Vectoring Differential (TVD) subsystems in [67, 68]. A gain-scheduling LQR controller was proposed to determine the steering input and yaw moment required to follow a set of desired yaw rate and body slip values. The author proposed as a potential improvement for the future the adoption of MPC to handle optimally chassis actuator constraints. This control formulation was employed by Zhu et al. in [150]. Specifically, Zhu et al. incorporated the actuator constraints into the MPC formulation but additional quantitative details regarding these constraints were not provided. The MPC was combined with a driving prediction module composed of *driver identification* and *driver model* blocks.

Finally, other centralised ICC systems have been developed employing “black-box” or data-based control techniques [140, 125]. Wei et al. proposed in [140] a rule-based Fuzzy controller to distribute a reference yaw moment between an AFS and a braking-based Direct Yaw moment Control (DYC) system. Similarly, Sun et al. proposed in [125] a Fuzzy logic controller aimed at providing the steering and yaw moment corrections required to maintain the vehicle stability. Specifically, the body slip and yaw rate errors (with respect to the desired stable values) were taken as the Fuzzy logic controller inputs. An eight-degree-of-freedom vehicle model was adopted to simulate the vehicle dynamic responses and evaluate the proposed ICC system under sinusoidal steering inputs.

2.4.2 Summary and research gaps

The following points summarise the most important conclusions and research gaps extracted from this discussion.

- **Chassis and tyre model complexity**: Overall, little details are provided regarding the validation or correlation procedure employed to assess the veracity of the chassis models used to test the proposed ICC structures. Simulations have been carried out predominantly in Carsim and CarMaker-Matlab/Simulink (employing custom full-vehicle modelisations). In some cases, the necessity of reproducing the actuation of complex MAGV configurations which are not available in commercial vehicles (e.g., in-wheel electric motors) justifies the necessity of adopting a simplified vehicle formulation. Realistic actuator constraints have been considered in a reduced number of works. In those cases in which electric motor constraints have been taken into account, peak power or torque versus speed curves have been incorporated into the simulation models. Regarding the tyre models employed to simulate the vehicle behaviour, the Magic Formula has been widely used, focusing the analysis on rigid asphalt surfaces. Finally, the proposed control systems have been verified experimentally in a reduced number of works, probably due to the prohibitive costs associated with current MAGV prototypes and proving ground testing.

- **Simulated test cases**: As mentioned in the previous point, the analysis of the control systems revised in this section has been carried out on rigid asphalt surfaces. All the works addressing ICC systems consulted to this point adopt the Beta method [45] proposed by Shibahata et al. [120] and Van Zanten [130] and assume that the maximum vehicle response is obtained restricting the body slip angle within low thresholds. The validity of the proposed stability solutions in other scenarios in which the Beta-method principle may fail (e.g., loose surfaces where the friction versus slip curve exhibits a monotonic shape, Fig. 2.5) has not been studied yet.

- **Real chassis implementation considerations**: Two trends can be clearly differentiated among the works consulted on ICC: "modding" multi-level approach and fully centralised approach. The modding concept has been proposed with the aim to alleviate the integration problems that might arise during the implementation of ICC solutions into real chassis platforms. These considerations have not been taken into account in other academic works in which steering and yaw moment input commands are provided by the same LQR or MPC controller. In brief, detailed comparisons between the performance of "modding" and centralised controllers have not been found in the literature and therefore it is difficult to extract further conclusions regarding the performance loss expected from non-optimal control coordination strategies. In the author's opinion, centralised strategies offer a more straight-forward and systematic approach than rule-based solutions to design ICCs in which a simultaneous longitudinal control and steering action are required to maintain the vehicle stability (e.g. during high body slip stabilisation at the limits of handling). A possible solution to avoid further integration problems might be to combine a centralised vehicle planar dynamics controller with other subsystems from other domains (e.g., suspension-CDC) adopting a "modding" strategy, giving, as a result, a multi-level ICC framework.

- **Future trends**: The increasing interest in recent years on MAGV configurations has been evidenced in the works consulted in this section. In particular, the superior motion control possibilities offered by modern chassis systems equipped with AFS and independently-driven wheels are very appealing for chassis researchers. According to the survey provided by Abe in [1], it is expected that future MAGVs will not only incorporate individual electric motors but also individually-steered wheels, which will offer a wide range of vehicle dynamics control strategies. Finally, regarding the use of artificially-intelligent structures, Chen et al. have foreseen in [45] that future MAGVs will be able to exhibit an "intelligent" adaptive behaviour to respond to changing environmental conditions or to match a certain driving style. It is expected that this adaptive behaviour will be accomplished making use of knowledge-based approaches.

To conclude, this review has demonstrated that current ICC architectures are able to efficiently coordinate the inputs from different subsystems (e.g., AFS, DYC, in-wheel EMs). As expert driving manoeuvring is often characterised by the strong coupling seen between the steering and driving commands at the limits of handling, rule-based ICC integration strategies seem less suited for this application. Instead, it is expected that centralised integration strategies for vehicle planar dynamics relying on optimal MIMO controllers will provide higher performance levels and will ease the ICC core design procedure. As mentioned previously, other control subsystems like CDC might be added to the centralised vehicle planar dynamics controller using a multi-level "modding" approach to fine-tune the overall system performance. As it is not possible at this research stage to know additional details regarding the suppliers or OEMs that will be involved in the application of the solutions developed in this academic work, additional integration considerations are left out of the scope of this thesis and may be addressed in the future.

The rest of this thesis is aimed at addressing the major research gaps identified during the elaboration of this chapter, illustrated schematically in Figure 2.10. Specifically, the main body of work in this study commences in the next chapter, where relevant virtual sensing tools developed during the course of this investigation are introduced.

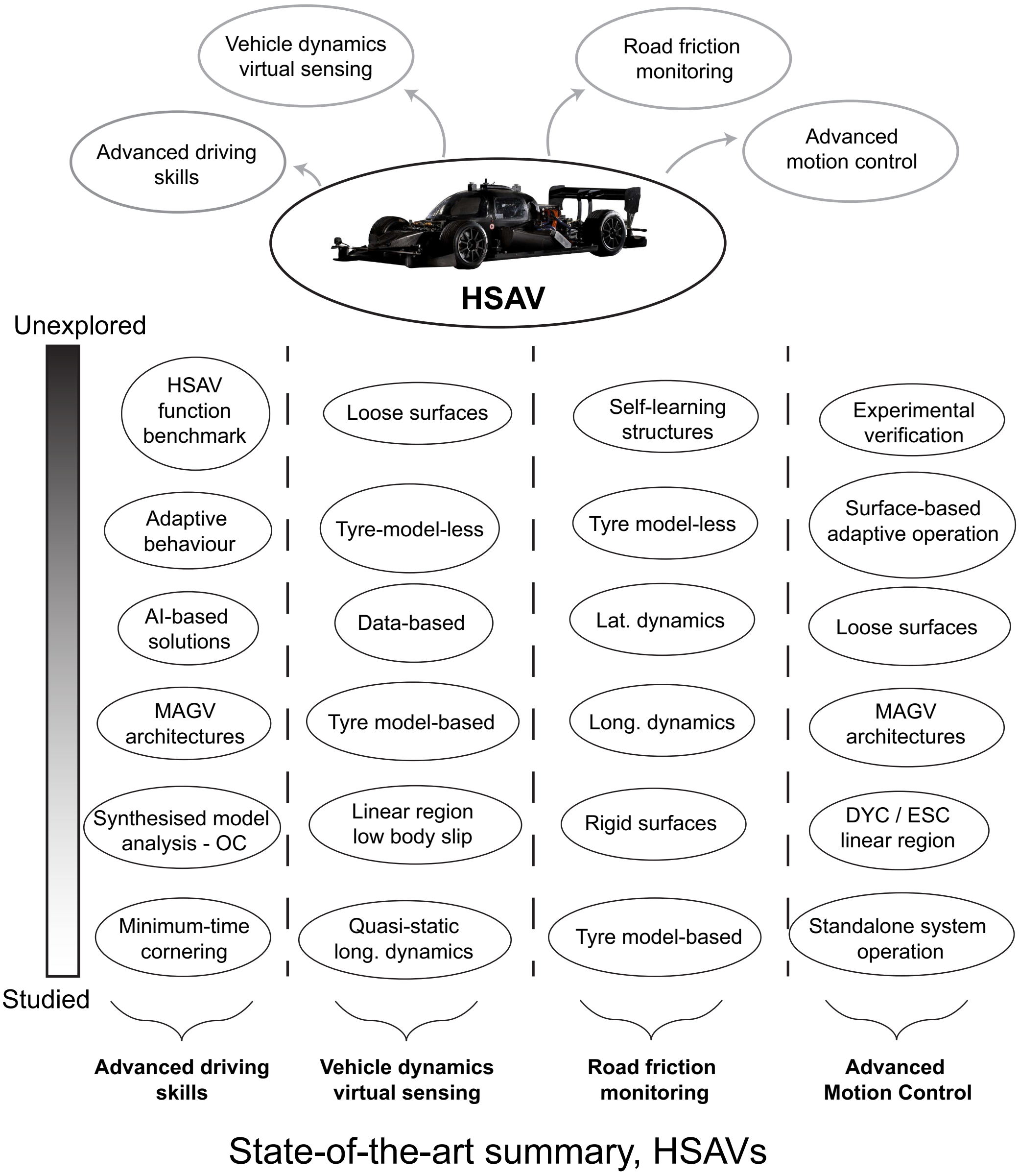

FIGURE 2.10: Most relevant research topics outlined in this chapter. From top to bottom, research topics that have not been fully addressed yet to concepts that have received greater attention on the existing literature.

Chapter 3

Vehicle Dynamics virtual Sensing

The virtual sensors developed in this thesis are derived in this section. Specifically, in order to fulfil the tyre-model-less premise introduced in the previous chapter, two observer designs are proposed to estimate the tyre forces and the vehicle planar motion states without utilising a tyre model: data-based and random-walk tyre force virtual sensing. The chapter is completed with the software-in-the-loop (SiL) verification of the observers in the Simulink/IPG-CarMaker framework and with a comprehensive discussion regarding the results obtained along the chapter.

3.1 Background

In the following, the synthesised vehicle models, Kalman filtering techniques and machine learning tools employed to build the virtual sensors are introduced. These concepts are not exclusive to this chapter but also used in other sections of this thesis.

3.1.1 Synthesised vehicle modelling

A synthesised seven degree-of-freedom vehicle model is used in this thesis to approximate the vehicle planar responses, Figure 3.1. This modelisation has been often adopted in other works on planar dynamics virtual sensing and yaw stability motion control [12, 134], as it is possible to achieve a reasonable accuracy maintaining a reduced computational effort. In order to include other active suspension systems for comfort-oriented or road holding studies, it would be necessary to increase the complexity of the model to account for the suspension vertical dynamics. These considerations are proposed for future research activities.

In the proposed vehicle model, the chassis is considered rigid, and the vehicle planar dynamics are described by the following set of equations,

$$m(\dot{v}_x - \dot{\psi} v_y) = (F_{x,fl} + F_{x,fr}) \cos\delta - (F_{y,fl} + F_{y,fr}) \sin\delta + F_{x,rl} + F_{x,rr} + mg \sin\theta_r \tag{3.1}$$

$$m(\dot{v}_y + \dot{\psi} v_x) = (F_{x,fl} + F_{x,fr}) \sin\delta + (F_{y,fl} + F_{y,fr}) \cos\delta + F_{y,rl} + F_{y,rr} - mg \cos\theta_r \sin\phi_r \tag{3.2}$$

$$\begin{aligned} I_\psi \ddot{\psi} &= ((F_{x,fl} + F_{x,fr}) \sin\delta + (F_{y,fl} + F_{y,fr}) \cos\delta) l_f - (F_{y,rl} + F_{y,rr}) l_r \\ &+ \frac{tw_f}{2}(F_{x,fr} - F_{x,fl}) \cos\delta + \frac{tw_f}{2}(F_{y,fl} - F_{y,fr}) \sin\delta + \frac{tw_r}{2}(F_{x,rr} - F_{x,rl}) \end{aligned} \tag{3.3}$$

where the three planar states are the longitudinal velocity v_x, lateral velocity v_y, and the yaw rate $\dot{\psi}$, and θ_r and ϕ_r are the road inclination and bank angles respectively.

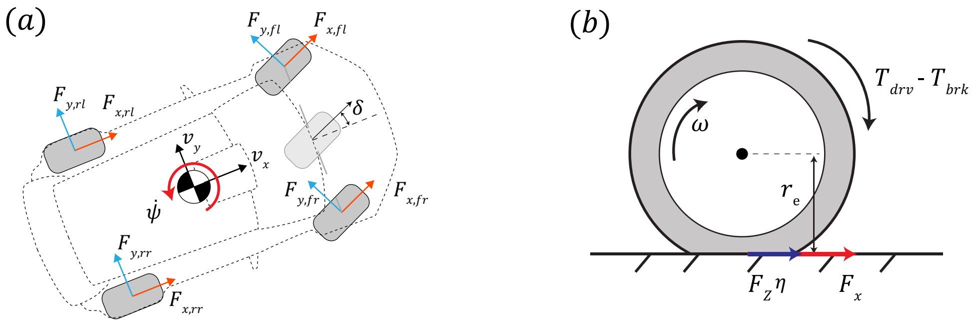

FIGURE 3.1: Illustration of: (a) Vehicle planar dynamics model and (b) wheel rotating dynamics model.

The vehicle mass is denoted as m, the yaw inertia is I_ψ, the front and rear track widths are tw_f, tw_r, and l_f, l_r are the distances from the centre of gravity to the front and rear axles. The average angle steered by the front wheels is δ, the longitudinal tyre force is denoted as $F_{x,i}$ and the lateral tyre force is $F_{y,i}$ (with $i \in \{fl, fr, rl, rr\}$). Following the approach presented in previous works on virtual sensing [70], the individual tyre lateral forces are often lumped into axle lateral forces (i.e. $F_{y,j} = F_{y-left,j} + F_{y-right,j}$, with $j \in \{front, rear\}$) in order to reduce the number of unknown states when tyre-model-less approaches are considered. Additional details are provided in the following sections of this chapter. If the longitudinal forces are also lumped into axle forces (i.e. $F_{x,j} = F_{x-left,j} + F_{x-right,j}$), the resulting model is denoted as the single-track or bicycle model. The tyre forces are traditionally described by a nonlinear relationship of the form,

$$F = f(\gamma, \alpha, \lambda, F_z) \tag{3.4}$$

where γ is the wheel inclination angle, α is the tyre lateral slip, λ is the wheel longitudinal slip, and F_z is the tyre vertical force. The function $f(\cdot)$ is often described by an empirical (*Magic formula* [104]) or semi-analytical (*Dugoff*) formulation [11]. These are commonly denoted as "tyre models". The major aim of the observers presented along this chapter is to propose alternative methods to avoid embedding these models into the state estimator structure. In order to facilitate a real-time implementation, the suspension kinematics are disregarded in this thesis, and the influence of the inclination angle is considered part of the vehicle model uncertainty. With regards to the tyre lateral slips α_i, these are derived from the vehicle planar states as follows,

$$\alpha_{fl} = \delta - \arctan\left(\frac{\dot{\psi} l_f + v_y}{v_x - \frac{t_{wf}}{2}\dot{\psi}}\right), \quad \alpha_{fr} = \delta - \arctan\left(\frac{\dot{\psi} l_f + v_y}{v_x + \frac{t_{wf}}{2}\dot{\psi}}\right) \tag{3.5}$$

$$\alpha_{rl} = \arctan\left(\frac{\dot{\psi} l_r - v_y}{v_x - \frac{t_{wr}}{2}\dot{\psi}}\right), \quad \alpha_{rr} = \arctan\left(\frac{\dot{\psi} l_r - v_y}{v_x + \frac{t_{wr}}{2}\dot{\psi}}\right) \tag{3.6}$$

If a single-track vehicle model is used, it is common practice working with the axle lateral slips, $\alpha_f = \delta - \arctan\left(\frac{\dot{\psi} l_f + v_y}{v_x}\right), \alpha_r = \arctan\left(\frac{\dot{\psi} l_r - v_y}{v_x}\right)$. The tyre longitudinal slips λ_i are calculated following the ISO slip convention [12],

$$\lambda_i = \frac{\omega_i r_e - V_{xc,i}}{V_{xc,i}} \tag{3.7}$$

with r_e being the wheel effective radius, $V_{xc,i}$ the longitudinal velocity at the wheel centre, and ω_i the rotational speed of the wheel, which is modelled by the wheel rotating dynamics equation,

$$I_\omega \dot{\omega}_i = T_{i,drv} - T_{i,brk} - F_{x,i} r_e - \eta F_{z,i} r_e \tag{3.8}$$

In this case, I_ω is the inertia of the wheel-driveline coupling, $T_{i,drv}$ and $T_{i,brk}$ the driving and braking torques respectively and η the rolling resistance factor. Regarding the longitudinal velocities at the wheel centre, these are obtained from the vehicle planar states [8] as,

$$V_{xc,fl} = \frac{v_x - \frac{t_{wf}}{2}\dot{\psi}}{(\cos\delta + \tan\alpha_{fl}\sin\delta)}, \quad V_{xc,fr} = \frac{v_x + \frac{t_{wf}}{2}\dot{\psi}}{(\cos\delta + \tan\alpha_{fr}\sin\delta)} \tag{3.9}$$

$$V_{xc,rl} = v_x - \frac{t_{wr}}{2}\dot{\psi}, \quad V_{xc,rr} = v_x + \frac{t_{wr}}{2}\dot{\psi} \tag{3.10}$$

Finally, the tyre vertical forces are modelled adopting a quasi-static weight transfer approach,

$$F_{z,i} = F_{st,i} \mp \Delta F_{z,x} \mp \Delta F_{z,yj} \tag{3.11}$$

where the static vertical force at each wheel is denoted as $F_{st,i}$ and the weight transfer caused by the longitudinal and lateral accelerations experienced at the centre of gravity as $\Delta F_{z,x}$, $\Delta F_{z,yj}$ respectively. These terms are approximated by the expressions [11],

$$\Delta F_{z,x} = m\frac{h_{CoG}}{2WB}a_x \tag{3.12}$$

$$\Delta F_{z,yj} = m\frac{a_y}{tw_j}h_s\frac{K_{\phi,j} - mh_s(WB - l_j)/WB}{K_{\phi_f} + K_{\phi_r} - mh_s} + m\frac{a_y h_{rc,j}}{tw_j}\frac{WB - l_j}{WB} \tag{3.13}$$

In this case, the height of the centre of gravity is denoted by h_{CoG}, the axle roll stiffness distribution is $K_{\phi,j}$, the roll centre height at each axle is $h_{rc,j}$ (with $j \in \{front, rear\}$), and the relative distance between the centre of gravity and the roll axis intersection as h_s. For better clarity, the wheelbase is designated as $WB = l_f + l_r$. In this formulation, the contribution of the unsprung mass is neglected and an even road surface is considered. For additional details regarding other vertical displacement-based models, the reader is referred to the works [11, 15] elaborated by the author of this thesis.

3.1.2 Extended Kalman Filter (EKF)

The Extended Kalman Filter (EKF) is a state estimation formulation adopted when nonlinear systems are handled. In particular, it is used in this chapter to reconstruct the vehicle planar states from a set of noise-corrupted measurements. To derive this state estimator, a general nonlinear system is presented using a forward-euler discrete representation,

$$\begin{cases} \mathbf{X_{k+1}} & = \mathbf{f_k}(\mathbf{X_k}, \mathbf{U_k}) + \mathbf{w_k} \\ \mathbf{Y_k} & = \mathbf{h_k}(\mathbf{X_k}) + \mathbf{v_k} \end{cases} \tag{3.14}$$

where the vector of inputs is denoted as $\mathbf{U_k}$, the vector of states is $\mathbf{X_k}$, the vector of measured signals is $\mathbf{Y_k}$, the uncertainty associated to the system is $\mathbf{w_k}$, and the uncertainty associated to the measured signals is $\mathbf{v_k}$. Both uncertainties are assumed to be Gaussian, uncorrelated and zero mean (i.e. $\mathbf{w_k} \approx N(0, \mathbf{Q_k}), \mathbf{v_k} \approx N(0, \mathbf{R_k})$) [48]. The terms $\mathbf{Q_k}$ and $\mathbf{R_k}$ are often known as the process covariance and measurement covariance matrices, and are used to tune the filter behaviour (e.g. trade-off between noise filtering and dynamic response characteristics). In order to ease the filter tuning, these matrices are often considered diagonal. The EKF action is performed in two steps.

$$\hat{\mathbf{X}}_{\mathbf{k+1|k}} = \mathbf{f_k}(\hat{\mathbf{X}}_{\mathbf{k|k}}, \mathbf{U_k}) \tag{3.15}$$

$$\mathbf{P_{k+1|k}} = \mathbf{A_k}\mathbf{P_{k|k}}\mathbf{A_k}^T + \mathbf{Q_k} \tag{3.16}$$

$$\mathbf{K_k} = \mathbf{P_{k+1|k}}\mathbf{H}_k^T[\mathbf{H_k}\mathbf{P_{k+1|k}}\mathbf{H_k}^T + \mathbf{R_k}]^{-1} \tag{3.17}$$

$$\hat{\mathbf{X}}_{\mathbf{k+1|k+1}} = \hat{\mathbf{X}}_{\mathbf{k+1|k}} + \mathbf{K_k}[\mathbf{Y_k} - \mathbf{h_k}(\hat{\mathbf{X}}_{\mathbf{k+1|k}})] \tag{3.18}$$

$$\mathbf{P_{k+1|k+1}} = [\mathbf{I} - \mathbf{K_k}\mathbf{H_k}]\mathbf{P_{k+1|k}} \tag{3.19}$$

Initially, an open loop approximation of the system states is carried out in the *Time update* stage of the filter (3.15-3.16) using the Jacobian matrix of the vector of states ($\mathbf{A} = \partial\mathbf{f}(\cdot)/\partial\mathbf{X}$). After that, in the *measurement update* stage (3.17-3.19), the system states are corrected with the measured quantities using the filter gain $\mathbf{K_k}$. The Jacobian matrix of the measurement vector ($\mathbf{H} = \partial\mathbf{h}(\cdot)/\partial\mathbf{X}$) is employed for this purpose. Additional details regarding the local observability of a nonlinear system are omitted in this thesis due to space limitations and can be consulted in [48].

3.1.3 Unscented Kalman Filter (UKF)

The Unscented Kalman Filter (UKF) is a state estimation formulation employed in problems exhibiting a strong nonlinear behaviour where the EKF linearisation can lead to inaccurate results. The filter is based on the Unscented Transformation (UT), which offers a statistical alternative to the EKF system linearisation. Specifically, a small set of deterministically selected sigma points are propagated through the system and the system nonlinearities are inferred from the statistics of these points. The spread of the sigma points is determined by the selection of the scaling parameters α_{ukf} and κ_{ukf}, and the length of the state vector L_{ukf}, which are related by the expression (3.20), [110, 138].

$$\lambda_{ukf} = \alpha_{ukf}^2(L_{ukf} + \kappa_{ukf}) - L_{ukf} \tag{3.20}$$

If the plant and measurement noises are considered additive, the formulation of the estimator is reduced to the formulation of the standard or unaugmented UKF [110]. The matrix of sigma points $\chi_\mathbf{k}$ is formed using the equation (3.21), where the number of rows is given by L_{ukf} and the number of columns corresponds to $2L_{ukf} + 1$.

$$\chi_\mathbf{k} = \left[\hat{\mathbf{X}}_\mathbf{k|k}, \hat{\mathbf{X}}_\mathbf{k|k} + \sqrt{\Theta\mathbf{P}_\mathbf{x,k|k}}, \hat{\mathbf{X}}_\mathbf{k|k} - \sqrt{\Theta\mathbf{P}_\mathbf{x,k|k}}\right] \tag{3.21}$$

In this expression, Θ is a constant factor equal to $(\lambda_{ukf} + L_{ukf})$ and the matrix square root $\sqrt{\mathbf{P}_\mathbf{x,k|k}}$ is calculated using the Cholesky method, expression (3.22).

$$\sqrt{\mathbf{P}_\mathbf{x,k|k}}\sqrt{\mathbf{P}_\mathbf{x,k|k}}^T = \mathbf{P}_\mathbf{x,k|k} \tag{3.22}$$

The sigma points are then propagated through the nonlinear system,

$$\chi_\mathbf{k+1|k}{}^i = \mathbf{f}_\mathbf{k}(\chi_\mathbf{k}{}^i, \mathbf{U}_\mathbf{k}) \tag{3.23}$$

and the post-transformation mean vector $\hat{\mathbf{X}}_\mathbf{k+1|k}$ and covariance matrix $\mathbf{P}_\mathbf{k+1|k}$ are calculated using weighted averages, (3.24-3.25).

$$\hat{\mathbf{X}}_\mathbf{k+1|k} = \sum_{i=0}^{2L_{ukf}} \eta_i^m \chi_\mathbf{k+1|k}{}^i \tag{3.24}$$

$$\mathbf{P}_\mathbf{k+1|k} = \mathbf{Q}_\mathbf{k} + \sum_{i=0}^{2L_{ukf}} \eta_i^c(\chi_\mathbf{k+1|k}{}^i - \hat{\mathbf{X}}_\mathbf{k+1|k})(\chi_\mathbf{k+1|k}{}^i - \hat{\mathbf{X}}_\mathbf{k+1|k})^T \tag{3.25}$$

The weights η_i^c and η_i^m are calculated using equations (3.26-3.28),

$$\eta_0^m = \frac{\lambda_{ukf}}{\lambda_{ukf} + L_{ukf}} \tag{3.26}$$

$$\eta_0^c = \eta_0^m + 1 - \alpha_{ukf}^2 + \beta_{ukf} \tag{3.27}$$

$$\eta_i^c = \eta_i^m = \frac{1}{2(L_{ukf} + \lambda_{ukf})} \tag{3.28}$$

where β_{ukf} is known as the secondary scaling parameter [110]. Similarly, the matrix of sigma points is propagated through the observation function ($\mathbf{h_k}$) using expression (3.29).

$$\mathbf{Y_{k+1|k}}^i = \mathbf{h_k}(\chi_{\mathbf{k+1|k}}{}^i) \tag{3.29}$$

The predicted output $\mathbf{\hat{Y}_{k|k}}$, output covariance matrix $\mathbf{P^{yy}_{k+1}}$ and cross-covariance matrix $\mathbf{P^{xy}_{k+1}}$ are calculated using equations (3.30-3.32).

$$\mathbf{\hat{Y}_{k+1|k}} = \sum_{i=0}^{2L_{ukf}} \eta_i^m \mathbf{Y_{k+1|k}}^i \tag{3.30}$$

$$\mathbf{P^{yy}_{k+1}} = \mathbf{R_k} + \sum_{i=0}^{2L_{ukf}} \eta_i^c (\mathbf{Y_{k+1|k}}^i - \mathbf{\hat{Y}_{k+1|k}})(\mathbf{Y_{k+1|k}}^i - \mathbf{\hat{Y}_{k+1|k}})^T \tag{3.31}$$

$$\mathbf{P^{xy}_{k+1}} = \sum_{i=0}^{2L_{ukf}} (\chi_{\mathbf{k+1|k}}{}^i - \mathbf{\hat{X}_{k+1|k}})(\mathbf{Y_{k+1|k}}^i - \mathbf{\hat{Y}_{k+1|k}})^T \tag{3.32}$$

The covariance matrices calculated in the previous step are then used to compute the Kalman gain ($\mathbf{K_{k+1}}$), equation (3.33).

$$\mathbf{K_{k+1}} = \mathbf{P^{xy}_{k+1}}(\mathbf{P^{yy}_{k+1}})^{-1} \tag{3.33}$$

Finally, the states estimated in the first stage of the filter are corrected using the expression (3.34), and the covariance matrix is updated with equation (3.35).

$$\mathbf{\hat{X}_{k+1|k+1}} = \mathbf{\hat{X}_{k+1|k}} + \mathbf{K_{k+1}}(\mathbf{Y_{k+1}} - \mathbf{\hat{Y}_{k+1|k}}) \tag{3.34}$$

$$\mathbf{P_{k+1|k+1}} = \mathbf{P_{k+1|k}} - \mathbf{K_{k+1}}\mathbf{P^{yy}_{k+1}}\mathbf{K_{k+1}}^T \tag{3.35}$$

3.1.4 Feedforward Neural Networks

Feedforward Neural Networks (NN) are used to characterise the time-independent properties of systems. Specifically, in this chapter NNs are employed to model the tyre's quasi-static nonlinear behaviour from a set of standardised manoeuvres performed with a target vehicle. The formal description of static systems is given by expression (3.36), [30].

$$\mathbf{Y_k} = f(\mathbf{U_k}, \mathbf{Z_k}) \tag{3.36}$$

Where $\mathbf{Y_k}$ is the output vector of the system, $\mathbf{U_k}$ is the input vector and $\mathbf{Z_k}$ comprises the system parameters. The simplest element of an NN structure is an Artificial Neural Network cell (Neuron), Figure 3.2. Neurons are grouped forming a structure of different layers, named Input layer, Hidden Layers, and Output Layer. Between the input and output layers, a series of simple operations are performed, given by the equations (3.37-3.38).

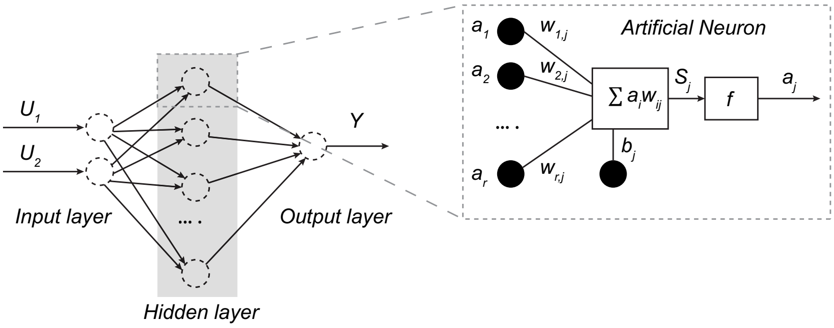

FIGURE 3.2: Neural Network structure and Neural Network cell [6].

$$S_j = \sum w_{ij} a_i + b_j \tag{3.37}$$

$$a_j = f(S_j) \tag{3.38}$$

Where S_j represents the output from the $j-th$ neuron, formed by the sum of the relevant products of weights (w_{ij}) and outputs (a_i) from the previous layer i. This sum is biased by the factor b_j. a_i represents the activation of the node at hand and f the activation function of the j layer. Normally, sigmoid functions are chosen for the hidden layers while linear functions are set for the output layers.

3.1.5 Adaptive Neuro-Fuzzy Inference Systems (ANFIS)

ANFIS structures can be efficiently used to model input-output relationships in an automated manner. In this chapter, ANFIS is proposed to learn the friction characteristics of an unknown terrain from a set of tyre force and wheel slip measurements. A general ANFIS structure consisting of two inputs and one output is depicted in Figure 3.3. Following the derivation presented in [75], a type-3 ANFIS architecture using Takagi and Sugeno's fuzzy if-then rules is formed by five different layers, which are described as follows:

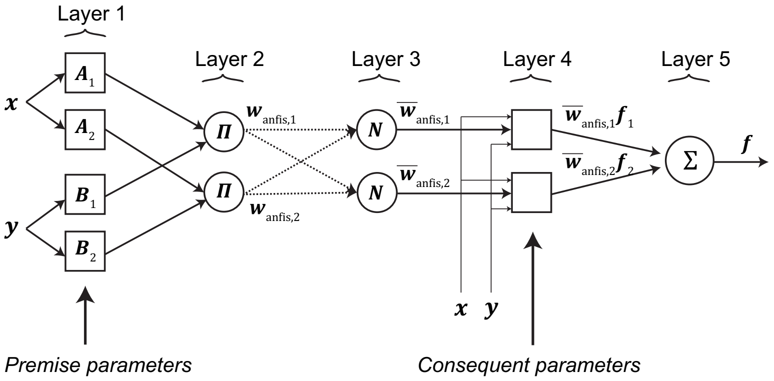

FIGURE 3.3: ANFIS type-3 schematic structure. Figure reproduced by the author from [75].

- Layer 1: A membership function $\mu_{A_i}(x)$ is employed to assess how the input x satisfies the quantifier A_i, expression (3.39).

$$O_i^1 = \mu_{A_i}(x) \tag{3.39}$$

A normalised bell-shaped function of the form (3.40) is regularly employed for this task,

$$\mu_{A_i}(x) = \frac{1}{1 + [(\frac{x-c_i}{a_i})^2]b_i} \tag{3.40}$$

where the parameters a_i, b_i, c_i are referred to as *premise parameters*, and are tuned during the training of the *ANFIS* model to modify the shape of the membership function.

- Layer 2: The input membership functions are multiplied, and the output from each node is denoted as the *firing strength* of a rule, expression (3.41).

$$w_{anfis,i} = \mu_{A_i}(x)\mu_{B_i}(y), i = 1, 2 \tag{3.41}$$

- Layer 3: In this layer the ratio of the i-th firing strength and the sum of all the rule's firing strengths is calculated, equation (3.42).

$$\overline{w}_{anfis,i} = \frac{w_{anfis,i}}{w_{anfis,1} + w_{anfis,2}}, i = 1, 2 \tag{3.42}$$

  The nomenclature employed in [75] denotes the outputs from this layer as *normalised firing strengths.*

- Layer 4: The node function (3.43) is employed during this step to compute the weighted term $\overline{w}_{anfis,i}f_i$,

$$O_i^4 = \overline{w}_{anfis,i}f_i = \overline{w}_{anfis,i}(p_i x + q_i y + r_i) \tag{3.43}$$

  with the parameters $\{p_i, q_i, r_i\}$ being denoted in the literature as the *consequent parameters.*

- Layer 5: Finally, the overall output from all the incoming inputs is computed, equation (3.44).

$$O_i^5 = \sum_i \overline{w}_{anfis,i}f_i = \frac{\sum_i w_{anfis,i}f_i}{\sum_i \overline{w}_{anfis,i}} \tag{3.44}$$

In [75] a *Hybrid Learning* algorithm is proposed to determine the set of *premise* and *consequent* parameters. As the gradient method is prone to be trapped in local minima and generally slow, this algorithm combines the gradient method with the Least Squares Estimate (*LSE*) method. According to the description provided in [75], the learning method is executed in two steps, which can be summarised as follows.

- Forward pass: The *premise* parameters are fixed, and the inputs x,y are propagated forward to the fourth layer. The *consequent* parameters are adjusted using a *LSE* method.

- Backward pass: The *consequent* parameters are fixed after the forward pass and the error rates are propagated backwards. The gradient method is used at this stage to compute the *premise* parameters.

3.2 Data-based virtual sensing

In this section, a preliminary single-track EKF for planar dynamics state estimation and road friction identification is introduced first. After that, an enhanced modular UKF structure for planar dynamics state estimation and three-axes tyre force virtual sensing is described. Both structures are subjected to a comprehensive SiL verification program with the commercial simulation package IPG-CarMaker.

3.2.1 Single-track EKF

The structure of the single-track EKF (ST-EKF) is depicted schematically in Figure 3.4. The major novelty of this design lies in the adoption of a hybrid planar dynamics block formed by Artificial Neural Networks (ANN) and a model-based state estimator (EKF). The proposed methodology is fundamentally different compared to other approaches [48, 92], in the sense that it does not assume an *a priori* knowledge of the tyre model nor does it treat the vehicle dynamics as a "black box". Instead, it combines the advantages of NNs in modelling the tyre's highly nonlinear behaviour using a data-based approach with a first principles vehicle model that captures the overall dynamic behaviour. Such a hybrid methodology has been applied by the author of this thesis in several works [6, 17].

In this structure, the vector of states of the core EKF is formed by the yaw rate, longitudinal velocity and lateral velocity ($\mathbf{X_{EKF}} = \{\dot{\psi}, v_x, v_y\}$), and the vector of measurements by the yaw rate and the longitudinal velocity ($\mathbf{Y_{EKF}} = \{\dot{\psi}, v_x\}$). The inputs to this system are the average angle steered by the front wheels, and the axle longitudinal tyre forces ($\mathbf{U_{EKF}} = \{\delta, F_{x,f}, F_{x,r}\}$). For simplicity, in this first design a single-track planar dynamics model is considered, and the influence of the differential braking action is assumed to be negligible. Moreover, these forces are assumed to be estimated in an external state estimation block. The states predicted by the EKF are used to estimate the axle lateral slips by means of a small angle approximation,

$$\alpha_f = \delta - \frac{\dot{\psi} l_f + v_y}{v_x}, \quad \alpha_r = -\frac{v_y - \dot{\psi} l_r}{v_x} \tag{3.45}$$

After that, the axle slips and the longitudinal acceleration a_x are used in the NN blocks to infer the axle lateral forces. In order to work with a manageable NN structure, the nonlinear relationship given by the expression (3.4) is rewritten here as $F_{y,j} = f_y(\alpha_j, a_x)$ under the assumption of quasi-static longitudinal weight transfer and longitudinal linear

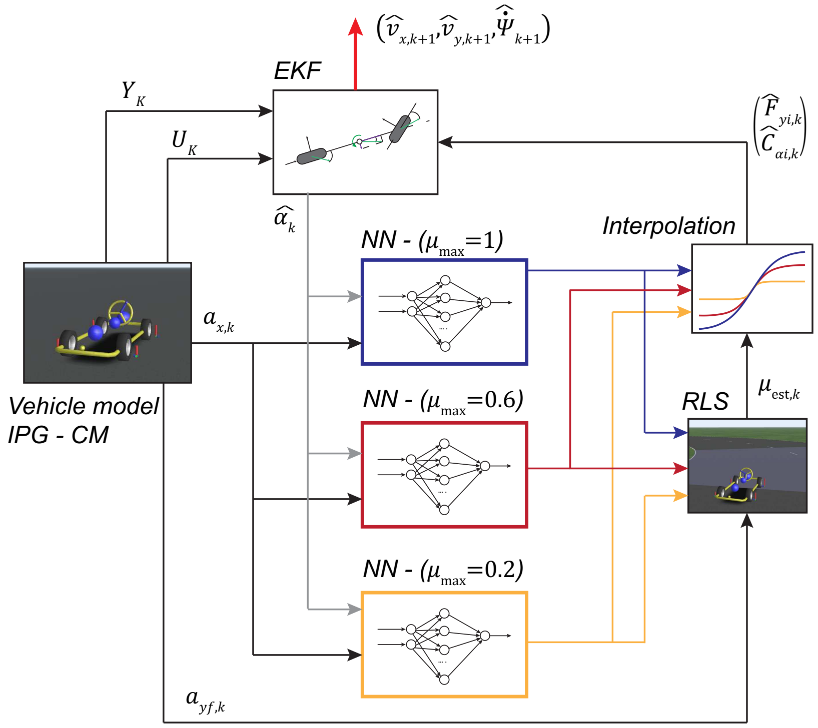

FIGURE 3.4: Structure of the proposed ST EKF [6].

region operation [6]. In brief, the longitudinal acceleration accounts for the reduction in the axle lateral force during combined longitudinal and lateral excitation (force coupling effect and longitudinal weight transfer). The nonlinear function f_y is approximated by an NN structure trained with data obtained from a set of standardised objective testing manoeuvres, Figure 3.5.

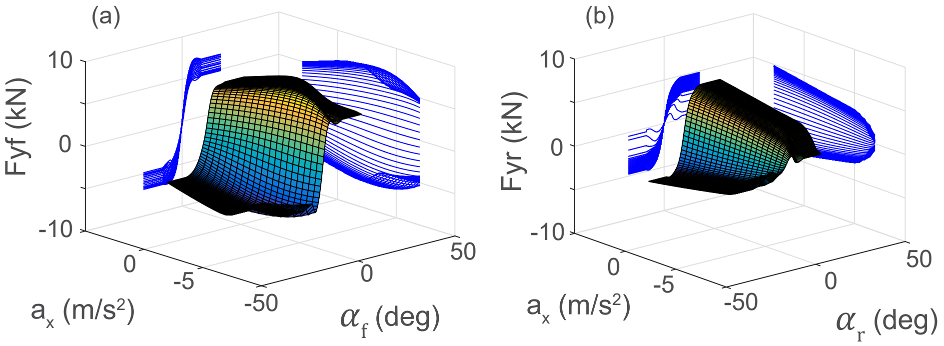

FIGURE 3.5: (a) Output from the front axle NN, $F_{yf} = NN_f(\alpha_f, a_x)$. (b) Output from the rear axle NN, $F_{yr} = NN_r(\alpha_r, a_x)$ [6].

The datasets necessary to train the NN structures were generated in IPG-CarMaker using an experimentally validated compact-class vehicle model (Ford Fiesta Zetec) and a state-of-the-art Magic Formula (MF) 6.1 tyre model (205-65/R16) [104]. Open Loop aggressive manoeuvres (Step steer) covering different longitudinal acceleration levels (Braking, coast down, Power On) were simulated for this purpose in three different friction coefficient levels ($\mu_{max} = 1, \mu_{max} = 0.6, \mu_{max} = 0.2$). These friction levels were adjusted on the simulation environment using the MF friction scaling approach. 2-10-1 NN structures were trained in *Matlab* using the Levenberg-Marquardt backpropagation algorithm and imposing a 70/15/15% dataset division, which was selected after performing a sensitivity analysis. The stability of the NN structure was studied following the methodology described in [30]. Additional details regarding the NN training process are omitted in this thesis due to space limitations and can be found in [6].

3.2.1.1 Road friction potential identification

In order to make the observer robust to different road friction levels, the NN outputs are used to compute a friction compensation factor adopting a linear interpolation approach,

$$\mu_1 = \left(F_{yf,meas} - \frac{a_2 \hat{F}_{yf,high} + b_2 \hat{F}_{yf,mid}}{a_1 \hat{F}_{yf,high} + b_1 \hat{F}_{yf,mid}} \right) \tag{3.46}$$

$$\mu_2 = \left(F_{yf,meas} - \frac{a_4 \hat{F}_{yf,mid} + b_4 \hat{F}_{yf,low}}{a_3 \hat{F}_{yf,mid} + b_3 \hat{F}_{yf,low}} \right) \tag{3.47}$$

where $F_{yf,meas}$ is a pseudo-measurement of the front axle lateral force computed from the vehicle lateral acceleration a_y as $F_{yf,meas} = \frac{ml_r}{l_f + l_r}(a_y + l_f \dot{\psi})$. a_p, b_p (with $p \in \{1, 2, 3, 4\}$) are constant coefficients determined following a segmentation approach, and the terms $\hat{F}_{yf,high}$, $\hat{F}_{yf,mid}$, $\hat{F}_{yf,low}$ are the front axle lateral forces obtained from the NNs trained at three intermediate friction levels $\mu_{max} = \{1, 0.6, 0.2\}$. These values defined two friction intervals, I_1 and I_2. Specifically, the total friction envelope was divided into two intervals in order to reduce the testing effort. Additional intervals may enhance the accuracy of the proposed approach at the expenses of more testing activities. This drawback may be compensated with the incorporation of synthetic data on the NN training process. The measurement $F_{yf,meas}$ is used to determine the current operating interval and use expression (3.46) or (3.47) to compute the friction estimate $\mu_j, j \in \{1, 2\}$. After that, a Recursive Least Squares (RLS) block is used to filter the friction compensation factor ($\mu_{est} = RLS(\mu_j)$). Finally, the tyre forces are linearly interpolated on the basis of the estimated friction correction factor and reinjected into the EKF block. The signals exchanged between the EKF, NN and RLS blocks are summarised in the Table 3.1 for the sake of clarity.

Table 3.1: Observer inputs and outputs, ST EKF [6].

Signal	EKF	NN	RLS
Inputs	δ, F_{xf}, F_{xr}	α, a_x	$\hat{F}_{yf,high-mid-low}$
Measurements	$\dot{\psi}, v_x$	-	-
Outputs	$\hat{\dot{\psi}}, \hat{v}_x, \hat{v}_y$	$\hat{F}_{yf,high-mid-low}$,$\hat{F}_{yr,high-mid-low}$	μ_{est}

3.2.1.2 SiL verification

As mentioned earlier, a compact-class virtual vehicle model with tyres of size 205-65/R16 (MF 6.1), was built in the high-fidelity simulation environment IPG-CarMaker to verify the proposed observer. Field tests (slalom and steady-state cornering) were carried out with a Ford Fiesta Zetec (Fig. 3.6) equipped with the experimental instrumentation detailed in Table 3.2 in order to validate the virtual vehicle model [6]. These standardised manoeuvres [72] are often performed as part of a chassis objective characterisation program. Their effectiveness and suitability to characterise different vehicle variants are widely accepted among the vehicle dynamics community [64].

Table 3.2: Experimental equipment used to validate the virtual vehicle model [6].

GPS	RaceLogic Dual Antenna
IMU	RaceLogic RLVBIMU04
Acquisition Unit	RaceLogic VBOX 3i
CAN	Connection through EOBD port
Acquisition frequency	100Hz

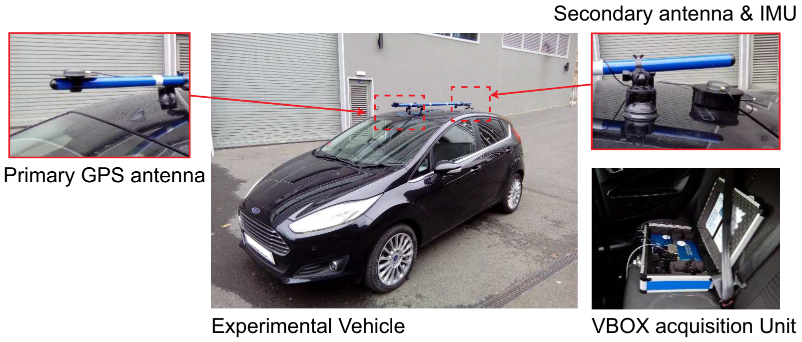

Figure 3.6: Experimental vehicle used to verify the virtual vehicle model implemented in IPG-CarMaker [6].

Overall, a good correlation between the experimental results and the outputs from the virtual vehicle model was observed, Fig. 3.7. The simulation outputs were generated using the experimental steering wheel angle signal and the measured speed profile, followed by means of a PID control. Additional experimental results (steady-state cornering) can be consulted in [6].

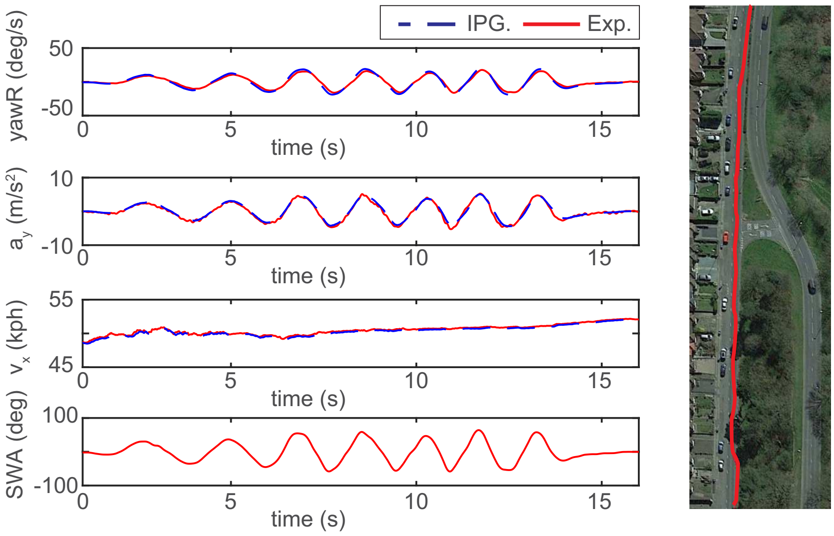

FIGURE 3.7: Slalom test carried out with the experimental vehicle, [6]. SWA: Steering wheel angle.

The virtual sensor was implemented in Matlab/Simulink adopting a sampling frequency of 100 Hz and a 1 ms running time. An additive white Gaussian noise model ($y_\sigma = y + \sigma$) was adopted to simulate noise-corrupted signals (the numerical values of the variances were extracted from technical data sheets and are detailed in [6]). The EKF structure was tuned manually following an iterative trial and error process using the Normalised Root Mean Square (NRMS) error of the estimated states as a reference metric. Once implemented, the virtual sensor was subjected to a comprehensive catalogue of manoeuvres formed by open loop (sine with dwell), closed loop (ISO Lane Change, ADAC Lane Change), and mu-jump (slalom, wet circle) tests, Table 3.4. These tests were performed in different friction conditions and different vehicle configurations, Table 3.3.

TABLE 3.3: Model configurations used during the ST-EKF SiL verification [6].

Configuration	Vehicle model	Tyre model	Tyre pressure
Reference	Fiesta-exp	MF 205-65/R16	2.4 bar
Ref-A	Fiesta-exp	MF 185-65/R15	2.4 bar
Ref-B	Fiesta-exp	MF 215-50/R17	2.4 bar
Ref-C	Fiesta-exp	MF 205-65/R16	2 bar
Ref-D	Fiesta-exp	MF 205-65/R16	2.8 bar
Ref-Sedan	Sedan	MF 245-40/R19	2.4 bar
Sedan-wet	Sedan	MF 245-40/R19 wet asphalt	2.4 bar
Sedan-ice	Sedan	MF 245-40/R19 ice	2.4 bar

Overall, different tyre sizes and pressures were simulated to assess the robustness of the observer trained in a nominal configuration to changes expected along the lifespan of the vehicle (tyre pressure variations or tyre replacement). Moreover, the observer training process was repeated in a different vehicle model and additional simulations were performed with MF 5.2 tyre models characterised in dry, wet, and icy conditions. Due to space limitations, only a sample of the results is illustrated in this section, Figures 3.8-3.9.

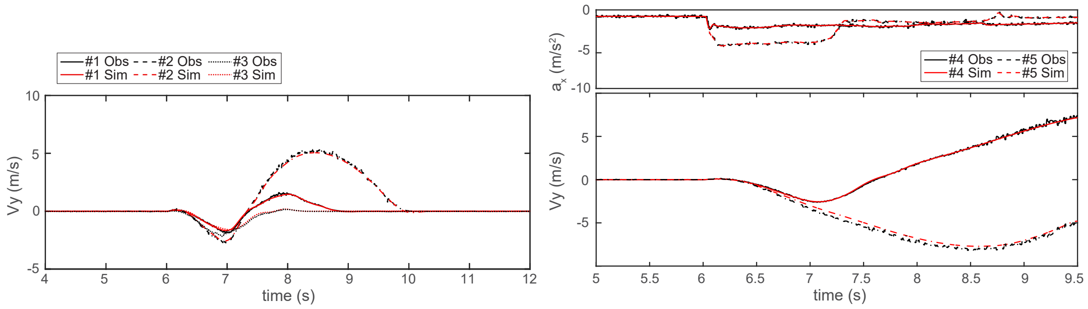

FIGURE 3.8: Left: Sine with dwell tests (1-3), $\mu_{max} = 1$, nominal configuration. Right: Sine with dwell tests (4-5), $\mu_{max} = 0.7$, nominal configuration [6].

As can be observed, the single-track EKF estimates precisely the lateral velocity (Fig. 3.8) and the axle lateral forces (Fig. 3.9) during aggressive manoeuvres performed in dry and wet conditions.

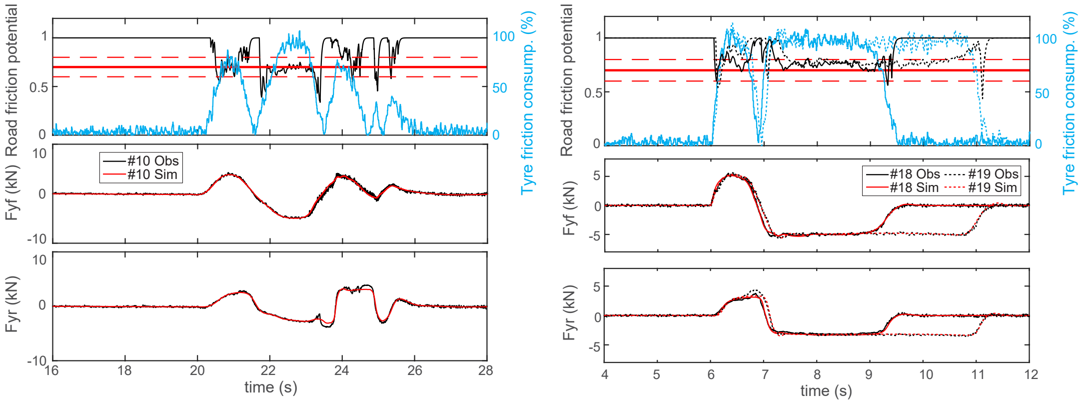

FIGURE 3.9: Left: ADAC Lane Change test (10), $\mu_{max} = 0.7$, nominal configuration. Right: Sine with dwell tests (18-19), $\mu_{max} = 0.7$, Ref-A and Ref-B configurations [6].

The NRMS error metric of the axle lateral forces and vehicle planar states were computed for each test and are given in Table 3.4. Overall, small errors are observed in the states estimated by the EKF (in the majority of tests values are kept below a 5% error threshold). Concerning the lateral velocity, a maximum error of 9.53% is obtained in test 16 due to the mismatch between the reference tyre model and the R15 tyre model. Nevertheless, this value remains below the 10% threshold and can be considered acceptable. Finally, axle lateral force errors kept within reasonable limits during the majority of the simulations. Large errors are found in the rear axle forces during the execution of tests 6, 20 and 23. These tests correspond to aggressive manoeuvres executed in extremely low mu conditions. As was discussed in [6], this error may be introduced by the delay

TABLE 3.4: NRMS error metrics. *Spd: Speed [km/h]. **SWA: Steering wheel angle [deg]. ***Braking (CD: Coast down, PB: Partial braking, HB: Hard Braking, MS: Maintain Speed) [6].

Test	Spd* /SWA**/Brk***/Grip	Configuration	e_{v_x}	$e_{\dot{\psi}}$	e_{v_y}	$e_{F_{yf}}$	$e_{F_{yr}}$
1-Sine with Dwell	80/90/CD/1	Reference	1.19	2.45	2.83	2.78	5.05
2-Sine with Dwell	80/150/CD/1	Reference	1.19	1.63	2.98	3.27	5.14
3-Sine with Dwell	80/90/PB/1	Reference	1.18	2.84	5.30	3.68	9.11
4-Sine with Dwell	80/90/CD/0.7	Reference	1.20	1.56	1.14	2.79	5.24
5-Sine with Dwell	80/90/PB/0.7	Reference	1.18	1.51	4.46	2.88	5.75
6-Sine with Dwell	80/70/CD/0.3	Reference	1.20	2.25	0.63	8.99	23.60
7-Sine with Dwell	80/70/HB/1	Reference	1.20	0.99	4.95	11.27	6.41
8-ISO LC	100/-/MS/1	Reference	0.94	2.76	1.56	1.92	2.86
9-ADAC LC	100/-/CD/1	Reference	0.94	3.22	2.44	1.94	3.14
10-ADAC LC	95/-/CD/0.7	Reference	1.00	1.55	0.86	3.14	5.01
11-ADAC LC	90/-/CD/0.5	Reference	1.05	2.52	1.19	3.81	9.23
12-Slalom 36m	80/-/MS/1	Reference	1.18	5.89	4.85	2.80	4.41
13-Slalom 36m	65/-/MS/0.4	Reference	1.32	6.29	5.12	5.55	6.87
14-Straight-line mu-jump	90/-/MS/[0.8:0.2:0.2]	Reference	1.16	3.55	6.47	4.91	3.90
15-Circle mu-jump	50/R50/MS/[0.8-0.4]	Reference	1.32	2.63	7.50	4.27	6.54
16-Sine with Dwell	80/150/CD/1	Ref-A	1.19	1.76	9.53	5.82	7.44
17-Sine with Dwell	80/150/CD/1	Ref-B	1.19	1.51	5.87	4.47	6.44
18-Sine with Dwell	80/90/CD/0.7	Ref-A	1.19	2.78	3.28	2.52	4.16
19-Sine with Dwell	80/90/CD/0.7	Ref-B	1.20	2.41	2.10	2.77	4.27
20-ADAC LC	70/-/CD/0.5	Ref-C	1.05	1.35	1.00	6.85	16.58
21-ADAC LC	70/-/CD/0.5	Ref-D	1.06	3.82	2.48	3.40	6.37
22-Sine with Dwell	80/120/CD/0.9	Sedan-Wet	1.36	2.43	5.37	3.18	4.30
23-Sine with Dwell	80/35/CD/0.35	Sedan-Ice	1.39	7.10	8.73	8.77	14.49

between the front and rear axles, which can cause a momentary overestimation of the rear axle forces and contributes to magnifying the estimation error. In spite of this, the EKF is able to correct these inaccuracies and the vehicle state errors are approximated within reasonable limits.

3.2.2 UKF for integral tyre force estimation

The ST-EKF was enhanced in subsequent works [17, 16], giving as a results an observer for integral tyre force estimation, Figure 3.10. Moreover, the core hybrid EKF structure was substituted by a hybrid UKF observer with the aim to provide an alternative to the linearisation step performed in the EKF formulation, which may lead to inaccurate results in the presence of strong nonlinearities.

In brief, the enhanced observer is constructed adopting a modular architecture in which three subsystems can be distinguished: F_y estimation (planar dynamics domain), F_x estimation (longitudinal force domain), and F_z estimation (vertical force domain). This modular architecture is aimed at avoiding the burden of tuning a single observer with a large number of states. Taking as a reference the scheme portrayed in Figure 3.10, the observer action can be summarised in the following manner.

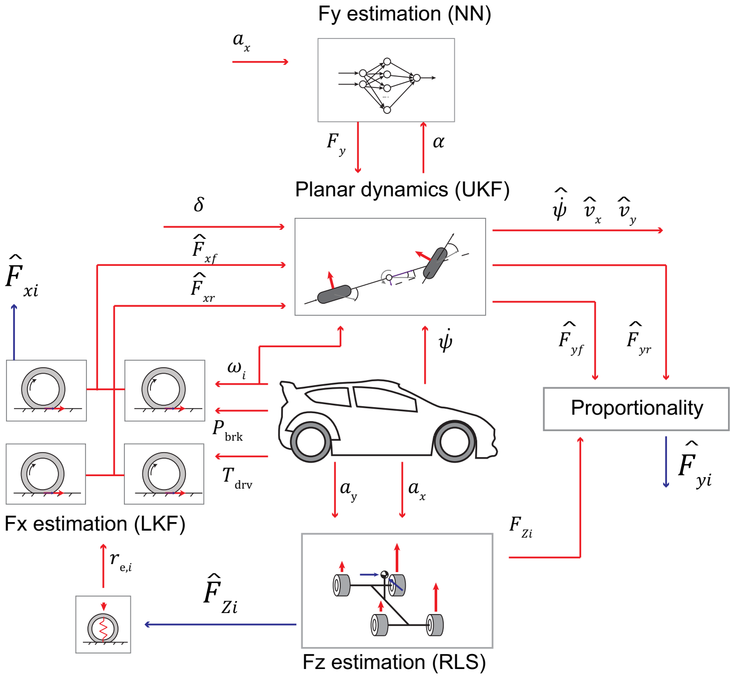

Figure 3.10: Structure of the proposed UKF observer for three-axes tyre force estimation [17].

The individual tyre longitudinal forces are estimated adopting a wheel rotating dynamics-based approach [11]. Specifically, the expression (3.8) was discretised and implemented in a Linear Kalman Filter. The vector of states was formed by the wheel rotational velocity and the tyre longitudinal force ($\mathbf{X_{LKF}} = \{\omega_i, F_{x,i}\}$), which is considered a "random-walk" variable. Essentially, this approach assumes that the "random-walk" state remains constant during the time update stage of the Kalman filter ($\dot{F}_{x,i} = 0$), and relies entirely on the measurement update stage to determine how the variable evolves in time (additional details regarding random-walk tyre force modelling are provided in Section 3.3). The vector of measurements was formed by the wheel rotational velocity ($\mathbf{Y_{LKF}} = \{\omega_\mathbf{i}\}$), and the vector of inputs by the net wheel torque ($\mathbf{U_{LKF}} = \{\mathbf{T_{drv,i}} - \mathbf{T_{brk,i}}\}$). In the case of a conventional Internal Combustion Engine (ICE) vehicle, the wheel driving torque (T_{drv}) can be derived from the engine driving torque and the driveline ratios [17]. If electric motors are considered, the wheel driving torque can be easily measured from the inverter feedback. The friction braking torque can be obtained from the braking pressure using a linear model ($T_{brk} = K_{brk,j}P_{brk,i}$), where $K_{brk,j}$ is a constant parameter determined by the calliper dimensions and brake pad friction coefficient, and $P_{brk,i}$ is the individual braking pressure ($i \in \{fl, fr, rl, rr\}$, $j \in \{front, rear\}$). The vertical force necessary to model the rolling resistance force ($F_{res} = F_z\eta r_e$) is assumed to be a disturbance input ($d_{LKF} = \{\hat{F}_{z,i}\}$).

The quasi-static weight transfer model given by expressions (3.11-3.13) was used to estimate the tyre vertical forces as a function of the chassis accelerations $F_{z,i} = f(a_x, a_y)$. Following a similar approach to [21], the vector of open-loop estimates was filtered adopting RLS ($\hat{F}_{z,i} = RLS(F_{z,i})$). Additional details regarding the RLS derivation can be found in [11, 146]. These forces were used to compute a time-varying wheel effective radius adopting a linear-stiffness model [17]. The vector of measurements of the UKF was formed by the yaw rate and the average rotational velocity of the non-driven wheels ($\mathbf{Y_{UKF}} = \{\dot{\psi}, \frac{\boldsymbol{\omega_{rl}+\omega_{rr}}}{\mathbf{2}}\}$), and the vector of inputs by the angle steered by the front wheels and the sum of the estimated individual longitudinal forces ($\mathbf{U_{UKF}} = \{\delta, \hat{F}_{x,fl} + \hat{F}_{x,fr}, \hat{F}_{x,rl} + \hat{F}_{x,rr}\}$). The vector of states remained unchanged with respect to the single-track EKF, as well as the NN structure adopted to approximate the axle lateral forces. In this case, at each time step, the UKF sigma-points are generated following the formulation given in Section 3.1.3 and the sigma axle lateral slips are formed. These sigma axle lateral slips are propagated through the NN to handle the tyre-road friction nonlinearities and the sigma-axle lateral forces are obtained and re-injected into the UKF, Figure 3.10-top. For simplicity, only the high-mu friction case was implemented in this observer design. The extension to different mu-cases is straightforward adopting the mu-scaling approach described in section 3.2.1 and is proposed as a continuation of this work. Finally, the individual tyre lateral forces are obtained from the axle lateral forces adopting the vertical load proportionality principle. In brief, this principle states that the forces generated by the tyres follow a Coulomb friction law, and can be obtained from the product of the tyre-road friction coefficient and the normal load. While this approximation does not consider the load sensitivity [104] associated to the weight transfer, it provides an estimate of the individual tyre forces with reasonable accuracy during even longitudinal slip conditions and has been employed in previous works to calculate the individual tyre lateral forces from the axle forces [21],

$$\hat{F}_{y_d} = \hat{F}_y \frac{\hat{F}_{z_d}}{\hat{F}_{z_{left}} + \hat{F}_{z_{right}}} + \Omega_{bias} \tag{3.48}$$

with $d \in \{left, right\}$. The constant Ω_{bias} has been added to take into account the tyre asymmetric behaviour derived from “ply-steer” or tyre conicity effects [104]. The signals exchanged between the LKF, RLS, UKF, and NN blocks are summarised in Table 3.5 for better clarity.

Table 3.5: Observer inputs and outputs, integral tyre force UKF.

Signal	LKF	RLS	UKF	NN
Inputs	$T_{drv,i}$,$T_{brk,i}$,$\hat{F}_{z,i}$	a_x, a_y	δ,$\hat{F}_{xf}$,$\hat{F}_{xr}$	α,a_x
Measurements	ω_i	-	$\dot{\psi}$,ω_{avg}	-
Outputs	$\hat{F}_{x,i}$,$\hat{\omega}_i$	$\hat{F}_{z,i}$	$\hat{\dot{\psi}}$,$\hat{v}_x$,$\hat{v}_y$	F_{yf},F_{yr}

3.2.2.1 SiL verification

The virtual sensor was implemented in Matlab/Simulink adopting a sampling frequency of 100 Hz and a 1 ms running time. The CarMaker vehicle model introduced in Section 3.2.1.2 was used during the SiL verification process. An additive white Gaussian noise model was used to simulate noise-corrupted signals. With regards to the observer tuning, the UKF and LKF structures were tuned following a systematic trial and error procedure. A covariance-scheduling approach was adopted in order to adequate the performance of the filters to different driving states. Specifically, in the case of the LKF, large weights are assigned in the process covariance matrix of the LKF ($\mathbf{Q_{LKF}}$) during transient manoeuvring (e.g. hard braking) in which the quasi-static longitudinal force assumption (i.e. $\dot{F}_x \approx 0$) is not valid. Conversely, these weights are lowered during steady-state situations (e.g. coast down) where the previous hypothesis holds. This strategy seeks to achieve a trade-off between sufficient dynamic response in transient events and noise filtering during steady-state driving. The values of the $\mathbf{Q_{LKF}}$ matrix are modified by means of a Fuzzy Logic Controller that monitors the rate of change of the brake pedal and the engine revolutions [17].

In what concerns the UKF, a variable measurement covariance matrix $\mathbf{R_{UKF}}$ was employed to reduce the relative importance given to the average wheel speed measurement during hard braking events. During these events, the average velocity calculated from the wheel rotational velocity may differ significantly from the real ground vehicle speed, which increases the uncertainty associated with this measurement. The braking events were captured by monitoring the master cylinder pressure signal. The virtual sensor was subjected to a comprehensive catalogue of manoeuvres composed of open loop and closed loop objective tests. During the first part of the virtual testing program, the manoeuvres were realised by a virtual driver (IPG driver model) [17] and during the second part executed by a real driver with the Driver-in-the-Loop (DIL) setup depicted in Figure 3.11 [16].

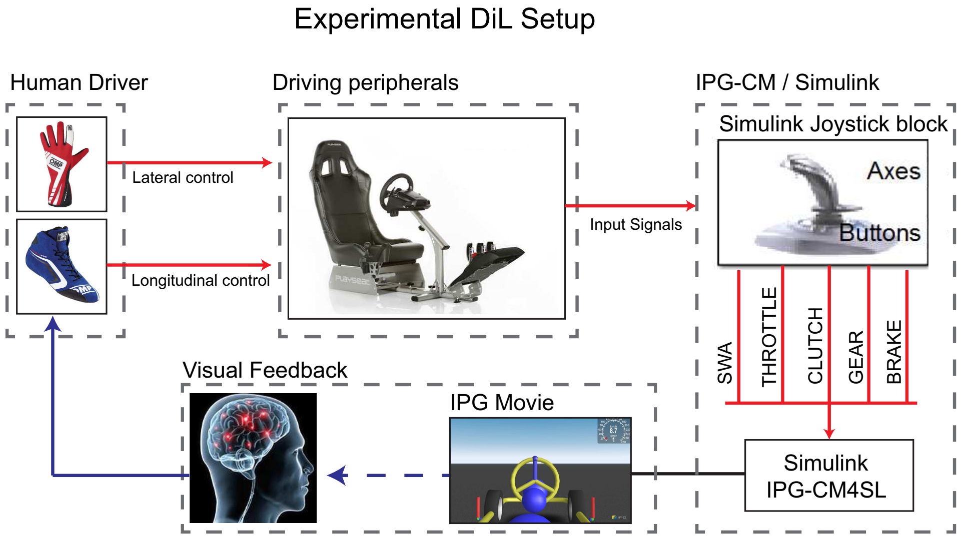

FIGURE 3.11: DIL setup used during the SiL verification to test the virtual sensor under realistic human inputs [16].

Specifically, the DiL setup consists of a static driving simulator formed by a *Playseat* baquet and *Logitech G27* driving peripherals. The peripherals signals are introduced in the IPG model using the Simulink Joystick block. In spite of the simplicity of this setup, it has been effectively used in several works during the course of this thesis [8, 12, 16] to substitute the IPG driver model in order to execute complex custom manoeuvres difficult to standardise. The results corresponding to a free acceleration-braking sequence performed manually are depicted in Figure 3.12. In the first case, Fig. 3.12-a, the vehicle is initialised at 90 kph, and a random sequence of abrupt pedal and braking inputs is performed by the driver while maintaining a straight-line trajectory. Overall, the tyre longitudinal forces (only the left-side forces are displayed to avoid redundant information) are accurately approximated by the proposed virtual sensing structure. The longitudinal velocity is computed accurately by the UKF observer in spite of the severe braking inputs ($t \approx 10$ s and $t \approx 25$ s). Similar results are obtained in the test depicted in Fig. 3.12-b, in which the vehicle is initialized at 50 kph.

This time, some oscillations are observed on the rear left force obtained from the simulation model, which might be caused by the longitudinal weight shift experienced during the braking event. Once again, the estimation of the tyre longitudinal forces carried out by the LKF and the longitudinal velocity estimate provided by the UKF match precisely the simulation signals. The results obtained during the manual execution of a Frequency response test are given in Figure 3.13. As the scope of this test is to evaluate the vehicle handling and stability in the linear region (e.g. lateral acceleration gain), the lateral acceleration is kept within 4 m/s^2. In brief, the manoeuvre consists of a steering sweep input executed while the vehicle is maintained at a constant speed. The speed was set

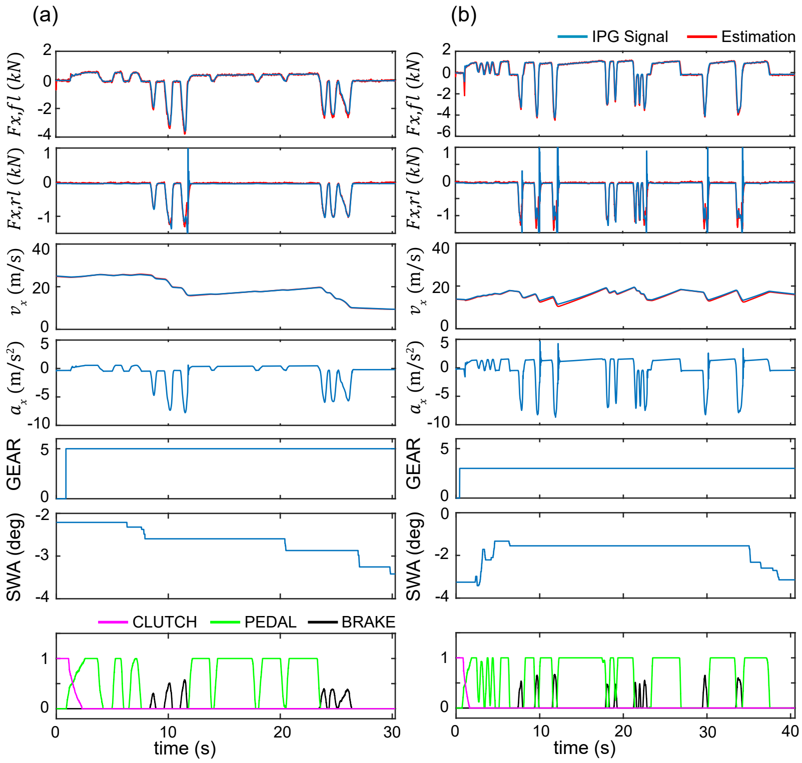

Figure 3.12: Sequence of manual acceleration and braking events. From top to bottom: Front-left tyre longitudinal force ($F_{x,fl}$), rear-left tyre longitudinal force ($F_{x,rl}$), chassis longitudinal velocity (v_x), chassis longitudinal acceleration (a_x), engaged gear (GEAR), steering wheel angle (SWA) and clutch-pedal-brake positions [16].

to 90 km/h in this case based on the experience of the author in vehicle testing. Specifically, the sweep steering input ranges approximately between 0.2 Hz (steady-state) and 4 Hz (close to the maximum steering frequency realisable by a human), Figure 3.14. As can be observed in the time histories of Figure 3.13, the signals provided by the virtual sensor follow closely the simulation signals in the low and high-frequency input ranges (zooms of the right side).

The magnitude and phase frequency response plots of the yaw rate and lateral acceleration gains are depicted in Fig. 3.14. The lateral acceleration estimate was obtained directly from the estimated tyre lateral forces. Slight differences are observed in the high-frequency range of the phase plots caused by the delay exhibited by the virtual sensing structure. Apart from this, the phase plots of the estimated signals match well the real simulated values up to an input frequency of 2 Hz. Regarding the magnitude of the estimated signals, these exhibit the characteristic yaw resonance frequency of compact vehicles (at around 0.8 Hz), and the lateral acceleration gain valley (in the interval 1-2 Hz). The precision of the virtual sensor was quantified numerically using the normalised root mean square error (NRMSE) [49]. The NRMSE values corresponding to the vehicle states and individual tyre lateral forces are provided in Table 3.6. The

NRMSE values corresponding to the individual tyre longitudinal and vertical forces are given in Table 3.7. Cells have been left blank when the level of excitation is null and a singularity is present during the calculation of the metric.

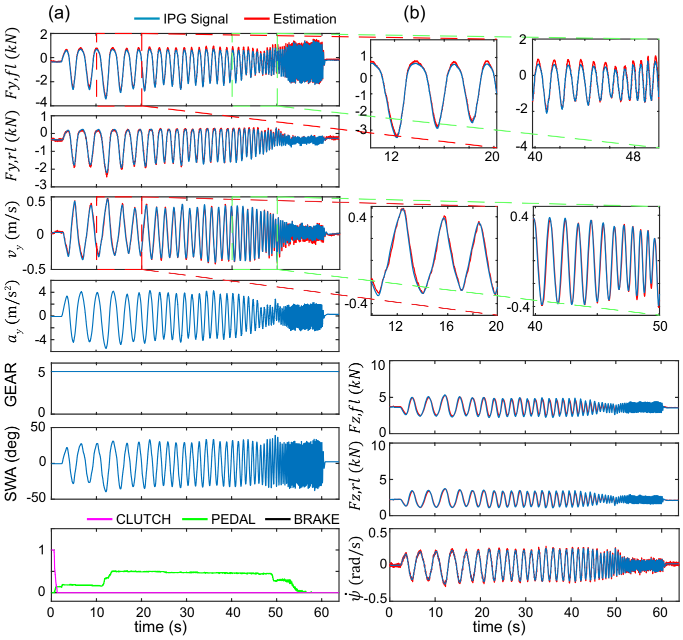

FIGURE 3.13: Frequency response test, 90 km/h. (a) From top to bottom Front-left tyre lateral force ($F_{y,fl}$), rear-left tyre lateral force ($F_{y,rl}$), chassis lateral velocity (v_y), chassis lateral acceleration (a_y), engaged gear (GEAR), steering wheel angle (SWA), and clutch-brake-pedal position. (b) From top to bottom: Zoom lateral tyre force, zoom lateral velocity, front-left vertical tyre force ($F_{z,fl}$), rear-left vertical tyre force ($F_{z,rl}$), and yaw rate ($\dot{\psi}$) [16].

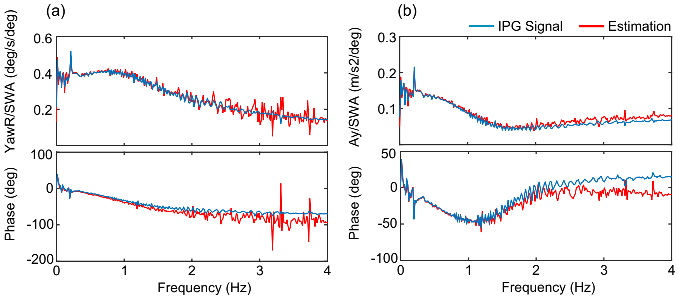

FIGURE 3.14: FFT plots, (a) yaw rate - Steering gain, (b) lateral acceleration - steering gain [16].

In what concerns the manoeuvres executed with the IPG-driver, the states are accurately estimated by the UKF, and the NRMS values keep below the 5% threshold for all the tests performed. Regarding the tyre lateral forces, the maximum NRMS values are seen in the tyres of the inner side (FL, RL) during the execution of a left-handed Braking-in-a-turn test (test 4). As these tyres are unloaded and develop low lateral forces the NRMS metric tends to magnify the signal error (see [17] for additional details). Apart from this, the accuracy of the virtual forces is good and values below the 5% threshold are observed

Table 3.6: NRMS error metrics from [17, 16], vehicle planar states and individual tyre lateral forces.

Test	v_{x0} [km/h] / $a_{x,\max}$ / $a_{y,\max}$ [m/s2]	Driver	$e_{\dot{\psi}}$	e_{v_x}	e_{v_y}
1-Hard Acc.	20/3/-	DIL-Manual	-	1.32	-
2-Free Acc.-Brk. sequence	90/8/-	DIL-Manual	-	0.46	-
3-Free Acc.-Brk. sequence	50/8/-	DIL-Manual	-	2.35	-
4-Brk. in a turn ($R = 50$)	60/4/6	DIL-Manual	2.34	1.37	6.08
5-Slalom 36m	90/-/8	DIL-Manual	3.14	1.54	3.07
6-Freq. response	90/-/4	DIL-Manual	5.63	1.97	7.86
7-Scandinavian Flick	90/8/9	DIL-Manual	1.67	4.03	4.66
8-Free steering seq.	90/-/9	DIL-Manual	2.40	0.65	1.98
9-Hard Acc.	20/3/-	IPG-Virtual	-	1.59	-
10-Hard Brk.	150/8/-	IPG-Virtual	-	0.99	-
11-ADAC LC	95/-/9	IPG-Virtual	1.63	1.04	1.31
12-Brk. in a turn	60/4/9	IPG-Virtual	3.39	1.22	1.92

in the forces generated by the outer tyres. With respect to the individual longitudinal forces, maximum NRMS errors are noticed during moments of low longitudinal excitation (e.g. coast down or free-rolling in the rear axle). When the longitudinal force is high (front axle during test 1, four wheels during test 2) the error level remains less than 10 per cent.

Table 3.7: NRMS error metrics from [17, 16], individual longitudinal and vertical tyre forces.

Test	$e_{F_{y,fl}}$	$e_{F_{y,fr}}$	$e_{F_{y,rl}}$	$e_{F_{y,rr}}$	$e_{F_{x,fl}}$	$e_{F_{x,fr}}$	$e_{F_{x,rl}}$	$e_{F_{x,rr}}$	$e_{F_{z,fl}}$	$e_{F_{z,fr}}$	$e_{F_{z,rl}}$	$e_{F_{z,rr}}$
1	-	-	-	-	4.87	4.89	26.87	29.43	4.51	1.19	1.91	2.86
2	-	-	-	-	3.08	3.07	4.47	4.91	2.70	1.99	3.91	4.42
3	-	-	-	-	3.79	3.79	8.97	9.15	3.11	2.79	5.94	5.99
4	7.44	5.00	26.47	5.02	4.25	4.92	9.22	1.49	4.82	2.50	4.29	2.48
5	3.86	4.00	3.72	4.10	4.35	4.30	36.72	38.90	5.79	5.57	5.82	5.76
6	6.40	8.48	3.47	4.42	11.26	11.35	40.24	40.75	5.60	5.86	6.02	6.41
7	13.64	10.48	7.18	5.66	11.41	16.01	8.83	12.76	7.82	7.24	7.29	7.65
8	4.65	4.69	4.09	4.27	14.75	14.11	33.83	26.27	5.91	5.72	6.06	5.88
9	-	-	-	-	7.52	7.52	22.25	22.25	3.57	3.54	2.76	2.79
10	-	-	-	-	5.34	5.35	3.66	3.81	3.13	3.10	4.37	4.34
11	2.42	2.88	2.52	3.34	11.26	13.24	36.86	8.90	3.38	3.79	3.37	3.49
12	18.27	3.73	23.84	4.92	6.68	6.63	7.69	2.30	5.28	1.39	2.54	1.89

With regards to the manoeuvres executed manually, the NRMSE of the vehicle planar motion states kept below the 10 % error band for all the test cases considered in the SiL verification. Regarding the tyre individual lateral forces, values above the latter band are observed on the front axle forces of the test 7 (Scandinavian flick), and in the unloaded rear-left wheel during the braking-in-a-turn test. The former errors are caused by the highly transient content of the manoeuvre, while the latter error is due to the reduced maximum normalising lateral force (see [16] for additional details). In what concerns the tyre individual longitudinal forces, highest NRMSE values are seen, as expected, on the rear non-driven wheels during driving or coast down manoeuvers, as the NRMS metric tends to magnify the error of signals with a reduced maximum normalising value.

Finally, the NRMSE values of the individual vertical tyre forces remain well below the 10% error band. Largest values are observed in the manoeuvres that exhibited a high transient content (tests 6, 7, and 8) due to the quasi-static weight transfer assumption.

3.2.3 Kalman filter optimisation

The SiL verification process described previously was carried out based on a preliminary manual tuning. This process is time-consuming and tedious and may be suitable for early development and research stages. Nevertheless, for industrial applications, it is convenient to propose ways of automating the tuning procedure in order to facilitate the implementation of EKF and UKF structures in a wide range of vehicle platforms. Additional works in this line have been elaborated by the author of this thesis to facilitate this task [7, 15, 5]. Following the scheme portrayed in Figure 3.15, the automated tuning procedure can be explained in the following manner.

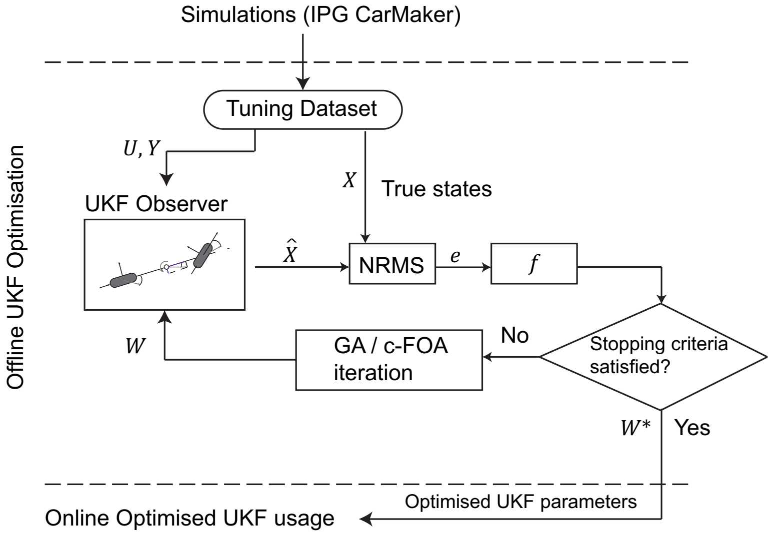

FIGURE 3.15: State estimator optimisation flow, UKF structure [7].

First of all, an optimisation dataset (tuning dataset) formed by a set of selected manoeuvres is generated in the virtual environment. At each iteration step, the observer (e.g. UKF) is initialised with a vector of decision variables ($\mathbf{W}$) formed by the Kalman filter tuning parameters (e.g. diagonal terms of the covariance matrices and α_{ukf} scaling parameter in the case of the UKF). The observer is then simulated using the vector of inputs ($\mathbf{U_{UKF}}$) and measurements ($\mathbf{Y_{UKF}}$) taken from the tuning dataset, and the NRMS errors (e) of the states estimated by the filter ($\mathbf{X_{UKF}}$) are calculated taking as ground truth the signals obtained from the simulation environment. The objective function (f) is evaluated using these errors and a new vector of decision variables is generated by a numerical (e.g. Sequential Quadratic Programming, SQP) or metaheuristic (e.g. Genetic Algorithms) multivariate optimisation routine. The objective function may be defined as $f = \sum w_i e_{x,i}$, with $e_{x,i}$ being the NRMS error associated to each state and w_i a weighting factor to adjust the relative importance of each state. This process is repeated iteratively until the stopping criteria (e.g. maximum number of iterations) is fulfilled.

This procedure was applied successfully to fine-tune the performance of the EKF and UKF structures described in the previous sections. Additional discussion regarding the numerical results derived from this optimisation procedure is omitted here due to space limitations and can be consulted in [7, 15, 5].

3.2.4 Summary of data-based observers

In this section, two novel observers have been proposed to estimate the vehicle planar motion states and tyre forces without requiring a tyre model. Instead, a machine-learning-based structure with the ability to capture the lateral tyre force behaviour directly from a set of open loop manoeuvres is proposed. Moreover, a friction potential identification routine has been introduced to ensure that the current data-based methodology is suitable for different friction levels. A comprehensive SiL testing program including manual manoeuvres executed with a DiL setup has been performed and accurate estimation results have been obtained.

The final goal of the proposed data-based methodology is to simplify and facilitate the implementation of intelligent perception systems in future autonomous vehicles. In brief, in the future a fleet of autonomous testing vehicles equipped with a data-based virtual sensor could perform a set of standardised open-loop manoeuvres to “learn” the tyre-road characteristics. This fleet may be formed by the different vehicle variants expected along the lifespan of the target vehicle. Additionally, this methodology may be combined with the automated tuning procedure described previously to calibrate the virtual sensor automatically. As an example, the testing vehicle could perform the tests with the aid of automated steering control, generate the training dataset required by the intelligent perception layer, and perform an automated tuning procedure to calibrate the system. This “learning” and “calibration” step could substitute current Electronic Chassis Control System (ECCS) testing programs, which are carried out manually in proving grounds by test engineers. This concept was introduced in [3] as an alternative to current in-vehicle tyre characterisation methods.

3.3 Random-walk virtual sensing

The data-based methodology introduced in the previous section may be expensive and difficult to implement at a mass scale level in autonomous vehicles expected to operate along aggressive off-road scenarios (e.g. gravel, snow) or in extreme sliding conditions (e.g. sustained high body slip control). In these conditions, the generation of a training dataset may lead to mechanical damage of the testing vehicles or maybe just not realisable in current proving grounds (in which the objective testing manoeuvres are carried out on tarmac skidpads). These limitations motivated the elaboration of a virtual sensor that could be implemented and used when no tyre model or training datasets are available.

A random-walk EKF for integral tyre force virtual sensing is presented in this section. The design is completed with a friction curve learning subsystem based on an Adaptive Neuro-Fuzzy Inference System (ANFIS). The complete structure is subjected to a SiL verification program with the commercial simulation package IPG-CarMaker.

3.3.1 Random-walk EKF

The structure of the proposed state estimator is depicted schematically in Figure 3.16.

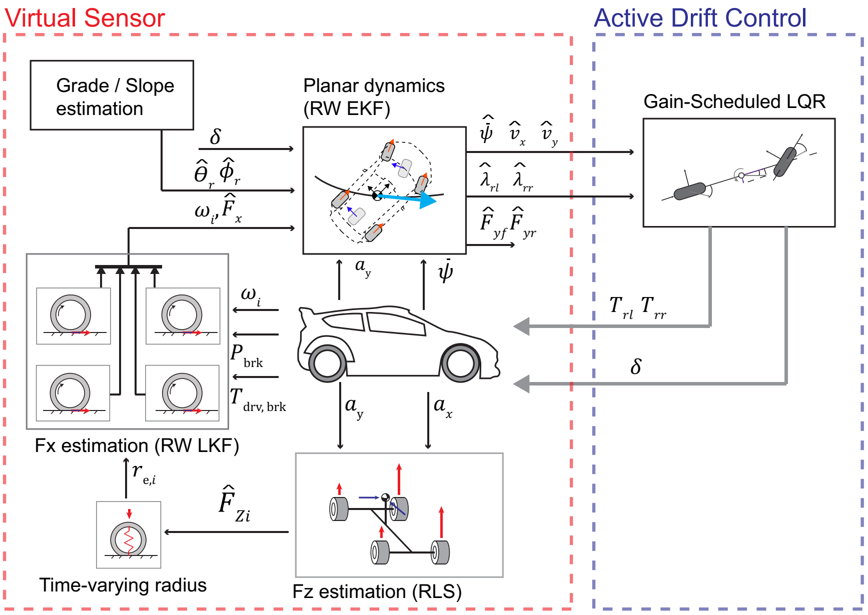

Figure 3.16: Structure of the proposed random-walk EKF for active drift control [12].

Essentially, a modular architecture similar than described in Section 3.2.2 is adopted, but in this case, the NN-UKF planar dynamics module is substituted by a Random-Walk EKF (RW-EKF). To avoid repetition, the attention in this section is given to the RW-EKF block, additional details regarding the vertical and longitudinal tyre force virtual sensing modules can be found in Section 3.2.2. Following a similar approach than [70, 109], an auto-regressive (AR) model of the form $F_{y,k+1} = a_1 F_{y,k} + \Gamma_k$ is adopted to represent the time evolution of the axle lateral tyre forces. In this case, Γ_k is considered a random noise that drives the axle lateral forces, and a_1 is the AR regression factor, set to unity for simplicity. Other coefficients extracted from [101] were tested and negligible improvement was obtained. These forces were incorporated directly into the vector of states of the RW-EKF as "random-walk" variables, $\mathbf{X_{RW-EKF}} = \{\dot{\psi}, v_x, v_y, F_{yf,RW}, F_{yr,RW}\}$, thus eliminating the necessity of an external NN structure. Instead, in this new configuration the time evolution of the axle lateral forces is given by the corrective action performed during the *measurement update stage* of the Kalman filter. The vector of inputs is made of the angle steered by the front wheels, the individual tyre longitudinal forces estimated in the RW-LKF modules, and the estimated road inclination $\hat{\theta}_r$ and bank $\hat{\phi}_r$ angles, $\mathbf{U_{RW-EKF}} = \{\delta, \hat{F}_{x,i\in\{fl,fr,rl,rr\}}, \hat{\theta}_r, \hat{\phi}_r\}$. In this case, individual longitudinal forces are considered in the vehicle modelisation to account for the effects derived from a non-uniform torque distribution on the yaw dynamics (e.g. during active drift control [18]). With regards to the road orientation angles, these can be estimated by an external state estimation block. An example of such structure was elaborated by the author of this thesis in collaboration with the University of Technology of Compiègne [2]. The vector of measurements is formed by the yaw rate, longitudinal velocity, compensated lateral acceleration $a_{y,comp}$, and a pseudo-measurement of the lateral velocity v_y^*, $\mathbf{Y_{RW-EKF}} = \{\dot{\psi}, v_x, a_{y,comp}, v_y^*\}$. As the ultimate goal of the proposed observer is to be applied in high body slip stabilisation problems (i.e. active drifting), a target vehicle with a rear-wheel-drive (RWD) configuration is considered, and the longitudinal velocity is calculated directly from the rotational speed of the front non-driven wheels,

$$v_x = \left(\frac{w_{fl} r_{e,fl} + w_{fr} r_{e,fr}}{2} \right) (\cos(\delta) + \tan(\alpha_f \sin(\delta))) \tag{3.49}$$

thus avoiding the necessity of employing additional equipment to measure the vehicle ground speed. Additional discussion regarding the modifications needed to satisfy all-wheel-drive (AWD) architectures is given in Section 3.3.2. Further details regarding the derivation of expression (3.49) can be found in [12]. The compensated lateral acceleration $a_{y,comp}$ is calculated from the measured lateral acceleration $a_{y,m}$,

$$a_{y,comp} = a_{y,m} - g\cos(\theta)\sin(\phi) + g\cos(\theta_r)\sin(\phi_r) \tag{3.50}$$

with θ, ϕ being the pitch and roll chassis orientation angles with respect to an inertial reference frame. Details regarding the calculation of the chassis orientation angles can be found in [2]. Finally, a pseudo-measurement of the lateral velocity is incorporated into the measurement vector in order to guarantee the structure observability during periods of reduced lateral excitation (i.e. during straight-line driving). Specifically, the lateral velocity is assumed to be zero ($v_y^* \approx 0$), and the measurement covariance term $R_{RW-EKF}(4,4)$ associated with this measurement is increased or decreased to weight the relative importance of the previous assumption depending on the driving situation (low weights during straight-line driving and large weights during high body slip control) [12].

3.3.1.1 Road friction learning

The RW-EKF block estimates the axle lateral forces without requiring any *a priori* knowledge of the tyre-road interaction (e.g. tyre model or data-based structure). This feature can be used to “learn” the friction characteristics (e.g. lateral force versus slip curve) of unknown surfaces adopting the structure depicted in Figure 3.17.

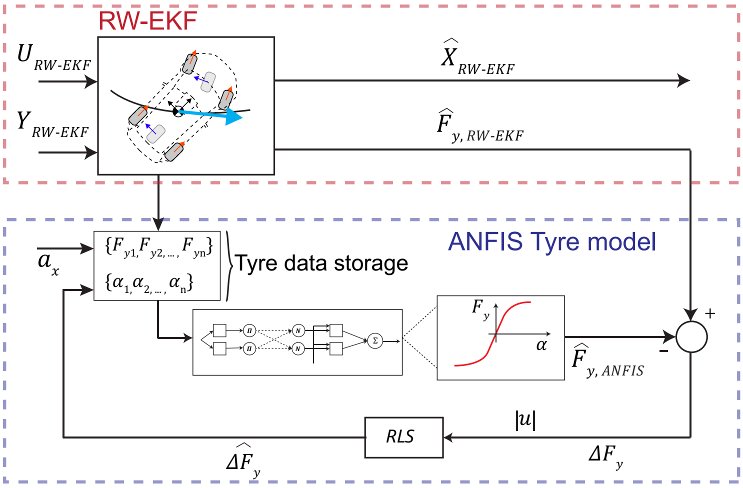

Figure 3.17: Vehicle planar dynamics block: Random Walk EKF and ANFIS surface characterisation modules [12].

Specifically, the upper-level (RW-EKF) provides continuous estimates of the axle lateral forces and vehicle planar motion states. Whilst these form part of the same state vector, two signals have been illustrated in Fig. 3.17 for better clarity. An ANFIS model is placed at a lower level to "learn" the lateral slip versus tyre force curve from the information provided by the RW-EKF. At each time step, the uncertainty associated with the current ANFIS model is quantified by means of the lateral force error ($\Delta\hat{F}_y$), which is smoothed using an RLS block. When this error is above a certain threshold (i.e. the current ANFIS model does not approximate well the real friction characteristics), the estimated axle lateral slips $\hat{\alpha}$ and axle lateral forces $\hat{F}_y$ are stored progressively until a minimum amount of data is gathered, at which point the ANFIS learning process is triggered. This batch learning approach is run in parallel during the function of the virtual sensor and can be considered quasi-online learning due to the reduced time required to train the ANFIS structure ($t \approx 0.2$ s for a training dataset of size 2301, 20 maximum epochs, and an ANFIS structure formed by 2 membership functions, [12]).

The ANFIS structure was implemented in Matlab by means of the *anfis.m* routine as a Single-Input Single-Output (SISO) Sugeno-type Fuzzy Inference System. The number of Membership Functions (MFs) was set to 2 after performing a sensitivity analysis with the aim to maintain a reduced training time, and the maximum number of epochs was limited to 20. Additional details regarding the ANFIS building process can be found in [12]. The ANFIS adaptation algorithm is presented schematically in Figure 3.18.

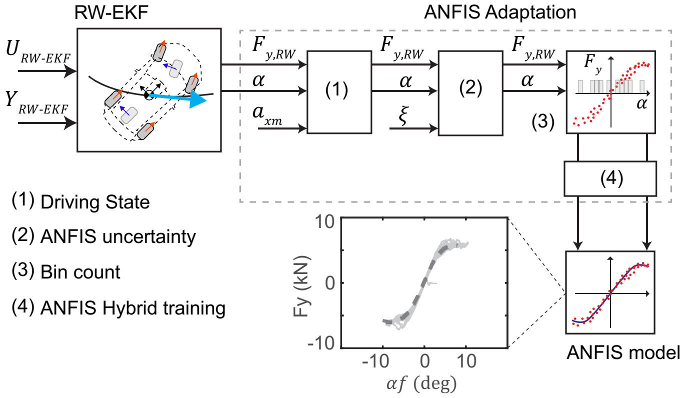

FIGURE 3.18: ANFIS friction learning sequence [12].

The first block (*driving state*) is employed to "filter" the input data, allowing the acquisition of new samples only during constant speed situations. This aims at eliminating non-representative samples of combined efforts (e.g. braking in a turn, power on) that would require the inclusion of additional inputs (longitudinal slip) in the ANFIS model. Such considerations may be implemented in further refinements of the proposed approach. A second block (*ANFIS uncertainty*) is used to avoid unnecessary adaptation, thus limiting the number of training events to situations in which the ANFIS model presents a certain level of uncertainty. A bounded normalised factor ($\xi_k \in [0, 1]$) is employed to quantify the uncertainty associated with the ANFIS model. Low values indicate a good match between the ANFIS model and the real road-friction characteristics whereas values close to unity indicate poor performance of the ANFIS model. This factor is determined with expressions (3.51-3.53).

$$\begin{aligned}\Delta F_{y,k} &= |\hat{F}_{yf,RW_k} - \hat{F}_{yf,ANFIS_k}| \\ &\quad + |\hat{F}_{yr,RW_k} - \hat{F}_{yr,ANFIS_k}|\end{aligned} \tag{3.51}$$

$$\Delta\hat{F}_{y,k} = RLS(\Delta F_{y,k}) \tag{3.52}$$

$$\xi_k = \frac{\Delta\hat{F}_{y,k}}{C} \tag{3.53}$$

First, the axle lateral force error ($\Delta F_{y,k}$) is computed using expression (3.51). An RLS block is employed to reduce the noise influence and provide the most probable values of the noise-corrupted signal [21, 6], expression (3.52). An exponential factor λ_{ANFIS} is employed to reduce the relative importance of the old samples on the current prediction. Smaller values are used to reduce the importance of the previous samples and increase the adaptation rate [146]. Finally, the weighting factor ξ_k is obtained after normalising the term $\Delta\hat{F}_{y,k}$ using equation (3.53). The constant C is the maximum admissible error of the estimate $\Delta\hat{F}_{y,k}$, and was adjusted empirically. $\Delta\hat{F}_{y,k}$ is rectified with this constant before applying equation (3.53) to have a normalised weight factor bounded in the interval $[0, 1]$. Accurate results were obtained setting C to 1 kN and employing a forgetting factor $\lambda_{ANFIS} = 0.999$ in the RLS algorithm. When the level of uncertainty (ξ_k) is above a certain threshold (ξ_{thres}) the training samples are stored in a third block (*bin count*). A *bin count* approach is used in the last step in order to avoid overfitting in local regions and extrapolation issues derived from uneven sample concentrations. The axle lateral slip range is evenly distributed in n_{int} intervals, and the number of valid samples entering the block and remaining within each range (n_s) is counted. When an interval reaches a minimum number of samples n_{min} this is assigned a binary value $c_i = 1$. At each time step, the filling factor c_{fill} is computed from expression (3.54).

$$c_{fill} = \frac{\sum_{j=1}^{n_{int}} c_i}{n_{int}} \tag{3.54}$$

The training of the ANFIS network is triggered once the filling factor c_{fill} reaches a certain threshold (e.g. 50%), indicating that there are sufficient samples distributed along at least 50% of a predefined ANFIS input range (α_{lim}). Finally, the new samples are concatenated into the existing training dataset and the last V samples are employed to train the ANFIS model using a hybrid learning algorithm which combines the gradient method and the Least Squares Estimate (LSE) [75]. The elimination of older samples guarantees quick adaptability of the model during mu-varying events. The parameters employed in the final ANFIS implementation are detailed in Table 3.8 and were determined empirically after testing the ANFIS model in different mu-varying situations.

Table 3.8: ANFIS adaptation parameters [12].

c_{fill} (%)	ξ_{thres}	n_{int}	α_{lim} (deg)	n_{min}	V
50	0.4	20	5	30	3000

3.3.1.2 SiL verification

Following the methodology described in previous sections, the virtual sensor was implemented in Matlab/Simulink using a discretisation time of 1 ms. The simulation signals were acquired from the virtual environment at 100 Hz by means of a zero-order hold and an additive white-Gaussian noise model was used to simulate noise-corrupted measurements. The virtual track depicted in Figure 3.19 was generated in IPG-CarMaker in order to test the observer under aggressive manoeuvring along an off-road countryside road. An isotropic Magic Formula modelisation was used to simulate the road friction properties of an extreme off-road terrain, characterised by the exponential friction shape described in Section 2.2 (Figure 2.5), and explained by the soft-soil theory. Specifically, the tyre parameters corresponding to the tyre-4 described in the minimum-time cornering work of Tavernini et al. [128] were adopted. This tyre modelisation was proposed by Velenis et al. in relevant vehicle motion control works [134] to simulate the vehicle planar dynamics under limit sliding conditions. In addition, the simulation results were supported by a set of full-vehicle-level experiments in an off-road terrain.

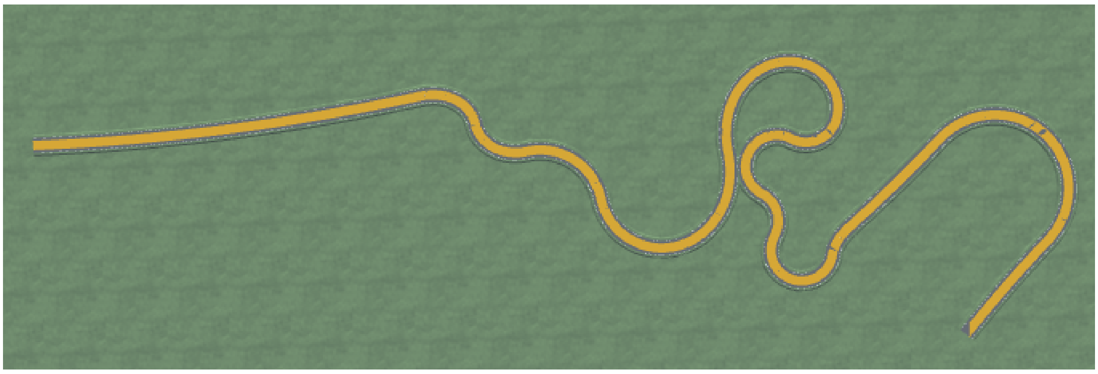

Figure 3.19: Virtual gravel road generated in IPG-CarMaker by concatenation of arc and clothoid segments [12].

Additional experiments were carried out by the author of this thesis in order to verify the soft-soil theory described by Velenis and Tavernini. Specifically, an experimental friction characterisation process was performed with an SUV test vehicle fitted with tyres of size 215/65 R16. The test vehicle was equipped with a differential GPS and a high-accuracy Inertial Motion Unit (IMU). The ESP of the vehicle was disconnected in order to facilitate reaching large tyre lateral slip angles and approximating the vehicle dynamics with a single-track model. Additional details regarding the experimental vehicle are omitted here due to confidentiality reasons. Steady-state steering ramp manoeuvres were performed at a constant speed in an off-road flat platform characterised by a dry gravel mixture. The rear axle lateral slip was computed from the inertial measurements as $\alpha_r = \arctan\left(\frac{\dot{\psi} l_r - v_y}{v_x}\right)$, and the rear axle normalised friction was calculated as $\mu_r \approx a_y/9.81$ under the assumption of steady-state conditions (i.e. negligible yaw acceleration, $\ddot{\psi} \approx 0$). After that, a constrained genetic algorithm optimisation routine was employed to fit a cloud of μ_r, α_r data pairs, obtaining the results depicted in Figure 3.20.

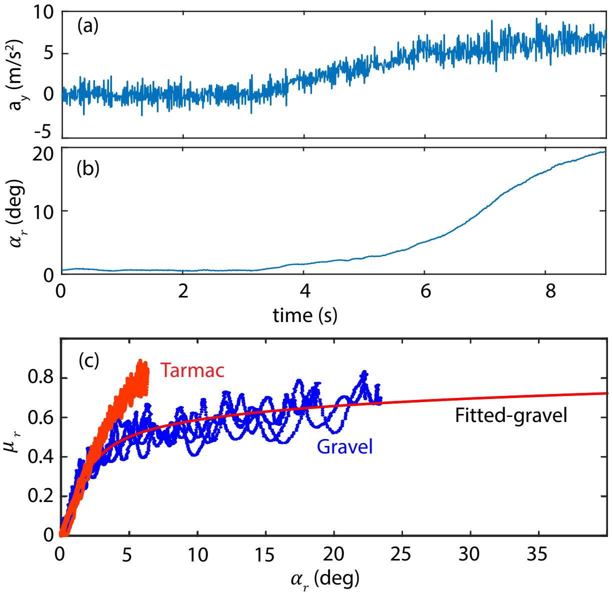

FIGURE 3.20: (a) Measured lateral acceleration on a constant-speed steering ramp manoeuvre - gravel, (b) reconstructed rear axle lateral slip - gravel, (c) experimental friction data (tarmac - gravel) and fitted friction model.

Additional steering ramp manoeuvres (up to lateral grip limit) were executed on a tarmac platform with the aim to establish a comparison between “rigid” and “loose” surfaces, Figure 3.20-c. These results evidence the significant difference that exists in the friction developed by the tyres on “rigid” (tarmac) and “loose” (gravel) surfaces. In particular, while maximum friction is developed at reduced tyre lateral slips (≈ 5 deg) on tarmac, significantly larger values are required on gravel. These experimental results correlate well with the "*bulldozing*" effect mentioned in the literature and adopted in Velenis' and Tavernini's works.

In addition to the friction modelling, a random profile generation process based on the Sayers pseudo-random model [118] was used to test the virtual sensor robustness to high vertical excitation levels. The random profiles were generated numerically in Matlab and implemented in IPG-CarMaker by means of *.crg* road property files. To validate the proposed approach, different road categories were generated and their Power Spectral Density (PSD) were compared to those recommended in ISO 8608:2016 [52]. Specifically, rough road profiles and smooth road profiles were employed for loose and asphalt surfaces respectively. Additional details regarding this process can be found in [12, 13].

Finally, the compact-class chassis model described in Section 3.2.2 was maintained for consistency and an RWD driveline equipped with an open differential was adopted. The virtual vehicle model was driven along the proposed road segment at the limits of handling using the DiL setup introduced in Section 3.2.2. The body slip angle is increased deliberately and maintained along the turns in order to maximise the lateral acceleration [134, 128]. Overall, the vehicle planar velocities estimated by the RW-EKF follow closely the simulation signals, Fig. 3.21. Slight offsets are seen on the lateral velocity during the time intervals 5-15 s and 90-100 s corresponding to aggressive braking inputs. In spite of this, the NRMSE remains well below the 5% threshold for all the vehicle planar motion states, Table 3.9. The individual longitudinal forces are depicted in Fig. 3.22.

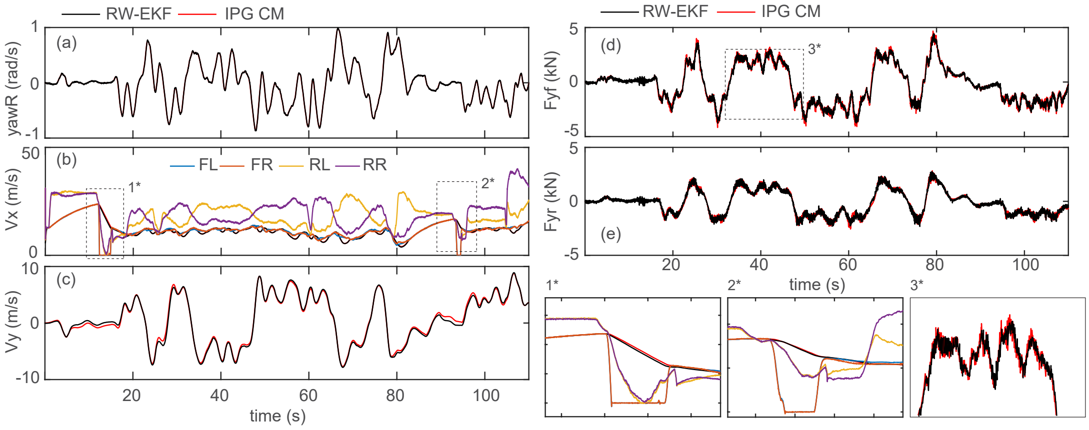

Figure 3.21: Limit drifting on gravel, manual test. (a) Yaw rate, (b) longitudinal velocity, (c) lateral velocity, (d) front axle lateral force and (e) rear axle lateral force [12].

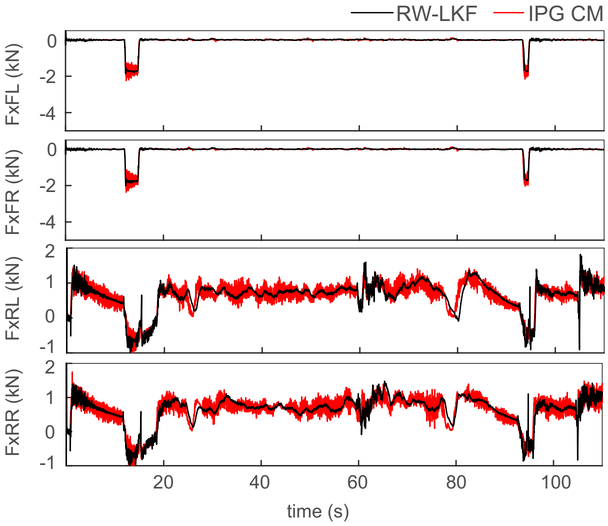

FIGURE 3.22: Tyre longitudinal forces estimated by the RW-LKF [12].

In spite of the aggressiveness of the manoeuvres, the RW-LKF approximates very well the simulation signals. Additional manual drifting tests ($R-20$ drift stabilisation) were performed and similar accuracy levels were obtained. To conclude with the RW-EKF verification, the state estimation structure was implemented successfully in the feedback loop of an RWD active drift controller based on an LQR formulation. Additional discussion regarding high body slip control is provided in Chapter 4. In general, good accuracy levels were seen during the tests performed with the active drift controller, Table 3.9.

TABLE 3.9: NRMS error metrics [12].

Test	$e_{\dot{\psi}}$	e_{v_x}	e_{v_y}	$e_{Fy,f}$	$e_{Fy,r}$	$e_{F_{x,fl}}$	$e_{F_{x,fr}}$	$e_{F_{x,rl}}$	$e_{F_{x,rr}}$
1-Manual drift ($R = 20$ m)	0.90	0.54	2.46	4.03	6.16	9.19	9.33	8.98	7.68
2-Manual drift (virtual road)	0.94	1.16	3.83	4.03	5.64	2.45	2.34	11.73	10.12
3-Active drift control ($R = 10$ m)	0.79	1.72	5.43	6.25	6.86	9.50	2.98	8.08	6.55
4-Active drift control (Clothoid)	1.92	1.52	5.81	7.38	7.44	18.93	24.31	4.97	7.21

Overall, all the errors lie well below the 10% threshold. Numerical errors from other works found in the literature range from 5 to 10%, [48, 58]. Nevertheless, in these virtual sensing works drifting manoeuvres were not considered, and thus a more detailed comparison cannot be established. Moreover, additional hypotheses such as the availability of a tyre model embedded in the observer, *a priori* known road-friction characteristics, or direct measurement of the ground vehicle velocity were assumed in the works cited previously. The proposed structure not only achieves similar performance levels but also eliminates these assumptions. Regarding the longitudinal force errors, values below the 10% error band are seen in the majority of the manoeuvres. Values exceeding this band are noticed occasionally when the longitudinal forces are reduced (e.g. non-driven wheels during power-slide). As was seen previously, the estimation of the vehicle motion states is very accurate in spite of these errors.

After testing the RW-EKF structure, additional manoeuvers were performed to verify the suitability of the ANFIS-based friction learning approach described in Section 3.3.1.1, Fig. 3.23. In total, 4 sinusoidal manoeuvres were executed manually at a constant speed on different surfaces. In cases (1), (2), and (3), the ANFIS model is initialised as an empty model and driven over asphalt ($\mu_{\max} = 1$,$\mu_{\max} = 0.6$) and gravel-like ($\mu_{\max} = 0.6$) surfaces. Asphalt surfaces were simulated using the 205-65/R16 MF 6.1 tyre model introduced in Section 3.2.1.2, while the gravel surface was modelled using the same isotropic MF tyre model of the RW-EKF tests described before. During the first seconds of the tests, the ANFIS adaptation algorithm stores the information provided by the RW-EKF. Once enough information is gathered, the ANFIS model is trained and updated. As can be seen in Fig. 3.23, the ANFIS model adapts remarkably well to the road friction characteristics in high-mu asphalt, low-mu asphalt, and gravel-like surfaces. An additional test is depicted at the bottom of the figure, case (4), where the ANFIS model obtained in the gravel test is reused in high-mu asphalt conditions. The ANFIS model re-adapts quickly to the new road friction characteristics and provides accurate estimates after $t \approx 32$ s, demonstrating the suitability of the ANFIS adaptation approach to tracking mu-varying conditions.

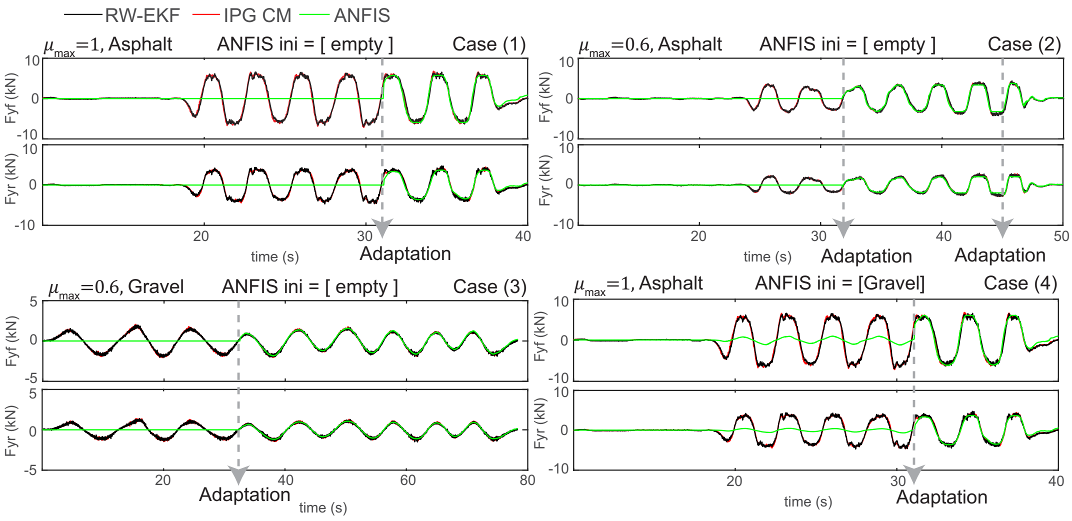

FIGURE 3.23: Evaluation of the proposed ANFIS model for road friction characterisation [12].

The fitted front axle force and front axle cornering stiffness versus lateral slip curves obtained with the ANFIS-based friction characterisation approach are depicted in Figure 3.24. Overall, a good correlation is observed between the output of the trained ANFIS structures and the simulation signals. This concept will be revisited in Chapter 5 with the description of the virtual sensing tool for in-vehicle tyre characterisation.

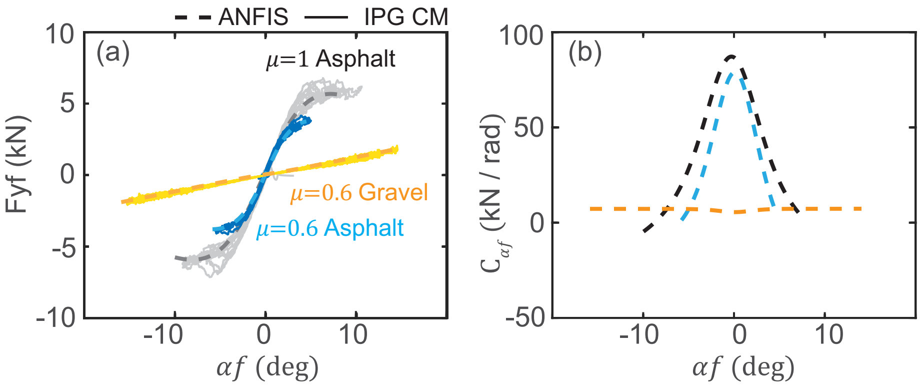

FIGURE 3.24: Road friction characterisation with ANFIS. (a) Front axle lateral force, (b) Front axle cornering stiffness ($C_{\alpha,f}$) versus lateral slip curve [12].

3.3.1.3 Comparison with the NN-EKF

In order to evidence the advantages of the RW-EKF when a wrong training dataset or an incorrect tyre model are considered, the proposed observer was benchmarked against the NN-EKF described in Section 3.2.1 and a tyre-model-based EKF constructed adopting an MF tyre model (MF-EKF), [12]. Specifically, in the MF-EKF design, the NN structure was substituted by a compact-class tyre model representative of a wet tarmac road (Fig. 3.25-a, tyre-2 [128]). For consistency, the virtual vehicle model described in Section 3.2.1 and fitted with the 205-65/R16 MF 6.1 tyre model was used during this comparison. Initially, a sinusoidal steering manoeuvre was simulated in wet tarmac conditions (setting the friction scaling factor of the MF 6.1 tyre model employed in the virtual vehicle to 0.6), Figure 3.25-a.

As can be seen, the RW-EKF, the MF-EKF and the NN-EKF approximate very well the vehicle body slip and the axle lateral forces. In this case, the NN-EKF is able to provide an online accurate estimation of the road friction potential, demonstrating the ability of this approach to estimate the maximum road friction ($\mu_{\max}$) of rigid surfaces. The same sinusoidal test was repeated on the low-mu loose surface (gravel, $\mu_{\max} = 0.6$), utilised during the RW-EKF SiL verification, Section 3.3.1.2. The parameters of the MF-EKF were kept unaltered, assuming that only the maximum road friction ($\mu_{\max} = 0.6$) is considered and used to correct a tyre model parameterised by conventional means (i.e. on a tarmac surface). As can be noticed in Fig. 3.25-b, the tyre model-based approach using a tyre model characterised in a rigid surface (MF-EKF) and the data-based approach trained with manoeuvres executed in a rigid surface (NN-EKF) fail to

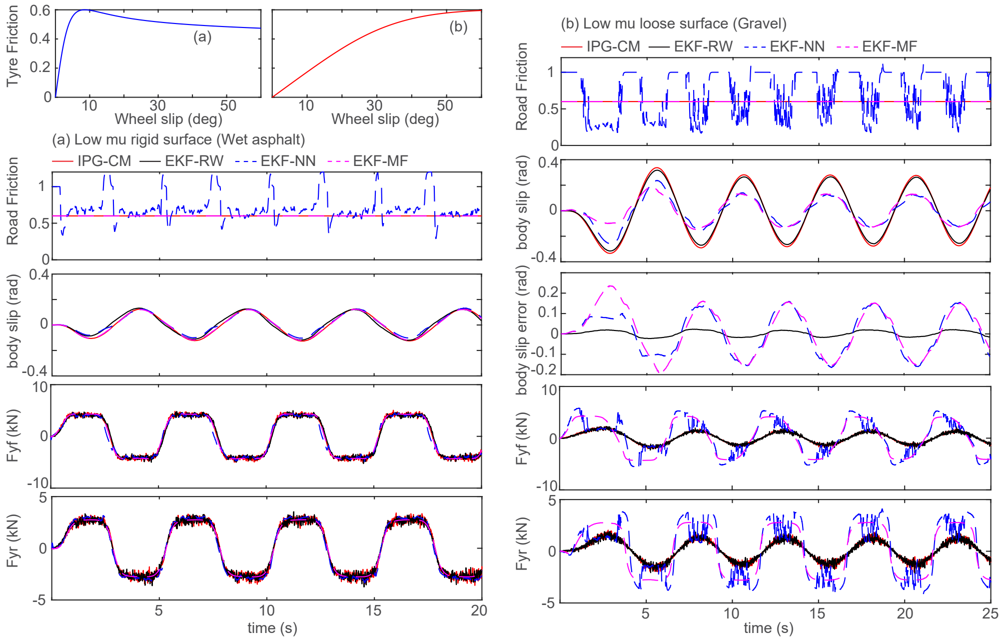

FIGURE 3.25: Sinusoidal test, 80 kph, 90 degrees steering input, Freq. 0.2 Hz. (a) Wet rigid surface, (b) Gravel Loose surface [12].

predict the vehicle body slip and the axle lateral forces. In particular, the NN-EKF is unable to estimate accurately the surface friction potential and underestimates the vehicle body slip. This malfunction is caused by the extreme reduction of the cornering stiffness and the monotonic friction characteristics exhibited by loose surfaces, where the maximum friction depends on phenomena such as the *buldozzing* effect, and is generated at high wheel slip angles [88, 128]. The maximum body slip error of the MF-EKF and NN-EKF observers is close to 10 degrees, which evidences the error introduced if only the maximum friction is considered to characterise drastically-different surfaces.

In order to assess the influence of the state estimator accuracy on the vehicle safety, the observers compared in the previous paragraph (NN-EKF and RW-EKF) were implemented in a Yaw Stability Control (YSC) system [78]. The YSC design described in [78] introduces a differential braking action to maintain the vehicle yaw rate and body slip angle within the linear region limits [78]. The controller gain was obtained using a Linear Quadratic Regulator formulation. It must be remarked that the focus of this comparison lies in the virtual sensor, and therefore the YSC is introduced here merely to study the influence of the observer accuracy on the vehicle stability. Sine with Dwell tests were simulated on rigid (asphalt high mu, low mu), and loose surfaces (gravel). Usually, the YSC activation threshold depends on the road friction potential [107, 78]. In this study, a worst case scenario is considered (e.g. a quick transition from high to low mu), and the same yaw rate and body slip thresholds were used during the three simulations ($|\dot{\psi}_{max}| = \frac{8m/s^2}{v_x}$, $|\beta_{\max}| \approx 8$ deg, [78]). The YSC equipped with the observers

(RW-EKF and NN-EKF) restricted the vehicle response within the desired thresholds during the tests performed on rigid surfaces, Fig. 3.26-a.

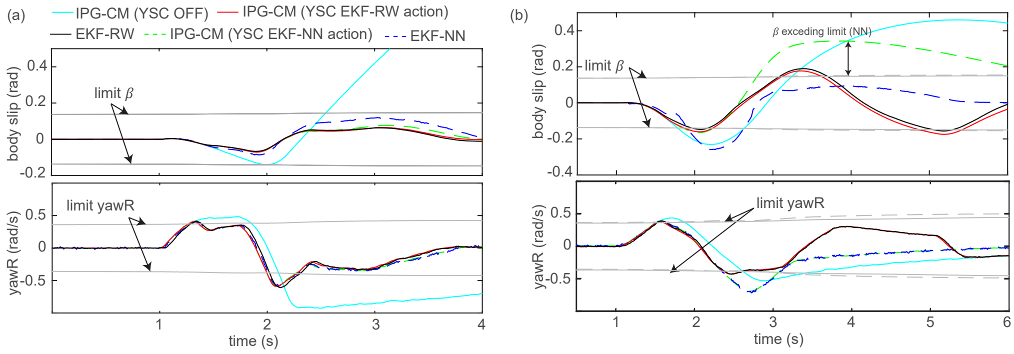

FIGURE 3.26: Sine with dwell test, 80 kph. (a) Wet asphalt, $\mu_{\max} = 0.6$, 160 degrees steering input. MF 6.1 tyre model [6]. (b) Gravel terrain, $\mu_{\max} = 0.6$, 245 degrees steering input, MF Isotropic gravel tyre model [128]. Figure reproduced from [12].

Severe vehicle instability (spin) was observed with the YSC disabled. A slight deviation is seen on the NN-EKF estimates due to the differential braking action of the YSC, which is not included in the virtual sensor model (single-track modelisation). Additional results regarding the high-mu tests are omitted due to space limitations. As can be seen in Fig. 3.26-b, the performance of the data-based observer (NN-EKF) was significantly worsened during the test executed on gravel (a large error is observed on the estimated vehicle body slip). This affects significantly the stability of the vehicle, as the YSC is not able to maintain the vehicle within the required body slip threshold and a maximum body slip angle $\beta \approx 20$ degrees is reached. On the other hand, the YSC equipped with the proposed observer (RW-EKF) was able to follow closely the maximum body slip thresholds. Overall, despite these results might vary in absolute terms in a real environment, the patterns exhibited by this analysis evidence that the use of a tyre model or a data-based structure characterised on rigid surfaces should be avoided when dealing with extreme off-road surfaces, even if the maximum friction coefficient is the same. In these unknown surfaces, a tyre-model-less approach in which no *prior* knowledge regarding the friction characteristics is needed for implementation will be preferred.

3.3.2 Extension to AWD architectures

Up to know, the RW-EKF has been evaluated in several drifting manoeuvres performed with an RWD vehicle. In order to apply this observer to more complex MAGV architectures incorporating AWD torque control, it is necessary to take additional considerations regarding the longitudinal velocity measurement. During aggressive powerslide with an AWD vehicle, high longitudinal slip values will be expected on the four wheels, and the longitudinal velocity calculated from the wheel rotational speed will differ significantly from the real ground velocity experienced at the centre of gravity. This reference velocity "lost" is a common problem of AWD chassis systems during hard traction requests in slippery surfaces. During these situations, some systems "open" a central clutch to recalculate the reference velocity momentarily from the non-driven wheels.

Such strategy could cause severe instability during the intervention of the control applications proposed in this work (high body slip stabilisation). Apart from this, despite the fact that relevant approaches have been introduced in the literature to estimate the ground velocity from longitudinal acceleration measurements [54], such integration-based strategies may be sufficiently accurate for short powerslide periods, but could lead to significant errors during prolonged drifting manoeuvres (e.g. Gymkhana, Chapter 5). In this thesis, the use of a GPS unit providing a low frequency (10 Hz) absolute velocity measurement is proposed as an intermediate solution between a fully integration-based approach prone to inaccuracies during prolonged drifting and direct planar velocity measurements relying on an expensive high-accuracy differential GPS unit. Due to space limitations, additional simulation results are omitted in this section, and this discussion is continued in Chapter 5, where high body slip stabilisation experiments adopting the proposed virtual sensing approach are carried out with the AWD DevBOT MAGV.

3.3.3 Summary of random-walk observers

In this section, a novel tyre-model-less observer for tyre force virtual sensing has been presented. The observer has been subjected to a SiL testing program comprising different aggressive drifting manoeuvres. Moreover, an ANFIS-based friction characterisation approach has been proposed to learn the friction characteristics of unknown terrains and verified for different lateral dynamics manoeuvres.

In essence, the major advantage of the proposed structure is that its implementation does not require any tyre model or training dataset. This advantage has been evidenced during the comparisons carried out with the NN-EKF observer developed in Section 3.2.1 and a tyre model-based MF-EKF. These observers presented significant errors when subjected to manoeuvres performed in a loose terrain not captured by the tarmac tyre model embedded in the MF-EKF, and drastically different from the rigid tarmac surface used to construct the training dataset of the NN-EKF.

One drawback derived from the proposed friction learning methodology is that a continuous lateral excitation during a certain period of time is required to build the ANFIS training dataset. A more comprehensive friction characterisation approach using the information acquired from other subsystem domains (e.g. longitudinal dynamics, braking

- acceleration) could help to reduce the friction learning time. This enhancement of the current design is proposed as an extension of this research.

3.4 Conclusions

In this chapter, different solutions to facilitate the implementation of intelligent perception layers on future Highly-Skilled Autonomous Vehicles (HSAVs) have been proposed. This layer is aimed at supporting the function of motion control systems and will reproduce the “learning” ability exhibited by professional drivers, who can easily identify changing friction conditions and adjust their behaviour accordingly.

In brief, a hybrid modelling methodology has been used during this chapter to design vehicle dynamics and tyre friction virtual sensors. This methodology combines a synthesised vehicle model to capture the overall dynamic behaviour with Artificially-Intelligent structures that can “learn” the characteristics of subsystems that are difficult to model and expected to change during the vehicle operation (tyre-road friction). Two observer designs have been proposed to realise the previous concept: data-based observers and random-walk observers. In what concerns the first group, EKF and UKF structures were studied at the beginning of this section as it was not possible to preliminarily determine which structure was more suited for the HSAV application. Further benchmarking activities would be advantageous to gain more insight into the suitability of these structures for each particular case.

To finalise with this chapter, the following points synthesise the most relevant conclusions extracted from this research on vehicle dynamics virtual sensing.

- Data-based virtual sensors need to be trained *a priori* (i.e. execution of a set of standardised manoeuvres) and don’t have the ability to learn new unknown surfaces during operation, only to provide a friction scaling factor when surfaces similar to those included in the training dataset are considered. This can be suitable for operation on rigid surfaces, but cannot be used as a robust “friction learning” tool when drastically-different terrains are faced.
- Conversely, random-walk virtual sensors do not require any *a priori* knowledge of the tyre-friction characteristics and can be used as a “friction learning” tool when unexplored terrains are encountered. On the other hand, the proposed friction learning procedure requires a continuous excitation during a certain amount of time (ANFIS training set generation), which may difficult the detection of quick friction changes along non-uniform rigid surfaces (e.g. mu-jumps on wet or icy segments).

- A combination of the proposed random-walk observer for "learning" operation and robust vehicle dynamics state estimation in unexplored terrains and the data-based observer for timely friction potential identification when driving on tarmac roads may be the best way to extract the maximum out of both methodologies. Such hybrid structure could be extended incorporating friction information extracted from subsystems working in other vehicle domains (e.g. Steering system, longitudinal dynamics) in order to reduce the friction identification time. Additionally, perception subsystems from other layers (e.g. machine vision-based terrain classification) could be added in a fusion sensing strategy to support the proposed systems during low-excitation driving (e.g. "rough" terrain identification during constant-speed driving).

The discussion in HSAVs is continued in the next chapter, where the advanced motion control functions developed during the course of this research are introduced.

Chapter 4

Advanced Vehicle Motion Control

The vehicle motion controllers developed during this research are presented in this chapter. As discussed in Section 2.2, expert manoeuvring at the limits of handling is often characterised by the strong coupling seen between the steering and driving commands (e.g. counter-steering and throttle modulation during active drift control). In order to avoid complex Integrated Chassis Control strategies and achieve superior performance levels in multi-actuated platforms, optimal centralised multi-input-multi-output (MIMO) controllers are adopted to develop the motion control functions. Specifically, controllers for high body slip stabilisation are provided first. In a second step, these are integrated into a modular structure to achieve simultaneous high body slip stabilisation and path-following control, giving, as a result, a driver-less expert system that resembles a highly-skilled driver. The chapter is completed with the SiL and HiL verification of the proposed controllers using the commercial package IPG-CarMaker and the professional HiL platform of ARRIVAL and ROBORACE.

4.1 Background

In the following, relevant background regarding model-based MIMO control techniques is provided. Specifically, the Linear Quadratic Regulator (LQR) and the Model Predictive Controller (MPC) are derived.

4.1.1 Linear Quadratic Regulator (LQR)

Linear Quadratic Control is often employed in multi-input problems to determine the optimal feedback gain based on the optimisation of a performance objective function. In the following, the Infinite-Time Horizon case (LQR) is presented. For the formulation of the continuous-time LQR, a Linear Time-Invariant (LTI) system expressed in the state-space form (4.1) is considered.

$$\dot{\mathbf{x}} = \mathbf{A}\mathbf{x} + \mathbf{B}\mathbf{u} \tag{4.1}$$

Assuming that the n states of the system are available for the controller (full feedback assumption), the optimal control vector that stabilises the plant around the origin is given by the expression (4.2),

$$\mathbf{u}(t) = -\mathbf{K}\mathbf{x}(t) \tag{4.2}$$

where K is the optimal feedback gain obtained from the optimisation of the objective performance function (4.3).

$$J = \int_0^{\infty} (\mathbf{x}^T\mathbf{Q}\mathbf{x} + \mathbf{u}^T\mathbf{R}\mathbf{u})dt \tag{4.3}$$

In this expression, the terms $\mathbf{Q}$ and $\mathbf{R}$ are positive-definite Hermitian matrices that account for the relative importance of the regulation error and actuator energy expenditure respectively. Substituting the control law (4.2) in the cost function (4.3), and following the derivation presented in [102] the LQR control law can be expressed as:

$$\mathbf{u}(t) = -\mathbf{R}^{-1}\mathbf{B}^T\mathbf{P}\mathbf{x}(t) \tag{4.4}$$

Where the constant matrix $\mathbf{P}$ is the unique positive-definite solution of the associated steady-state Riccati equation (4.5).

$$\mathbf{P}\mathbf{A} + \mathbf{A}^T\mathbf{P} - \mathbf{P}\mathbf{B}\mathbf{R}^{-1}\mathbf{B}^T\mathbf{P} + \mathbf{Q} = 0 \tag{4.5}$$

The Positive-definite solution of this equation ($\mathbf{P}$) always exists provided that the matrix ($\mathbf{A} - \mathbf{B}\mathbf{K}$) is a stable matrix (i.e. the closed-loop poles of the system lie on the left side of the complex plane). The infinite-horizon LQR formulation can be easily extended to the discrete-time case. For convenience, the regulation problem around non-zero state references is studied. Given a discrete state-space system of the form,

$$\mathbf{\Delta x}(k+1) = \mathbf{A_{ss}}\mathbf{\Delta x}(k) + \mathbf{B_{ss}}\mathbf{\Delta u}(k) \tag{4.6}$$

with $\mathbf{A_{ss}}$, $\mathbf{B_{ss}}$ being the system matrices linearised around the desired steady-state (ss) equilibrium states $\mathbf{x_{ss}}$ and equilibrium feedforward inputs $\mathbf{u_{ss}}$, and the vector of state errors and input corrections defined as,

$$\boldsymbol{\Delta}\mathbf{x}(k) = \mathbf{x}(k) - \mathbf{x_{ss}}, \quad \boldsymbol{\Delta}\mathbf{u}(k) = \mathbf{u}(k) - \mathbf{u_{ss}} \tag{4.7}$$

If the objective performance function (4.3) is expressed in discrete-time notation,

$$J = \sum_{k=1}^{\infty} \big(\boldsymbol{\Delta}\mathbf{x}(k)^T \mathbf{Q} \boldsymbol{\Delta}\mathbf{x}(k) + \boldsymbol{\Delta}\mathbf{u}(k)^T \mathbf{R} \boldsymbol{\Delta}\mathbf{u}(k)\big) \tag{4.8}$$

the feedback law given by the expression (4.9) can be found following the derivation presented in [84].

$$\boldsymbol{\Delta}\mathbf{u}(k) = -\mathbf{K}\boldsymbol{\Delta}\mathbf{x}(k) = -(\mathbf{B_{ss}}^T \mathbf{P} \mathbf{B_{ss}} + \mathbf{R})^{-1} (\mathbf{B_{ss}}^T \mathbf{P} \mathbf{A_{ss}}) \boldsymbol{\Delta}\mathbf{x}(k) \tag{4.9}$$

Where $\mathbf{P}$ is the infinite-horizon solution of the discrete-time Ricatti equation,

$$\mathbf{A_{ss}}^T \mathbf{P} \mathbf{A_{ss}} - \mathbf{P} - (\mathbf{A_{ss}}^T \mathbf{P} \mathbf{B_{ss}})(\mathbf{B_{ss}}^T \mathbf{P} \mathbf{B_{ss}} + \mathbf{R})^{-1} (\mathbf{B_{ss}}^T \mathbf{P} \mathbf{A_{ss}}) + \mathbf{Q} = 0 \tag{4.10}$$

provided that the system defined by the matrices $\mathbf{A_{ss}}$,$\mathbf{B_{ss}}$ is stabilisable, has no unobservable modes on the unit circle, and the tuning matrices $\mathbf{Q}$ and $\mathbf{R}$ are positive. The final control input can be easily extracted from (4.7) as,

$$\mathbf{u}(k) = \boldsymbol{\Delta}\mathbf{u}(k) + \mathbf{u_{ss}} \tag{4.11}$$

4.1.2 Model Predictive Control (MPC)

MPC is a powerful control formulation especially suited for systems incorporating state, input, or output constraints. The real advantage in comparison to other linear-feedback-law controllers (e.g. LQR) lies in the ability of the former to determine optimally nonlinear feedback laws when constrained systems are faced. This is achieved through online numerical optimisation [39]. To derive the MPC, the discrete state-space system introduced in the previous section, expression (4.6), is considered. Following the derivation presented in [139], the evolution of the previous state-space model in the future N_p steps as a result of a sequence of N_c future inputs can be expressed in compact form as:

$$\mathbf{\Delta X} = \mathbf{F_{ss}} \mathbf{\Delta x}(k) + \mathbf{\Phi_{ss}} \mathbf{\Delta U} \tag{4.12}$$

where $\mathbf{\Delta X} = [\mathbf{\Delta x}(k{+}1|k)^T, \mathbf{\Delta x}(k{+}2|k)^T, ..., \mathbf{\Delta x}(k{+}N_p|k)^T]^T$ and $\mathbf{\Delta U} = [\mathbf{\Delta u}(k)^T, \mathbf{\Delta u}(k+1)^T, ..., \mathbf{\Delta u}(k + N_c - 1)^T]^T$. The augmented equilibrium matrices $\mathbf{F_{ss}}$ and $\mathbf{\Phi_{ss}}$ are calculated from the linearised matrices $\mathbf{A_{ss}}, \mathbf{B_{ss}}$ as follows:

$$\mathbf{F_{ss}} = \begin{bmatrix} \mathbf{A_{ss}} \\ \mathbf{A_{ss}}^2 \\ ... \\ \mathbf{A_{ss}}^{N_p} \end{bmatrix} \tag{4.13}$$

$$\mathbf{\Phi_{ss}} = \begin{bmatrix} \mathbf{B_{ss}} & 0 & ... & 0 \\ \mathbf{A_{ss}}\mathbf{B_{ss}} & \mathbf{B_{ss}} & ... & 0 \\ ... & & & \\ \mathbf{A_{ss}}^{N_p-1}\mathbf{B_{ss}} & \mathbf{A_{ss}}^{N_p-2}\mathbf{B_{ss}} & ... & \mathbf{A_{ss}}^{N_p-N_c}\mathbf{B_{ss}} \end{bmatrix} \tag{4.14}$$

The sequence of N_c future control inputs is obtained by solving the optimisation problem:

$$\begin{aligned} \underset{\mathbf{\Delta U}}{\text{minimize}} \quad & J(\mathbf{\Delta U}) \\ \text{subject to} \quad & \mathbf{A_c} \mathbf{\Delta U} \leq \mathbf{b}(k) \end{aligned}$$

where the matrices $\mathbf{A_c}$, $\mathbf{b}$ account for the input amplitude and slew rate constraints respectively. For simplicity the derivation of these matrices is presented in the following for a single-input case and one-step control horizon ($\mathbf{\Delta U} = \mathbf{\Delta u}(k)$). The extension to

MIMO systems can be consulted in [139]. Assuming an actuator bounded in the interval $[U_{min}, U_{max}]$, this condition can be expressed numerically by means of the expressions (4.15),

$$\begin{bmatrix} 1 \\ -1 \end{bmatrix} u(k) = \begin{bmatrix} 1 \\ -1 \end{bmatrix} (u_{ss} + \Delta u(k)) < \begin{bmatrix} U_{max} \\ -U_{min} \end{bmatrix} \tag{4.15}$$

which can be rearranged as,

$$\begin{bmatrix} 1 \\ -1 \end{bmatrix} \Delta u(k) < \begin{bmatrix} U_{max} - u_{ss} \\ -U_{min} + u_{ss} \end{bmatrix} \tag{4.16}$$

The same procedure can be followed if the actuator velocity, expressed as $\frac{u(k)-u(k-1)}{T_{s,MPC}}$, must remain within the limits $[U_{SR,\mathrm{min}}, U_{SR,\mathrm{max}}]$, expression (4.17),

$$\begin{bmatrix} 1 \\ -1 \end{bmatrix} \left(\frac{u(k) - u(k-1)}{T_{s,MPC}}\right) = \begin{bmatrix} 1 \\ -1 \end{bmatrix} \left(\frac{u_{ss} + \Delta u(k) - u(k-1)}{T_{s,MPC}}\right) < \begin{bmatrix} U_{SR,max} \\ -U_{SR,min} \end{bmatrix} \tag{4.17}$$

where $T_{s,MPC}$ denotes the MPC discretisation time. This expression can be rearranged as,

$$\begin{bmatrix} 1 \\ -1 \end{bmatrix} \Delta u(k) < \begin{bmatrix} U_{SR,max} T_{s,MPC} + u(k-1) - u_{ss} \\ -U_{SR,min} T_{s,MPC} - u(k-1) + u_{ss} \end{bmatrix} \tag{4.18}$$

If the expressions (4.16) and (4.18) are grouped, the matrices $\mathbf{A_c}$ and $\mathbf{b}$ can be defined as,

$$\mathbf{A_c} = \begin{bmatrix} 1 \\ -1 \\ 1 \\ -1 \end{bmatrix}, \mathbf{b}(k) = \begin{bmatrix} U_{max} - u_{ss} \\ -U_{min} + u_{ss} \\ U_{SR,max} T_{s,MPC} + u(k-1) - u_{ss} \\ -U_{SR,min} T_{s,MPC} - u(k-1) + u_{ss} \end{bmatrix} \tag{4.19}$$

Finally, the objective function $J(\mathbf{\Delta U})$ is defined in a suitable Quadratic Programming form to reduce the computational expenses and facilitate a real-time implementation, expressions (4.20-4.22),

$$J(\mathbf{\Delta U}) = \mathbf{\Delta U}^T \mathbf{H} \mathbf{\Delta U} + 2\mathbf{\Delta x}(k)^T \mathbf{M}^T \mathbf{\Delta U} \tag{4.20}$$

$$\mathbf{H} = \mathbf{\Phi_{ss}}^T \hat{\mathbf{Q}} \mathbf{\Phi_{ss}} + \hat{\mathbf{R}} \tag{4.21}$$

$$\mathbf{M} = \mathbf{\Phi_{ss}}^T \hat{\mathbf{Q}} \mathbf{F_{ss}} \tag{4.22}$$

where $\hat{\mathbf{Q}}$ and $\hat{\mathbf{R}}$ are weighting matrices used to adjust the relative importance of the tracking error and input energy expenditure respectively. A receding horizon approach is adopted and the first term of the vector $\mathbf{\Delta U}$ is implemented at each time step.

4.2 High body slip stabilisation of MAGVs

The centralised MIMO controllers for high body slip stabilisation of MAGVs are described in this section. A model-based reference generation approach for maximum lateral dynamics exploitation is introduced first. After that, a data-based reference derivation methodology is proposed to "teach" an Artificially Intelligent (AI) MAGV to drift directly from field tests.

4.2.1 Centralised control architecture

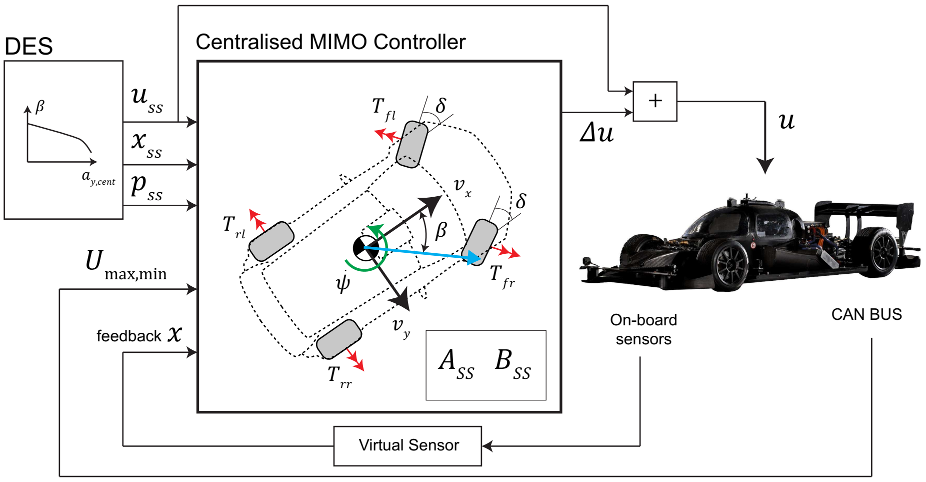

FIGURE 4.1: Centralised control architecture for MAGVs.

A generic MAGV control architecture is depicted schematically in Fig. 4.1. The MIMO controller (e.g. LQR, MPC) provides the regulation action $\mathbf{\Delta u}$ to stabilise the vehicle around a set of high body slip steady-state references $\mathbf{x_{ss}}$ (i.e. drive the vector of state errors $\mathbf{\Delta x}$ to zero). The matrices $\mathbf{A_{ss}}$ and $\mathbf{B_{ss}}$ embedded in the controller, expression (4.6), are obtained linearising the vehicle planar dynamics expressions (3.1)-(3.13) around the vector of equilibrium states $\mathbf{x_{ss}}$ and feedforward inputs $\mathbf{u_{ss}}$. A linearised tyre force model [8] is employed to facilitate the adoption of the linear controllers introduced in Section 4.1.1. In particular, if a first order Taylor series expansion is performed on the nonlinear tyre force expression $F = f(\gamma_{ss}, \alpha, \lambda, F_{z,ss})$ around the tyre lateral (α) and longitudinal (λ) slips, and the cross-stiffness terms are neglected [14, 8], the linearised tyre force expressions (4.23-4.24) are obtained.

$$F_{y,i} \approx F_{yss,i} + C_{\alpha,i}|_{\gamma_{ss},\lambda_{ss},F_{z,ss}} \Delta\alpha_i \tag{4.23}$$

$$F_{x,i} \approx F_{xss,i} + C_{\lambda,i}|_{\gamma_{ss},\alpha_{ss},F_{z,ss}} \Delta\lambda_i, \quad i \in \{fl, fr, rl, rr\} \tag{4.24}$$

Where $C_\alpha|_{\gamma_{ss},\lambda_{ss},F_{z,ss}}$ and $C_\lambda|_{\gamma_{ss},\alpha_{ss},F_{z,ss}}$ are the cornering and longitudinal tyre stiffness at each equilibrium point. For simplicity, these are denoted as C_α,C_λ in the following. $F_{y,ss}, F_{x,ss}$ are the steady-state tyre equilibrium forces, and $\Delta\alpha, \Delta\lambda$ are perturbations around these equilibrium points. The steady-state equilibrium tyre forces are eliminated when the regulator problem is formulated (i.e. $\Delta F_{y,i} = F_{y,i} - F_{yss,i} \approx C_{\alpha,i}\Delta\alpha_i$). In this thesis, controllers are proposed for MAGV platforms equipped with 2 (RWD) and 4 (AWD) Electric Motors (EM). Each controller design can be synthesised by the following vector of inputs $\mathbf{u}$, parameters $\mathbf{p}$, and states $\mathbf{x}$.

$$\mathbf{u_{RWD}} = \{\delta, T_{rl}, T_{rr}\} \tag{4.25}$$

$$\mathbf{x_{RWD}} = \{\dot{\psi}, v_x, v_y, \omega_{rl}, \omega_{rr}\} \tag{4.26}$$

$$\mathbf{p_{RWD}} = \{C_{\alpha,i}, C_{\lambda,rl}, C_{\lambda,rr}\} \tag{4.27}$$

$$\mathbf{u_{AWD}} = \{\delta, T_{fl}, T_{fr}, T_{rl}, T_{rr}\} \tag{4.28}$$

$$\mathbf{x_{AWD}} = \{\dot{\psi}, v_x, v_y, \omega_{fl}, \omega_{fr}, \omega_{rl}, \omega_{rr}\} \tag{4.29}$$

$$\mathbf{p_{AWD}} = \{C_{\alpha,i}, C_{\lambda,i}\}, \quad i \in \{fl, fr, rl, rr\} \tag{4.30}$$

The MAGV actuator limits $U_{\max,\min}$ (i.e. available wheel torque and steering angle limits) are assumed to be provided by a high-level Drive Control Unit (DCU). In addition, fixed slew rate limits are imposed to the MIMO controller to prevent the steering system, driveline unit and electric motors from mechanical failure. The feedback needed by the controller is provided by a set of onboard measurements and a virtual sensor embedded in the feedback loop. The virtual sensor design will vary depending on the vehicle driveline configuration, as was discussed in Chapter 3. Finally, the vector of reference states $\mathbf{x_{ss}}$, feedforward inputs $\mathbf{u_{ss}}$, and equilibrium parameters $\mathbf{p_{ss}}$ can be computed numerically from a synthesised vehicle model (Section 4.2.2) or extracted from field tests using a machine-learning-based approach (Section 4.2.3). Depending on the methodology adopted, the Drift Equilibrium Solutions (DES) block may be constructed using look-up tables or NN structures.

4.2.2 Model-based reference derivation

If a model-based approach is adopted, the vectors $\mathbf{x_{ss}}$, $\mathbf{u_{ss}}$, and $\mathbf{p_{ss}}$ needed by the centralised controller are obtained offline solving a nonlinear multivariate optimisation problem [18] of the form,

$$\begin{aligned} \underset{\boldsymbol{\Omega}}{\text{minimise}} \quad & f(\boldsymbol{\Omega}) \\ \text{subject to} \quad & \mathbf{f_{eq,nonl}}(\boldsymbol{\Omega}) = 0 \\ & \mathbf{f_{ineq,nonl}}(\boldsymbol{\Omega}) < 0 \\ & \mathbf{lb} \leq \boldsymbol{\Omega} \leq \mathbf{ub} \end{aligned}$$

The methodology used in this thesis to solve this optimisation problem is illustrated schematically in Figure 4.2 and can be explained in the following manner.

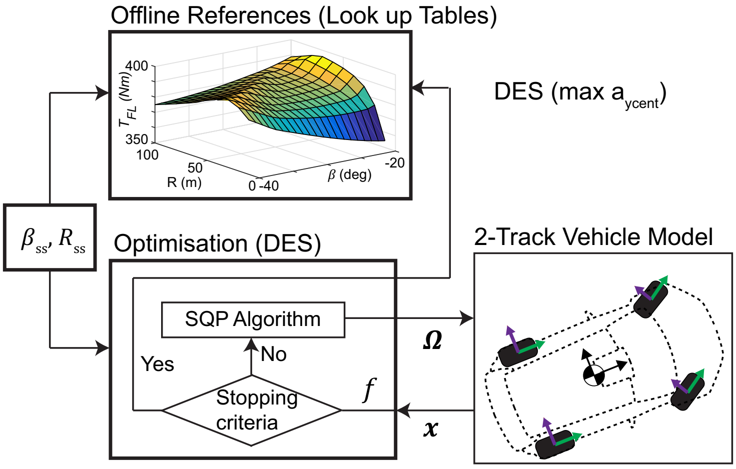

FIGURE 4.2: Offline model-based generation of Drift Equilibrium Solutions (DES), [18].

In brief, a Sequential Quadratic Programming (SQP) optimisation routine is run to find the set of design variables $\mathbf{\Omega}$ that minimise the objective function $f(\mathbf{\Omega})$ [18]. The solutions must fulfil the set of equality $\mathbf{f_{eq,nonl}}(\mathbf{\Omega})$ and inequality $\mathbf{f_{ineq,nonl}}(\mathbf{\Omega})$ nonlinear constraints. Specifically, the equality constraints are obtained after applying steady-state conditions ($\dot{x} = 0$) to the vehicle modelling equations introduced in the previous chapter, expressions (3.1)-(3.13). The inequality constraints account for the maximum torque that can be applied to each wheel, and that is obtained from the EM torque-speed curves. The vector of design variables is formed by the vehicle velocity module ($V = \sqrt{v_x^2 + v_y^2}$), the angle steered by the front wheels, and the individual tyre longitudinal slip $\mathbf{\Omega} = \{V, \delta, \lambda_{fl}, \lambda_{fr}, \lambda_{rl}, \lambda_{rr}\}$. This vector is bounded by the upper and lower bound vectors $\mathbf{ub} = \{V_{\max}, \delta_{\max}, \lambda_{\max}, \lambda_{\max}, \lambda_{\max}, \lambda_{\max}\}^T$,$\mathbf{lb} = \{0, -\delta_{\max}, 0, 0, 0, 0\}^T$ with the aim to limit the equilibrium steering wheel angle below $\delta_{\max}$ and eliminate non-physical solutions (e.g. negative vehicle speed, or backward motor rotation). Following the approach presented in previous works [134, 14, 18], a target radius R_{ss} and body slip angle β_{ss} are imposed at each iteration step. The optimisation routine is repeated for different operating points (combination of β_{ss} and R_{ss} values), giving as a result the grid of $\beta - R$ points that determines the total operating envelope of the MAGV controller (e.g. maximum radius along which a body slip angle β_{ss} can be maintained), Figure 4.2-top. A maximum centripetal acceleration function is defined $f(\mathbf{\Omega}) = -V_{ss}\dot{\psi}_{ss}$ with the aim to exploit the full chassis potential. In brief, it is pursued to find a combination of MAGV inputs (e.g. in-wheel torque distribution) that enhances the lateral dynamics during sustained drifting cornering. This can be of particular interest in minimum-time cornering problems on loose surfaces [128] where high body slip control (active drifting) is necessary to take advantage of the *bulldozzing* effect and achieve maximum centripetal acceleration [14], Figure 4.3. As can be observed in Figure 4.3-left, maximum a_{ycent} values are obtained in gravel if the vehicle is stabilised around a high body slip angle ($|\beta_{ss}|$ = 30-40 degrees). The major reason for this behaviour resides in the exponential friction shape exhibited by the tyres on loose surfaces, Figure 2.5. For additional discussion on this topic [14] can be consulted.

Finally, after completing the optimisation for a given operating point, the vectors of reference states $\mathbf{x_{ss}}$ and feedforward inputs $\mathbf{u_{ss}}$ are extracted from direct substitution of the optimisation solutions $\mathbf{\Omega_{sol}}$ on the system formed by the equality constraints $\mathbf{f_{eq,nonl}}(\mathbf{\Omega})$. The tyre stiffness terms needed to construct the vector of parameters $\mathbf{p_{ss}}$ are computed from the equilibrium solutions and tyre friction model adopting a finite differences approach [14, 18]. The rest of vehicle parameters appearing on the MAGV modelling equations (e.g. vehicle mass, yaw inertia) are considered constant for the complete operating envelope of the controller.

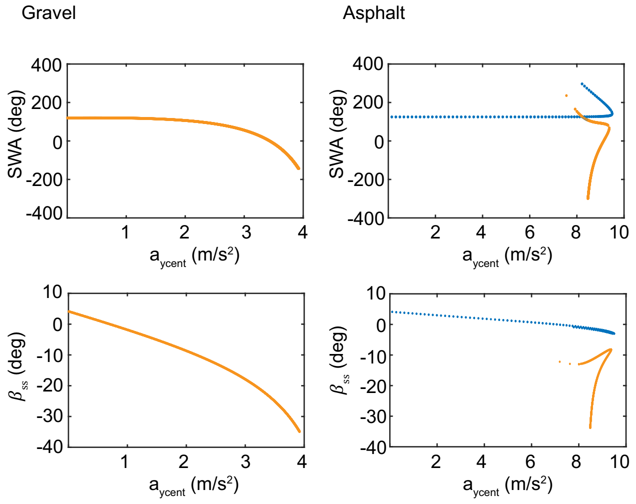

FIGURE 4.3: DES solutions generated with a single-track RWD planar dynamics model for R_{ss} = 20 m [14]. The gravel and tarmac tyre-friction behaviour is modelled by an isotropic magic formula tyre model [128]. SWA: steering wheel angle, a_{ycent} centripetal acceleration. Blue: Low body slip steady-state solutions / Orange: High body slip steady-state solutions.

4.2.2.1 SiL verification

Due to the lack of suitable MAGV platforms during early stages of this research, the controllers were implemented and tested first in compact-class and sport-class (Section 4.2.3) chassis models built from the IPG-CarMaker library, Table 4.1. These were used to generate the results described in [8, 18] and summarised in the following. This preliminary SiL process led to the execution of the "drifting project" in which the proposed controllers were tested in the ROBORACE HiL simulation platform with a fully-validated MAGV model, see Section 4.2.4.

TABLE 4.1: Synthesised parameters employed in the compact-class high body slip controller [18]. Steering ratio: ($SR = 20$).

m $[kg]$	I_ψ $[kgm^2]$	l_f, l_r $[m]$	tw_f, tw_r $[m]$	r_e $[m]$
1200	1700	1.0/1.6	1.5/1.5	0.32
h_{CoG} $[m]$	$K_{\phi,f}$,$K_{\phi,r}$ $[kNm/rad]$		I_ω $[kgm^2]$	h_{rc} $[m]$
0.56	57/57		1	0

An AWD electric model was constructed using the *custompowertrain.slx* CarMaker template and the torque versus speed characteristics of the electric motors were taken from the results presented in [71]. In addition, the maximum steering wheel amplitude $\delta_{\max}$ was set to 475/SR degrees, and the maximum steering wheel rate $\dot{\delta}_{\max}$ was limited to 1200/SR degrees per second in order to simulate the controller performance under realistic actuator constraints. The CarMaker virtual environment introduced in Section

3.3.1.2 was used to simulate the controller robustness under severe vertical excitation levels, and the isotropic MF tyre modelisation introduced in Velenis' [134] and Tavernini's works was adopted to simulate the vehicle behaviour in an extreme off-road terrain (Tyre-4 [128]).

The centralised MIMO controllers were implemented in Simulink and simulated using a 1 ms running frequency in a PC Intel Core *i7-3632QM* CPU at 2.20 GHz. The DES solutions were obtained for a grid of radii $\mathbf{R_{ss}} = [10 : 10 : 90]$ and a target body slip angle of $|\beta_{ss}| = 35$ degrees following the model-based approach described in Section 4.2.2. This process was repeated for RWD and AWD driveline architectures. In particular, solutions for the former configuration were obtained imposing the conditions $\lambda_{fl} = 0, \lambda_{fr} = 0$ on the optimisation problem. A custom MPC was implemented in Simulink by means of Matlab user-defined functions and the *quadprog.m* routine. The discretisation time $T_{s,MPC}$ was set to 20 ms taking into account that the yaw resonance frequency of ground vehicles often lies around 1 Hz [8, 18]. The number of future steps N_p and future control inputs N_c were set to 50 and 1 respectively with the aim to permit a real-time implementation. The MPC weights ($\mathbf{Q}$, $\mathbf{R}$), were determined following a systematic trial-and-error process. In order to incorporate an infinite preview horizon into the MPC, a suitable terminal cost $\overline{\mathbf{Q}}$ was set on the last term of the total weighting matrix $\hat{\mathbf{Q}}$.

$$\hat{\mathbf{Q}} = \begin{bmatrix} \mathbf{Q} & 0 & \cdots & 0 \\ 0 & \mathbf{Q} & \cdots & 0 \\ \vdots & \vdots & \ddots & \vdots \\ 0 & 0 & \cdots & \overline{\mathbf{Q}} \end{bmatrix}, \hat{\mathbf{R}} = \begin{bmatrix} \mathbf{R} & 0 & \cdots & 0 \\ 0 & \mathbf{R} & \cdots & 0 \\ \vdots & \vdots & \ddots & \vdots \\ 0 & 0 & \cdots & \mathbf{R} \end{bmatrix} \tag{4.31}$$

Following the approach described in [39], the terminal cost was found solving the Lyapunov expression,

$$\overline{\mathbf{Q}} - (\mathbf{A_{ss}} + \mathbf{B_{ss}}\mathbf{K_{lqr}})^T \overline{\mathbf{Q}} (\mathbf{A_{ss}} + \mathbf{B_{ss}}\mathbf{K_{lqr}}) = \mathbf{Q} + \mathbf{K_{lqr}}^T \mathbf{R} \mathbf{K_{lqr}} \tag{4.32}$$

where the feedback gain $\mathbf{K_{lqr}}$ is the Linear Quadratic-optimal solution of the infinite-horizon cost, expression (4.8). Finally, for simplicity, a full-feedback assumption was considered for this initial evaluation. Vehicle experiments incorporating a virtual sensor embedded in the control feedback loop are detailed in Section 5.2.2.1.

The results obtained with the high body slip controller for a left-handed $R_{ss} = 40$ metres target radius and a $\beta_{ss} = -35$ degrees target body slip angle are depicted in Figures

4.4 and 4.5. As can be noticed, the vehicle is initialised from standstill conditions, and the planar dynamics states converge wheel to the high body slip references in the AWD and RWD configurations. The latter controller exhibits the traditional counter-steering behaviour observed during RWD drift stabilisation, Fig. 4.5, while the AWD controller tends to steer towards the centre of the turn, Fig. 4.4, which is often seen during AWD power slide motion.

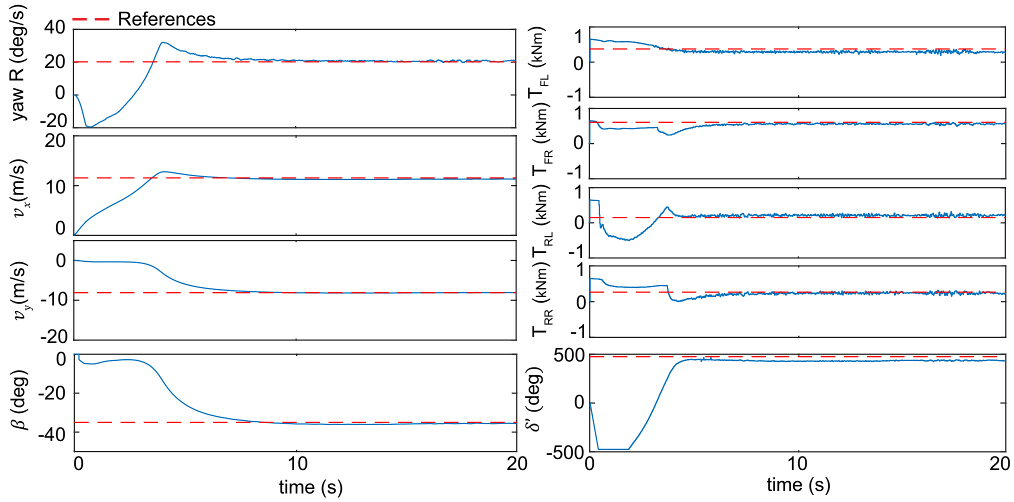

FIGURE 4.4: AWD vehicle stabilisation around a target body slip $\beta_{ss} = -35$ degrees and a target radius $R_{ss} = 40$ metres. $\delta' = \delta \cdot SR$.

With regards to the cornering performance, the controller maximises the full chassis potential in AWD mode, generating higher centripetal acceleration levels at the expense of higher power consumption. Specifically, an average improvement of approximately 1.5-2 m/s^2 was observed in AWD mode, see [18] for further details. Overall, these results suggest the use of variable traction-distribution strategies for MAGV. For instance, a low power consumption traction distribution might be employed during regular driving conditions and an AWD maximum-acceleration strategy could be triggered to maximise the vehicle lateral dynamics during limit situations (e.g. lateral lane departure avoidance).

Additional simulations (omitted here due to space limitations) were executed for a wide range of radii (with the vehicle initialised in static conditions), and successful results were obtained. Finally, the NRMSE of the planar dynamics states is given in Table 4.2. The initial stabilisation time (t <5 s) was not considered when computing these errors with the aim to focus on the system tracking capabilities when the drifting steady-state motion has been achieved. Overall, the high body slip controller tracks closely the reference signals, keeping the NRMSE below the 5% band.

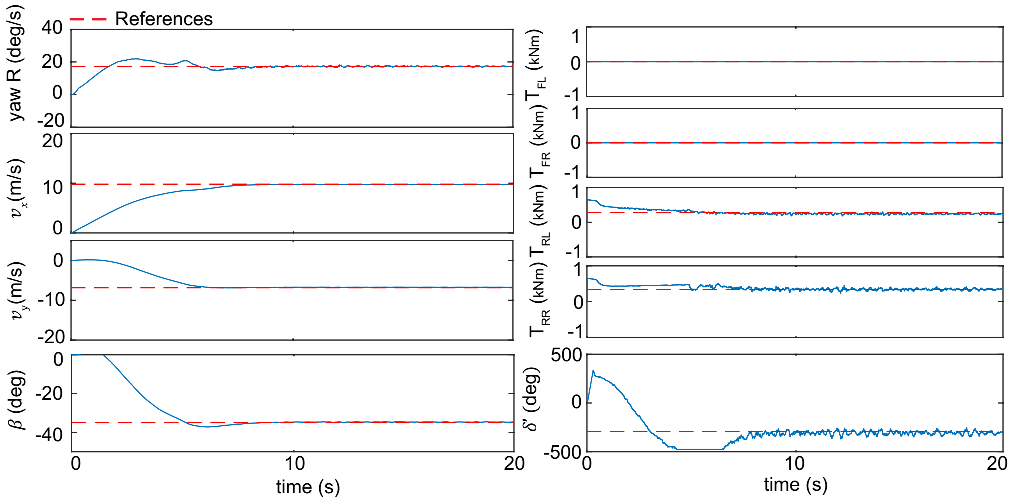

FIGURE 4.5: RWD vehicle stabilisation around a target body slip $\beta_{ss} = -35$ degrees and a target radius $R_{ss} = 40$ metres. $\delta' = \delta \cdot SR$.

TABLE 4.2: NRMSE of the vehicle planar motion states (%).

Test	R_{ss}	β_{ss}	Configuration	$e_{\dot\psi}$	e_{v_x}	e_β
1	10	-35	AWD	0.88	0.21	3.70
2	20	-35	AWD	2.61	1.15	1.55
3	30	-35	AWD	4.28	1.92	3.09
4	40	-35	AWD	8.04	2.36	5.86
5	10	-35	RWD	0.97	1.42	2.82
6	20	-35	RWD	2.20	1.18	1.37
7	30	-35	RWD	3.25	2.63	2.30
8	40	-35	RWD	5.10	3.91	2.06

4.2.3 Data-based reference derivation

When a data-based approach is employed, the vectors $\mathbf{x_{ss}}$, $\mathbf{u_{ss}}$, and $\mathbf{p_{ss}}$ required by the high body slip controller are extracted directly from field experiments. This methodology is particularly interesting when no information regarding the tyre-friction characteristics is available, and therefore it is not possible to derive the DES analytically. On the other hand, the necessity of manually “driving” the target vehicle to generate a suitable dataset limits the potential advantages exhibited by MAGVs. In particular, it is necessary to fix the torque distribution or to design a virtual central differential *a priori* to make the MAGV driveable using a single accelerator pedal command. This fact limits the exploitation of the maximum centripetal acceleration strategies introduced in Section 4.2.2. For simplicity, a proportional torque response ($T_{output,i} = T_{\max,i}P_{pos}$) is assumed in this thesis to make a generic MAGV fully driveable, with P_{pos} being the pedal command (between 0 - 1), and $T_{\max,i}$ the maximum torque available at the $i-th$ motor. Under this consideration, the set of equations defining the MAGV steady-state equilibrium (expressions (3.1)-(3.13)) forms a determined system, and the dependence of the feedforward inputs $\mathbf{u_{ss}}$, reference states $\tilde{\mathbf{x}}_{\mathbf{ss}}$, and tyre parameters $\mathbf{C}_{\alpha,\mathbf{ss}}$, $\mathbf{C}_{\lambda,\mathbf{ss}}$ on the target body slip β_{ss} and target road radius R_{ss} can be expressed by the following nonlinear functions,

$$\tilde{\mathbf{x}}_{\mathbf{ss}} = [V_{ss}, \omega_{fl,ss}, \omega_{fr,ss}, \omega_{rl,ss}, \omega_{rr,ss}] = f_{x_{ss}}(\beta_{ss}, R_{ss}) \tag{4.33}$$

$$\mathbf{u_{ss}} = [\delta_{ss}, T_{fl,ss}, T_{fr,ss}, T_{rl,ss}, T_{rr,ss}] = f_{u_{ss}}(\beta_{ss}, R_{ss}) \tag{4.34}$$

$$\mathbf{C}_{\alpha,\mathbf{ss}} = [C_{\alpha,ss,fl}, C_{\alpha,ss,fr}, C_{\alpha,ss,rl}, C_{\alpha,ss,rr}] = f_{C_{\alpha,ss}}(\beta_{ss}, R_{ss}) \tag{4.35}$$

$$\mathbf{C}_{\lambda,\mathbf{ss}} = [C_{\lambda,ss,fl}, C_{\lambda,ss,fr}, C_{\lambda,ss,rl}, C_{\lambda,ss,rr}] = f_{C_{\lambda,ss}}(\beta_{ss}, R_{ss}) \tag{4.36}$$

The extraction of the rest of reference vehicle states that form the vector $\mathbf{x}_{ss}$ is straightforward (e.g. $\dot{\psi}_{ss} = V_{ss}/R_{ss}$). In this thesis, NNs are proposed to "learn" these nonlinear expressions directly from real manoeuvres performed by a test driver [8]. As mentioned before, this approach is presented as an alternative to the model-based reference derivation described previously and may be employed when reduced information of the tyre-friction characteristics of a target vehicle is available. In the following, a comprehensive SiL process is introduced to describe how an artificially-intelligent MAGV incorporating these learning skills could be trained to drift by an expert driver.

4.2.3.1 NN drift training and SiL verification

The strategy employed to derive the high body slip references (functions (4.33)-(4.36)) is depicted schematically in Figure 4.6 [8]. In brief, drifting manoeuvres on circular roads of different radii (R_{ss}) and covering different reference body slip angles (β_{ss}) are performed with a target "driveable" MAGV. Due to limitations on the MAGV platform available, a virtual training procedure is proposed with the DiL setup introduced in the previous chapter. Specifically, a sports-class AWD vehicle model, Table 4.3, was built in IPG-CarMaker following the steps described in Section 4.2.2.1 and the proportional torque response mentioned in the previous paragraphs. Moreover, an additive White-Gaussian noise model was employed to reproduce realistically the noise associated with state-of-the-art vehicle instrumentation. The noise variance values can be consulted in [8]. Apart from this, a virtual extreme off-road surface was simulated following the approach described in Section 3.3.1.2.

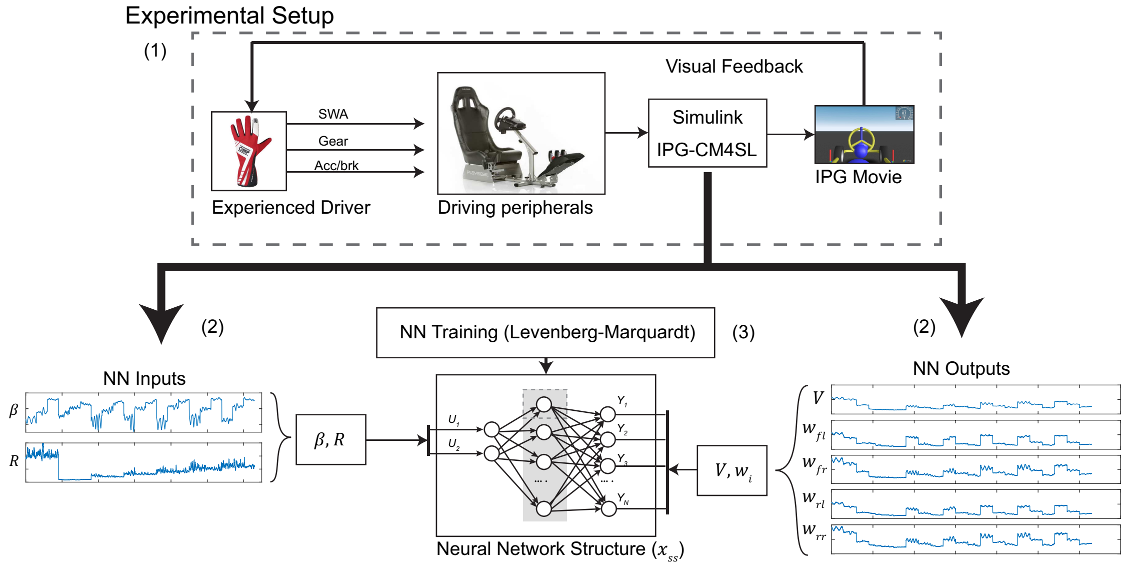

FIGURE 4.6: Scheme of the intelligent drift control training process. (1) Execution of drifting manoeuvres in IPG-CarMaker - (2) Preparation of training datasets - (3) Training of neural networks [8].

TABLE 4.3: Synthesised parameters of the sports-class MAGV [8].

m $[kg]$	I_ψ $[kgm^2]$	l_f, l_r $[m]$	tw_f, tw_r $[m]$	r_e $[m]$
1580	2325	1.20/1.45	1.5/1.5	0.32
h_{CoG} $[m]$	$K_{\phi,f}$,$K_{\phi,r}$ $[kNm/rad]$		I_ω $[kgm^2]$	SR
0.55	70/70		2	20

The runs generated in IPG-CarMaker during the execution of these manoeuvres are logged, post-processed, and employed to construct the training datasets. For each operating point (β_{ss}, R_{ss}), a data vector is extracted from the complete run and added into the complete training dataset by direct concatenation, Figure 4.7.

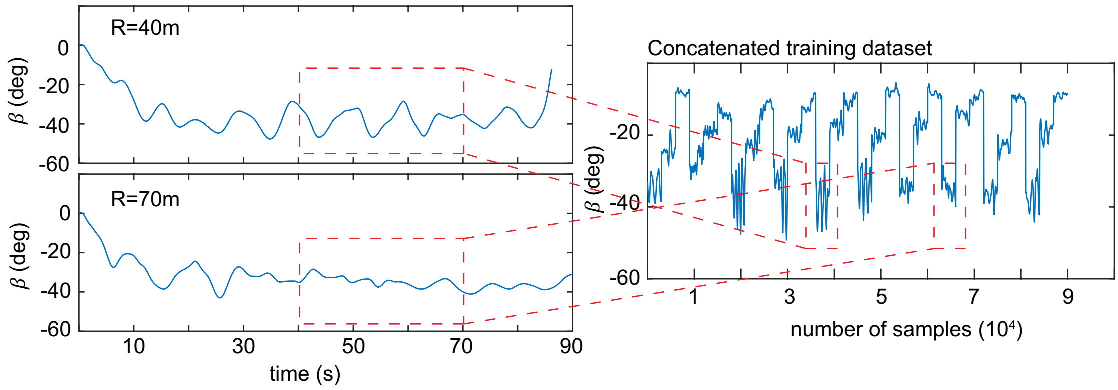

FIGURE 4.7: Direct concatenation of individual drifting runs once steady-state high body slip conditions have been achieved [8].

In order to diminish the probability of outliers on the training dataset, only data corresponding to steady-state intervals ($t \in [40s, 70s]$) were used. This process was repeated for the vector of radii $\mathbf{R_{ss}} = [10 : 10 : 100]$ and three different target body slip angle ranges: low body slip $|\beta_{ss}| \approx 10 - 15$ degrees, medium body slip $|\beta_{ss}| \approx 15 - 25$ degrees, and high body slip "drift" $|\beta_{ss}| \approx 30 - 40$ degrees. In total, 30 runs were generated and concatenated to train the NNs, Figure 4.7-right.

The Levenberg-Marquardt algorithm was employed to infer the nonlinear functions $f_{x_{ss}}$ and $f_{u_{ss}}$ using a data partition of 70/15/15 %. The NN training was repeated for several hidden-layer neurons and good results were obtained with a hidden layer formed by 6 neurons (2-6-5 NN structure). As acceptable results were already obtained using the preliminary training method and dataset partition, additional simulations were not performed. With regards to the approximation of the nonlinear functions $f_{C_\alpha,ss}$ and $f_{C_\lambda,ss}$, additional post-processing steps were necessary. Due to the fact that the measured data present some inherent noise (from the rough road excitation and the sensor equipment), the direct differentiation of the tyre forces versus tyre slips would lead to poor tyre stiffness estimates. Instead, a two-step approach is adopted in this work, Figure 4.8.

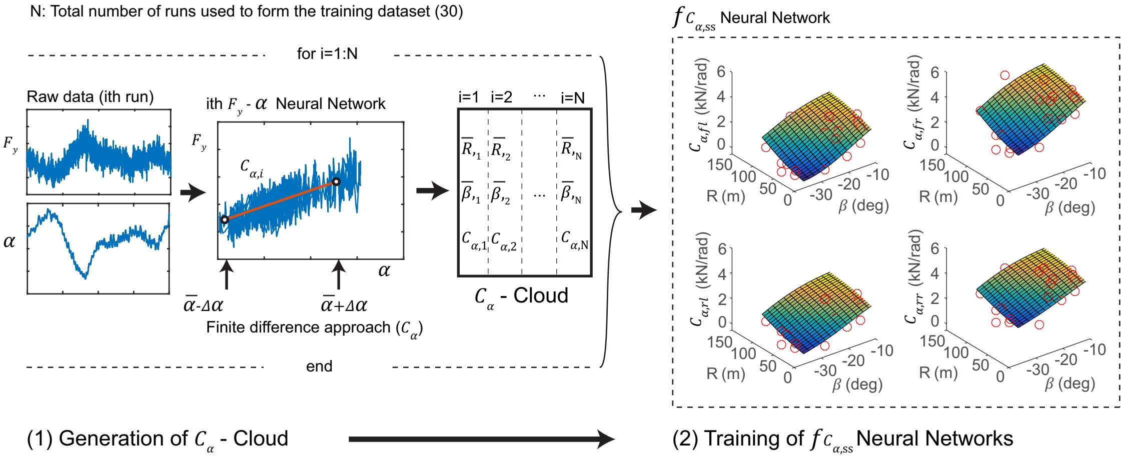

FIGURE 4.8: Generation of the $f_{C_{\alpha,ss}}$ NN function. (1) A 1-2-1 NN structure is trained to approximate the pair $(F_y - \alpha)$ at each run and the matrix of C_α points is generated. (2) A second NN structure is trained to approximate the cloud of points generated in step 1 [8].

If the problem is particularised on the lateral dynamics case (function $f_{C_\alpha,ss}$), the following procedure is followed: First, a 1-2-1 NN structure is trained to fit a cloud of $F_y - \alpha$ values obtained from each test run (steady-state interval, $t \in [40s, 70s]$). The average tyre lateral slip ($\bar{\alpha}$) is calculated on this time interval, and the cornering stiffness (C_α) for the given steady-state drift equilibrium is obtained employing a finite differences approach,

$$C_\alpha \approx \frac{F_{y,up} - F_{y,down}}{\Delta\alpha_{up} + \Delta\alpha_{down}} \tag{4.37}$$

where the forces $F_{y,up}$ and $F_{y,down}$ are the outputs from the 1-2-1 NN evaluated on the lateral slip limits $\bar{\alpha} + \Delta\alpha_{up}$ and $\bar{\alpha} - \Delta\alpha_{down}$. The increments $\Delta\alpha_{up}$ and $\Delta\alpha_{down}$ were obtained from expressions,

$$\Delta\alpha_{up} = \min(0.4(\max(\alpha) - \min(\alpha)), \max(\alpha) - \bar{\alpha}) \tag{4.38}$$

$$\Delta\alpha_{down} = \min(0.4(\max(\alpha) - \min(\alpha)), -\min(\alpha) + \bar{\alpha}) \tag{4.39}$$

which guarantee that the lateral slip limits will remain within the interval defined by the experimental slip data used to train the 1-2-1 NN. The factor 0.4 was determined empirically with the aim to capture the small oscillations derived from the continuous steering and throttle corrections to stabilise the vehicle around the drift steady-state equilibrium. Small oscillations around the slip steady-state equilibrium facilitate the extraction of the correct tyre stiffness and avoid misleading results derived from linearisations in too short slip intervals. Then, the average values of the body slip $\bar{\beta}$ and radius $\bar{R}$ are associated to each cornering stiffness estimate $C_{\alpha,i}$. This process is repeated at each test run until the complete cloud of points $(R_{ss}, \beta_{ss}, C_{\alpha,ss})$ is formed, Figure 4.8-(1).

In the second step, a new NN structure is trained to fit the function $f_{C_\alpha,ss}$ defined by the cloud of tyre stiffness points calculated previously. The same two-step procedure was followed to compute the nonlinear function $f_{C_\lambda,ss}$, this time using the tyre longitudinal slips λ and tyre longitudinal forces F_x. Regarding the selection of the NN structure used in the second step, NNs with distinct hidden layer sizes (hidden neurons ranging from 2 to 8) were trained using the Levenberg-Marquardt algorithm and a dataset division 70/15/15. For consistency, these parameters were maintained during the training of each NN structure. The high body slip controller was fitted with these NN structures and remarkable performance differences were not noticed. In order to avoid overfitting problems and guarantee a smooth surface shape, the NN structure with the smallest number of hidden neurons was selected (2-2-4). For additional details regarding the NN training process, [8] can be consulted. Finally, the MPC was implemented in Simulink following the procedure presented in Section 4.2.2.1. The NN structures were implemented in Simulink by means of the *Matlab Neural Networks* toolbox, and integrated into the high body slip controller adopting a similar modular scheme than depicted in Figure 4.16. For simplicity, the full-feedback assumption was adopted.

In the first place, the AI-controller was subjected to a set of left-handed spiral tests (10 - 100 metres target radius ramp) maintaining a fixed target body slip angle, Fig. 4.9.

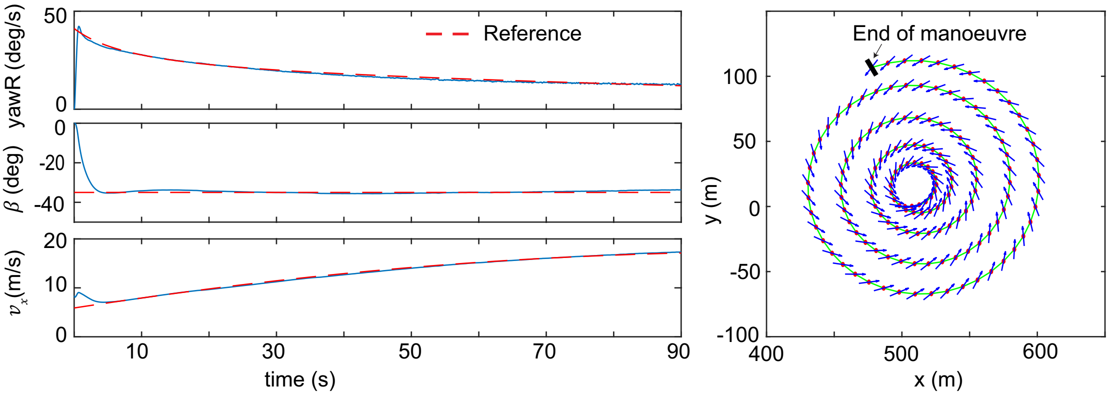

FIGURE 4.9: Ramp radius test with high body slip reference, $|\beta_{ss}| = 35$ degrees [8].

The vehicle is initialised at low speed (30 kph) and converges quickly to the target reference radius. Once in drifting motion, the controller is able to track closely the reference states and the vehicle describes an even spiral trajectory. Additional tests were repeated with different target body slip angles, Table 4.4 [8]. After that, the AI-controller was tested under a time-varying body slip reference and constant radius request, Fig. 4.10.

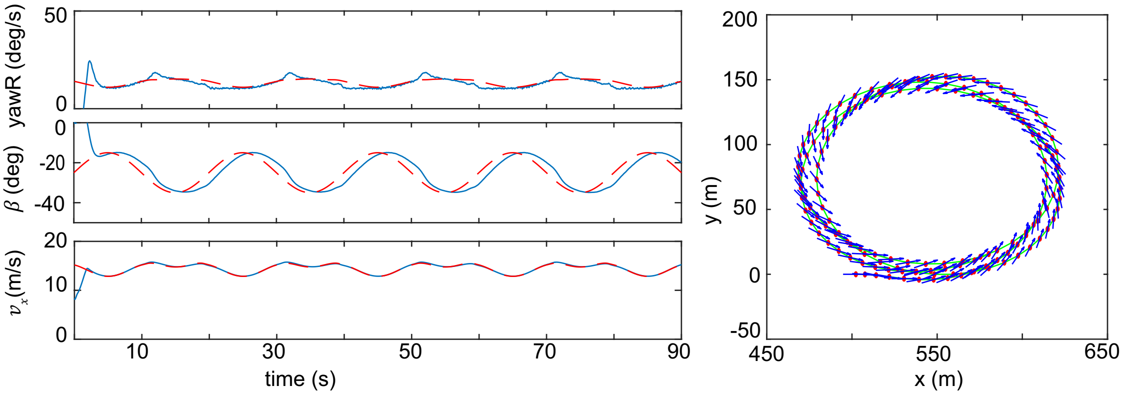

FIGURE 4.10: Constant target radius, $R_{ss} = 70$ metres, and sinusoidal body slip reference $|\beta_{ss}| = 35$ - 15 degrees at 0.05 Hz [8].

Overall, the proposed system is able to follow closely the sinusoidal body slip reference. Some delay is noticed on the drift controller response for a reference body slip of frequency 0.05 Hz. In this case, significant variations on the vehicle trajectory are identified in this test when tracking non-constant body slip angles, Figure 4.10-right. These variations are unacceptable if a reference path is to be followed simultaneously and demonstrate the necessity of introducing the path-following feature described in Section

4.3. Finally, the NRMSE of the tracked vehicle planar motion states is presented in Table 4.4.

Table 4.4: NRMSE of the tracked vehicle planar motion states (%).

Test	R_{ss}	β_{ss}	$e_{\dot{\psi}}$	e_{v_x}	e_{β}
1	$10-100$ m ramp	-35 deg	1.76	0.79	1.80
2	$10-100$ m ramp	-15 deg	1.71	0.57	3.01
3	70 m	$-25+10sin(2\pi 0.05t)$ deg	10.17	1.17	9.82

For consistency, and with the aim to focus on the body slip tracking capabilities of the proposed system, the initial stabilisation period was not considered, and the errors were calculated for $t > 5$ s in all the tests presented in this section. Expectedly, the largest body slip errors are observed on the tests where a time-varying body slip angle is tracked. These errors are kept close to the 10% error band, and therefore, are considered acceptable for the proposed application. As similar results have not been found in the literature (previous drift control works considered time-invariant body slip and radius references), these errors will be taken as a reference for further refinements of the proposed system.

4.2.4 HiL verification

The previous results motivated the implementation of the proposed algorithms in a real MAGV platform (DevBOT). The technical parameters corresponding to the DevBOT research platform are detailed in Appendix A. In order to optimise the testing time on the track, all the systems to be assessed experimentally were developed, pre-calibrated and signed-off in a virtual environment, Figure 4.11.

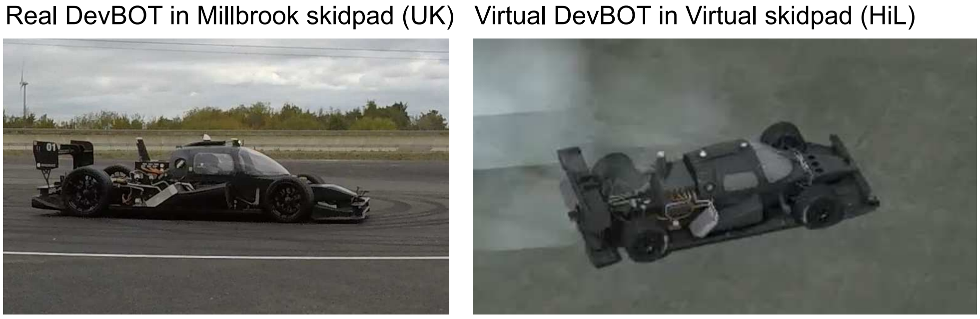
Real DevBOT in Millbrook skidpad (UK)
Virtual DevBOT in Virtual skidpad (HiL)

Figure 4.11: Real and virtual testing environments. The core development work was predominantly carried out in the virtual environment.

In brief, the HiL platform used in this thesis is formed by a Real-Time target machine (SPEEDGOAT) connected to a PC equipped with the RFPro simulation package and a virtual vehicle ECU. The virtual ECU incorporates all the vehicle actuator constraints, fail-safe strategies, virtual sensor communications (e.g. CAN), handshake protocols, warnings, soft-stops and emergency stops of the real MAGV vehicle. With regards to the virtual vehicle, RFPro uses a high-fidelity experimentally-verified simulation model. Additional specific details regarding the HiL platform are omitted here due to confidentiality reasons.

The implementation of the full Highly Skilled Autonomous Vehicle (HSAV) model was subdivided into 3 work packages: high body slip stabilisation, simple path-following and advanced path-following. Experimental results relevant to each work package are provided in Section 5.2. The models were implemented in three steps, which can be summarised in the following manner:

- Drift Equilibrium Solutions (DES): As DevBOT is an AWD electric vehicle (4 EMs) based on a Le Mans Prototype (LMP) chassis, it was literally impossible to manually drift imposing a fixed pre-defined torque distribution. This motivated the adoption of a model-based reference derivation approach, Section 4.2.2. This process was carried out updating the planar dynamics models defined by expressions (3.1)-(3.13) with a set of vehicle parameters provided by ROBORACE. The tyre-friction characteristics were extracted from MF 5.2 tyre models (295-30 R18 - front, 345-30 R20 - rear), Table A.5.
- SiL and preliminary tuning: A virtual model was built in IPG-CarMaker based on the set of parameters and tyre models provided by ROBORACE. This model was compared against experimental data extracted from step steer and steady-state cornering tests. For simplicity, and due to the lack of experience working with the target MAGV, the LQR formulation was adopted along the course of this project. Moreover, in order to reduce the computational cost of the target machine, the controller gains were solved offline for different target operating points and implemented in the virtual model following a gain-scheduling approach. It is expected that future evolutions of the proposed system will lead to the implementation of a linear MPC formulation in which the current work in LQR will be used to adjust the MPC terminal weight matrix, as described in Section 4.2.2.1. Finally, different robustness analyses were performed (feedback noise level, vertical disturbances, parameter uncertainty) and a preliminary LQR calibration was found.
- HiL and sign-off: The models were implemented in SPEEDGOAT following the handshake protocols and fail-safe strategies defined by ROBORACE. Additional

details regarding this process are provided in Chapter 5. The preliminary calibrations found in IPG-CarMaker were tested and signed-off with the ROBORACE software team. Specifically, different calibrations (e.g. *soft*, *nominal*, *harsh*), were tested and approved for experimental testing. Overall, it was not necessary to perform additional iteration loops with the SiL testing, evidencing the ability of the proposed controller to cope with the parameter uncertainties or communication delays introduced by the HiL environment.

The results corresponding to the HiL sign-off of a left-handed 10 metres drift test (β_{ss} = − 40 degrees) are given in Figure 4.12.

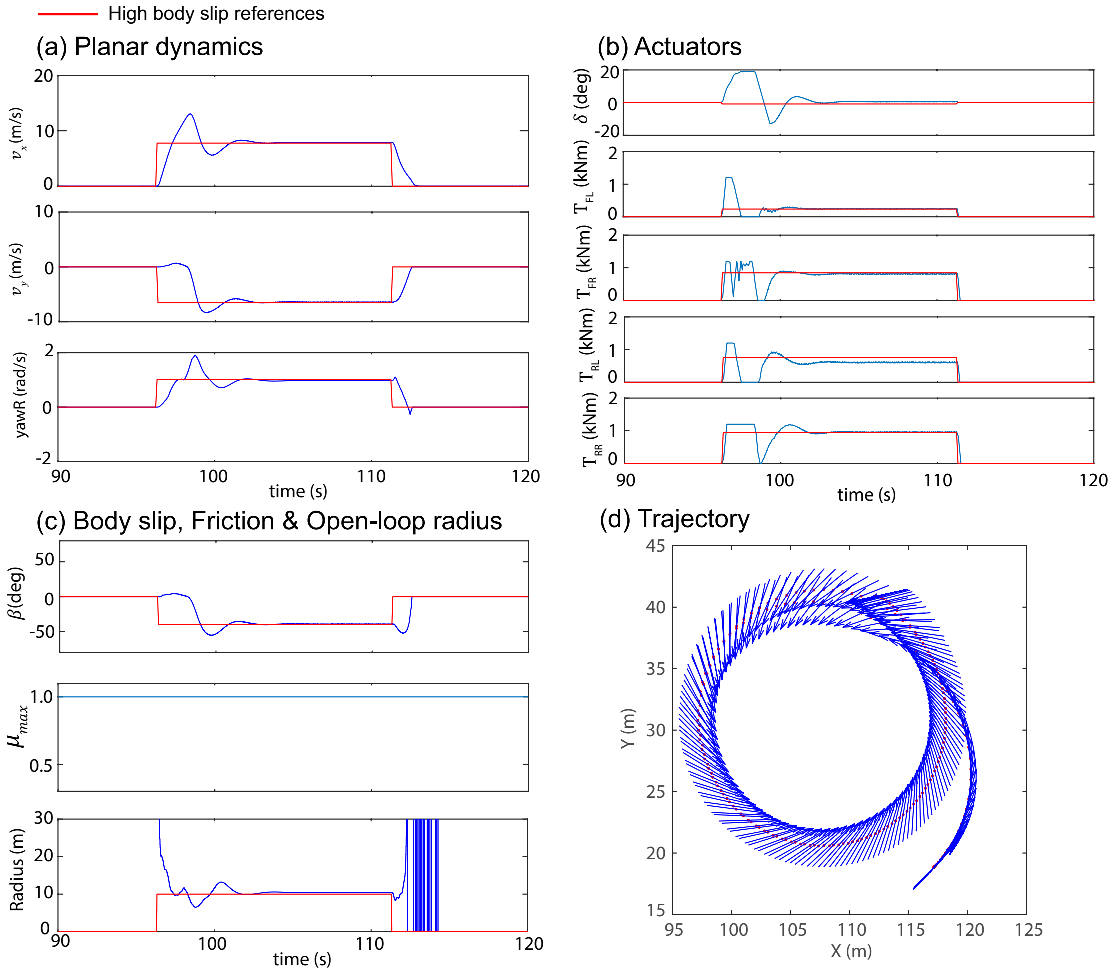

FIGURE 4.12: 10 metres high body slip stabilisation, β_{ss}= - 40 degrees. ROBORACE HiL sign-off.

Due to restrictions in the DevBOT AI-mode initialisation, it was necessary to start the system from standstill conditions in this first project stage. In spite of this, the vehicle planar states (a), the vehicle body slip (c), and the actuator requests (b) converge well to the reference states and feedforward inputs. With regards to the latter, the DES were obtained for a near-zero steering angle with the aim to maintain a sufficient margin in case steering correction were needed to compensate severe model uncertainties. Apart from this, slew rate constraints were applied to the steering angle and wheel torque requests to avoid mechanical failure on the real platform (e.g. driveshaft breakage). Similar conclusions can be extracted from the 20 metres drift test depicted in Figure 4.13.

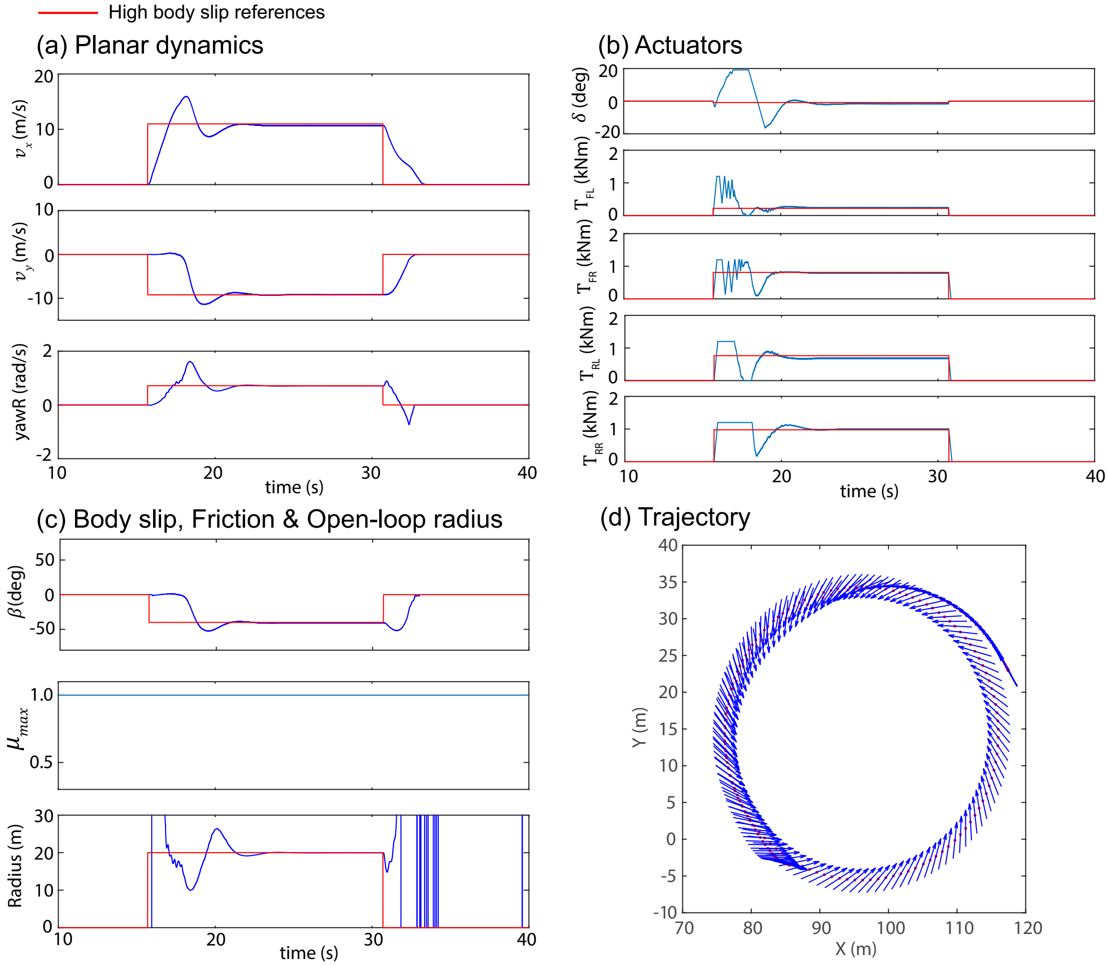

FIGURE 4.13: 20 metres high body slip stabilisation, β_{ss}= - 40 degrees. ROBORACE HiL sign-off.

These manoeuvres were limited to 15 seconds for safety reasons, the moment at which the brakes were gently applied to stop the vehicle. Finally, the NRMSE of the tracked vehicle planar states is given in Table 4.5.

Table 4.5: NRMSE of the tracked vehicle planar motion states (%). *Nominal* Vehicle Dynamics (VD) calibration.

Test	R_{ss}	β_{ss}	$e_{\dot{\psi}}$	e_{v_x}	e_{β}
1	10 m	-40 deg	4.03	2.17	3.59
2	15 m	-40 deg	2.76	1.54	2.02
3	20 m	-40 deg	3.11	2.74	2.00

For consistency with the results shown in previous sections, the metrics were computed for t$>$ 5 s. Overall, low error values were observed for the manoeuvres performed during this sign-off, evidencing the validity of the proposed controller and synthesised models used to derive the DES.

4.2.5 Summary of high body slip stabilisation

In this section, relevant solutions to achieve the high body slip stabilisation of a MAGV platform have been proposed. Two methods have been described to build centralised MIMO controllers depending on the information available regarding the tyre-friction characteristics: model-based and data-based reference derivation. The advantages and drawbacks derived from each methodology have been outlined. Finally, the proposed controllers have been subjected to a virtual testing program formed by SiL tests and HiL experiments.

The systems described in this section evidenced advanced driving patterns only exhibited by highly-skilled drivers. Nevertheless, this behaviour is still limited to “open-loop path” manoeuvres in which the road geometry is not considered. In addition, aspects like the robustness of the proposed systems to time-varying friction conditions have not been taken into account. These considerations are addressed in the following section of this chapter, where the Autonomous Drift Control (ADC) and Highly-Skilled Autonomous driver models are introduced.

4.3 Highly-skilled autonomous driving

Driver models for autonomous driving at the limits of handling are introduced in this section. The autonomous drift control for simultaneous path-following and high body slip stabilisation is described first, followed by the derivation of model-based and data-based solutions for varying-friction compensation. The section is completed with the introduction of a complete driver model that resembles professional rally drivers.

4.3.1 Autonomous Drift Control (ADC)

The Autonomous Drift Control (ADC) concept was developed by the author of this thesis and introduced for the first time in [8, 12, 18]. In essence, ADC consists of a hierarchical structure formed by a high-level trajectory control layer and a low-level vehicle dynamics controller, Figure 4.14. The main aim of ADC is to accurately keep a target high body slip angle along arbitrary road geometries, which can not be achieved with traditional path-following driver models [40] or existing high body slip stabilisation solutions [134]. The proposed concept can be described in the following manner.

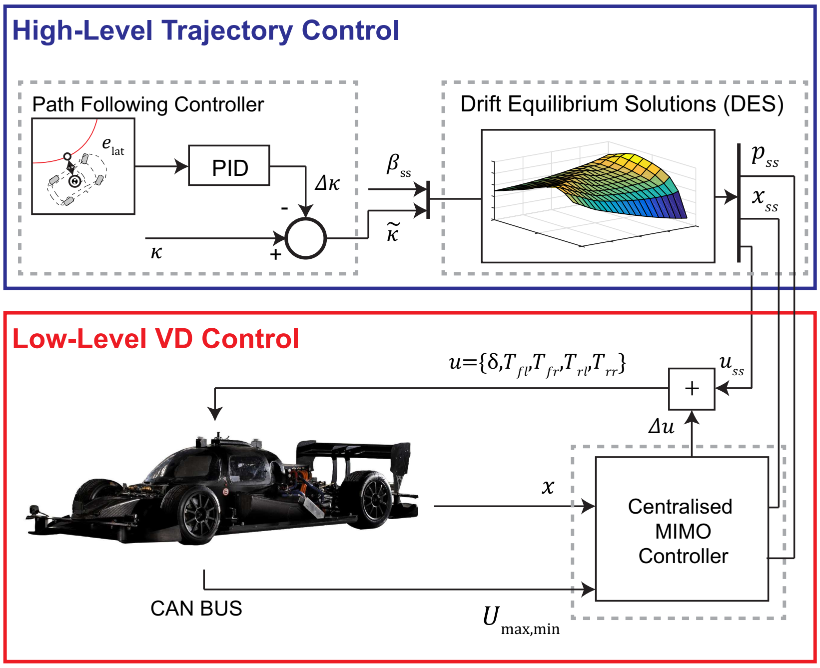

FIGURE 4.14: Architecture of the proposed Autonomous Drift Control for simultaneous path-following and high body slip stabilisation [18].

Assuming a circular reference trajectory defined by a curvature κ, a proportional-integral-derivative (PID) control law of the form,

$$\tilde{\kappa} = \kappa - \Delta\kappa = \kappa - \left(k_{p,e_{lat}} e_{lat} + k_{d,e_{lat}} \dot{e}_{lat} + k_{i,e_{lat}} \int e_{lat}\right) \tag{4.40}$$

is derived to drive the lateral deviation error e_{lat} of the vehicle with respect to a reference path to zero. Taking as a reference the left-handed turn depicted in Figure 4.15, the previous control law can be explained as follows. When e_{lat} is positive the corrected curvature $\tilde{\kappa}$ is decreased to straighten the current vehicle trajectory, Fig. 4.15-a. On the other hand, if e_{lat} is negative, the reference road curvature is increased to tighten the vehicle trajectory, Fig. 4.15-b. The sign criteria for the lateral deviation error is adopted from the road model presented in [128, 14]. At each time step, the inverse of the corrected curvature ($R_{ss} = 1/\tilde{\kappa}$) and the desired equilibrium body slip angle β_{ss} are used to derive the set of DES ($\mathbf{u_{ss}}, \mathbf{p_{ss}}, \mathbf{x_{ss}}$) passed to the low-level Vehicle Dynamics (VD) controller. For simplicity, it is assumed that the rate of change of the pair (R_{ss}, β_{ss}) is negligible in comparison to the low-level system dynamics. If the PID gains ($k_{p,e_{lat}}$,$k_{d,e_{lat}}$,$k_{i,e_{lat}}$) are carefully chosen, the proposed control law will drive the vehicle lateral deviation error to zero, and the vehicle will eventually converge to the reference path. As an analytical Lyapunov stability proof for the proposed system is not trivial, the closed loop stability under different initial errors is studied by means of a phase-space coverage analysis (see Section 4.3.1.2 for further details).

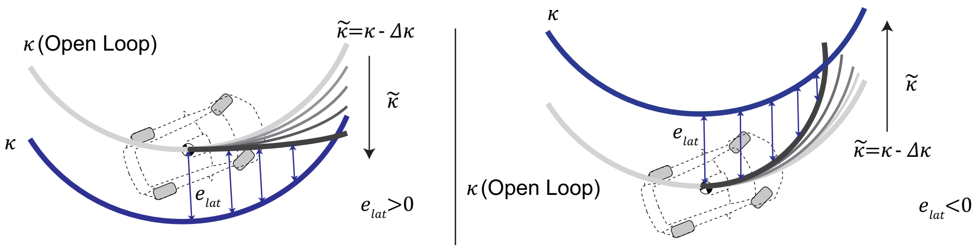

FIGURE 4.15: Illustration of the drift path-following concept for a left-handed turn. (a) Positive lateral deviation error, (b) negative lateral deviation error [8].

Finally, the proposed path-following concept can be applied to other arbitrary road geometries (e.g. clothoid) if a time-varying reference curvature is considered. Specifically, κ is defined as the local curvature of the reference path calculated at the intersection between the MAGV centre of gravity and the reference path perpendicular. In terms of experimental implementation, κ and e_{lat} are computed in this thesis employing a high-accuracy GPS unit and a predefined reference trajectory (see Chapter 5 for additional details regarding the experimental implementation of this approach). The extraction of these parameters using a more sophisticated perception layer formed by LiDARs and Machine Vision is proposed for future work.

4.3.1.1 Road friction adaptation

In order to make the proposed system robust to a wide range of road terrains, it is necessary to monitor the road friction characteristics and adapt the system behaviour to time-varying friction conditions. Two friction adaptation approaches are proposed in this thesis depending on the surface considered. Specifically, rigid surfaces (e.g. tarmac, surfaces that can be considered infinitely rigid with respect to the tyre carcass [19]) in which different friction levels can be parameterised by a unique friction potential factor [104] are handled by the system adopting a model-based reference derivation approach, Section 4.2.2. The friction variations are monitored by means of a friction factor estimate (μ_{est}), computed during sustained drifting as,

$$\mu_{est} = (\mu_{upper} - \mu_{lower})\frac{(a_{ycent} - a_{ycent,min})}{(a_{ycent,max} - a_{ycent,min})} + \mu_{lower} \tag{4.41}$$

where a_{ycent} is the vehicle centripetal acceleration, and $a_{ycent,min}, a_{ycent,max}$ are the centripetal acceleration values expected from two extreme friction conditions (e.g. $\mu_{upper} = 1$, $\mu_{lower} = 0.7$). The raw estimate μ_{est} is filtered adopting RLS. The tarmac drifting references corresponding to different friction levels, as well as the associated centripetal acceleration values, are computed offline using a suitable friction model.

On the other hand, loose surfaces (e.g. gravel, surfaces in which the soft-soil material can lead to the *bulldozzing* effect [128]) requiring a more comprehensive feature vector to model the tyre-friction interaction, are faced adopting a data-based reference derivation approach [8], Section 4.2.3. This concept is illustrated schematically in Figure 4.16 and can be summarised in the following manner. An AI-references block contains a set of feedforward NNs trained at different road terrains following the approach given in Section 4.2.3. The references ($\mathbf{x_{ss}}$, $\mathbf{u_{ss}}$) and tyre parameters ($\mathbf{C_{\alpha,ss}}$, $\mathbf{C_{\lambda,ss}}$) are adapted depending on the current road terrain, which is identified by an NN-based road terrain classifier, Figure 4.17. In this structure, the first block (*Braking event detection*) monitors the master cylinder pressure signal (MC_{press}) and identifies whether a braking intervention is taking place. During the braking situation, the tyre vertical and longitudinal forces, as well as the tyre longitudinal slips are logged (block 2, *Data Logging*). Once the braking event has concluded, an ANFIS structure is trained to approximate the friction curve formed by the cloud of normalised longitudinal force (defined as $\mu_x = F_x/F_z$) versus longitudinal slip data (block 3, *ANFIS Friction Curve Learning*). In order to acquire a cloud of points representative of the terrain friction characteristics, only braking interventions in which a certain longitudinal slip value is developed (i.e. enough longitudinal excitation is present) are considered. The feature vector required by the terrain classifier is obtained directly from the trained ANFIS structure and consists of a set of uniformly-spaced friction values, $\mu_{\mathbf{x}} = \{\mu_{1,x}, \mu_{2,x}, ..., \mu_{n,x}\}$. This vector is passed through a Neural Network classifier (block 5) trained with braking data from different terrains to infer the road class that best matches the current friction characteristics. The use of ANFIS as an intermediate step permits a straightforward extraction of a noise-free feature vector. Otherwise, e.g. computing the previous vector from raw data, would require the execution of non-trivial post-processing steps (such as data averaging in a predefined region) to reduce the influence of outlier points. The suitability of ANFIS networks to approximate the friction versus slip characteristics of an unknown tyre was assessed experimentally in this thesis with the Vehicle-Based Objective Tyre Testing (VBOTT) testbed of Jaguar Land Rover, Chapter 5.

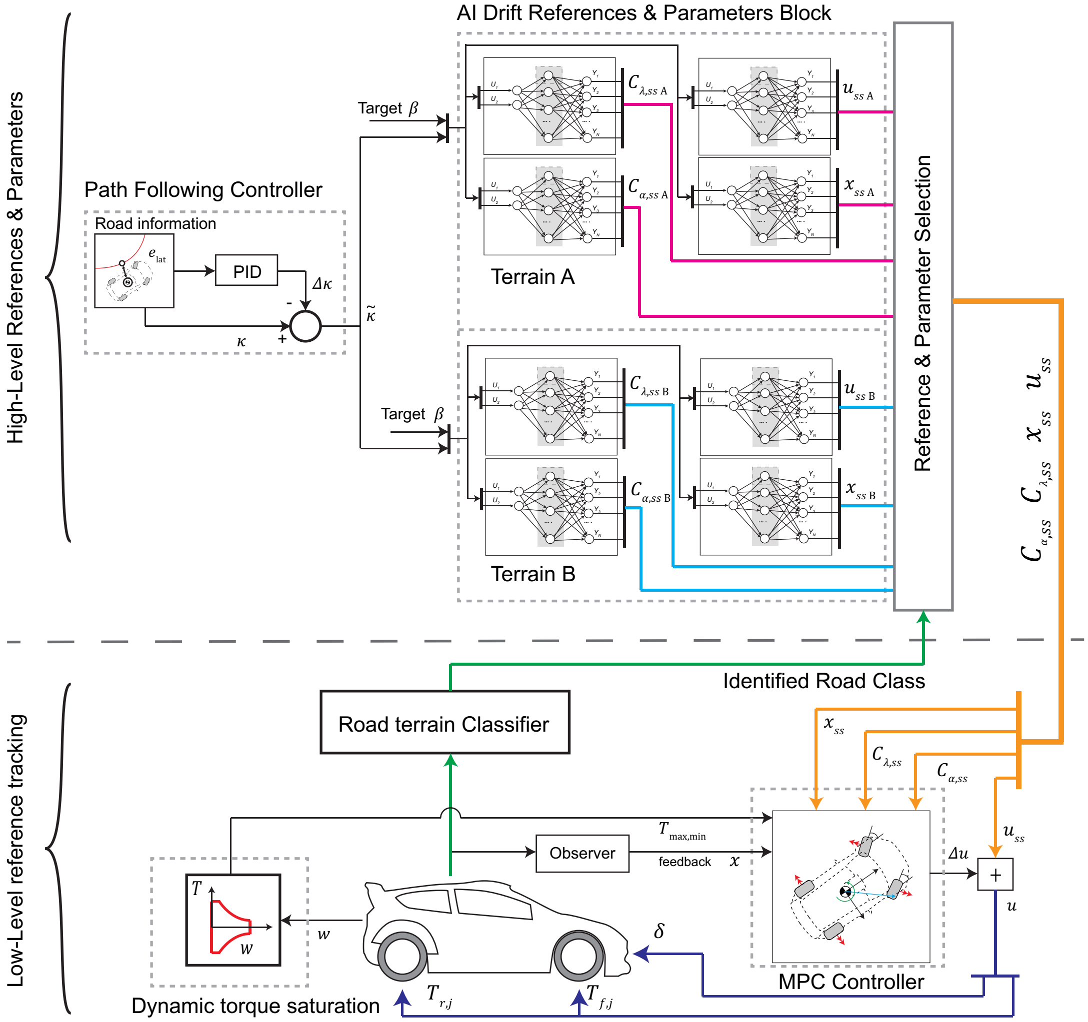

FIGURE 4.16: Artificially-intelligent drift control system with road-class adaptation proposed in [8].

4.3.1.2 SiL experiments

The high body slip controllers described in Section 4.2 were enhanced with the path-following feature introduced in the previous paragraphs, giving, as a result, the ADC system. This was subjected to the SiL verification described in the following. To start with, the AWD compact-class model introduced in Section 4.2.2.1 (model-based reference derivation) was tested in constant-radius and clothoid turns, Figure 4.18.

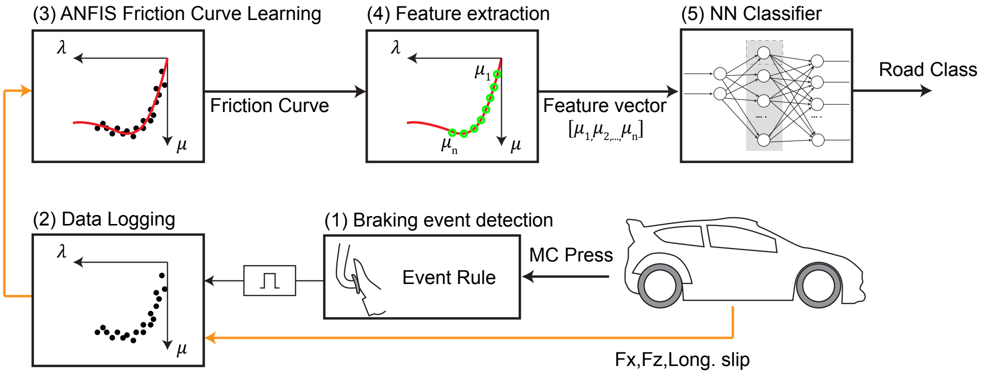

FIGURE 4.17: Scheme of the road terrain classifier introduced in [8]. Once the road terrain is identified (road class), the high-level drift references and parameters are adjusted accordingly.

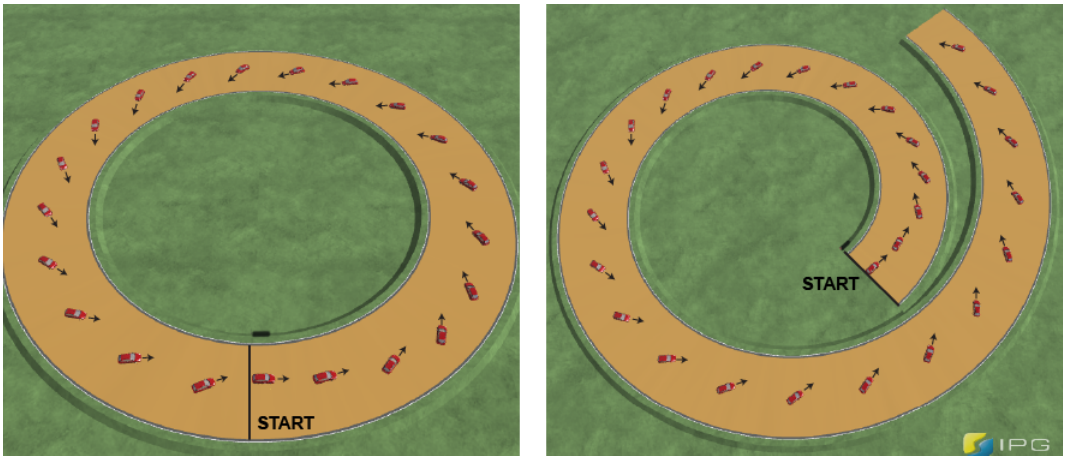

FIGURE 4.18: Left: 50 metres constant-radius trajectory. Right: 40-90 metres increasing radius clothoid. Target body slip angle β_{ss}= -35 degrees [18].

The vehicle was initialised with a positive lateral deviation error (e_{lat} =2 m), straight-line conditions ($\dot{\psi}$ =0 deg/s, β = 0 deg), and a longitudinal velocity error Δv_x = - 5 m/s. These initial errors were chosen arbitrarily to show the closed loop convergence of the proposed system. As can be noticed in Figure 4.19, the system converges quickly to the reference vehicle states. The lateral deviation error presents an initial overshoot but keeps within a 1 metre band once high body slip stabilisation has been achieved. For simplicity, the e_{lat} signal is taken from the IPG-CarMaker environment using *RoadProperty* sensors. This step is realised experimentally adopting a high-accuracy differential GPS unit, Section 5. Additional details regarding this preliminary ADC evaluation can be consulted in [18]. After that, the AI-based ADC (Figure 4.16) was implemented in the sports-class AWD model introduced in Section 4.2.3.1. The PID gains of the high-level trajectory control layer were tuned carefully and the phase-space coverage analysis depicted in Figure 4.20 was performed.

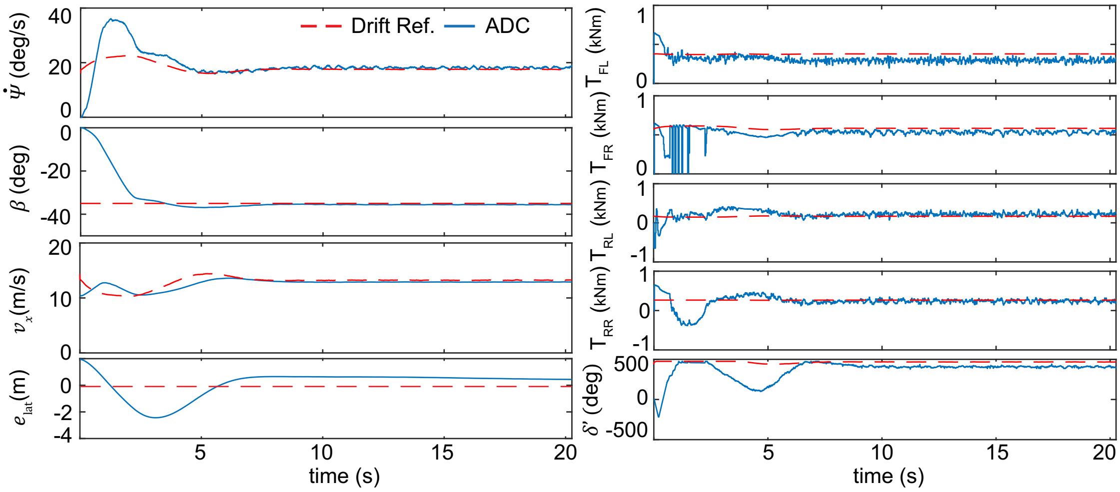

FIGURE 4.19: Results of the constant-radius path-following test, $\beta_{ss} = -35$ degrees [18].

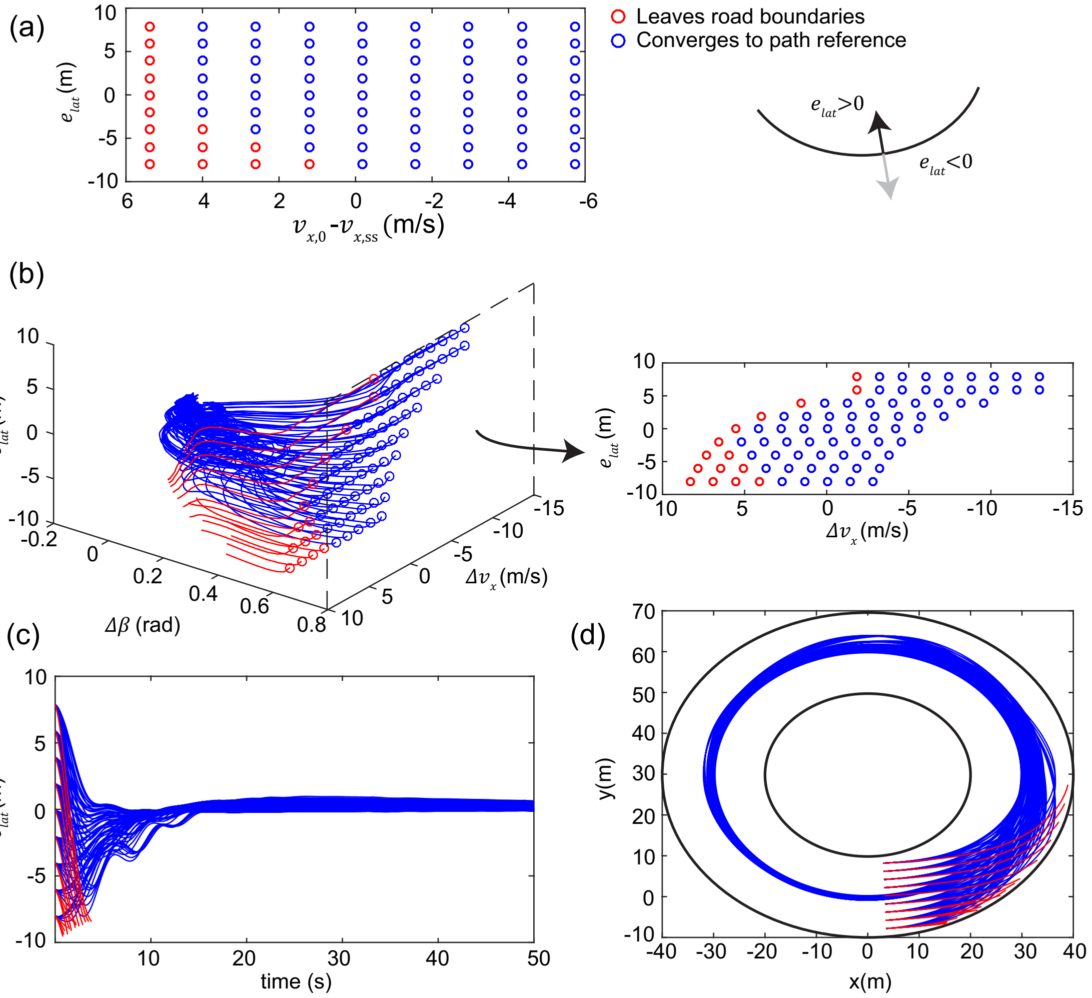

FIGURE 4.20: Phase space coverage analysis. (a) Initial longitudinal velocity and lateral deviation errors, (b) three-dimensional state error trajectories, (c) time histories of the lateral deviation error, (d) vehicle trajectories [8].

The vehicle was initiated in straight line conditions (null body slip angle and null yaw rate) at different initial speeds and lateral deviation errors, Figure 4.20-a. The three-dimensional trajectories of the body slip, lateral deviation, and longitudinal velocity state errors are depicted in Figure 4.20-b. The distortion of the longitudinal velocity error Δv_x is caused by the action of the upper-level PID controller, which modifies the tracked references to reduce the lateral deviation error. As can be noticed, the proposed system converged to the reference trajectory for the majority of initial errors, Figures 4.20-c and 4.20-d. Additional simulations were repeated in a wide range of road radii and similar results were obtained, evidencing the ability of the proposed ADC to drive the vehicle to the reference path in a finite time [8].

The AI-based ADC evaluation was completed with the friction robustness assessment illustrated in Figures 4.21 and 4.22.

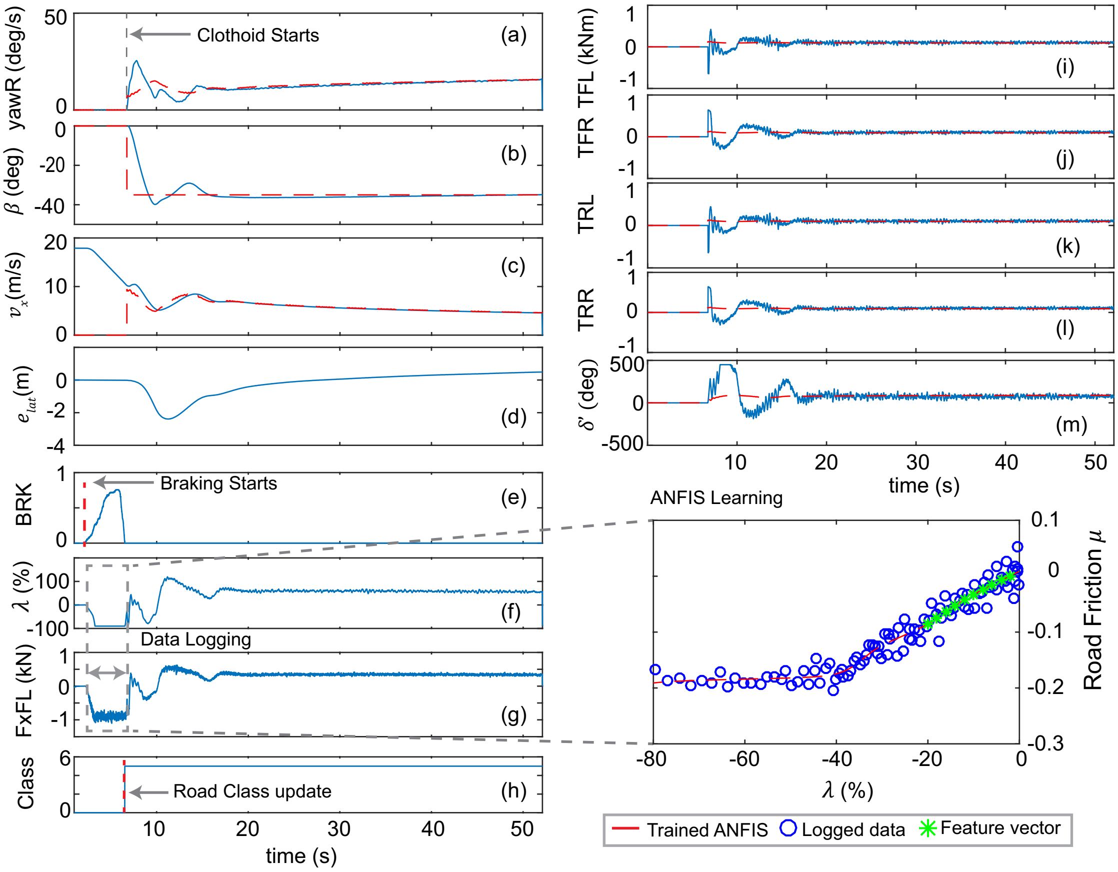

Figure 4.21: Time histories of the clothoid test case simulated in a low-mu loose surface with the proposed AI-based ADC. (a) Yaw rate, (b) body slip angle, (c) longitudinal velocity, (d) lateral deviation error, (e) Braking pedal position, (f) Front-left longitudinal slip, (g) Front-left wheel force, (h) Identified road class, (i) Front-left wheel torque, (j) Front-right wheel torque, (k) Rear-left wheel torque,(l) Rear-right wheel torque and (m) Steering wheel angle [8].

In brief, the vehicle is driving over a low-mu loose terrain (see [8] for further details) at high speed (18 m/s), and a hard braking intervention is performed to reduce the speed when a clothoid segment is approached. During the braking event (t > 2 s to t < 8 s) the NN-based classifier described in Section 4.3.1.1 recognises the current road terrain from the friction feature vector provided by the trained ANFIS structure and the references and tyre parameters of the low-level VD MPC are adjusted accordingly.

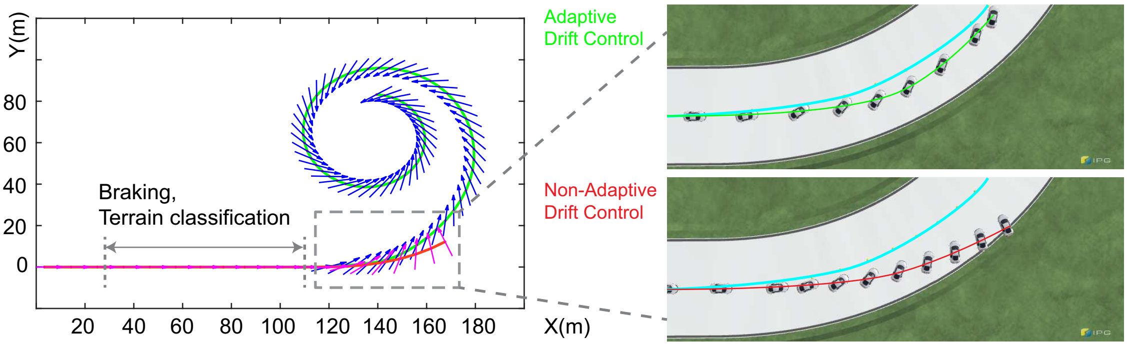

Figure 4.22: Trajectories of the adaptive (green) and non-adaptive (red) AI-based ADC system [8].

After that, the vehicle starts the desired drifting motion and follows the clothoid road segment with minimum lateral deviation, Fig. 4.21. In order to evaluate the importance of an adaptive terrain-based control strategy, a second simulation eliminating the terrain classifier action was executed. In this case, the system is initialised with the set of NNs trained in the gravel-like terrain (Section 4.2.3.1). As can be observed in Figure 4.22, the non-adaptive system is unable to cover the clothoid segment and leaves the road in an uncontrolled spinning motion. Additional details regarding the NN training process are omitted in this thesis due to space limitations and can be consulted in [8]. Finally, additional simulations, Figure 4.23, were performed to study the AI-based ADC robustness to mass variations and slight changes in the friction characteristics (which might not be identified as a different road terrain by the classifier). According to recent results on off-road tyre data analysis [20], maximum friction values can vary within a 0.1 band if different tyres (e.g. summer tyres, studded tyres) are tested in the same off-road surface (e.g. gravel). Additional tests were performed in the previous clothoid test case increasing and decreasing by a factor of 0.05 the maximum friction parameter corresponding to the gravel-like terrain, Figure 4.23. The set of NNs trained in this terrain was employed in the driverless controller for consistency. The previous test case was repeated introducing several variations in the vehicle mass and weight distribution ($+\Delta m \approx 150$ kg on front and rear positions). These results are omitted here due to space limitations and the NRMSE of the tracked states can be consulted in Table 4.6. Overall, the proposed system performed well to changes in the vehicle mass and slight variations in the road friction characteristics (e.g. due to the use of different tyres [20]).

In addition, the ability of the proposed system to cope with more significant terrain changes was demonstrated in the previous paragraphs.

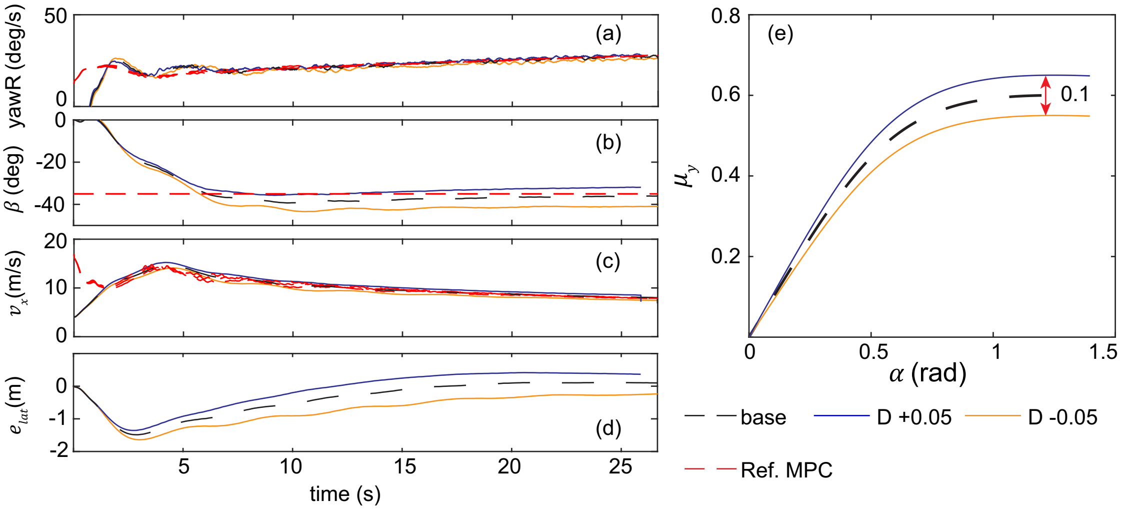

FIGURE 4.23: Results obtained after varying the maximum friction coefficient in the simulation environment (D parameter [128]) by a factor of 0.05. (a) yaw rate, (b) body slip angle, (c) longitudinal velocity, (d) lateral deviation error, (e) lateral friction versus lateral wheel slip curve [8].

TABLE 4.6: NRMSE of the planar vehicle dynamics states. front∗: $\Delta m \approx 150$ kg on front position / rear∗: $\Delta m \approx 150$ kg on rear position. D^{**}: maximum friction factor [8].

Test	Configuration	$e_{\dot\psi}$	e_{vx}	e_β
1	D**+0.05	4.20	3.29	5.58
2	D**-0.05	7.02	4.02	18.36
3	$+\Delta m$ front∗	3.33	2.02	4.40
4	$+\Delta m$ rear∗	4.08	2.73	4.31
5	$+\Delta m$ front∗ + Δm rear∗	3.76	2.55	5.23

4.3.1.3 HiL experiments

The path-following and friction adaptation feature described in this section were also tested in the real DevBOT MAGV, Chapter 5. Before that, the proposed solutions were signed-off in the ROBORACE HiL platform introduced in Section 4.2.4. Specifically, in order to progress to the project stage 2 (*simple path following*), the enhanced system was developed and tested first in IPG-CarMaker.

Following the rigid-surface friction adaptation approach described in Section 4.3.1.1, model-based DES were generated varying the friction scaling factor of a MF 5.2 tyre model (covering a friction vector $\mu_{\max} = [0.4 : 0.1 : 1.2]$). The expression (4.41) was implemented in Simulink and the LQR feedback gain was computed offline for a grid of DES (defined by the vector of reference radius $\mathbf{R_{ss}} = [5 : 1 : 25]$, reference body slip angle $\beta_{ss} = -40$ degrees, and previous friction vector). These offline DES were implemented in the model by means of multi-dimensional look-up tables. After that, the IPG DevBOT model was subjected to a time-varying friction evaluation during high body slip stabilisation in a wide-open virtual platform, Figure 4.24.

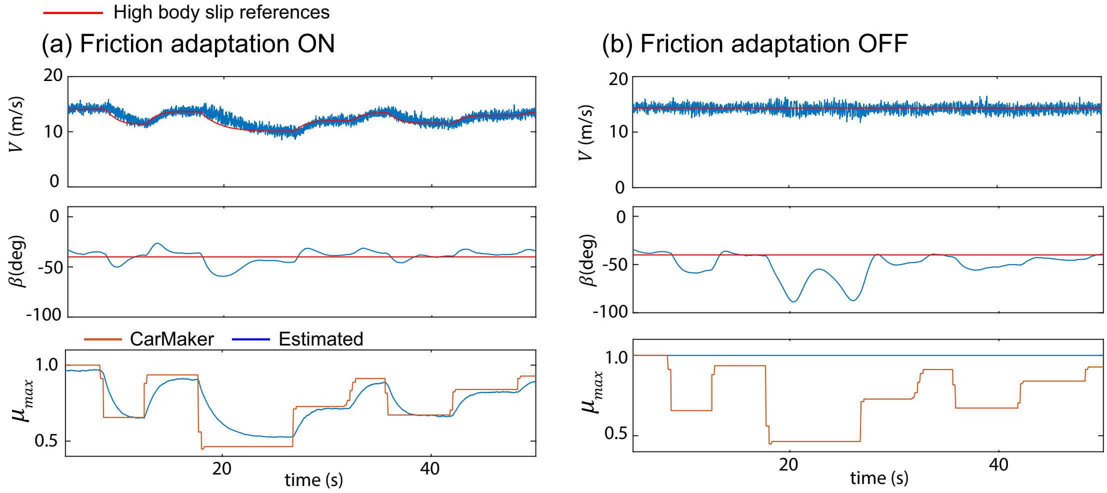

Figure 4.24: Time-varying friction tracking experiment performed in IPG-CarMaker. Left: Friction adaptation ON, right: Friction adaptation OFF. $\beta_{ss} = -40$ degrees, $R_{ss} = 10$ metres.

Overall, the adaptive-mu system is able to identify timely the friction changes and performs the corrections needed to maintain the reference body slip angle, Fig. 4.24-a. When the friction compensation is switched off, the system is unable to maintain the stability during the transition to low mu ($t \approx 18$s), and the vehicle is about to spin ($|\beta|$ increases to 90 degrees). Additional simulations were performed to fine-tune the dynamic response of the friction compensation algorithm (RLS forgetting factor adjustment), which are omitted here due to space limitations. After that, the ADC system was implemented in SPEEDGOAT and constant-radius and spiral path-following manoeuvres were tested in the ROBORACE HiL platform, Figure 4.25.

As can be noticed in the time histories illustrated in Figure 4.26, the lateral deviation error e_{lat} presents some oscillations during the first seconds of the manoeuvre. This is caused by the restriction of enabling AI in DevBOT from standstill conditions. This matter is addressed in Section 4.3.2, where a more sophisticated Finite State Machine (FSM) incorporating different driving modes is proposed. In spite of this, the vehicle converges quickly to the desired path and the lateral error is reduced after a few seconds. With regards to the friction estimate μ_{est}, it converges to a 0.95 factor. The difference with respect to the $\mu_{\max} = 1$ factor corresponding to an ideal dry tarmac is caused by the uncertainty introduced by the DevBOT HiL model, which incorporates additional degrees of freedom (e.g. suspension kinematics) not considered in the synthesised modelisation used during the DES generation.

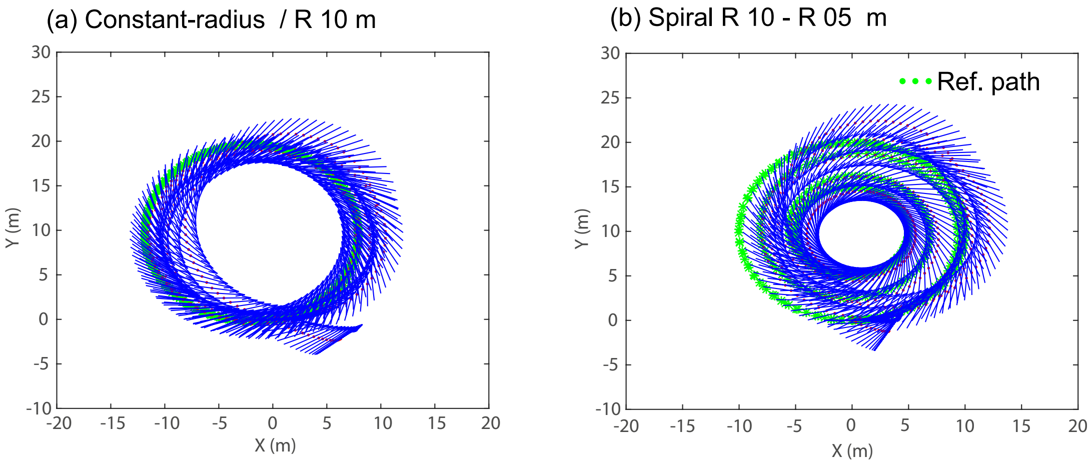

FIGURE 4.25: *Simple path-following* HiL tests, vehicle trajectories. Left: 10 metres constant-radius test. Right: 10-5 metres spiral test. Virtual DevBOT initialised in standstill conditions. $\beta_{ss} = -40$ degrees.

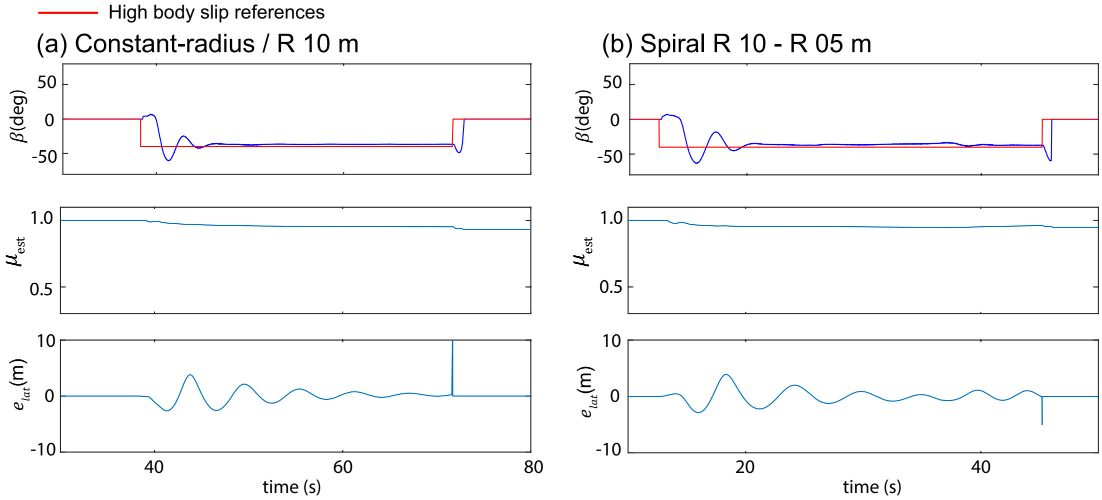

FIGURE 4.26: *Simple path-following* HiL tests, time histories. Left: 10 metres constant-radius test. Right: 10-5 metres spiral test. Virtual DevBOT initialised in standstill conditions.

Finally, in spite of some initial oscillations, the reference body slip angle is tracked closely during the course of the manoeuvre. This initial evaluation evidenced the effectiveness of the path-following and friction compensation features introduced in this section. The DevBOT ADC robustness to more challenging friction conditions was evaluated by means of field tests carried out in Millbrook proving ground (UK). Specifically, the ability of the real DevBOT platform to cope with rainy conditions (slippery tarmac with water puddles) can be consulted in Section 5.2.

4.3.2 Complete driver model

To conclude with this section, a brief insight into a more sophisticated complete driver model for driverless competition vehicles is provided. This model is denoted in the following as RALLYCROSS and is proposed as an enhancement of the ADC system introduced in Section 4.3.1. In essence, the RALLYCROSS model is aimed at achieving an extended operating envelope that could alleviate the limitations exhibited by the preliminary ADC (e.g. standstill drift initialisation on DevBOT). The RALLYCROSS is constructed adopting a modular architecture in which two blocks can be distinguished: layered motion control block and friction learning block, Figure 4.27.

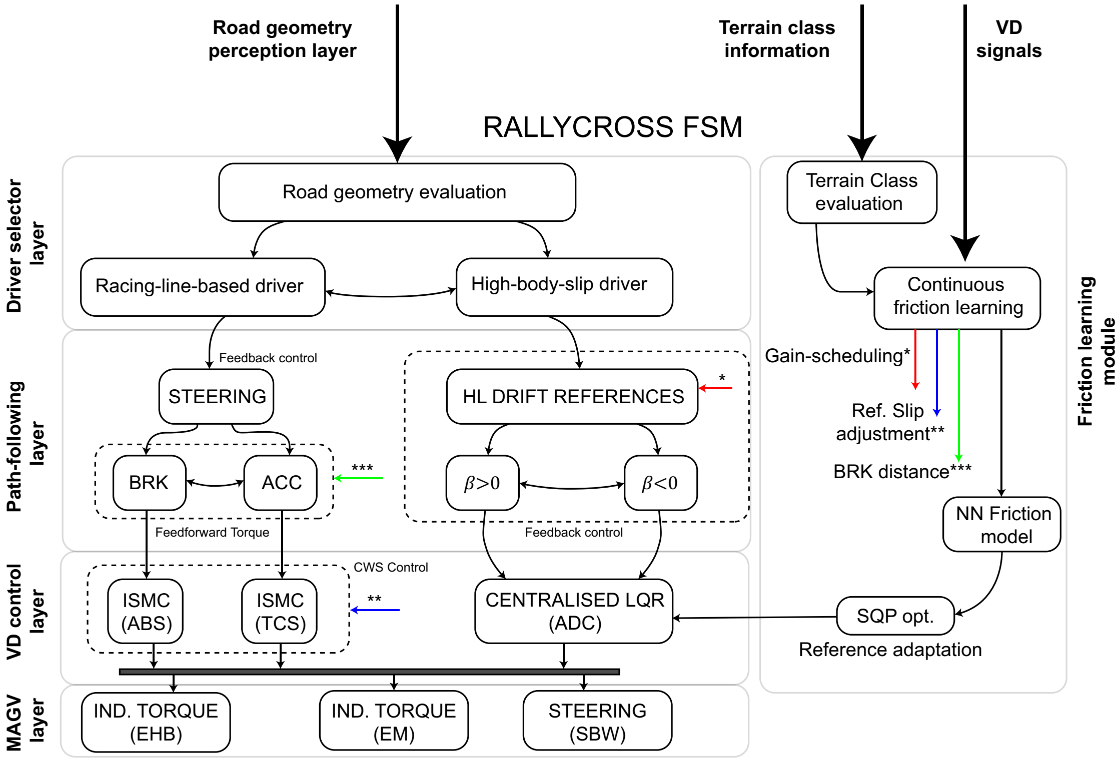

FIGURE 4.27: Complete driver model for highly-skilled autonomous competition vehicles proposed in [4].

Overall, the layered control block is formed by a Finite State Machine (FSM) that combines two driving modes: racing line path-following [40] and high body slip path-following. Similarly to the approach introduced in [14], each driving mode is selected by a high-level agent (*road geometry evaluation*) based on a set of *if-then* rules and the road geometry information. The road geometry information is supplied to this layer as a vector $\kappa = \{\kappa_{d_i}\}$ that contains the discrete values of the reference trajectory curvature (κ) at a distance ($d_i = \{0, 10, 20, 30\}$ metres) ahead of the vehicle. This information is assumed to be supplied by an upper-level perception layer that may use machine vision, LiDAR, RADAR sensors or a combination of all. Once a suitable driver model has been selected, the high-level control references are generated to keep the vehicle along the reference path. In brief, the racing line path-following task is realised adopting a proportional steering feedback control law and a racing-like ACCELERATION/BRAKING longitudinal control (see [4] for additional details). With regards to the high body slip path-following, the ADC control law given in Section 4.3.1 is enhanced with a set of preview-distance correction terms, Figure 4.28.

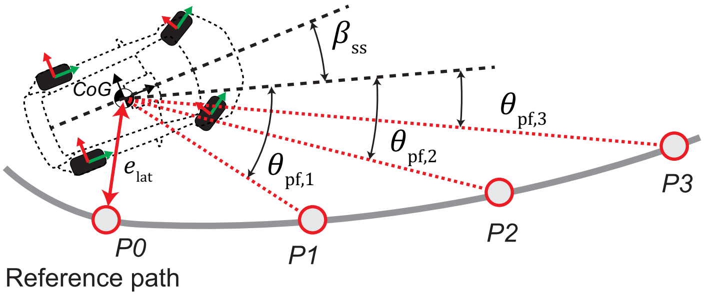

FIGURE 4.28: Scheme of the enhanced high body slip path-following control law [4].

Following this scheme, the preview distance information is incorporated into the system by means of the heading angle error terms ($\theta_{pf,i}$). These are defined as the angle comprised between the line connecting the preview point P_i and the vehicle centre of gravity (CoG), and the desired vehicle heading direction (given by the reference body slip angle β_{ss}). The updated control law is given by expression (4.42).

$$\tilde{\kappa} = \kappa - (K_{p,e_{lat}} e_{lat} + K_{d,e_{lat}} \dot{e}_{lat} + K_{i,e_{lat}} \int e_{lat}) - \sum K_{p,pfi} \theta_{pf,i} - \sum K_{d,pfi} \dot{\theta}_{pf,i} \tag{4.42}$$

The incorporation of the proportional and derivative components of the heading angle errors ($K_{p,pf}$, $K_{d,pf}$) permits anticipating to future curvature changes and pre-adjusting the vehicle trajectory to fit the future path geometry, thus avoiding the risk of track departure during abrupt radius changes (e.g. severe radius reduction or curvature transitions [14]). A low-level Vehicle Dynamics (VD) control layer is in charge of realising the driving commands dictated by the high-level path-following blocks. Specifically, the high body slip stabilisation is achieved by the centralised LQR described in Section 4.2. In addition, continuous wheel slip (CWS) control is realised in this layer to maintain optimum longitudinal slip levels during hard acceleration and emergency braking. Following the methodology introduced in [117], these functions are realised by means of Integral Sliding Mode Control (ISMC). Finally, the VD control requests are sent to the EMs, steering system and Electro-Hydraulic Braking (EHB) system located on the MAGV layer [4].

In what concerns the friction learning block, a distinction is made between rigid or loose surfaces due to the friction modelling peculiarities discussed in the preceding sections of this thesis. For simplicity, it is assumed that a high-level intelligent perception layer exists and is able to make a distinction between these surfaces. This may be achieved in a Rallycross track adopting a GPS-based localisation approach, by means of a "rough" machine vision-based terrain identification, or relying on a braking-based road classification routine [8]. For rigid surfaces, the model-based friction adaptation approach described in Section 4.3.1.1 is used. With regards to loose surfaces, the machine learning approach depicted in Figure 4.29 is proposed.

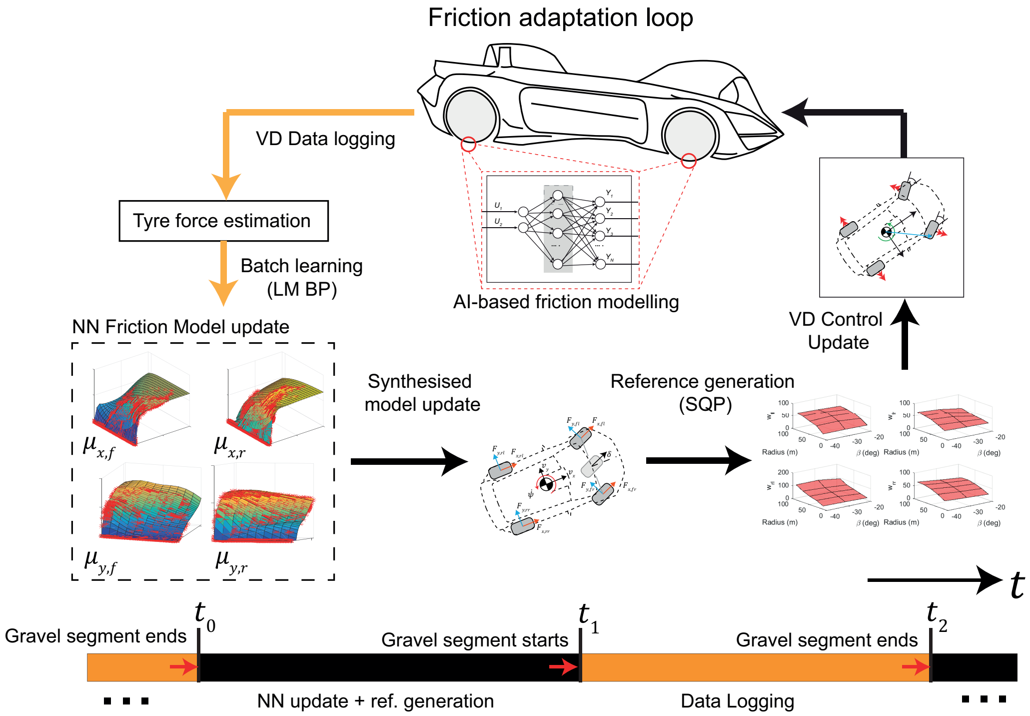

FIGURE 4.29: FSM friction adaptation loop proposed in [4].

Essentially, this approach combines the advantages of the model-based reference derivation (Section 4.2.2) with a data-based tyre friction modelling. This methodology is analogous to the hybrid data-based modelling derived in the previous chapter, as it combines a first principles model (synthesised planar dynamics for model-based reference derivation) with a "black-box" model (NNs) of the unknown tyre friction characteristics. For the sake of clarity, the proposed approach is applied to a Rallycross race case described in the following manner.

Before the race, the NNs are initialised with synthetic friction data obtained from a warm-up session. These friction NNs are employed to generate the initial VD control references. Once the race is started, each time the HSAV covers the loose surface segment, the weights of the NN friction structures are updated with new friction data using the Levenberg-Marquardt (LM) backpropagation training algorithm. Specifically, four NN structures are employed to model the tyre friction in the longitudinal and lateral combined-slip cases (i.e. $\mu_x = F_x/F_z$ and $\mu_y = F_y/F_z$, with F_x, F_y, F_z being the tyre forces in the three axes). In the next step, a synthesised vehicle planar dynamics model is updated with the new friction characteristics learned by the NNs and a Sequential Quadratic Programming (SQP) optimisation routine is launched to find the drifting references that maximise the vehicle lateral dynamics [18], Section 4.2.2. Finally, it is important to remark that the previous steps (NN training and SQP optimisation) need to be executed within the time interval required to cover the tarmac segment $(t_1 - t_0)$, Fig. 4.29-bottom. In terms of aerospace or military applications, the race case may be seen as a minimum-time route execution problem in which the HSAV seeks to cover a certain predefined route in the minimum possible time. In such a scenario, the target route may be continuously passed by several MAGVs with the ability to log and send data to a central base station using vehicle-to-infrastructure (V2I) communication technologies. Such information might be employed to monitor the friction characteristics of the path and generate updated system references to be loaded into new incoming vehicles.

4.3.2.1 SiL experiments

The proposed system was tested in a virtual Rallycross track (Fig. 4.31) modelled in the vehicle dynamics simulation software IPG-CarMaker. The proposed FSM was implemented in a validated DevBOT chassis model incorporating steering and drivetrain actuator constraints. For simplicity, the vehicle dynamics signals and tyre forces were directly taken from the Car-Maker/Simulink framework. Virtual sensing solutions to obtain these from inexpensive vehicle dynamics measurements were presented in the previous chapter. In order to study a high-demanding scenario, the time-varying friction models illustrated in Figure 4.30 were implemented in the virtual track.

In brief, at the start of the race ($t = 0$) dry conditions are assumed on both surfaces (red friction curves). The tarmac surface is modelled adopting an isotropic MF tyre model and a maximum friction value $\mu_{\max} = 1$ [128]. The MF parameters of the gravel terrain at $t = 0$ were fitted from constant-speed steering-ramp tests carried out on a dry packed gravel platform (see Section 3.3.1.2). After 10 minutes of rain (t = 600s, cyan friction curves), the tarmac surface is slippery ($\mu_{\max} = 0.7$) [128], and the dry packed gravel has turned into an extreme off-road terrain with a reduced friction stiffness and a high soft-soil content (large bulldozing effect [128]). The change between these conditions is assumed to be progressive, and modelled in IPG-CarMaker by means of the linear interpolation friction surfaces depicted in Figure 4.30. Finally, a rough road profile was

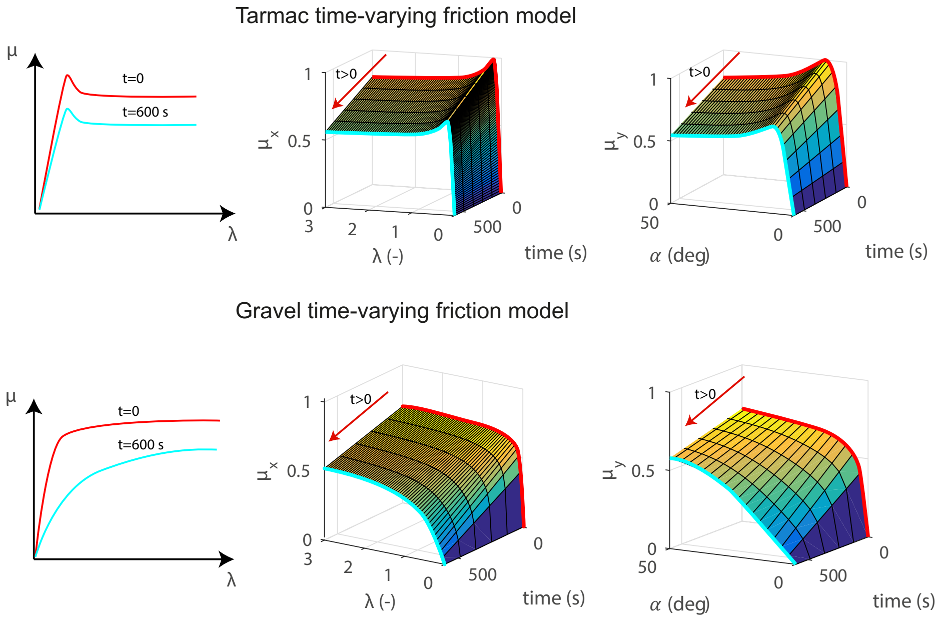

FIGURE 4.30: Tarmac and gravel time-varying friction models implemented in the virtual Rallycross track [4].

added to the gravel terrain adopting the approach presented in Section 3.3.1.2 in order to model realistically severe vertical disturbances. The results obtained during the course of the race are depicted in Figures 4.31 and 4.32.

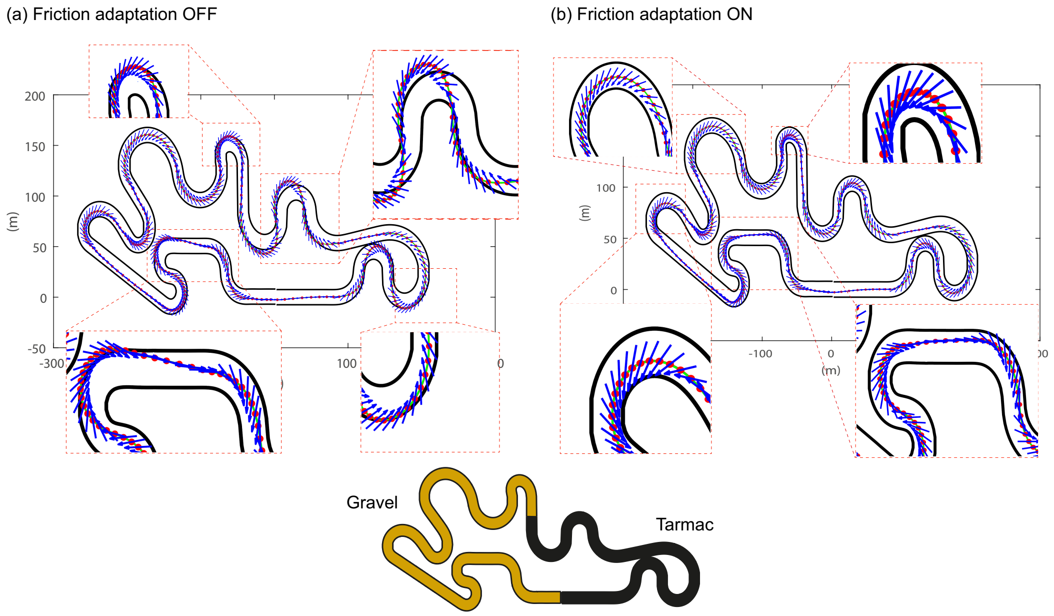
(a) Friction adaptation OFF

(b) Friction adaptation ON

FIGURE 4.31: (a) Friction adaptation OFF, (b) Friction adaptation ON. Vehicle heading and trajectory obtained during the third lap [4].

The trajectories obtained during the third lap (chosen randomly for illustration purposes) are depicted in Figure 4.31. During the tarmac segment, the HSAV computes continuously the friction estimate (μ_{est}, Fig. 4.32-top) and adapts the tarmac friction references accordingly. In parallel, the friction adaptation loop depicted in Figure 4.29 is executed (Fig. 4.32-bottom). Overall, an acceptable average time update of 30s (within the tarmac time window $(t_1 - t_0) \approx 40s$, Fig. 4.29) was obtained for the complete NN weight update and SQP optimisation using a computer equipped with an Intel i7-8th generation processor and 8GB RAM memory.

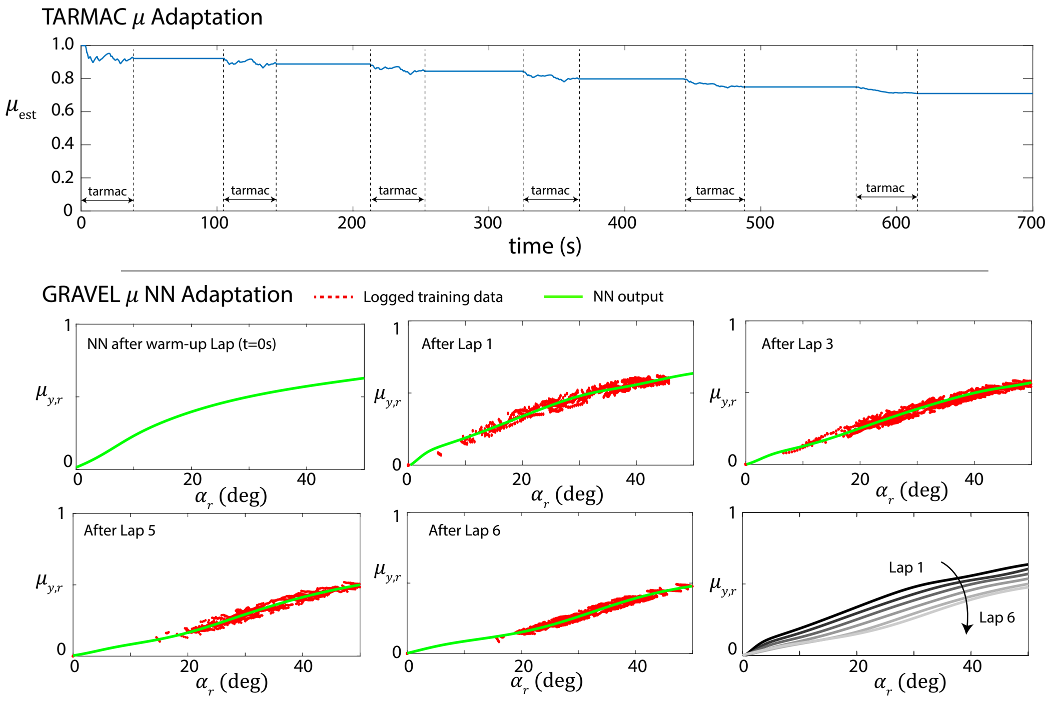

FIGURE 4.32: Top: Tarmac friction estimate μ_{est} versus total simulation time. Bottom: Section and training data of the rear axle combined-lateral-slip NN $\mu_{y,r}$ for a longitudinal slip value $\lambda_r = 0.5$ [4].

Finally, the maximum and Root Mean Square (RMS) errors of the lateral deviation (e_{lat}) are given in Table 4.7. When the friction adaptation feature is enabled, the maximum deviation is maintained below the maximum semi-track width ($7.5m$) in spite of the time-varying friction conditions for the 6 laps of the race. On the other hand, if the friction adaptation is switched off, the vehicle is unable to cover the full race and leaves the road during the third lap, Figure 4.31-a. The lateral deviation error metrics increased progressively (Table 4.7) until a maximum absolute error of 13.28 metres occurred in the third lap and the simulation was stopped.

These results illustrate the difficulty of controlling a vehicle at high body slip angles during time-varying friction conditions along tight road geometries. In such scenarios, future HSAVs will be required to demonstrate not only expert driving skills but also an outstanding perception and adaptation ability.

Table 4.7: Maximum absolute and RMS lateral deviation errors [4].

FRICTION ADAPTATION ENABLED						
Metric	1	2	3	4	5	6
$RMS(e_{lat})$	2.41	2.30	2.24	2.14	2.23	2.21
$\max(\lvert e_{lat}\rvert)$	4.62	3.99	4.11	4.12	4.95	4.81
FRICTION ADAPTATION DISABLED						
Metric	1	2	3	4	5	6
$RMS(e_{lat})$	2.36	2.65	4.33	X	X	X
$\max(\lvert e_{lat}\rvert)$	5.85	6.94	13.28	X	X	X

4.3.3 Summary of highly-skilled autonomous driving

In this section, the path-following and friction adaptation attributes have been incorporated into the high body slip controllers derived previously. A preliminary Autonomous Drift Control (ADC) system has been proposed to achieve simultaneous path-following and high body slip stabilisation on this basis. This design has been embedded into a modular control structure giving, as a result, a Rallycross FSM for driver-less competition MAGVs. The path-following ability of the proposed driver models has been evidenced in a comprehensive SiL and HiL testing program formed by a wide range of road geometries.

In what concerns the friction adaptation ability of the proposed driver models, three approaches have been adopted depending on the surface considered. To start with, a model-based friction compensation routine has been proposed for rigid tarmac surfaces in which friction variations can be parameterised adopting an MF friction scaling approach. With regards to the loose surfaces, two machine learning-based solutions have been proposed. In a first step, a braking-based terrain identification strategy has been introduced to select the set of NNs of an AI-based ADC that correspond to a recognised terrain. In order to avoid the necessity of generating a training dataset for each potential road terrain, a hybrid approach has been proposed in the Rallycross FSM. Essentially, this hybrid methodology alleviates the necessity of converting the MAGV into a "driveable" platform and removes the human driver from the "teaching" loop. Instead, the intelligent system learns to drift over new unknown surfaces autonomously by successive adaptation loops. This latter statement is formulated under the assumption of progressive friction variations and several repetitions over the same path. Such scenarios will be realisable in the future with the aid of V2I communication technologies.

4.4 Conclusions

In this chapter, different solutions to incorporate advanced driving skills into future driver-less MAGV platforms have been described. Several vehicle models have been used along this chapter in order to assess the robustness and performance of the proposed controllers against different vehicle variants (e.g. sports class, compact class, see Table A.1, Appendix A). Once the proposed solutions were developed conceptually in a SiL level, the focus was shifted towards the experimental validation of these in a state-of-the-art multi-actuated driver-less platform (ROBORACE DevBOT), for which SiL and HiL correlated DevBOT vehicle models were introduced.

The motion control functions have been developed in a progressive manner, starting with controllers for high body slip stabilisation and finishing with an FSM that can drive along a complex road layout and resembles a professional Rallycross driver. In addition to the driving skills, the proposed solutions have been designed to show friction adaptation ability. In brief, model-based and data-based approaches have been proposed to handle time-varying friction conditions. The most relevant conclusions extracted from this chapter are summarised in the following points.

- High body slip stabilisation is achieved adopting a centralised multi-actuated control framework. Solutions employing LQR and MPC formulations have been proposed and tested. Specifically, constrained LQR has been developed first and used to implement the MPC, which handles actuator constraints optimally. With regards to the controller references, two methodologies have been proposed depending on the tyre-friction information available: model-based and data-based. With respect to the former, it is assumed that a suitable tyre model exists and can be employed during the reference optimisation.
- If data-based reference derivation is adopted, the autonomous vehicle is treated as an AI system that can learn to drift from a skilled driver. On the other hand, the tyre-model-less advantage offered by this method has the drawback of making the MAGV platform “driveable” for the execution of the field tests. This limit the application of maximum centripetal acceleration strategies. A third hybrid methodology has been proposed to overcome the limitations derived from purely model-based and data-based approaches. In this case, the tyre friction model is substituted by an NN structure that is embedded in the model-based optimisation loop.
- Trajectory control has been achieved by means of a high-level layer based on a PID control law. The long term objective of this concept is to derive systems that can

sustain a high body slip angle along tight road geometries. This operation can be advantageous on low-manoeuvrability surfaces if maximum centripetal acceleration strategies are exploited. As an example, high body slip-based lane departure prevention systems may be developed on this basis for snow or off-road emergency scenarios.

- Different friction adaptation strategies have been described in this chapter, grouped into model-based and data-based. In the case of the latter group, it is required to measure the tyre forces in order to extract relevant tyre parameters (tyre stiffness) or to generate a friction training dataset. This reinforces the necessity of developing virtual tyre force sensors that can support the friction adaptation strategies of advanced motion control systems.

The proposed controllers are aimed at exploiting the full chassis potential on low manoeuvrability surfaces where high tyre lateral slip angles are required to maximise the friction developed by the tyre. On this basis, the author of this thesis believes that the high body slip control system can significantly improve the accuracy and stability of HSAVs operating at the limits of handling. To this end, pieces of evidence of traditional yaw rate-based stability systems achieving a sustained high body slip stabilisation have not been found in the literature, what reinforces the importance of the virtual sensing solutions introduced in the preceding sections and the novel contribution of the work described in this chapter.

The implementation of the virtual sensors and motion controllers introduced during this thesis in a real vehicle is discussed in the next chapter, where a comprehensive testing program with a fully instrumented vehicle and an AWD MAGV platform is presented.

Chapter 5

Vehicle Experiments

The vehicle experiments on tyre force virtual sensing and advanced motion control are presented in this chapter. In brief, the SiL and HiL results introduced in Chapters 3 and 4 motivated the execution of several industrial research activities with Jaguar Land Rover and ARRIVAL Software during the course of this thesis, Figure 5.1.

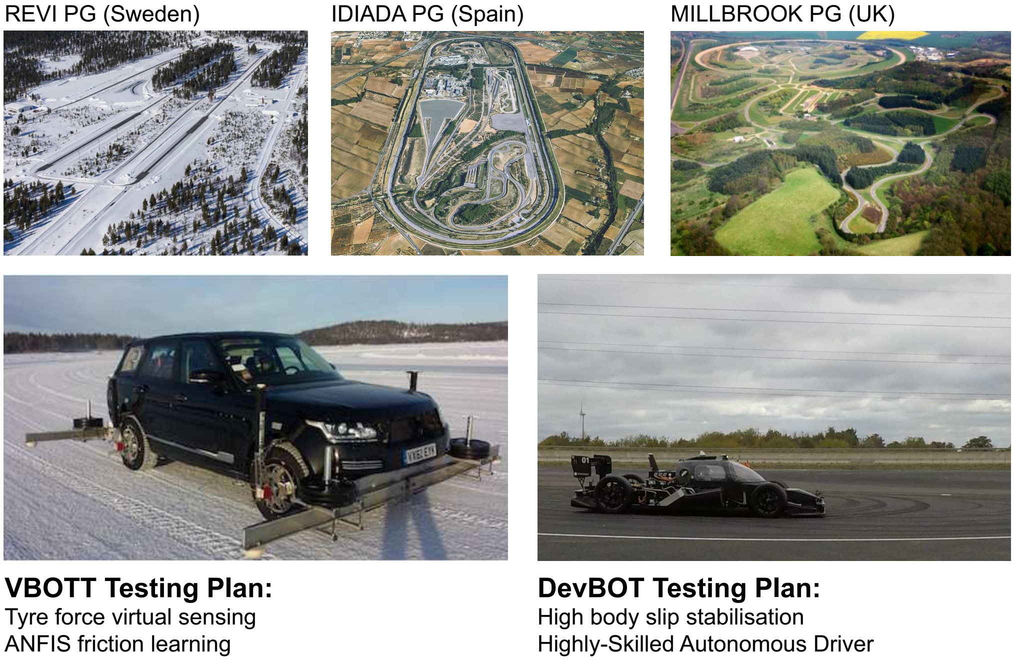

Figure 5.1: Industrial research activities were carried out with the VBOTT (JLR) and DevBOT (ARRIVAL & ROBORACE) platform. Field tests were executed in REVI (Snow), IDIADA (Dry tarmac) and MILLBROOK (Dry and wet tarmac).

Different simulation models have been employed during the course of this research (see Tables A.1 and A.2 for a comprehensive vehicle model summary). Expectedly, it would be prohibitive and impractical to use a different dedicated experimental vehicle platform to validate each section of this research. In order to achieve a trade-off between experimental validation scope and employed resources, two research platforms were used during the virtual sensing and motion control experiments. Specifically, the Vehicle-Based Objective Tyre Testing (VBOTT) platform of Jaguar Land Rover was selected for the virtual sensing experiments due to its comprehensive instrumentation and suitability to operate among different road terrains with different tyres. The ROBORACE DevBOT platform was chosen for the motion control experiments based on its multi-actuated layout and easiness to implement real-time driver-less controllers. The technical specifications of these vehicles are detailed in Appendix A.

Due to space limitations, only the most important achievements derived from these activities are provided in the following. Specifically, the first part of the chapter is dedicated to the research on tyre force virtual sensing and ANFIS friction learning done with the JLR VBOTT testbed [3]. The second part of the chapter introduces the research on high body slip stabilisation and highly-skilled autonomous driving carried out with the DevBOT MAGV of ARRIVAL Software and ROBORACE.

5.1 Virtual sensing experiments

The virtual tyre force sensing and friction learning experiments are presented in this section. Specifically, the tyre-model-less virtual sensing structure introduced in Chapter 3, Section 3.3, is adapted to the VBOTT testbed and verified in a comprehensive tyre characterisation program formed by tarmac and snow experiments. The vehicle testing plan was agreed with the tyre modelling department of Jaguar Land Rover following a systematic testing methodology characterised by the same open-loop standardised vehicle manoeuvres with the aim to reflect the sensitivity of the virtual sensor performance to different tyre models.

5.1.1 VBOTT experimental testbed

The VBOTT testing car is depicted in Figure 5.2. Essentially, the VBOTT is a heavily modified, fully instrumented vehicle used by JLR for in-vehicle tyre characterisation. The vehicle includes adjustable suspension to parametrise the inclination angle sensitivity, ballast adjustment for load sensitivity analysis, and constant-speed braking by means of an in-house developed braking control logic. With regards to the vehicle instrumentation, wheel force transducers (WFT) and high-accuracy GPS inertial motion units (IMU) are attached to each wheel in order to provide an accurate measurement of the three-axes tyre forces, tyre slip angles, and wheel orientation angles. Specifically, the GPS-IMU units provide the slip angles with an accuracy of 0.1 degrees, the camber angle with an accuracy of 0.03 degrees, and the wheel centre velocities with an accuracy of 0.05 kilometres per hour. Regarding the tyre longitudinal slips, these are computed from wheel speed measurements taken from high-accuracy encoders attached to the wheels and the wheel centre speeds measured by the GPS-IMU units. Apart from this, the vehicle instrumentation is completed with infrared tyre tread temperature sensors, tyre pressure sensors, tyre gas temperature sensors, CAN acquisition unit, ride height potentiometres, and wheel-centre laser height sensors. Additional details regarding the acquisition equipment or the control logic employed in this vehicle are omitted here due to confidentiality reasons.

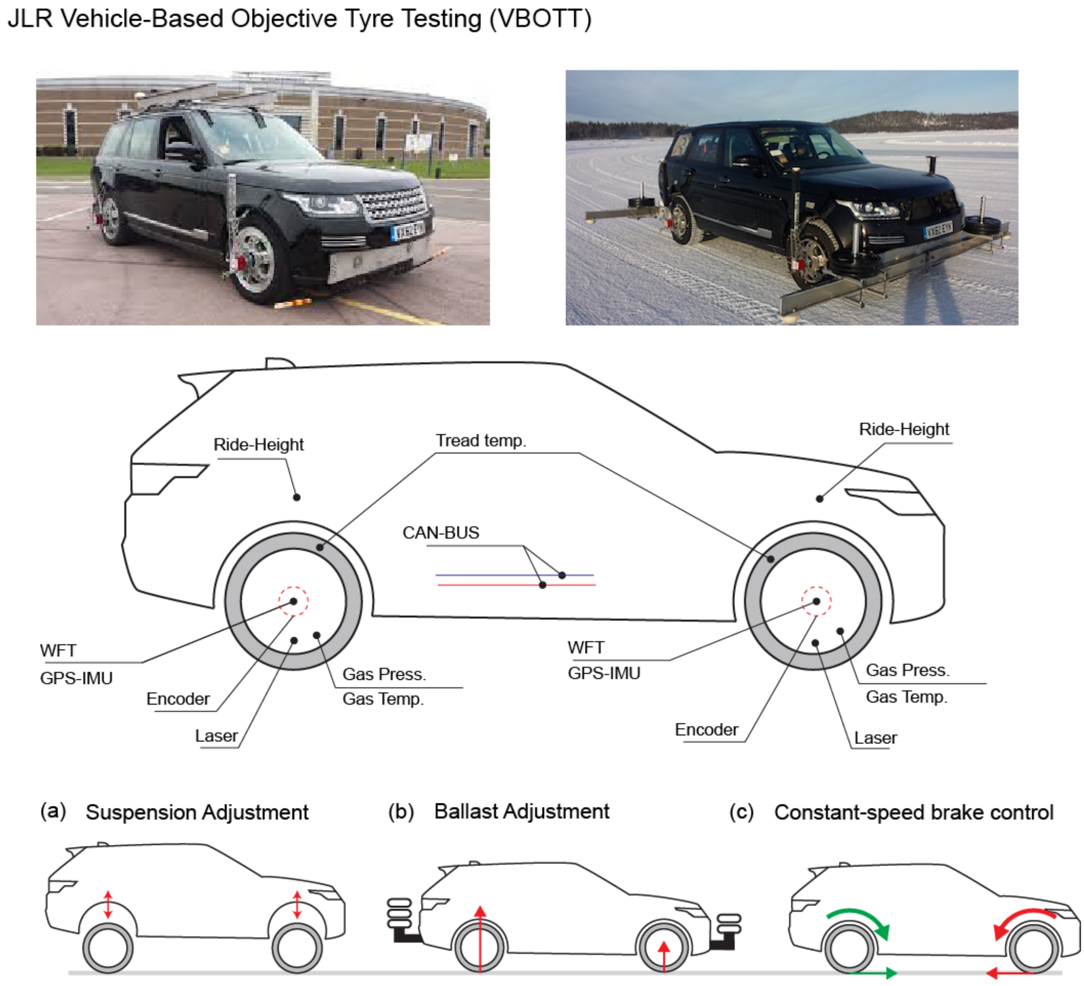

Figure 5.2: VBOTT testing vehicle. (a) suspension adjustment, (b) ballast adjustment and (c) constant-speed braking control [3].

The instrumentation described previously is prohibitive for commercially available platforms (VBOTT costs around 500K £). In what concerns in-vehicle tyre characterisation, it would be attractive to develop more affordable platforms in order to maximise the testing productivity and implement automated testing procedures [3]. With regards to future HSAVs, the exploitation of tyre force-based friction adaptation strategies (like those described in Chapter 4) at a mass scale would require inexpensive ways of measuring the tyre forces. The work described along this section was carried out with the aim to offer a cost-effective alternative to VBOTT, substituting the most expensive components (i.e. WFT) by tyre force virtual sensors [3].

5.1.2 Random Walk Virtual Sensor

The structure of the virtual sensor proposed in this section is illustrated in Figure 5.3. The virtual sensor is constructed adopting a modular approach where three state estimation blocks can be clearly differentiated: vertical tyre forces, longitudinal tyre forces and vehicle planar dynamics (axle lateral forces). A second block, automated tyre attribute extraction, is added to infer the tyre friction characteristics using an ANFIS-based approach. This structure is very similar to the tyre-model-less RW-EKF presented in Section 3.3.1. Due to the particularities of VBOTT, some modifications with respect to the preliminary design were necessary. These are introduced in the following.

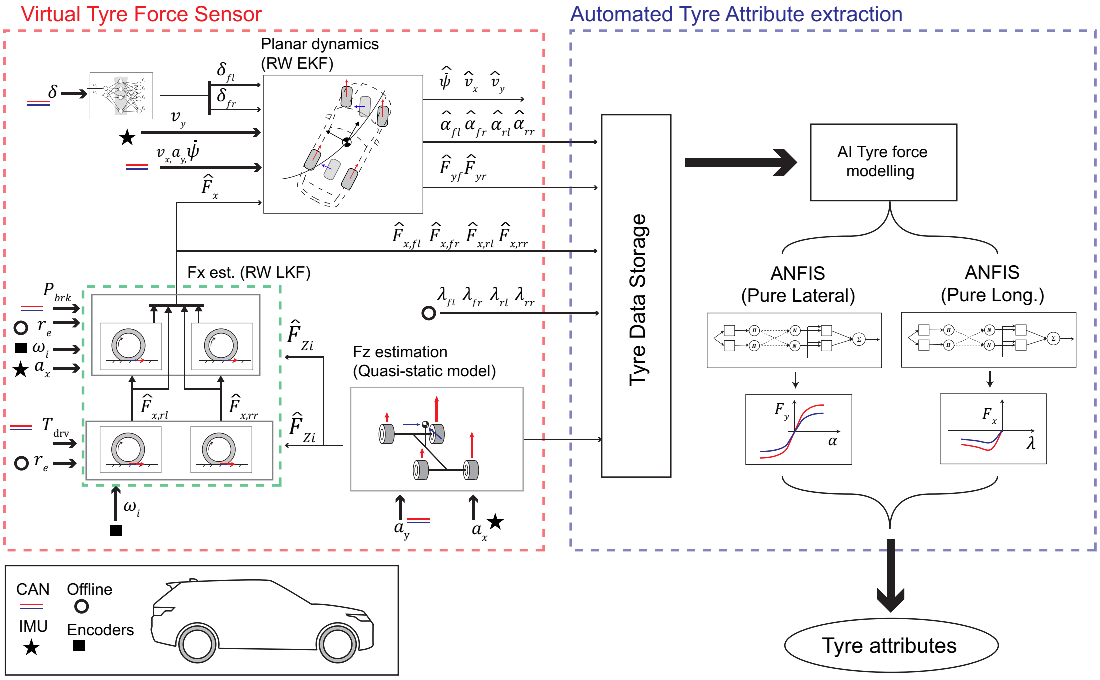

FIGURE 5.3: Structure of the random-walk tyre force virtual sensor [3].

Similarly to the structure introduced in Section 3.3.1, the tyre longitudinal forces are estimated adopting a wheel rotating dynamics-based LKF. In this case, a distinction is made between the approach used to estimate the rear and front tyre forces. This design is motivated by the special characteristics of the testing vehicle, Figure 5.2, which brakes only with the front wheels during pure-longitudinal-slip tyre characterisation tests. The rear longitudinal forces are estimated using the random-walk LKFs introduced in Section 3.2.2. The estimation of the front longitudinal forces, on the other hand, is performed using a single LKF structure. In this case, the vector of states is formed by the wheel rotating velocities and longitudinal forces of the front axle wheels $\mathbf{X_{LKF,f}} = \{\omega_{fl}, F_{x,fl}, \omega_{fr}, F_{x,fr}\}$, and the vector of inputs is formed by the individual braking torques $\mathbf{U_{LKF,f}} = \{T_{brk,fl}, T_{brk,fr}\}$. A pseudo-measurement of the front axle braking force is added to the measurement vector $\mathbf{Y_{LKF,f}} = \{\omega_{fl}, \omega_{fr}, F^*_{xf}\}$ in order to account for the braking torque uncertainties derived from changes on the braking pad friction coefficient [111]. The term F^*_{xf} is computed in the following manner:

$$F^*_{xf} = ma_x - (\hat{F}_{x,rl} + \hat{F}_{x,rr}) \tag{5.1}$$

where $\hat{F}_{x,rl}$ and $\hat{F}_{x,rr}$ are the rear longitudinal forces estimated in the rear LKF modules.

The axle lateral forces are estimated using the RW-EKF structure described in Section 3.3.1, revisited here for the sake of clarity. The vector of inputs is formed by the average angle steered by the front wheels and the estimated individual longitudinal forces $\mathbf{U_{EKF}} = \{\delta, \hat{F}_{x,i}\}$, and the vector of states by the vehicle planar velocities, yaw rate, and axle lateral forces $\mathbf{X_{EKF}} = \{v_x, v_y, \dot{\psi}, F_{yf}, F_{yr}\}$. Finally, the vector of measurements consists of the longitudinal velocity, yaw rate, lateral acceleration, and lateral velocity $\mathbf{Y_{EKF}} = \{v_x, \dot{\psi}, a_y, v_y\}$. With respect to the RW-EKF structure given in Section 3.3.1, a direct measurement of the lateral velocity was considered in order to benchmark the virtual tyre force sensors assuming that only the WFTs are replaced from the original VBOTT [3].

5.1.3 ANFIS friction learning

Following the friction learning concept introduced in Section 3.3.1.1, ANFIS structures are adopted to fit a nonlinear two-dimensional force versus slip curve. This is proposed as an automated approach that could permit the extraction of relevant tyre attributes from estimated data in a simple and straightforward manner. This approach may be particularised for the lateral or longitudinal force case depending on the amount of data available. In particular, pure lateral and pure longitudinal slip cases were evaluated during the course of this research. As can be observed in Fig. 5.4, the tyre attribute extraction procedure proposed in this work consists of three major steps.

In step 1, the input (e.g. tyre lateral slip, α) and output (e.g. tyre lateral force, F_y) data are gathered. This situation may correspond to the acquisition and concatenation of data from a set of manoeuvres executed in a certain vehicle configuration. After that, in step 2, the ANFIS learns the tyre force curve following a hybrid learning algorithm based on a combination of the gradient and Least Squares Estimate (LSE) methods [75]. In the third step, relevant tyre metrics are extracted from the trained ANFIS structure. Peak tyre force, tyre slip at which maximum force is developed, or tyre stiffness at different tyre slips are examples of valuable tyre metrics that can be easily extracted following this approach.

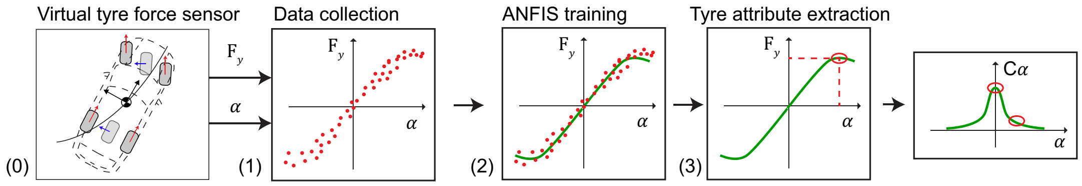

Figure 5.4: ANFIS tyre characterisation module [3].

5.1.4 Results

In order to assess experimentally the virtual sensing and friction learning approaches introduced in the previous paragraphs, the testing program presented in Table 5.1 was carried out with VBOTT.

Table 5.1: In-vehicle tyre characterisation program (IDIADA and REVI) [3].

Tyre	Proving Ground	Tyre Size	Tyre	Proving Ground	Tyre Size
1	IDIADA	245/50R20	4	IDIADA	295/35R22
2	IDIADA	265/40R22	5	IDIADA	245/45R20
3	IDIADA	265/45R21	6	REVI	255/55R20

In brief, a complete in-vehicle tyre characterisation program was completed with 5 different tyres in IDIADA proving ground (Spain) and with 1 tyre in Revi winter testing facilities (Sweden). After that, the virtual sensor was implemented in Simulink using a discretisation time of 1 ms. A channel BUS was created with the signals acquired with the experimental vehicle and the channels presented in Table 5.2 were fed into the virtual sensor model in order to estimate the tyre forces in the three axes and the individual tyre lateral slips.

The average angle steered by the front wheels (δ) was taken directly from the vehicle CAN-BUS. A linearised steering ratio factor was used to compute this variable from the steering wheel angle signal. An artificial NN was adopted to calculate the exact angle steered by each individual front wheel (δ_{fl}, δ_{fr}) from the previous signal, thus avoiding the complexity derived from adding an analytical steering kinematic model.

The individual steering angles necessary to train the NN structure were reconstructed offline for different steering manoeuvres using a vehicle planar kinematics model. To avoid extrapolation issues derived from different suspension and steering system operating points, different NNs were trained for different vehicle configurations (i.e. ride height). The lateral velocity (v_y) was calculated as the average value of the individual lateral velocities measured by the IMUs attached to the rear wheels ($v_y = \frac{1}{2}(v_{y,rl} + v_{y,rr})$) and translated to the vehicle centre of gravity by means of the CAN yaw rate signal. These steps will be eliminated in future investigations by attaching a fifth IMU unit close to the vehicle centre of gravity. The wheel rotational velocity signals (ω) were taken directly from the high-accuracy wheel encoders. Additional investigations to remove these sensors and use the signals provided by the CAN-BUS will be explored in the future.

Table 5.2: Input signals of the virtual sensor [3].

Signal	Nomenclature	Class	Module
AVG. Steering wheel angle	δ	CAN	INPUT-Steering NNs
FL Steering wheel angle	δ_{fl}	NN	INPUT-EKF
FR Steering wheel angle	δ_{fr}	NN	INPUT-EKF
Lateral velocity	v_y	IMU	MEASUREMENT-EKF
Longitudinal velocity	v_x	CAN	MEASUREMENT-EKF
Lateral acceleration	a_y	CAN	MEASUREMENT-EKF
Yaw rate	$\dot{\psi}$	CAN	MEASUREMENT-EKF
Wheel velocity	ω	ENCODER	MEASUREMENT-$LKF_{f,r}$
Brake pressure	P_{brk}	CAN	INPUT-LKF_f
Longitudinal acceleration	a_x	IMU	INPUT-LKF_f
Rear wheel driving torque	T_{drv}	WFT	INPUT-LKF_r

The estimated braking torques were computed from the individual brake pressures acquired from the vehicle CAN-BUS using a proportional braking torque model ($T_{brk,i} = P_{brk,i}K_{brk}$). As evidenced in previous works [111], the gain K_{brk} presents some fluctuations caused by the change of the brake pad friction coefficient. In brief, during braking events the brake pad temperature can increase significantly, inducing a notable change on the brake linings friction properties [113]. Such variations may be captured by a relevant model dependent on factors like the brake pad chemical content or sliding speed (e.g. Ostermeyer model [103]). As this approach requires further calibration steps with experimental data, in this work a simpler solution is adopted. Specifically, the longitudinal acceleration a_x was added to the virtual sensing structure in order to counteract the errors introduced by the previous variations (Section 5.1.2). This channel was calculated as the average value of the rear IMU signals. Regarding the driving torque necessary to compute the rear longitudinal forces, the traditional approach found in the literature is to estimate this input from the engine driving torque using the gear and differential ratios [11]. In this case, the vehicle driveline architecture (torque converter) complicated the application of the previous approach. As additional information regarding the torque converter characteristics was not available, the driving torque was extracted directly from the WFT signals. An enhanced data-based model to calculate the previous signal from the engine drive torque is proposed for future refinements of the virtual sensor. On the other hand, this problem may be resolved in the future with the adoption of Electric Motors (EM) on the testing VBOTT.

Finally, in order to establish a consistent comparison with current JLR in-vehicle tyre characterisation methods, individual longitudinal wheel centre velocities were considered ($v_{x,i}$) to compute the individual longitudinal slips. An alternative approach using a single ground velocity signal provided by a central IMU unit will be studied in the future. Significant differences are not expected for the pure longitudinal slip cases presented in this section. The tyre forces and the wheel orientation angles and speeds are measured with different sensors. Due to the mounting positions of these sensors their coordinate systems will be affected differently by the kinematics of the suspension. It is therefore of utmost importance to convert all output signals, in each time step, to a common coordinate system. In this case, an ISO W [123] system was used to reference all the forces to the ground plane using the wheel orientation angles measured by the GPS-IMU units. Additional details regarding the virtual sensor implementation are omitted here due to space limitations and can be consulted in [3].

5.1.4.1 Lateral dynamics manoeuvres

The results presented in this section were obtained with the vehicle calibrated in LOW and STANDARD ride height conditions and 0 kg ballast, Figure 5.2. Specifically, the virtual sensor calibration (steering system NNs training and quasi-static weight transfer model) was carried out using the data extracted from different manoeuvres executed in the corresponding vehicle configuration and with a single set of tyres. In order to extend the operating envelope of the virtual sensor, this calibration process may be repeated for a wider range of standardised vehicle configurations (ride height and ballast) and implemented adopting a configuration-scheduling approach. After that, the LKF and EKF structures were tuned following a metaheuristic (Genetic algorithm, [62], Section 3.2.3) optimisation approach. Once the Kalman filter was tuned, the same settings were fixed and remained unaltered for the six tyres characterised in the following, Table 5.1.

In order to characterise the tyre's steady-state lateral responses, several ramp steering manoeuvres were performed in IDIADA, Fig. 5.5.

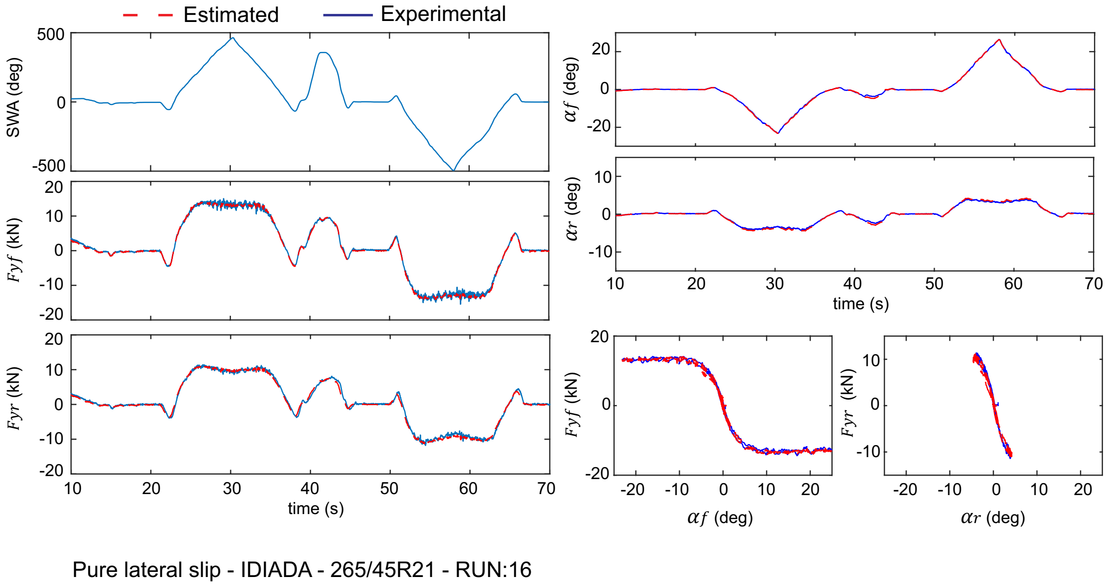

FIGURE 5.5: Estimated axle forces and slip angles for a tyre of size 265/45 R21 tested in tarmac conditions (IDIADA) [3].

These manoeuvres were executed with the VBOTT vehicle in LOW ride height and fitted with the tyres 1-5, Table 5.1. As can be seen in the sample run depicted in Figure 5.5, the axle lateral forces as well as the axle lateral slips are approximated accurately by the proposed virtual sensor. The axle lateral slips were calculated as the average value of the individual tyre lateral slips ($\hat{\alpha}_f = (\hat{\alpha}_{fl} + \hat{\alpha}_{fr})/2$). Tyres of different dimensions and from different manufacturers were tested in order to verify the suitability of the virtual sensor to infer slight performance variations between tyres. In addition, the tyre pressures were alternated between 3.3, 2.6, and 2.1 bar in order to assess the virtual sensor robustness to different tyre pressures. In total, 22 tests were executed with the experimental vehicle in order to generate the axle force versus axle lateral slip graphs portrayed in Figures 5.6 and 5.7. Due to space limitations, only the front axle curves are depicted in the following. After simulating each test run on the virtual sensor, the data corresponding to the steering ramp inputs ($t \approx 20 - 30$ s and $t \approx 50 - 60$ s, Fig. 5.5) were cropped and concatenated to form a new ANFIS training dataset. A single training dataset was generated for each tyre. The ANFIS-based tyre attribute extraction approach presented in Section 5.1.3 was implemented in *Matlab* by means of the *anfis.m* function. In particular, several pure longitudinal and pure lateral slip experimental tests were executed with a single tyre in order to determine in a systematic manner the number of membership functions that best fit a generic tyre force versus slip curve.

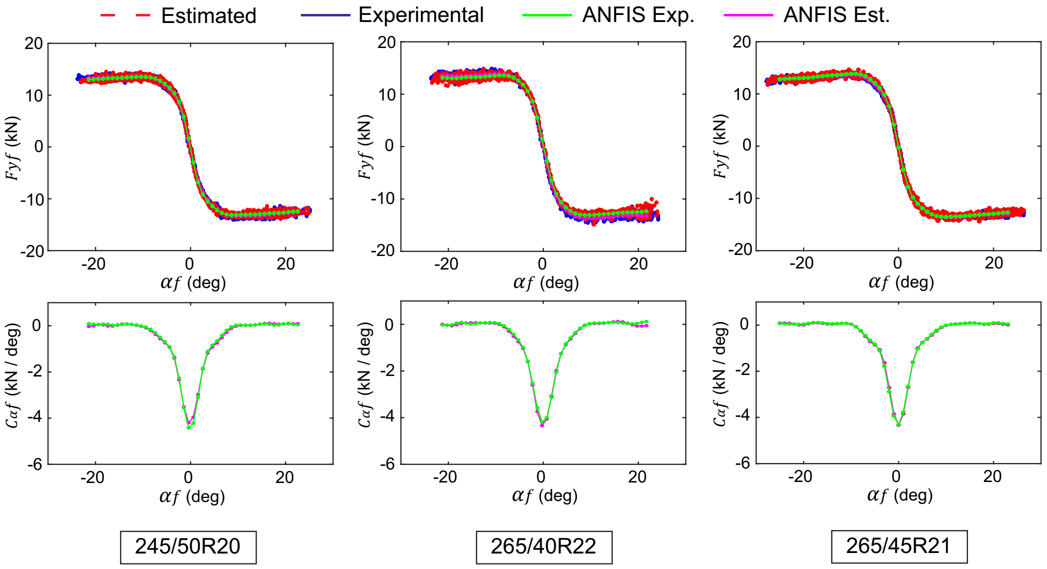

Figure 5.6: Axle lateral force versus lateral slip graphs obtained for tyres 1-3. ANFIS structures trained with experimental and estimated data [3].

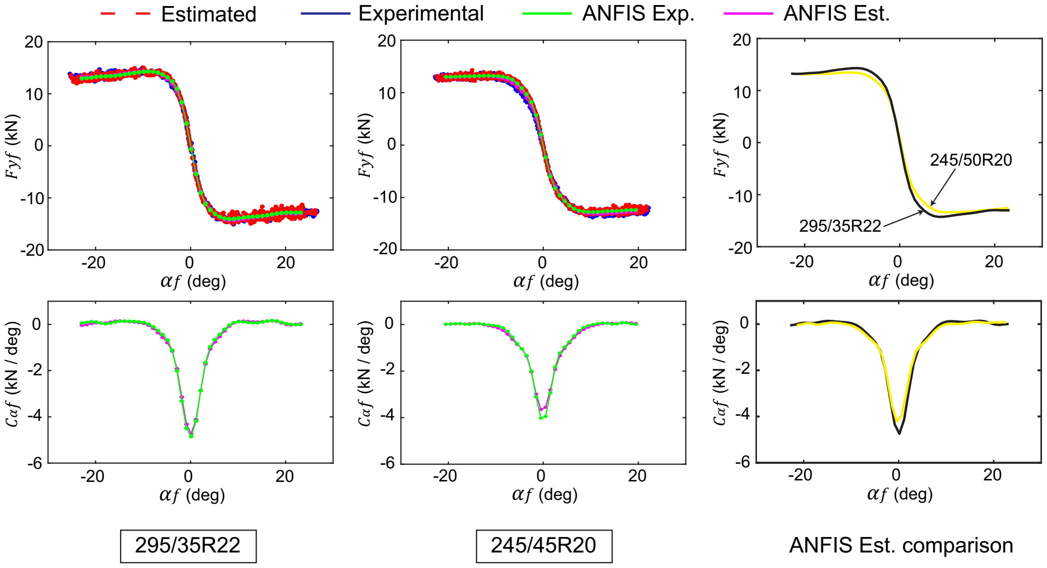

Figure 5.7: Axle lateral force versus lateral slip graphs obtained for tyres 4-5. As can be noticed in the "ANFIS Est. comparison", a significant difference between tyres 1 and 4 is evidenced by the ANFIS structure trained with estimated data [3].

Finally, this number was set to 5 to minimise potential overfitting issues, and the maximum number of training epochs was limited to 300. These parameters provided average training times of 1.0 s in a computer *Dell precision M6800* for 1000-sample training datasets. For consistency, the same ANFIS parameters were maintained during the complete tyre characterisation program presented in Table 5.1. Once the ANFIS training was finalised, the extraction of relevant tyre attributes was carried out. In this case, the axle lateral stiffness C_α was obtained differentiating the ANFIS output at different slip angles. These metrics were selected as have a great influence on key vehicle attributes like the self-steering behaviour (e.g. understeer gradient) or the vehicle stability (e.g. yaw damping). The relative errors $e_{C_\alpha} = |(C_{\alpha,est} - C_{\alpha,meas})/C_{\alpha,meas}|$ derived from the estimated axle stiffness values are presented in Table 5.3.

Table 5.3: Relative errors (%) of the axle stiffness values obtained from the ANFIS trained with estimated data [3].

Tyre	$e_{C_\alpha}(-4deg)$	$e_{C_\alpha}(-2deg)$	$e_{C_\alpha}(0deg)$	$e_{C_\alpha}(2deg)$	$e_{C_\alpha}(4deg)$
1-245/50R20	3.06	0.98	5.38	2.11	6.88
2-265/40R22	2.93	3.76	3.21	2.05	0.03
3-265/45R21	4.36	6.28	0.57	1.87	3.94
4-295/35R22	4.32	5.21	2.74	0.59	8.57
5-245/45R20	0.80	1.80	8.21	0.48	7.58

Overall, the average error is approximately 3.5%, with all the individual error values lying below the 10% band. As shown in Figure 5.7, the virtual sensor can detect subtle differences between tyres rather than providing just a generic force versus slip curve. The accuracy of the proposed approach is also evidenced in Table 5.4, where the Normalised Root Mean Square Error (NRMSE) values of the axle lateral forces and axle lateral slips are given (the NRMSE is calculated for the training dataset used to train the ANFIS structures). In this case, the errors are kept close to the 5% band.

Table 5.4: NRMSE of the estimated axle lateral tyre forces and axle lateral slips [3].

Tyre	$e_{F_{yf}}$	$e_{F_{yr}}$	e_{α_f}	e_{α_r}
1-245/50R20	2.47	4.12	1.59	5.52
2-265/40R22	4.11	5.39	0.66	4.98
3-265/45R21	2.41	4.58	0.93	5.43
4-295/35R22	2.78	4.71	0.83	6.44
5-245/45R20	2.48	4.02	2.36	4.61

Additional tests were performed in snowy conditions (Revi facilities) with the VBOTT vehicle in STANDARD ride height and fitted with a tyre 255/55R20. In this case, a set of constant-speed sinusoidal steering manoeuvres were performed to extract the axle lateral force versus slip curves depicted in Figure 5.8. As can be seen in this figure, the forces are accurately approximated by the proposed virtual sensing structure. Of particular interest is the fact that accurate results have been obtained for drastically-different friction conditions without altering the virtual sensor tuning. Moreover, both ANFIS structures (trained with estimated and trained with experimental data) match well the cloud of force versus slip data points. Due to severe testing limitations, only one tyre was characterised in these testing conditions.

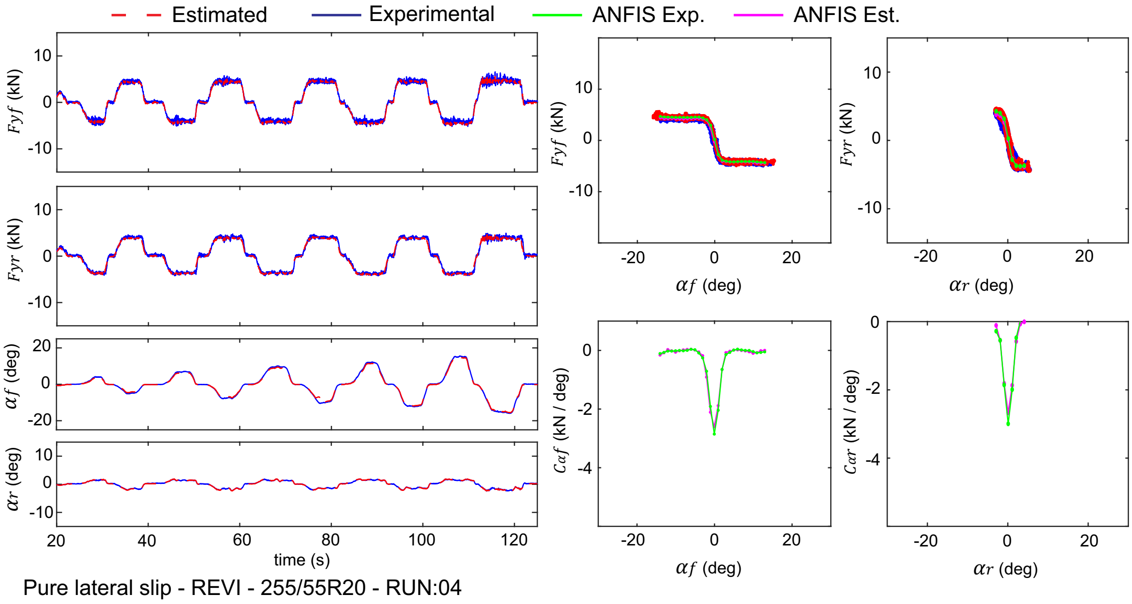

Figure 5.8: Axle lateral force versus lateral slip graphs obtained for a tyre 255/55R20 characterised in snow (Revi facilities, Sweden) [3].

5.1.4.2 Longitudinal dynamics manoeuvres

The tyre's longitudinal steady-state responses were characterised by means of controlled ramp-like braking torques applied to the front wheels. A positive driving torque was applied to the rear wheels in order to maintain a constant speed during the execution of the braking manoeuvre, Figure 5.2-c. For consistency, the virtual sensor tuning used in the previous cases was maintained during the execution of these tests. In total, 29 braking manoeuvres were performed in IDIADA with the VBOTT vehicle in STANDARD ride height, obtaining the longitudinal force versus longitudinal slip plots depicted in Figures 5.9 and 5.10.

Once again, ANFIS structures were trained to approximate the cloud of force versus slip points. For consistency, the ANFIS parameters detailed in the previous section (e.g. number of membership functions) were maintained. Apart from this, negligible asymmetry between the left and right tyres was assumed, and a single training dataset was formed for each tyre by concatenation of the left and right tyre responses (i.e. $F_{x,f} = [F_{x,fl}, F_{x,fr}]$, $\lambda_f = [\lambda_{fl}, \lambda_{fr}]$). Regarding tyres exhibiting an asymmetrical behaviour (e.g. outside tyres), significant differences were not noticed. In this case, the longitudinal tyre stiffness was extracted differentiating the ANFIS output at different longitudinal slip values. As can be observed in these figures, the estimated forces matched well the experimental forces measured by the WFTs. Moreover, significant differences in the longitudinal stiffness estimates were noticed between tyres 4 and 5, evidencing the suitability of the proposed approach to detect slight differences between tyres. As occurred in the lateral stiffness case, the accuracy of the longitudinal stiffness values C_λ provided by the ANFIS networks trained with state estimated data were quantified by means of the relative errors presented in Table 5.5.

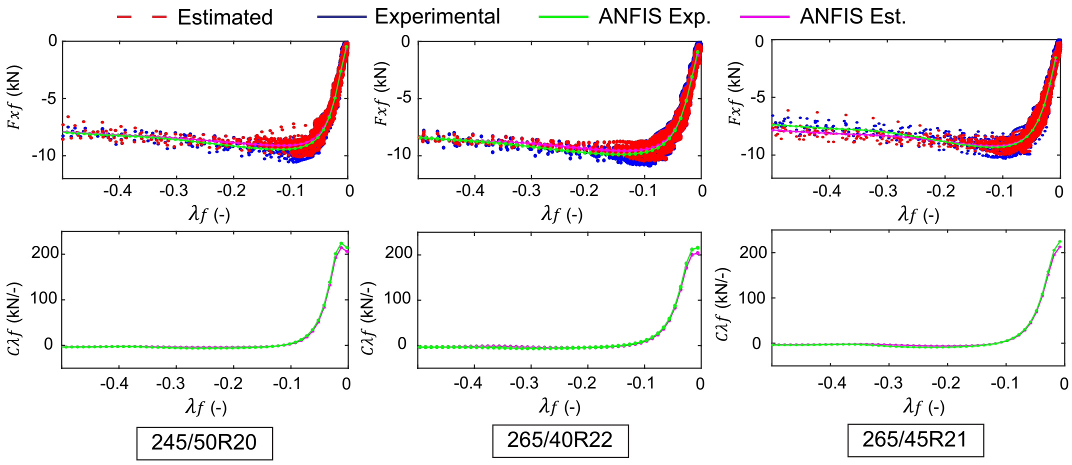

FIGURE 5.9: Tyre longitudinal force versus longitudinal slip graphs obtained for tyres 1-3. ANFIS structures trained with experimental and estimated data [3].

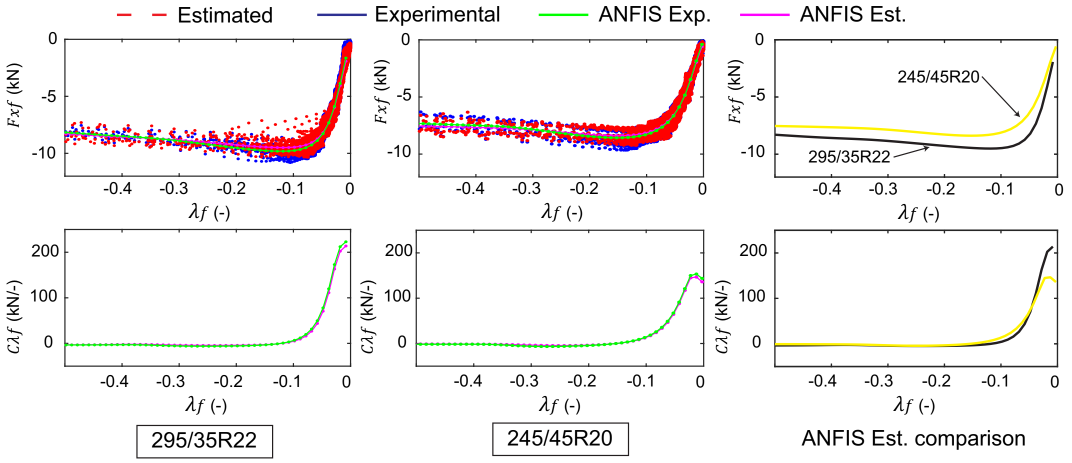

FIGURE 5.10: Tyre longitudinal force versus longitudinal slip graphs obtained for tyres 4-5. As can be noticed in the "ANFIS Est. comparison", a significant difference between tyres 4 and 5 is evidenced by the ANFIS structure trained with estimated data [3].

Overall, low error values (below the 10 % band) were obtained for the majority of slip values considered. For high slip values (0.08), the relative error is magnified due to the reduced normalising longitudinal stiffness value. The NRMS errors of the estimated tyre longitudinal forces are presented in Table 5.6. Once again, values below the 5% error band were obtained for the tyres characterised in tarmac conditions.

Finally, additional braking manoeuvres were executed in snowy conditions (Revi facilities, Sweden) with the VBOTT in STANDARD ride height and running on tyres

TABLE 5.5: Relative errors (%) of the tyre longitudinal stiffness values extracted from the ANFIS networks trained with estimated data [3].

Tyre	$e_{C_\lambda}(-0.02)$	$e_{C_\lambda}(-0.04)$	$e_{C_\lambda}(-0.06)$	$e_{C_\lambda}(-0.08)$
1-245/50R20	4.52	5.28	9.29	15.99
2-265/40R22	5.35	4.77	6.60	11.17
3-265/45R21	4.84	4.20	6.24	9.81
4-295/35R22	4.82	7.46	12.41	18.35
5-245/45R20	3.64	3.60	5.20	6.80

TABLE 5.6: NRMSE of the estimated tyre longitudinal forces [3].

Tyre	$e_{F_{x,fl}}$	$e_{F_{x,fr}}$
1-245/50R20	2.46	2.45
2-265/40R22	2.57	2.38
3-265/45R21	2.38	3.60
4-295/35R22	2.96	3.19
5-245/45R20	2.19	2.11

255/55R20. For consistency, the virtual sensor tuning was maintained. Similar ramp-like braking inputs were performed in order to generate the graphs depicted in Figure 5.11.

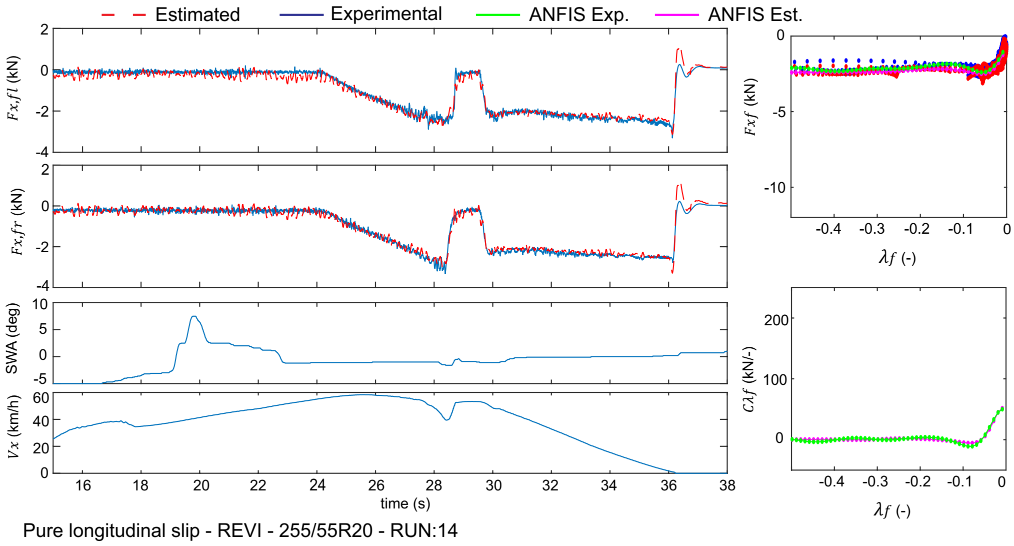

FIGURE 5.11: Longitudinal force versus longitudinal slip graphs obtained for a tyre 255/55R20 characterised in snow (REVI, Sweden) [3]

Overall, accurate results are obtained with the proposed virtual sensor. In relation to the low-mu tyre characterisation, the author of this thesis believes that the current research accomplishments in wheel slip control based on EMs working in regenerative braking mode and Decoupled Electro-Hydraulic Brake (DEHB) system architectures [117, 116] can help to improve the tyre characterisation process in low-adherence conditions. In particular, the reason for the interest on in-wheel EMs is twofold: First, a closed-loop tracking of the desired set of longitudinal slip values may be accomplished adopting a regenerative-based braking strategy (e.g. implemented by means of Sliding Mode Control, SMC [117]). Second, a very accurate estimation of the braking torque provided by the EM can be obtained directly from the EM energy management system, which will definitely contribute to ensuring an accurate tyre force estimate. These considerations will be carefully studied in order to determine future VBOTT electrification steps.

5.1.4.3 Individual tyre lateral forces

In order to obtain the individual tyre lateral forces from the vehicle planar dynamics it is necessary to incorporate additional equations to make the system given by expressions (3.1-3.3) solvable. The traditional approach found in the literature is to apply the vertical load proportionality principle described in Section 3.2.2, which consists of the expressions,

$$\hat{F}_{y,fl} = \hat{F}_{y,f} \frac{\hat{F}_{z,fl}}{(\hat{F}_{z,fl} + \hat{F}_{z,fr})}, \quad \hat{F}_{y,fr} = \hat{F}_{y,f} \frac{\hat{F}_{z,fr}}{(\hat{F}_{z,fl} + \hat{F}_{z,fr})} \tag{5.2}$$

where $\hat{F}_z$ is the estimated vertical force. The bias Ω_{bias} introduced in Section 3.2.2 was not considered in these expressions as *a priori* information regarding the tyres being characterised was not available. This principle was applied to the results presented in Section 5.1.4.1, and the individual tyre lateral force versus slip plots presented in Figure 5.12 were obtained. As shown in this figure, the proposed vertical proportionality approach introduces some inaccuracies in the forces estimated during severe loaded (b) and unloaded conditions (c). Overall, the author of this thesis believes that the exclusive use of the vertical loads is insufficient to infer (with the accuracy required by in-vehicle tyre characterisation) the individual tyre lateral forces from the axle forces due to the nonlinear load sensitivity effects exhibited by the tyres [104]. In particular, an enhanced virtual sensing structure making use of strain-based measurements on the steering system could help to sense more accurately the lateral load asymmetries, camber thrust, or asymmetrical forces derived from the use of outside tyres (e.g. plysteer or conicity). Such an approach will be explored in the future.

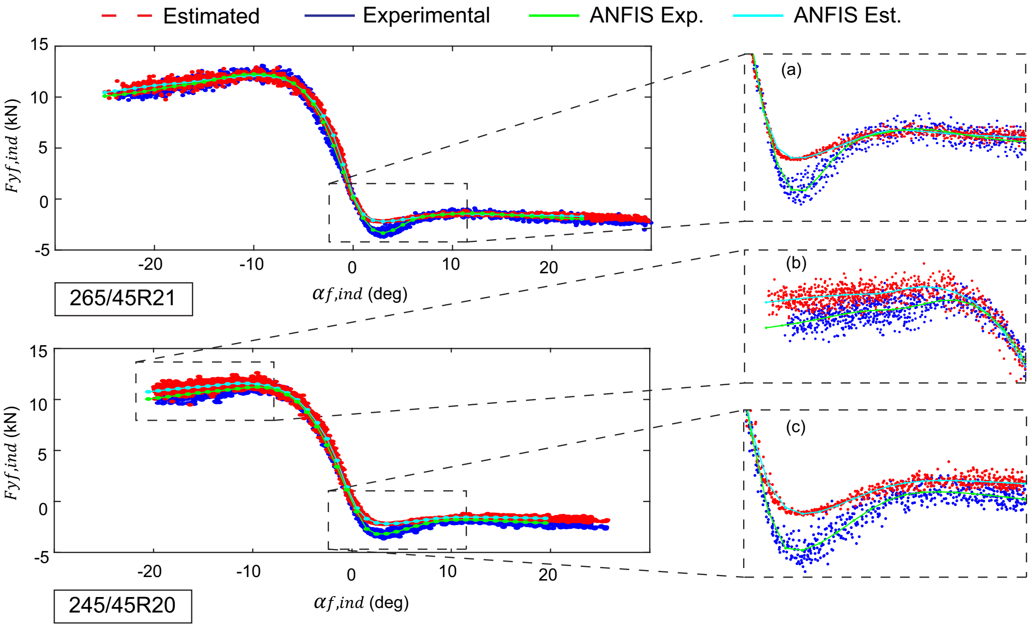

FIGURE 5.12: Individual tyre lateral force versus lateral slip graphs. The inaccuracies introduced by the vertical load proportionality principle can be noticed in the zoom details (a,b and c) [3].

5.1.5 Summary of virtual sensing experiments

The tyre force virtual sensing experiments have been presented in this section. Specifically, the random-walk EKF derived in Chapter 3 has been benchmarked against the tyre force measurements provided by the fully instrumented VBOTT platform in a wide range of lateral and longitudinal manoeuvres performed in dry tarmac and snowy conditions. Moreover, in order to assess the validity of the tyre-model-less approach under tyres of different size, 6 different tyres have been characterised in this section. These experimental results were generated as a consequence of an intensive in-vehicle tyre testing program carried out in IDIADA proving ground and REVI facilities.

Following the machine learning-based approach introduced in Chapter 3, the tyre force estimates provided by the virtual sensor have been used in an ANFIS-based friction learning structure to infer the longitudinal and lateral friction characteristics of each tyre. In order to quantify the accuracy of this approach, relevant tyre stiffness metrics have been extracted and compared to the reference measurements provided by the wheel force transducers. The results given in this section evidenced the ability of the virtual sensor to provide accurate estimates of the individual longitudinal and axle lateral forces in pure lateral and longitudinal slip conditions. Overall, the proposed solution exhibited good robustness to different tyre friction characteristics, achieving similar error levels for all the tyres considered during the testing activities. With regards to the individual tyre lateral forces, additional research efforts are still needed in order to improve the accuracy of these estimates due to the limitation of the vertical load proportionality principle. In essence, it is expected that aspects like the nonlinear load sensitivity effect, differential longitudinal slip or tyre asymmetry will require the incorporation or additional measurements (e.g. strain-based) in order to capture the lateral load asymmetries. These considerations are proposed for future extensions of this research, Chapter 6.

Finally, as mentioned previously, the virtual sensor was run at faster-than-real-time simulation rates adopting a 1 ms discrete time in a computer Dell precision M6800 equipped with an Intel i7-4800MQ processor. Similar virtual sensing structures have been implemented by the author of this thesis in different rapid-prototyping ECUs and major difficulties regarding real-time implementation have not been identified to this end.

5.2 Advanced motion control experiments

The experiments carried out with the MAGV DevBOT platform are presented in this section. In particular, high body slip stabilisation experiments are presented first, followed by the description and experimental validation of a highly-skilled autonomous driver model.

5.2.1 DevBOT MAGV platform

The driver-less experiments discussed in this section were performed with the DevBOT vehicle illustrated in Figure 5.13. Essentially, DevBOT is a MAGV platform designed and built by ROBORACE and ARRIVAL with the aim to speed up the development of autonomous driving technology in a controlled environment (e.g. race track). The vehicle is equipped with four EMs capable of providing a total peak power of 450 kW during driving conditions and 70 kW during regenerative braking. Each motor can deliver a maximum torque of 200 Nm and is connected to the wheels by means of an individual gearbox. Moreover, the motors can be controlled independently in drive and regenerative modes, Figure 5.13-a. In addition to the regenerative braking, the vehicle incorporates an electro-hydraulic braking (EHB) unit that permits independent friction braking on the front and rear axles, Figure 5.13-b. Apart from this, in order to facilitate the vehicle operability and the adoption of machine-learning-based strategies, the vehicle can be driven in manual or fully AI modes. The steering inputs demanded by the system during AI operation are realised by a steering control unit, Figure 5.13-c. DevBOT is equipped

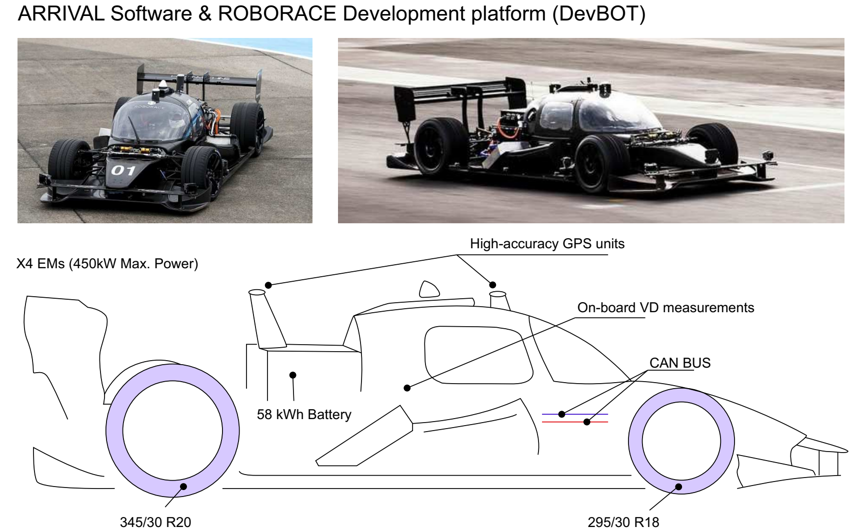

(a) Independent torque control (b) Front/rear braking control (c) Steer control

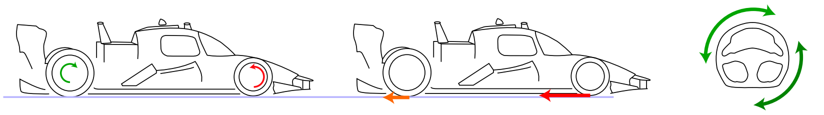

Figure 5.13: DevBOT platform. (a) Independent AWD torque control, (b) independent front-rear braking control and (c) steering control.

with several VD onboard sensors (individual wheel speed, chassis accelerations, yaw rate) to enable the implementation of motion control functions. These measurements, as well as relevant signals supplied by the Dynamic Control Unit (DCU), can be easily accessed on the vehicle CAN-BUS. The vehicle instrumentation is completed with the systems that form the high-level perception layer (LiDARS, Cameras and differential GPS). The differential GPS information is sent to the rest of vehicle systems using User Datagram Protocol (UDP) messages. Additional information regarding the LiDARS or Cameras is omitted here due to confidentiality reasons. The steps executed to implement the motion control strategies described in this thesis are summarised in Figure 5.14.

The stages (0) - synthesised vehicle model, (1) - SiL testing and (2) - HiL testing already introduced in the previous chapter have been depicted for the sake of clarity. After debugging and pre-calibrating the models in the HiL, a sign-off is performed in the virtual environment. If the sign-off is positive, the model progresses to stage 3, track experiments. In order to avoid DevBOT IP disclosure, all the implementation and fine-tuning work are carried out exclusively within a software developer “ACCESSIBLE” layer. Specifically, the Real-Time (RT) target machine receives all the feedback required by the model from a motion control CAN-BUS and via UDP communication. At each time step, SPEEDGOAT writes an input request message on the motion control CAN-BUS. The rest of vehicle ECUs and communication systems required to realise the input requests and write the VD sensor readings onto the motion control CAN-BUS

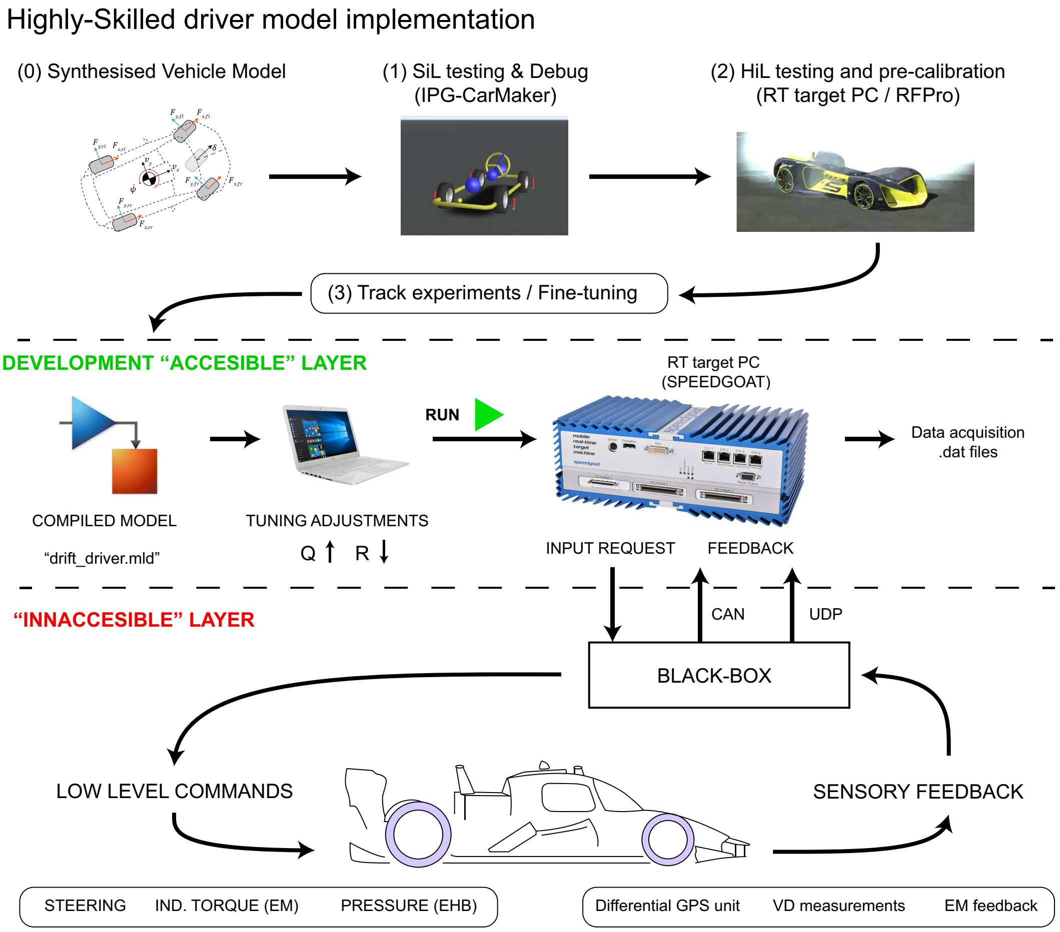

Figure 5.14: Scheme of the implementation steps performed to run the Highly-Skilled driver model. The software development work is carried out in the DEVELOPMENT “ACCESSIBLE” LAYER.

are assumed to be contained in a “black-box” not accessible by the model developer (“INACCESSIBLE” layer). As mentioned in the previous chapter, AI-mode is enabled with the vehicle in standstill conditions. A handshake between SPEEDGOAT and the “black-box” is performed and, if successful, the model starts to send input requests. Finally, the vehicle is stopped once the target path is completed or a maximum running time condition is met. In addition, the manoeuvre can be aborted by the model fail-safe rules, by the “black-box” if the emergency stop conditions are triggered, or remotely by the engineering crew.

5.2.2 High body slip stabilisation

The HiL experiments introduced in Section 4.2.4 were repeated with the real DevBOT-01 platform in Millbrook proving ground (UK). A shakedown session was performed first in UPPER-HEYFORD airfield (UK) to check that the feedback signals were acquired correctly by the model, Figure 5.15-top.

DB-01 / UPPER HEYFORD Shakedown (UK)

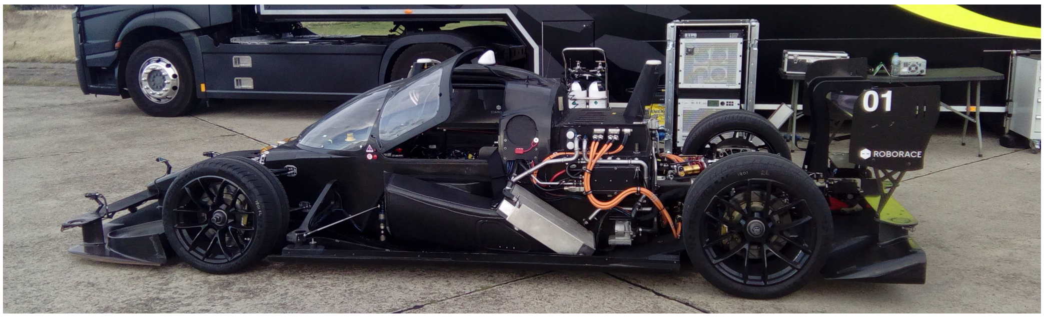

DB-01 / Open Loop Drift Stabilisation in MILLBROOK skidpad (UK)

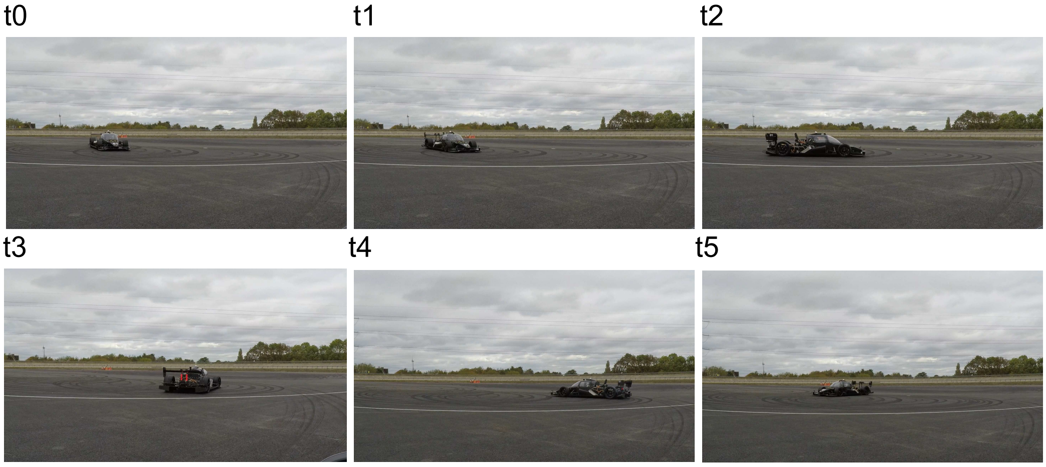

FIGURE 5.15: Top: DB01 in Upper-Heyford airfield (UK). Bottom: Frame sequence of a high body slip stabilisation test.

After that, the vehicle was subjected to a comprehensive testing program to verify the high body slip stabilisation ability of the constrained gain-scheduling LQR derived previously, Figure 5.15-bottom. Due to limitations on the available skidpad, the maximum tested radius was restricted to 25 metres. The target body slip angle was set to $|\beta_{ss}| = 40$ degrees for all the experimental manoeuvres discussed in this chapter. In addition, in order to maximise the testing productivity, the tarmac friction adaptation approach described in Section 4.3 was also tested during this session. The feedback required by the motion control system was taken from the vehicle CAN-BUS (wheel speed, chassis accelerations) and the high-accuracy differential GPS unit (planar dynamics velocities and yaw rate). Finally, the vehicle was set up in a nominal racing configuration similar to that employed in the HiL vehicle model. The difficulty of manually drifting the car in this setup was verified in a set of driving experiments in which the ROBORACE driver was unable to drift DevBOT.

The results corresponding to the 10 and 20 metres drift in dry tarmac are depicted in Figures 5.16 and 5.17.

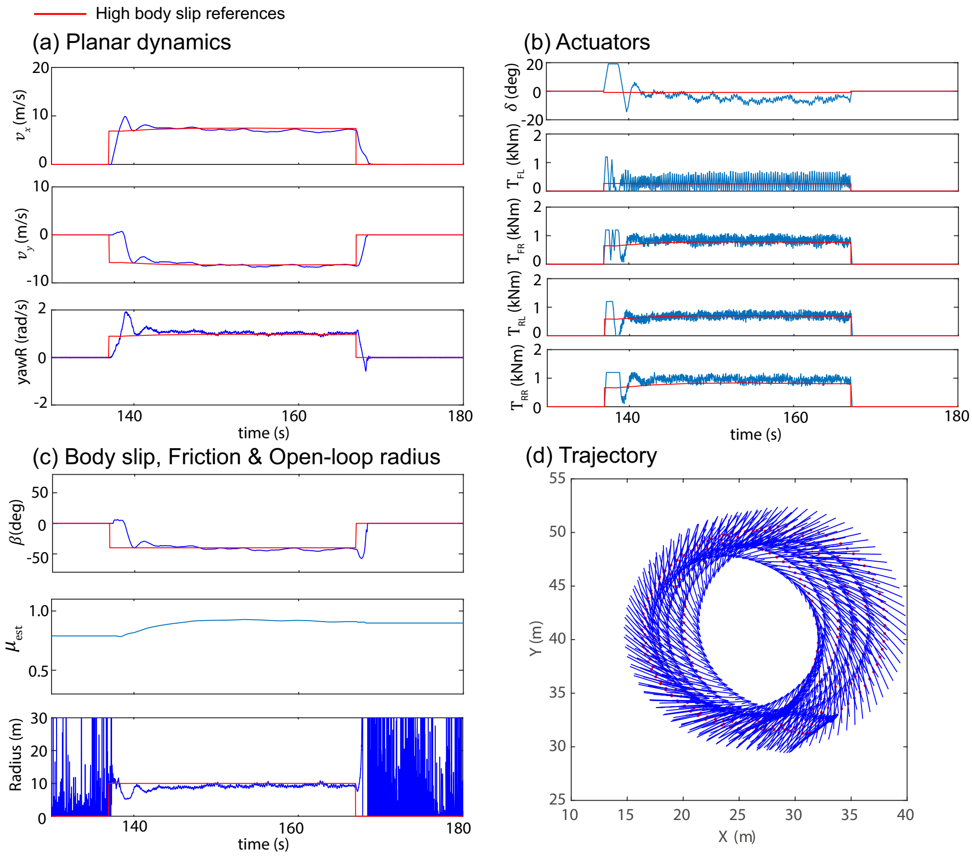

FIGURE 5.16: Test 2, R_{ss} = 10 metres high body slip stabilisation in dry tarmac. $\mu_{est,0} = 0.80$.

As can be seen in the 10 metres drift case, the system is able to track the reference states closely, Fig. 5.16-a, and convergence to the target body slip angle and reference radius is achieved quickly, Fig. 5.16-c. The radius described by the vehicle was computed from the vehicle planar states as $R = V/\dot{\psi}$. In addition, the steering angle and individual torques remained close to the feedforward inputs, Fig. 5.16-b, evidencing the validity of the synthesised model employed to derive the DES references. With regards to the friction compensation factor (μ_{est}), this increased steadily from a $\mu_{est,0} = 0.8$ initialisation value and oscillated within a 0.90 - 0.95 band, resulting in an average value $\overline{\mu}_{est} = 0.92$, Table 5.7. Lowest values ($\overline{\mu}_{est} \approx 0.85$) were observed at the end of the session due to the severe tyre wear, tests 7 and 8 (Table 5.7). Different calibrations were tried in the proposed system (*nominal*, *harsh*, *very harsh*, *soft*) and the *harsh* calibration was found to show the best trade-off between reference tracking accuracy and actuator aggressiveness. Only results corresponding to this calibration are given here due to space limitations. Similar conclusions can be extracted from the 20 meters drift test.

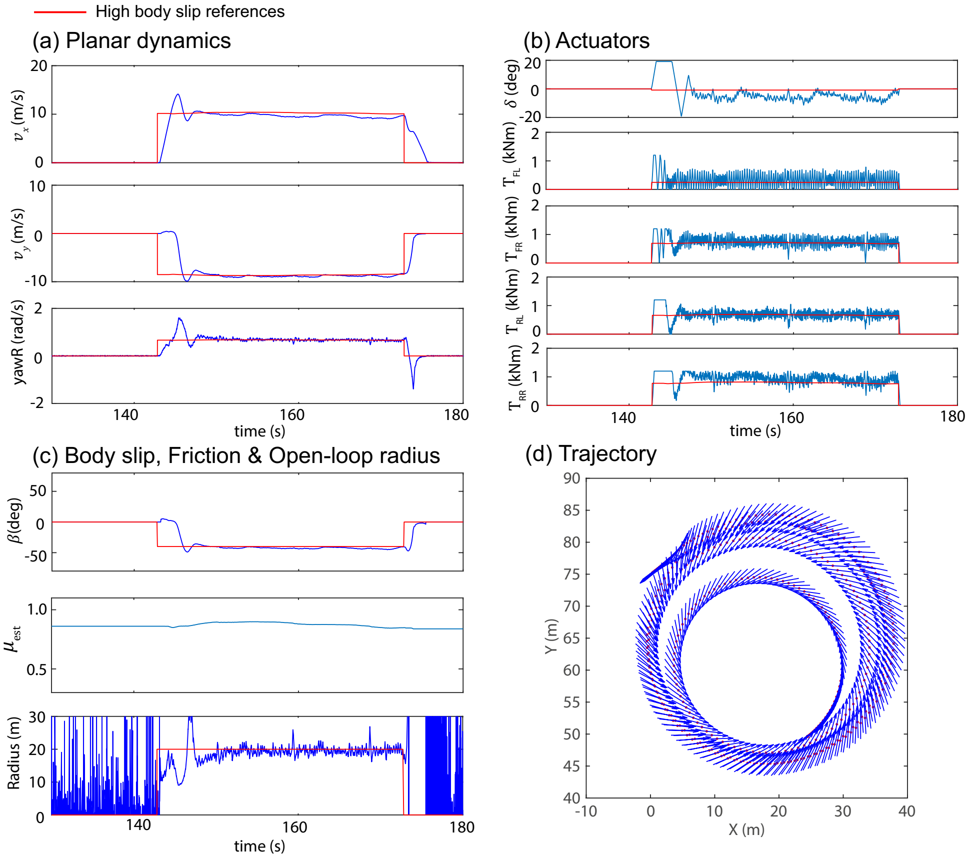

FIGURE 5.17: Test 6, $R_{ss} = 20$ metres high body slip stabilisation in dry tarmac. $\mu_{est,0} = 0.85$.

Several tests were performed initialising the friction observer with different "incorrect" values (from $\mu_{est,0} = 0.5$ to $\mu_{est,0} = 0.85$), in order to study the stability of the complete system in the presence of severe friction uncertainty. This uncertainty may be introduced by a wrong initial terrain classification performed by a high-level perception layer (e.g. machine vision based). The results corresponding to the test 1, 10 metres drift with $\mu_{est,0} = 0.5$, are depicted in Figure 5.18. As can be observed in the figure, the friction estimate increases progressively until converging to a steady value ($\overline{\mu}_{est} = 0.89$). The same trend is exhibited by the body slip angle and vehicle radius. Finally, the 10 metres drift test was repeated in a second session (wet skidpad full of water puddles, Figure 5.19) with the aim to check the system robustness to more challenging conditions. The *harsh* calibration was maintained in this test for consistency. Once again, high body slip stabilisation was achieved, with the friction estimate converging to a steady $\overline{\mu}_{est} = 0.74$ value. A slight offset was noticed on the body slip signal, which may be reduced with the execution of additional calibration steps in wet tarmac conditions. The NRMSE of the tracked vehicle planar motion states is given in Table 5.7.

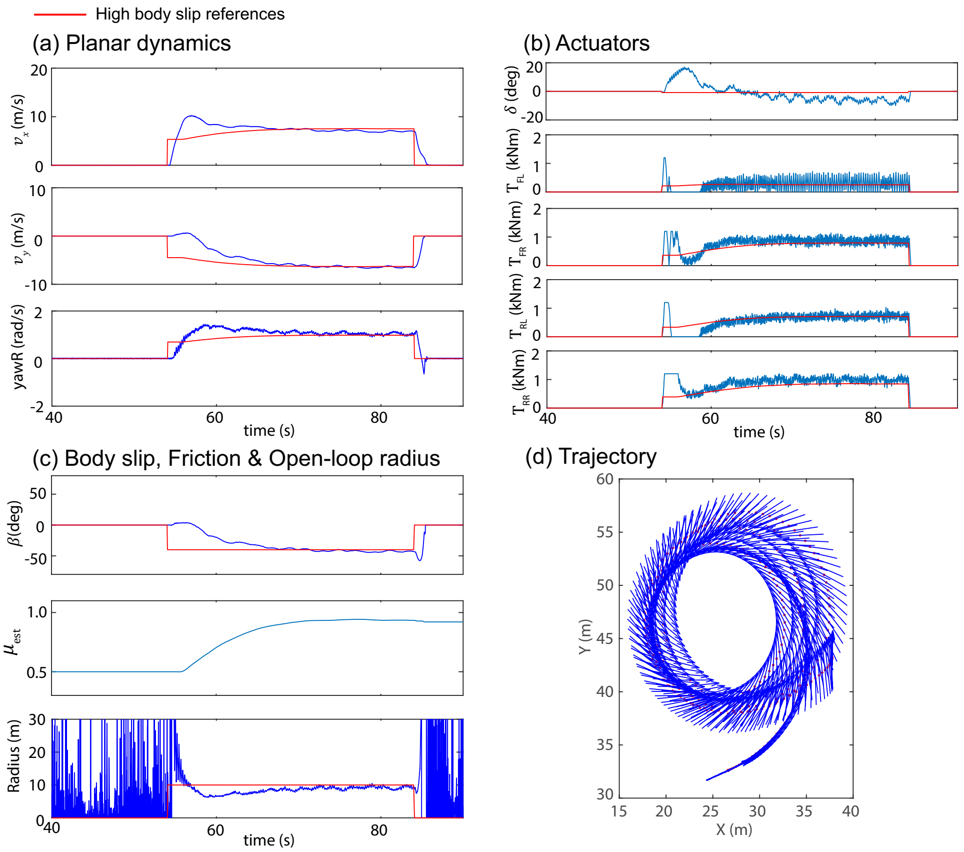

FIGURE 5.18: Test 1, R_{ss} = 10 metres high body slip stabilisation in dry tarmac. Wrong friction initialisation, $\mu_{est,0} = 0.5$.

TABLE 5.7: NRMSE of the tracked vehicle planar motion states (%) and average μ_{est} value. *Harsh* calibration.

Test	R_{ss} [m]	β_{ss} [deg]	$\mu_{est,0}$	$\overline{\mu}_{est}$	$e_{\dot{\psi}}$	e_{v_x}	e_{β}
1-dry	$R-10$	-40	0.50	0.89	21.91	10.07	18.11
2-dry	$R-10$	-40	0.80	0.92	7.82	6.20	7.02
3-dry	$R-15$	-40	0.50	0.86	19.82	7.37	12.03
4-dry	$R-15$	-40	0.70	0.88	11.65	6.16	7.55
5-dry	$R-20$	-40	0.50	0.85	19.01	6.52	10.04
6-dry	$R-20$	-40	0.85	0.88	7.45	6.28	6.70
7-dry	$R-25$	-40	0.50	0.83	20.08	6.79	9.42
8-dry	$R-25$	-40	0.80	0.85	9.14	6.53	6.91
9-wet	$R-10$	-40	0.80	0.74	11.16	8.12	17.48

For consistency with the results given in previous sections, these metrics were computed for $t > t_0 + 5$, with t_0 being the time at which the drifting action was triggered. Overall, the majority of the error values remained below a 10% error band. Expectedly, high errors are observed when the friction observer is initialised with the lowest values (tests 1,3,5,7) due to the longer convergence time. Apart from this, the highest error is noticed in the test performed in wet tarmac. As was mentioned in Section 4.3.1.1, the DES solutions were generated applying the MF friction scaling approach over a tyre characterised in dry tarmac conditions. This may differ from the real behaviour exhibited by the tyre in the presence of water puddles or track dust, thus affecting the controller accuracy.

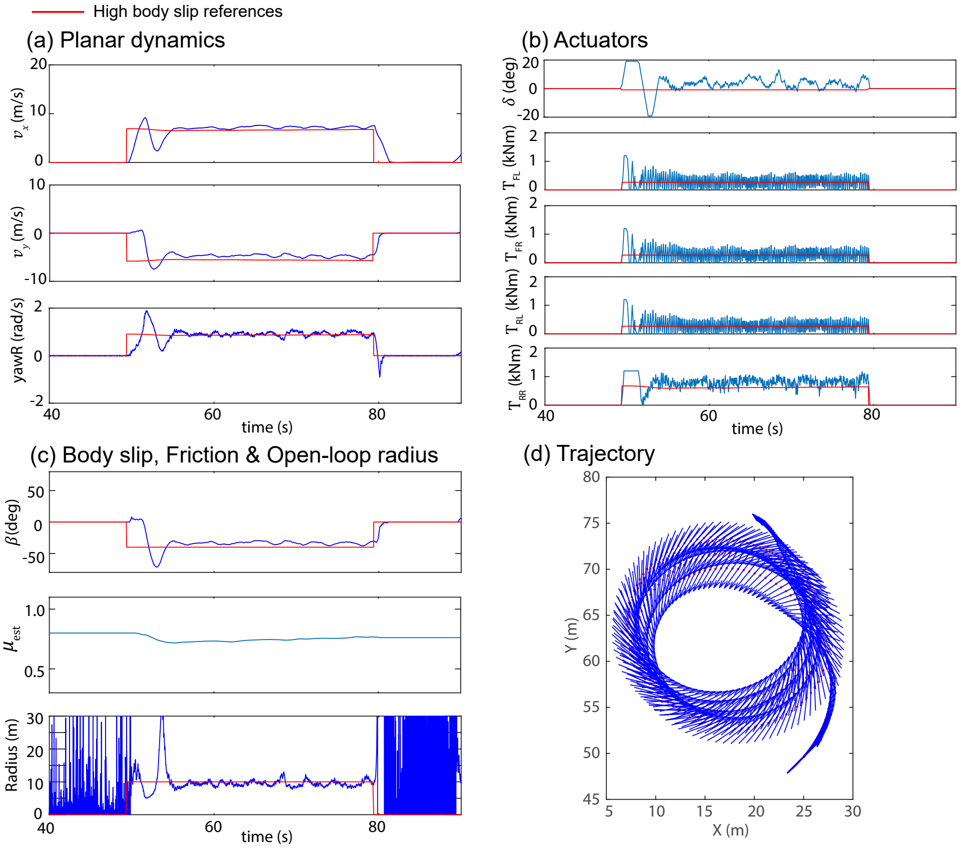

FIGURE 5.19: Test 9, $R_{ss} = 10$ metres high body slip stabilisation in wet tarmac.

5.2.2.1 High body slip stabilisation with virtual sensor

The previous experiments were carried out taking the vehicle planar velocities required by the controller from a high-accuracy differential GPS unit. This solution is expensive and may prevent the proposed system from implementation in more affordable vehicle platforms. In order to propose an alternative to the existing GPS unit, the RW-EKF virtual sensor introduced in Section 3.3.1 was integrated into the feedback loop of the controller. Specifically, the proposed solution aims at substituting the expensive high-accuracy system by a low-frequency GPS unit (10 Hz).

The modular RW-EKF was adapted to the target vehicle platform following the discussion provided in Section 3.3.2, and the vector of measurements of the EKF was reformulated to include the velocity module provided by the low-cost GPS unit $\mathbf{Y_{EKF}} = \{V, \dot{\psi}, a_y\}$. In order to test the proposed solution without altering the existing hardware, a fictitious low-frequency GPS was considered, and the velocity measurement was built from the existing signals in the following manner. The velocity module V was computed as $V = \sqrt{v_x^2 + v_y^2}$, discretised at 10 Hz using a zero-order hold and delayed 0.1 s. This fictitious measurement may differ slightly from the output provided by commercially available GPS units but was sufficient to perform an initial assessment of the closed-loop stability of the proposed system with a delayed low-frequency velocity signal in the feedback loop.

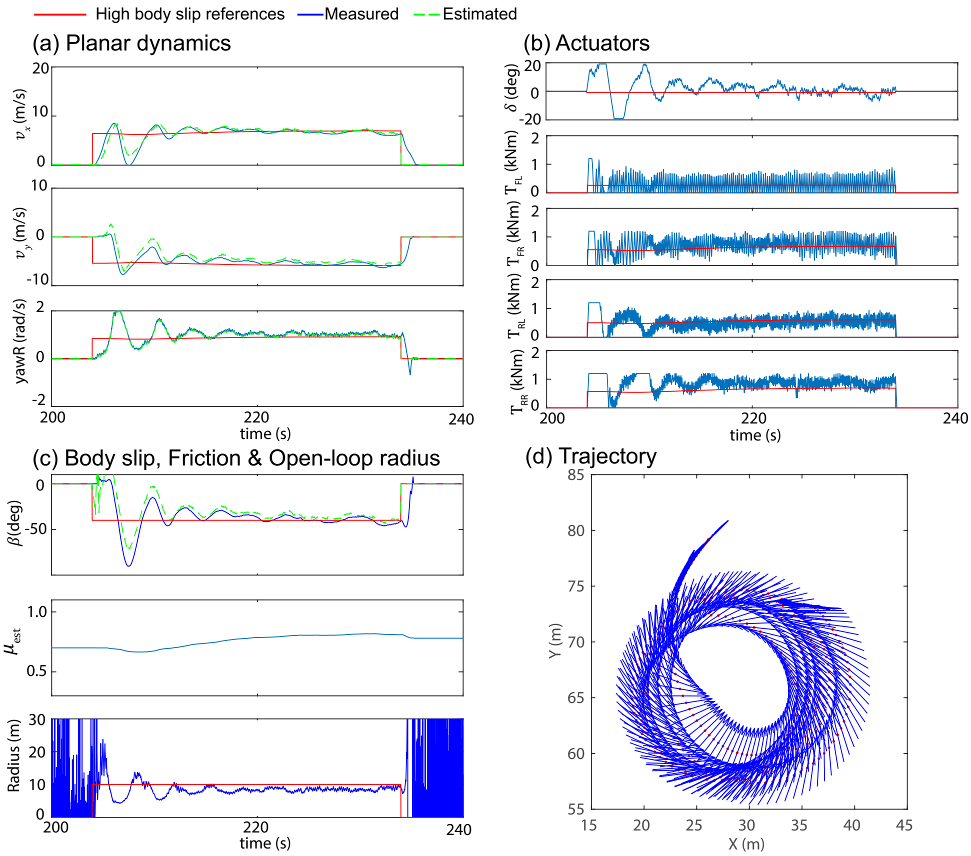

FIGURE 5.20: R_{ss} = 10 metres high body slip stabilisation in wet tarmac with the virtual sensor embedded in the controller feedback loop. Blue: Signals measured with the differential GPS unit, Green: Estimated planar dynamics states.

The RW-EKF was implemented in Simulink and tuned in IPG-CarMaker using the synthesised DevBOT model. Once the SiL tests were concluded, high body slip stabilisation experiments were performed with the HiL platform introduced in Section 4.2.4 to sign off the complete system (virtual sensor + controller). After that, the model was loaded onto the real DevBOT platform and high body slip stabilisation experiments were carried out in wet conditions (Millbrook proving ground, UK). The results corresponding to a 10 metres drift stabilisation experiment are depicted in Figure 5.20. In spite of the initial overshoot, high body slip stabilisation is achieved and the vehicle states converge well to the controller references, Fig. 5.20-a. A low initial friction value was selected in this test due to the slippery conditions and water puddles present in the skidpad. The planar velocities presented some error during the start of the manoeuvre when the vehicle transient content is maximum. After that, the estimated signals matched well the measured signals. This deviation may be reduced with the execution of additional fine tuning steps on the RW-EKF structure. The test was repeated and similar results were obtained, Figure 5.21. Due to limitations on the vehicle instrumentation available, it was not possible to compare the tyre forces estimated by the virtual sensor with reference measurements provided by WFTs.

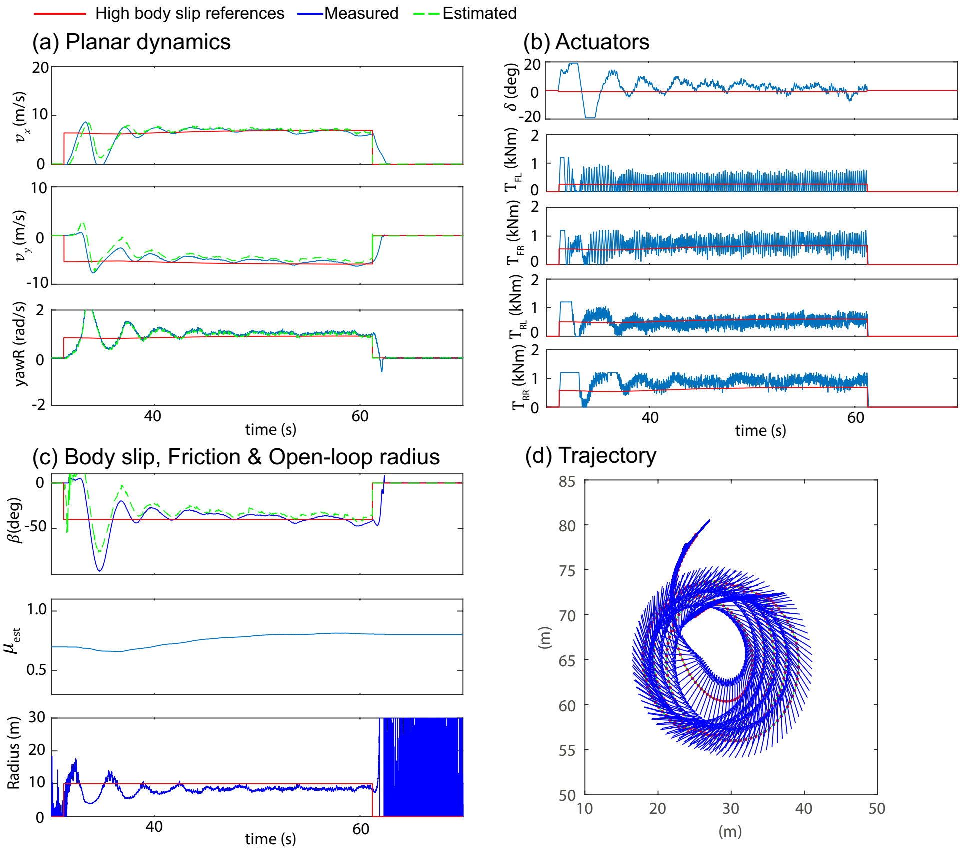

FIGURE 5.21: $R_{ss} = 10$ metres high body slip stabilisation in wet tarmac with the virtual sensor embedded in the controller feedback loop. Repetition. Blue: Signals measured with the differential GPS unit, Green: Estimated planar dynamics states.

Overall, high body slip stabilisation was achieved with the virtual sensor. The initial overshoot caused by the delay introduced in the feedback loop may be reduced by means of additional fine-tuning activities and a less aggressive drift initiation strategy (e.g. with a progressive body slip build up and reduced transient content). Additional experiments will be performed in the future on this basis.

5.2.3 Highly-skilled autonomous driving

The previous experiments evidenced the ability of the proposed centralised MIMO controller to achieve high body slip stabilisation in a real MAGV platform. Moreover, the system was tested in "adaptive friction" mode and a virtual sensing structure was integrated into the controller feedback loop. These results motivated the execution of additional testing activities that led to the implementation of a complete highly-skilled autonomous driver model. For the sake of clarity, it must be remarked that the proposed system was not benchmarked against a "baseline" or "reference" non-skilled driver as simultaneous torque control of the four motors is not achievable by a human driver. Moreover, when the ROBORACE test driver was asked to drift with a fixed favourable driving torque distribution, he was unable to stabilise the vehicle and ended up in a uncontrolled spin multiple times. These results are omitted in this chapter due to space limitations.

In order to facilitate the model debugging, the new control modules were implemented in a progressive manner, similarly to the process described in Chapter 4. Specifically, a *simple path-following* stage was carried out first to evidence the ability of the system to drift along spiral and constant-radius segments, Section 5.2.3.1. After that, a more comprehensive FSM similar than described in Section 4.3.2 was implemented giving, as a result, a fully operative HSAV model able to perform more complex manoeuvres, Section 5.2.3.2.

5.2.3.1 Simple path following

During this project stage, the Autonomous Drift Control (ADC) system introduced in Section 4.3.1 and signed off in the ROBORACE HiL was tested experimentally. In order to extract the additional path-geometry information required by ADC from the instrumentation available (differential GPS), it was necessary to develop the interface depicted in Figure 5.22.

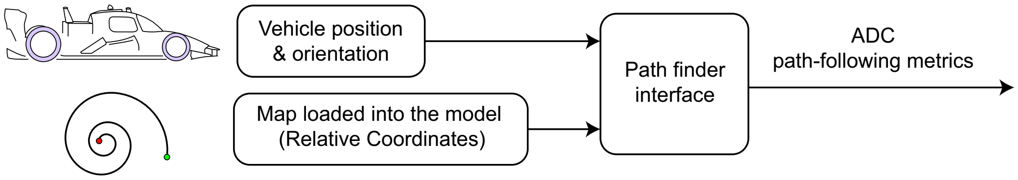

FIGURE 5.22: Path-finder interface prepared to obtain the path-following metrics (e.g. lateral deviation error) from raw GPS measurements.

Following this scheme, the global position and orientation signals provided by the GPS unit are used in combination with a reference trajectory loaded into the model to find the path-following metrics required by the ADC. In essence, the proposed scheme substitutes the *RoadProperty* sensors used in IPG-CarMaker to develop the ADC concept during early research stages. Additional explicit information regarding this interface is omitted here due to confidentiality reasons.

Once ADC was implemented in DevBOT following the steps illustrated in Fig. 5.14, relevant field tests were performed in dry tarmac (Millbrook proving ground, UK). A shakedown session was carried out first to confirm the validity of the new modules and, after that, a set of constant-radius and spiral tests were performed. With regards to the system tuning, the *harsh* calibration tested in the previous session was maintained on the low-level LQR controller, Section 5.2.2. Different calibrations ("loose", "tight") were determined in the HiL systems for the PID control law of the high-level trajectory control layer (Section 4.3.1). The results depicted in Figure 5.23 correspond to a 10 metres circular path test initiated from standstill conditions and carried out with the "loose" trajectory calibration.

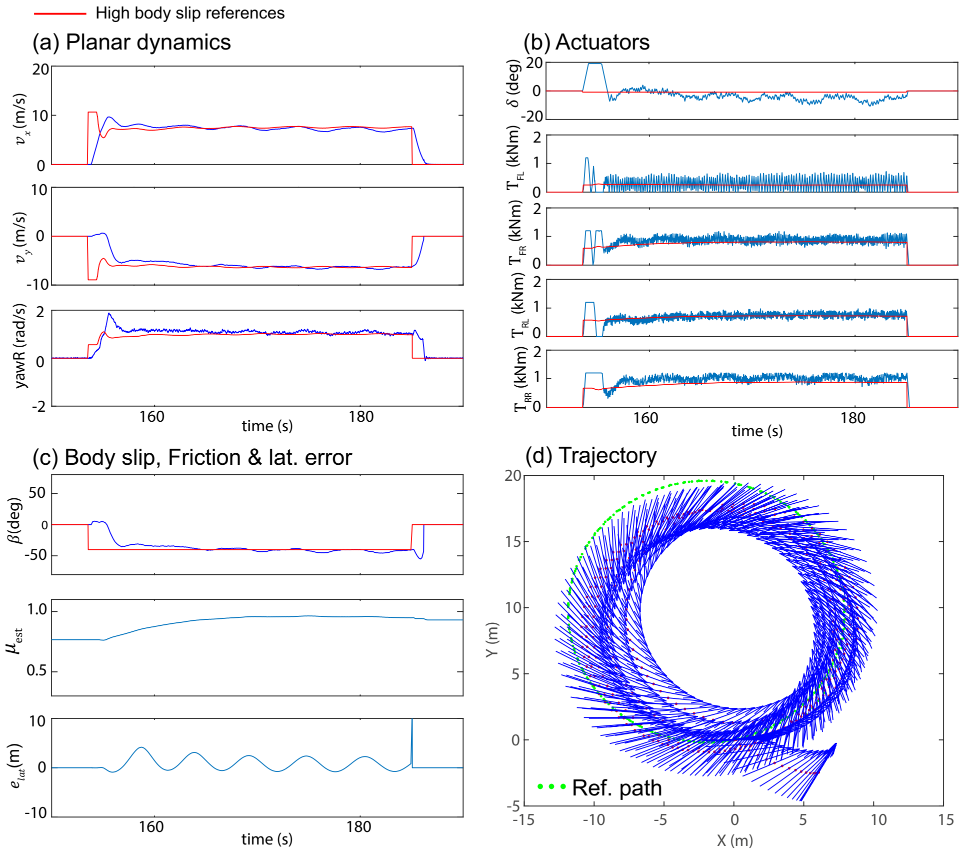

FIGURE 5.23: Test 1, 10 metres circular path test performed in dry tarmac conditions, $\beta_{ss} = -$ 40 degrees. "Loose" trajectory control calibration.

During this preliminary test, the ADC was able to achieve the drifting motion from standstill conditions, Fig. 5.23-a. Nevertheless, a significant oscillation was noticed on the lateral deviation error, what motivated the test repetition with the “tight” trajectory calibration, Figure 5.24. In this case, the amplitude of the oscillations is reduced significantly and the RMSE of the lateral deviation is kept close to 1 metre, Table 5.8.

An additional spiral test was performed maintaining the previous controller calibration, Figure 5.25. Once again, ADC is able to complete the manoeuvre without major difficulties, maintaining the target body slip angle in spite of the radius reduction (10 to 5 metres). The NRMSE of the vehicle planar states were computed for the tests described in this section and are given in Table 5.8. For consistency with the results shown previously, these metrics were computed 5 s after triggering the ADC action. Overall, acceptable results were obtained, with the majority of the vehicle state errors below the 10% band. Apart from this, the RMS of the lateral deviation was kept close to 1 metre for the manoeuvres executed with the “tight” trajectory control calibration.

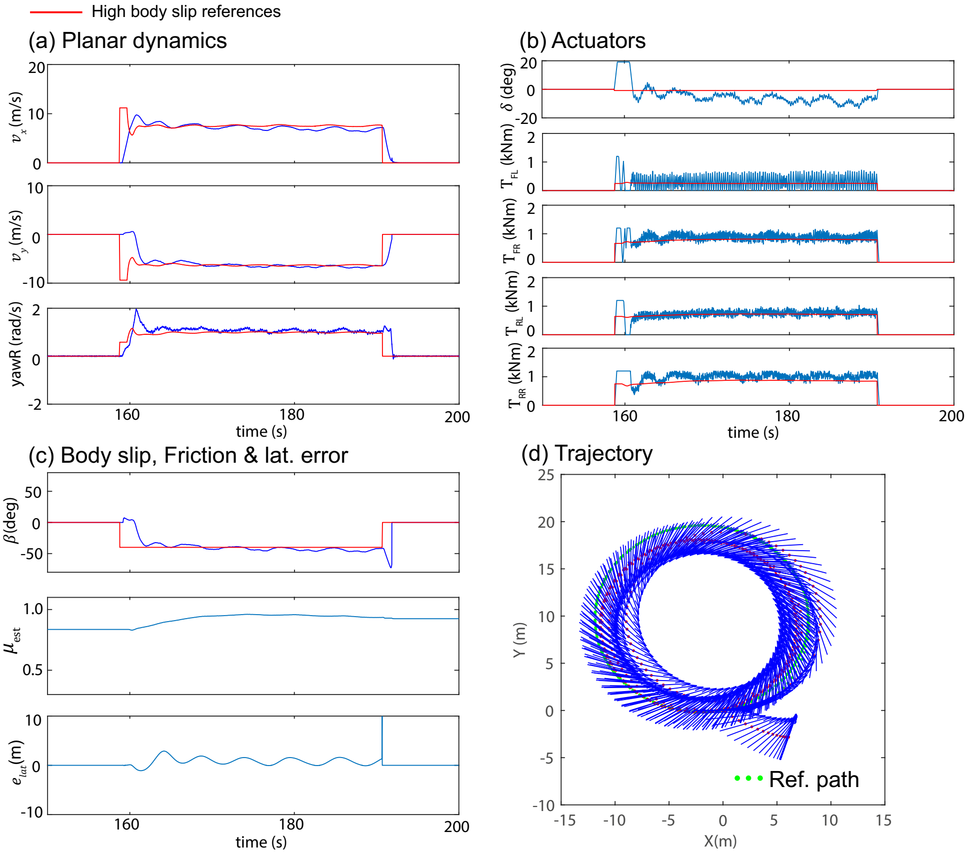

FIGURE 5.24: Test 2, 10 metres circular path test performed in dry tarmac conditions, $\beta_{ss} = -40$ degrees. “Tight” trajectory control calibration.

Despite acceptable results were obtained at this stage, ADC exhibited some difficulties during the first seconds of these manoeuvres. Specifically, the system struggled to follow the reference trajectory during the body slip build up from standstill conditions. This problem was addressed in the third stage of the project with the introduction of an

FSM that permitted the drift initiation from non-static conditions and the adoption of regenerative braking strategies for enhanced vehicle agility.

TABLE 5.8: NRMSE of the tracked vehicle planar motion states (%), average μ_{est} value, RMS and max. value of the lateral deviation error (e_{lat}).

Test	Description	R_{ss} [m]	β_{ss} [deg]	$\mu_{est,0}$	$\overline{\mu}_{est}$	$e_{\dot{\psi}}$	e_{v_x}	e_{β}	$e_{lat,RMS}$	$e_{lat,\max}$
1-dry	Constant-radius “loose” cal.	10	−40	0.80	0.94	9.89	3.44	8.33	1.56	4.16
2-dry	Constant-radius “tight” cal.	10	−40	0.80	0.94	8.64	4.73	9.46	1.14	2.89
3-dry	Spiral “tight” cal.	10-5	−40	0.80	0.92	11.17	6.51	9.82	1.04	2.39

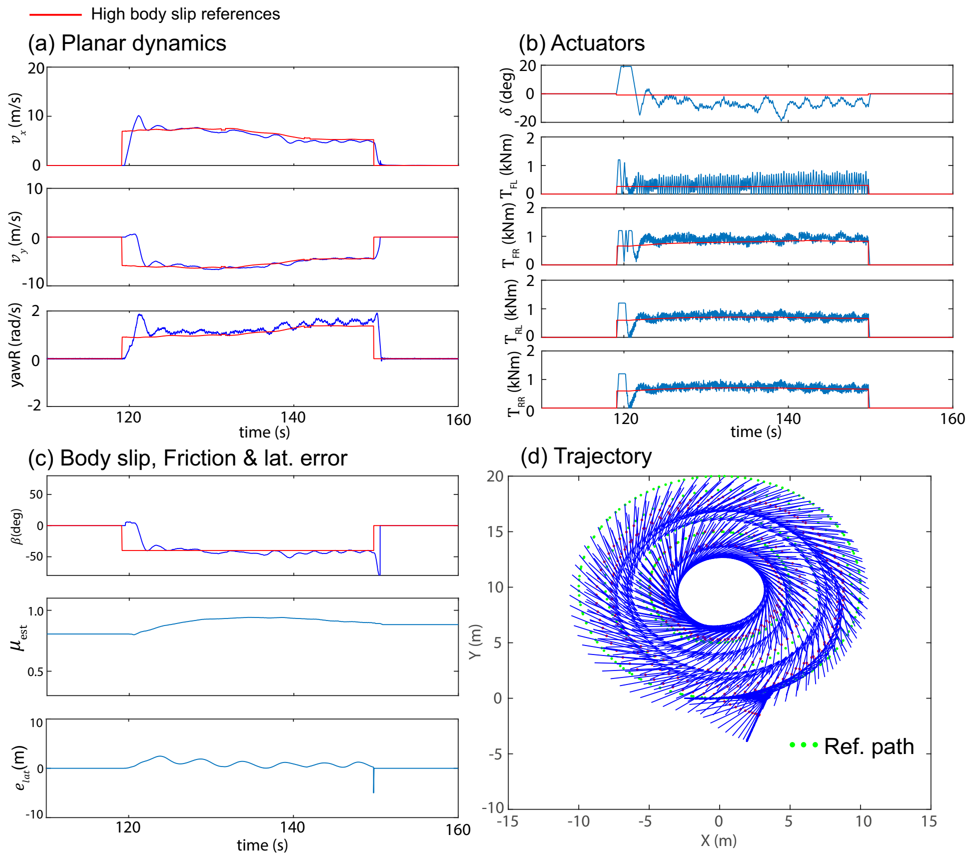

FIGURE 5.25: Test 3, 10 to 5 metres spiral drift test performed in dry tarmac conditions, $\beta_{ss} = -40$ degrees. “Tight” trajectory control calibration.

5.2.3.2 Advanced path following

Once the ADC system was verified experimentally, a more comprehensive driver model was implemented in DevBOT. Taking as a reference the SiL work presented in the preceding chapter, the FSM driver model depicted in Figure 4.27 (see Section 4.3.2 for additional details) was simplified and converted into the HSAV driver model illustrated in Figure 5.26.

In brief, the proposed HSAV model incorporates two driving modes, racing line-based driver and high body slip driver. These driving modes are alternated depending on the curvature of the reference path. The steering corrections required by the racing line-based driver were obtained following a feedback proportional controller based on the lateral deviation and heading errors, [11]. For simplicity, during racing line driving (straight-line or wide circular segments), the speed regulation is achieved by means of a simple PID control that tracks a reference speed profile. ABS and TCS systems will be added at a lower level in the future. Due to the testing restrictions on the available experimental vehicle, only the rigid-surface HSAV feature was implemented. It is expected that the results obtained during this research will facilitate the execution of additional experiments in loose surfaces with a more convenient MAGV platform. The HSAV action is summarised schematically by the sequence of onboard frames depicted in Figure 5.27.

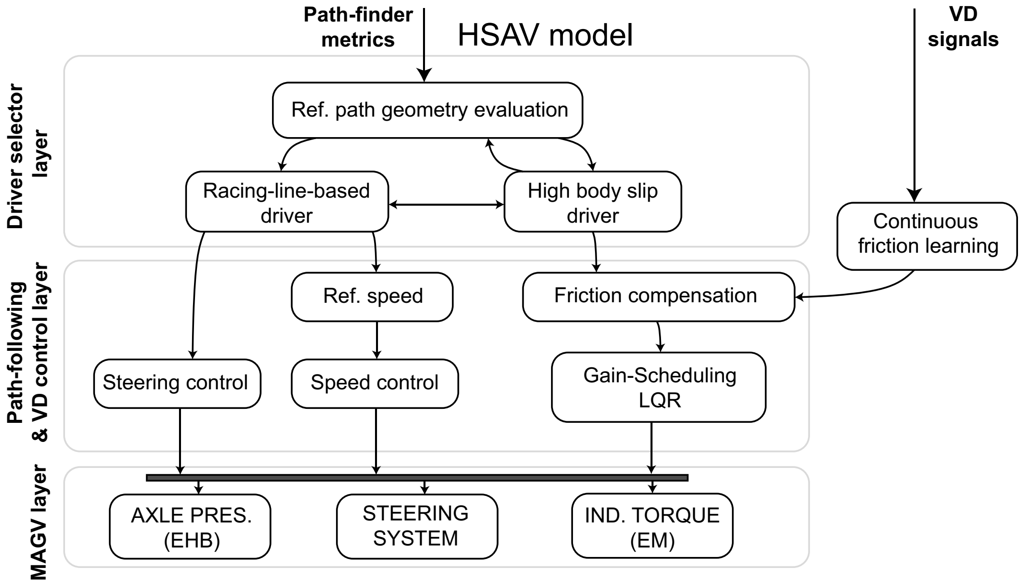

Figure 5.26: HSAV driver model implemented and verified experimentally in DevBOT.

At the start of the test, the HSAV model is initialised in standstill conditions and AI is allowed by the ROBORACE crew ("AI enabled"). The handshake between SPEEDGOAT and the low-level "black-box", Figure 5.14, is successful and the HSAV model takes over DevBOT ("Launch"). The racing-line driver starts controlling the vehicle and switches to the drifting driver when the curved segment is initiated. During drifting driving, several transitions occur between positive and negative body slip angle depending on the sign of the target path curvature. Finally, the racing-line driver takes over the vehicle during the last part of the manoeuvre, and the vehicle is stopped once the full path is covered.

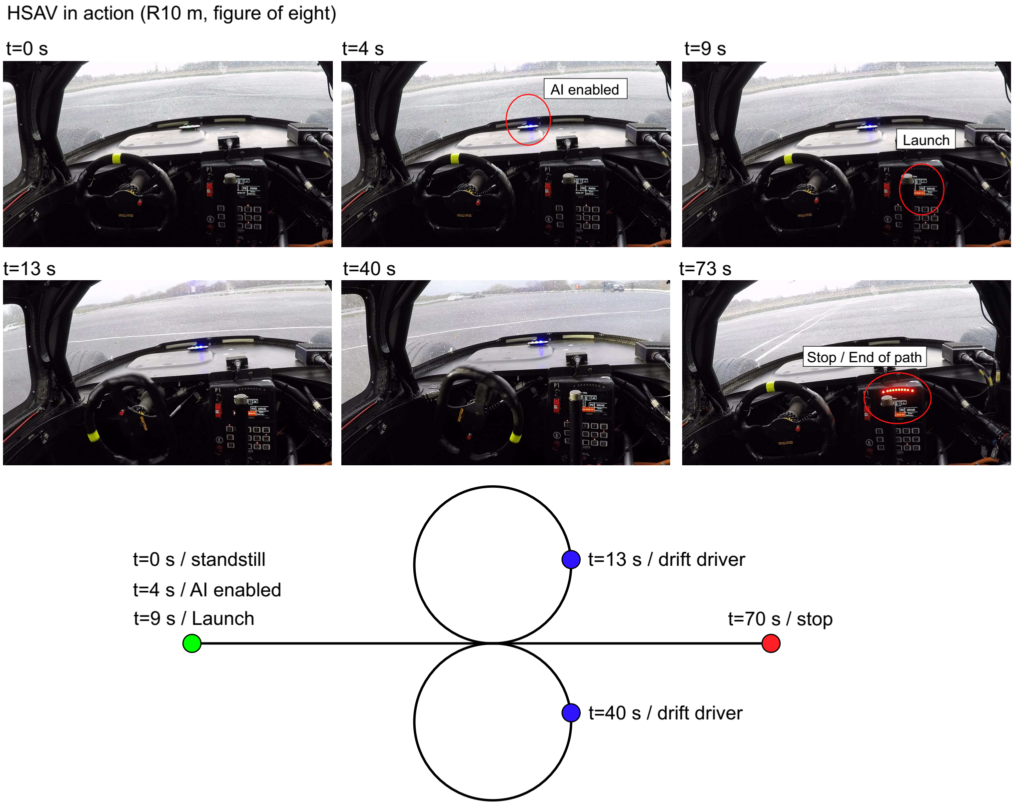

FIGURE 5.27: DevBOT onboard frames during the HSAV model action. $t = 0$ s system off in standstill conditions, $t = 4$ s AI enabled by the ROBORACE team, handshake starts, $t = 9$ s vehicle is launched and the racing-line driver is in control, $t = 13$ and $t = 40$ s drifting driver taking control, $t = 73$ s return to racing-line driver and end of the manoeuvre.

With regards to the drifting mode, the enhanced path-following control law presented in Section 4.3.2 was implemented in the HSAV model. In order to reduce the stress on the DevBOT actuators, a switching-gain strategy was adopted to implement the proposed control law. Specifically, due to the noise associated to the heading error derivative terms required by the proposed control law, these terms were only utilised during short periods of time in which significant anticipation to abrupt curvature changes was required. For example, to initiate the drifting action from straight-line conditions or to follow changes in the curvature sign of the reference path (agile transitions). During sustained drifting along steady-curvature segments (e.g. constant-radius, spiral), the lateral deviation error terms are utilised and the gain associated with the heading error terms is lowered. These modes denoted as PF-I (fine tracking) and PF-II (anticipation), were integrated following the logic depicted in Figure 5.28.

When the racing line driver is enabled, the PF-II algorithm computes the corrected curvature $\tilde{\kappa}$ and triggers the drifting action when $\tilde{\kappa}$ is above a certain threshold. Once

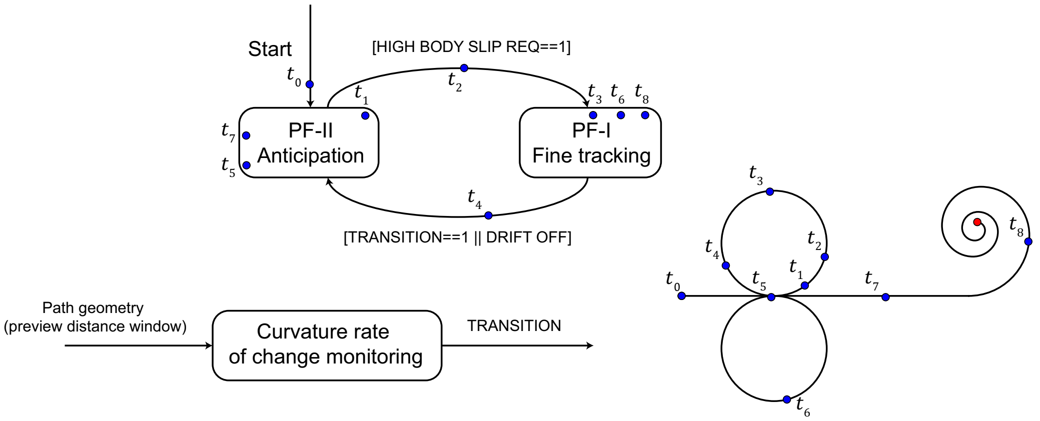

FIGURE 5.28: Proposed drift path-following gain switching strategy.

this happens and after a stabilisation time t_{stab} has passed, the PF-I is activated to fine-track the reference path. During this fine-tracking system state, a high-level supervisor monitors the rate of change of the road curvature $\dot{\kappa}$ along a preview distance window Δs. When a foreseen change in the curvature sign causes an abrupt increase in the previous derivative, the PF-II algorithm is enabled to execute the drift transition and converge to the new reference path. In order to maximise the vehicle agility during the drift initiation and body slip transitions, regenerative braking was allowed in PF-II mode. In essence, the EM amplitude constraints were extended to negative values with the aim to permit the application of negative torque on one side of the vehicle and positive torque on the opposite side. This increases the positive (responsiveness) and corrective (damping) yaw moment and helps to decouple the yaw rotation and lateral deviation of the vehicle, which is of vital importance to change the vehicle attitude during abrupt curvature transitions with minimum lateral deviation [14]. Due to the regenerative charging limitations of DevBOT, additional corrective layers were incorporated into the system to maintain the charging power within safe limits. Fortunately, the net power balance (driving motors on one side - battery draining, regenerative motors on the opposite side - battery charging) during this operation was close to zero for the manoeuvres studied in this section. The HSAV model was subjected to a wide range of HiL tests and field experiments in wet tarmac conditions (Millbrook proving ground, UK). Due to space limitations, only the experimental tests are described in the following.

The results corresponding to the straight to 10 metres circular path test are depicted in Figure 5.29. The HSAV model achieves the target cruise speed (35 kph) in racing-line driving mode and switches to the drifting driver when the curved segment is approached. In spite of some oscillations, Fig. 5.29-c, the vehicle keeps close to the reference trajectory and maintains a high body slip angle. The tarmac friction observer was initialised to a low friction value ($\mu_{est,0} = 0.6$) due to the unfavourable track conditions, full of water

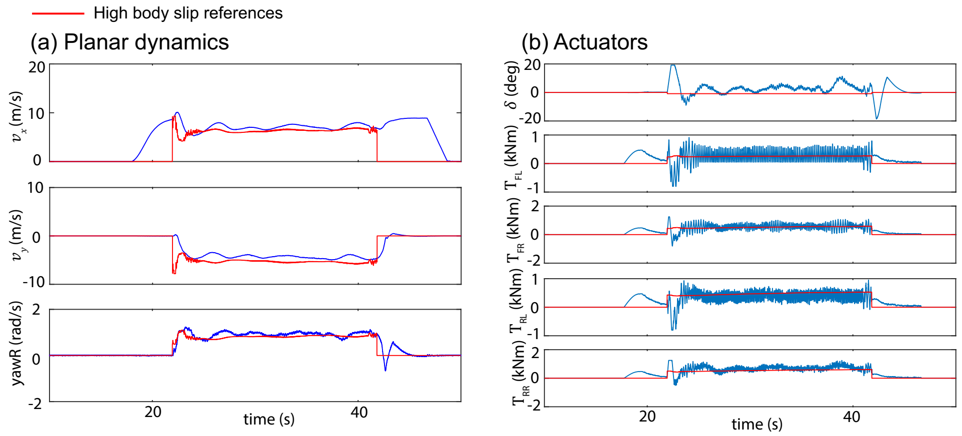

(a) Planar dynamics

(b) Actuators

(c) Body slip, Friction & lat. error

(d) Trajectory

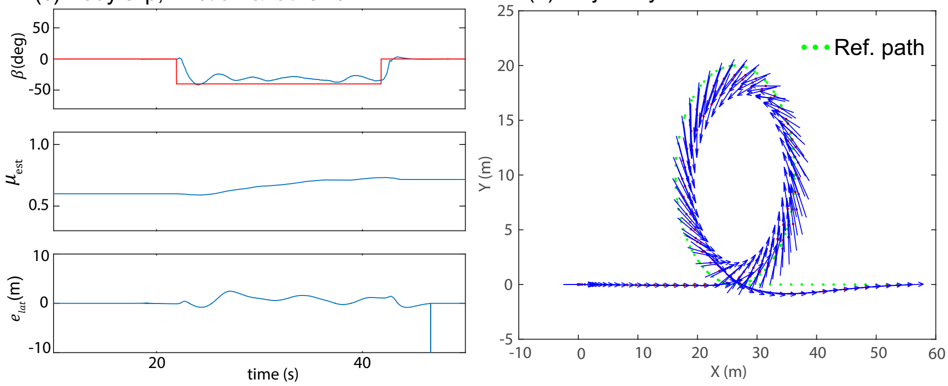

Figure 5.29: Test 1, straight to 10 metres circular path, $\beta_{ss} = -40$ degrees. DevBOT 01.

paddles. The *harsh* LQR calibration was maintained during these tests for consistency. With regards to the trajectory control layer, it must be remarked that the preliminary system calibration was performed in the HiL assuming dry tarmac conditions. The fact that acceptable results were obtained after a few iterations on a wet track demonstrates the effectiveness of the proposed tuning methodology (HiL pre-calibration) and robustness of the proposed system to uncertain track conditions. In addition, during the whole testing program carried out at the handling platform of Millbrook proving ground the path tracking feature was influenced by the platform banking, which could have magnified the lateral deviation error. Additional experiments will be performed in the future in a completely flat platform. Finally, due to limitations on the MAGV available, the testing program was carried out with DevBOT-01 and DevBOT-03 vehicles. For consistency, both vehicles were set up in exactly the same configuration. The results corresponding to a straight-line to 15 metres circular path are depicted in Figure 5.30. In this case, the vehicle presents some positive lateral deviation during the last part of the manoeuvre (return to straight-line). For simplicity, a fixed drift-exit condition was maintained during the whole testing program. Further refinements will be performed in the future with the aim to adjust the drift-exit condition to different track geometries.

In order to assess the system robustness to severe tyre pressure variations, this test was repeated in a minimum tyre pressure configuration ($\Delta Press \approx$ -0.5 bar), and the results depicted in Figure 5.31 were obtained. Overall, noticeable performance changes are not observed in spite of the abrupt pressure reduction. This demonstrates the ability of the proposed friction adaptation approach to handling abrupt friction changes (slippery conditions) as well as subtle variations in the vehicle configuration (tyre pressure reduction). After this initial assessment, more challenging manoeuvres were tested. Specifically, the results corresponding to a 8 - 5 - 8 metres spiral are depicted in Figure 5.32.

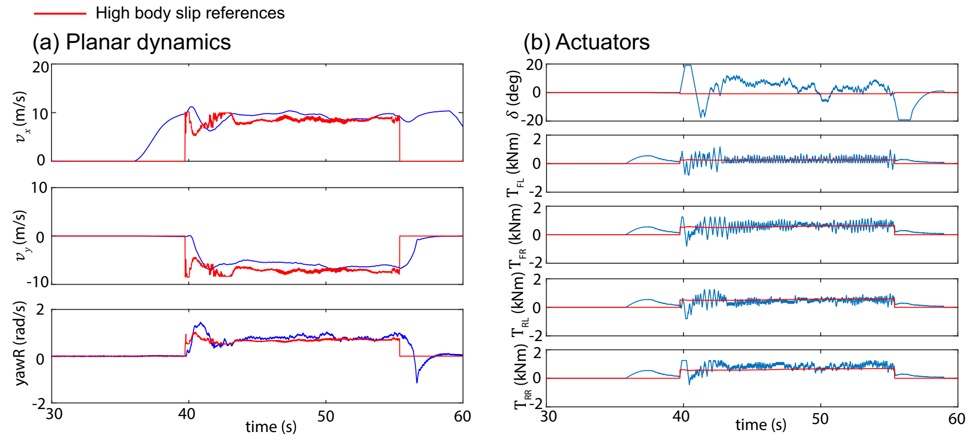

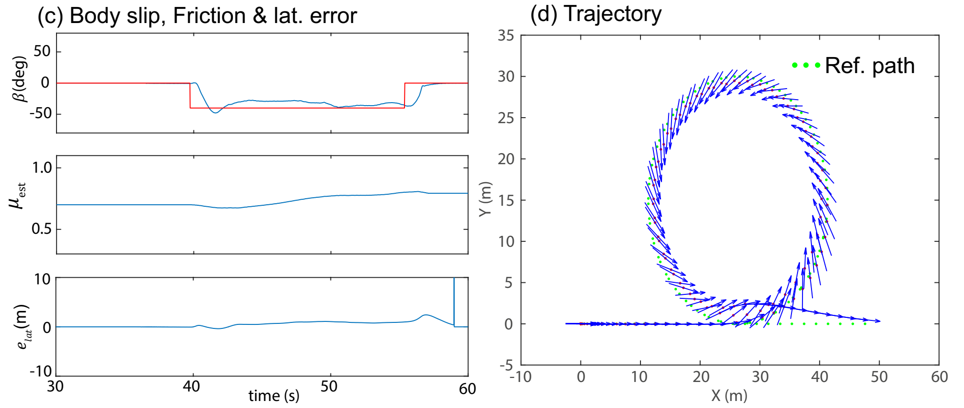

FIGURE 5.30: Test 2, drift along 15 metres circular trajectory, $\beta_{ss} = -40$ degrees. DevBOT 03.

The system tracks closely the reference path, achieving an RMS lateral deviation error below 1 metre, Table 5.9. Some offset is noticed with respect to the tracked body slip angle due to the slippery track condition. As was mentioned in Section 5.2.2, the low-level VD controller was calibrated in dry conditions, and this error may be reduced if additional fine-tuning activities were performed in wet conditions. Apart from this, additional iterations should be carried out in the future in order to adjust the DES derived from the synthesised vehicle model and the experimental vehicle references in a wide range of friction levels. Once again, the DES solutions generated applying the

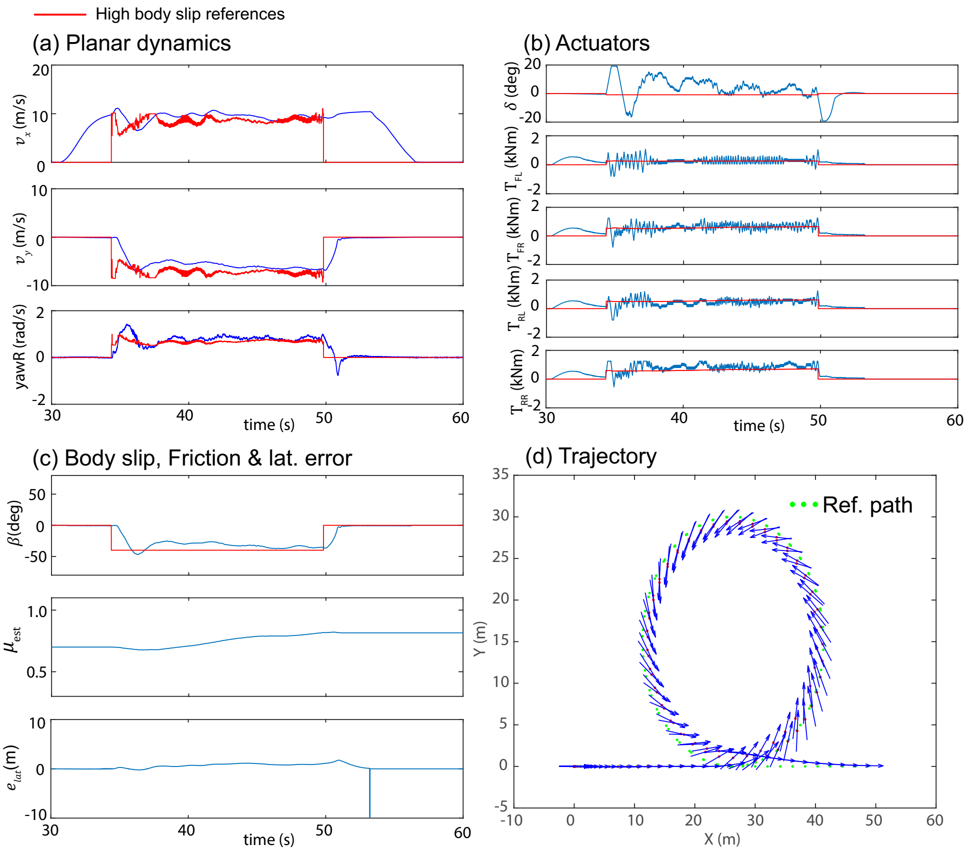

FIGURE 5.31: Test 3, drift along 15 metres circle, $\beta_{ss} = -40$ degrees. DevBOT 03. $\Delta Press \approx$-0.5 bar.

MF friction scaling approach may differ from the real tyre behaviour in the presence of water puddles or track dust.

This test was repeated introducing an offset of 2 metres in the straights of the reference trajectory with the aim to check the ability of the system to cope with severe lateral deviation errors when high body slip stabilisation is requested. The trajectories obtained imposing positive and negative lateral offsets on the straights are given in Figure 5.33. Overall, the system was able to converge to the reference spiral during high body slip control without major difficulties. The RMS error of the lateral deviation increased in these manoeuvres due to the offset introduced in the straights, Table 5.9.

The results corresponding to the 10 metres figure of eight are presented in Figure 5.34. This manoeuvre is particularly challenging for the system as stepped body slip changes (e.g. -40 to 40 degrees requests) take place during the transitions between clockwise and counter-clockwise high body slip driving. Moreover, in order to verify the system agility in most adverse conditions, the reference path was constructed imposing a G1-tangent continuity on the circular segments. As can be noticed in Figure 5.34, the system performance is very good, and the lateral deviation error is maintained within a 1-metre band for the majority of the test, giving, as a result, an RMS error below 1 metre, Table 5.9. Some initial deviation is observed during the drift initiation, which is quickly corrected after the high body slip stabilisation is achieved. The body slip angle exhibits some overshoot during the stepped changes due to the aggressive vehicle heading change. This is quickly corrected by the yaw damping action of the low-level VD controller. With regards to the friction compensation factor, this remains around 0.7 during the first seconds of the manoeuvre and converges to a steady $\overline{\mu}_{est} = 0.76$ value once the tyres have gained some temperature, Table 5.9. The results described up to now motivated the execution of the Gymkhana test illustrated in Figure 5.35. This test combines a 10 metres figure of eight, a triple s-like arc transition, a decreasing-radius spiral, a constant-radius 5 metres circle, and an increasing-radius spiral.

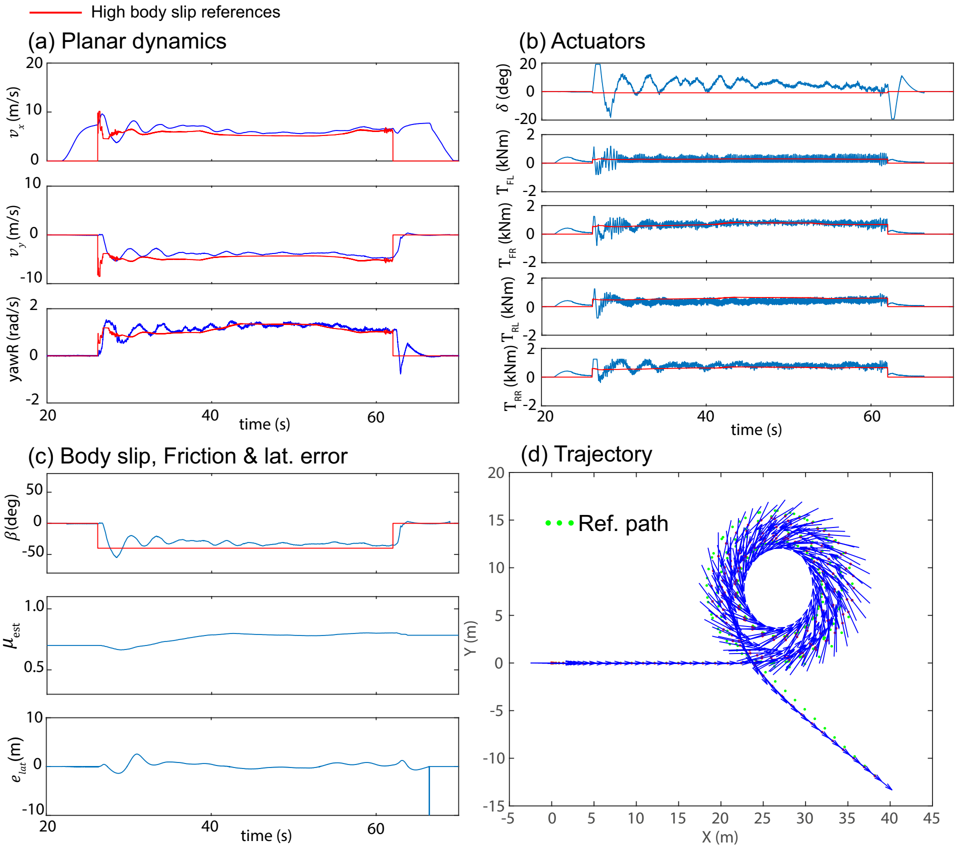

FIGURE 5.32: Test 4, drift along spiral, $\beta_{ss} = -40$ degrees. DevBOT 03.

Overall, the vehicle was able to complete the manoeuvre successfully, keeping within the 9 metres deviation threshold set to trigger the emergency stop. The maximum error is noticed at the beginning of the manoeuvre, probably caused by the cold tyre starting condition. In order to keep track of the vehicle vital signs (e.g. inverter temperature), it was necessary to perform several data analysis and model uploading steps between runs (which can last between 5 to 10 minutes). This process contributed to cool down the tyres between runs, what led to system tracking inaccuracies during the tyre warm-up process.

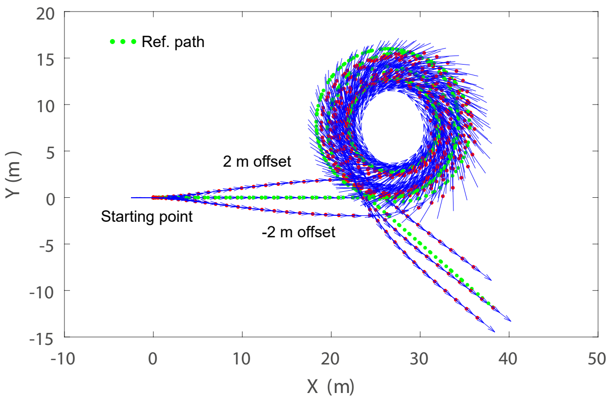

FIGURE 5.33: Spiral test, $\beta_{ss} = -40$ degrees. DevBOT 03. Convergence analysis in the presence of $+2, -2$ lateral offsets on the straight-line segments.

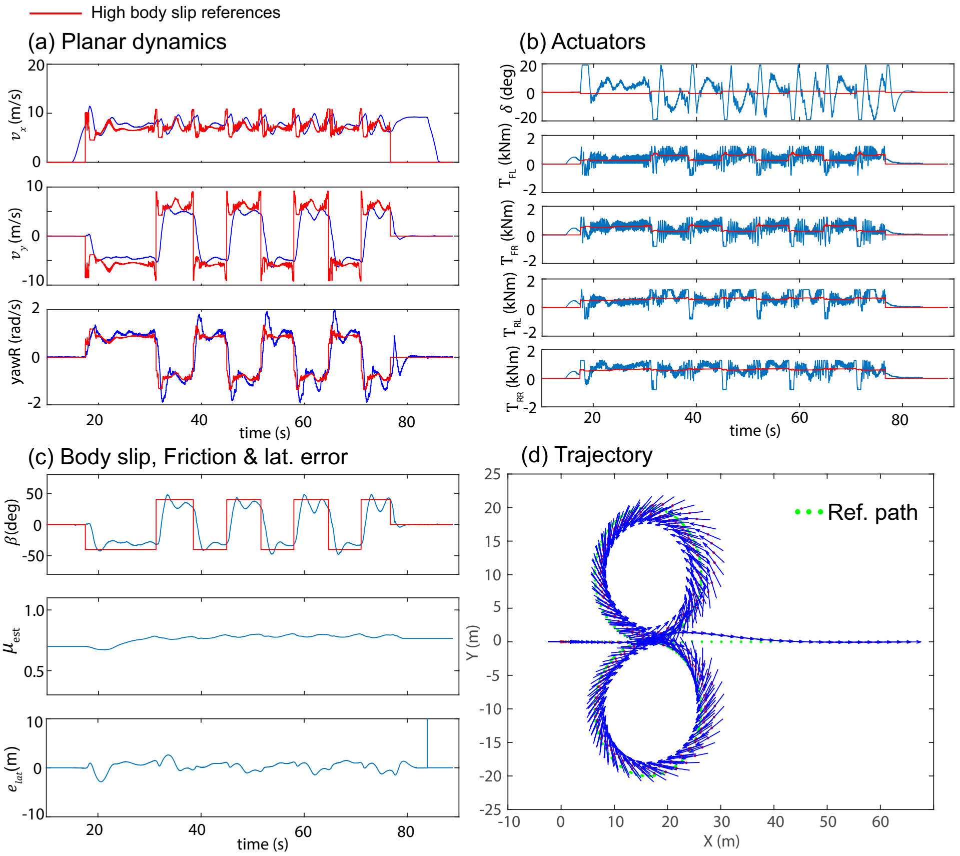

FIGURE 5.34: Test 7, 10 metres eight figure test, $\beta_{ss} = -40$ degrees. DevBOT 01.

The tyre temperature evolution can be inferred from the trend exhibited by the friction compensation factor. This starts from $\mu_{est,0} = 0.7$, and increases steadily achieving a maximum value close to 0.8 during the increasing radius spiral, the moment at which maximum power is demanded by the system (the system power consumption increases with the target radius). In spite of these inaccuracies, the RMS lateral deviation error is kept close to 1 metre, Table 5.9. Finally, the NRMSE errors of the tracked states and the RMS error of the lateral deviation are given in Table 5.9.

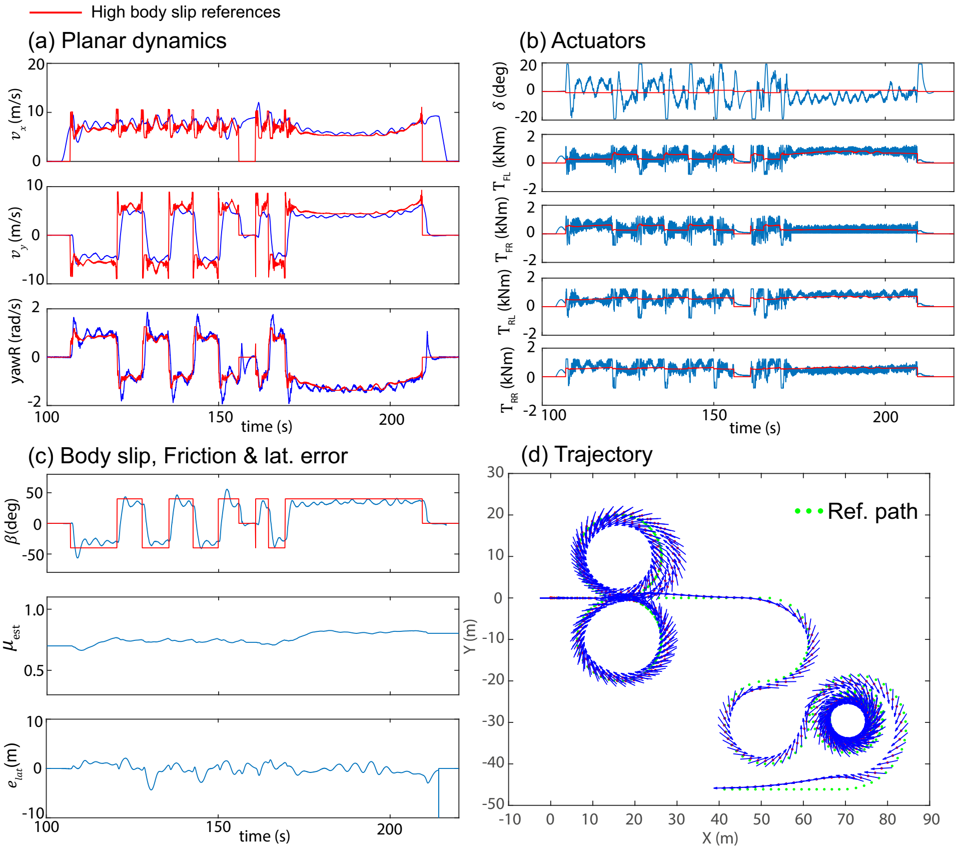

FIGURE 5.35: Test 8, Gymkhana, $\beta_{ss} = -40$ degrees. DevBOT 01.

TABLE 5.9: NRMSE of the tracked vehicle planar motion states (%), average μ_{est} value and RMSE of the lateral deviation.

Test	Description	R_{ss} [m]	$\lvert\beta_{ss}\rvert$ [deg]	$\mu_{est,0}$	$\overline{\mu}_{est}$	$e_{\dot{\psi}}$	e_{v_x}	e_{β}	$e_{lat,RMS}$	$e_{lat,\max}$
1-wet	Constant radius	10	40	0.60	0.66	12.27	10.41	24.84	1.01	2.46
2-wet	Constant radius	15	40	0.70	0.73	15.69	12.16	24.64	0.88	2.42
3-wet	Constant radius $\Delta Press$ =-0.5 bar	15	40	0.70	0.74	16.89	11.38	25.76	0.77	1.76
4-wet	Spiral 0 m offset	$8-5-8$	40	0.70	0.75	11.14	9.36	25.01	0.66	2.56
5-wet	Spiral 2 m offset	$8-5-8$	40	0.70	0.76	10.83	8.86	23.705	0.96	2.72
6-wet	Spiral -2 m offset	$8-5-8$	40	0.70	0.76	11.43	9.26	24.62	0.88	2.50
7-wet	Figure of eight	10	40	0.70	0.76	27.74	14.85	52.03	0.96	2.84
8-wet	Gymkhana	$5-20$	40	0.70	0.76	24.54	12.06	46.09	1.08	4.34

Overall, low error levels are observed regarding the lateral deviation. Aspects like the tyre temperature or skidpad banking will be further investigated in the future. In this case, the error metrics were computed during the whole manoeuvre, which led to a significant increase in the NRMSE of the vehicle planar motion states. Specifically, the NRMSE levels are magnified in the case of the yaw rate and body slip angle due to the delay between the stepped sign change request and the vehicle state convergence. Due to the lack of similar tests on the existing literature, these values will be employed as a reference during future refinements of the proposed system.

5.2.4 Summary of advanced motion control experiments

In this section, the motion controllers described in Chapter 4 have been implemented in a real MAGV platform and verified in a comprehensive testing program carried out in dry and wet tarmac conditions. Specifically, an HSAV driver model incorporating the high body slip path-following and friction adaptation features has been developed to drive DevBOT autonomously. The model construction has been divided into three working packages following the methodology introduced in Chapter 4.

During the first stage of the project, *high body slip stabilisation*, a constrained gain-scheduling LQR has been subjected to a wide range of high body slip tests imposing a fixed open-loop target radius (between 10 and 25 metres). These experiments were performed in dry and wet tarmac conditions. Apart from this, additional experiments were carried out to verify the performance of the system when the feedback is provided by an RW-EKF virtual sensor relying on a low-frequency (10 Hz) velocity measurement.

After that, the path-following feature was introduced in the system and several constant-radius and spiral tests were performed in dry tarmac conditions, stage 2 *simple path-following*. Overall, in spite of some difficulties during the first seconds of the tests (caused by the standstill system initiation), the system was able to converge to the reference path and maintain a high body slip angle simultaneously. The complete HSAV driver model was derived in the last project stage, *advanced path-following*, and tested in wet tarmac conditions. The system was subjected to circle, spiral, figure of eight and gymkhana tests, and remarkable results were obtained, with the system exhibiting strong robustness to the disturbances and uncertainty introduced by factors like the platform banking, tyre temperature or water puddles. Moreover, additional tests were performed in order to verify the system robustness to changes in the vehicle configuration (-0.5 bar tyre pressure, driver in and out of the vehicle), or initial lateral offsets.

To conclude with this section, it is worth remarking that these results were obtained with a pre-calibration found in the HiL (configured to represent accurately dry tarmac conditions) and with minimum tuning corrections on track. This evidences the ability of the HSAV to not only execute advanced driving tasks but also to adapt to varying friction conditions, as professional drivers do.

5.3 Conclusions

In this chapter, the results obtained during the industrial research activities carried out with Jaguar Land Rover and ARRIVAL Software have been presented. Overall, a wide range of virtual sensing and advanced motion control solutions introduced in the previous chapters have been verified experimentally with state-of-the-art vehicle instrumentation and MAGV platforms. Specifically, the most relevant conclusions extracted from these industrial research activities can be summarised in the following points.

- The random-walk virtual sensors for integral tyre force estimation have been verified in an off-road experimental testbed. The preliminary virtual sensors have been re-designed to fit the particularities of the JLR VBOTT testbed and a complete tyre characterisation program has been executed in tarmac and snow terrains. Overall good results have been obtained with the proposed estimation structures for the individual longitudinal and axle lateral forces. In what concerns the individual tyre lateral forces, it is expected that additional measurements (e.g. strain based) will be required in order to capture the lateral tyre force asymmetries.
- The advanced motion control solutions have been progressively tested in the DevBOT MAGV platform. The high body slip stabilisation has been verified in a set of experiments executed in dry and wet tarmac. These experiments were carried out first taking all the feedback measurements from the DevBOT equipment and then with the random-walk virtual sensor introduced in the previous chapters embedded in the control feedback loop. Apart from this, for the first time, a complete HSAV driver model has been verified comprehensively in a real MAGV platform. Finally, due to technical limitations on the available MAGV, it has been not possible to test the proposed HSAV driver model in off-road terrains. This is proposed as part of future research activities with a more convenient platform.

Overall, the author of this thesis expects that the results described in this chapter will lead to the execution of additional experiments and will eventually contribute to the development of a new generation of HSAVs. A proposal for future experiments and system enhancements is given in the last chapter of this thesis.

Chapter 6

Conclusions and future work

Professional drivers are able to control the car at the limits of handling, often exhibiting unparalleled driving skills. It is expected, therefore, that in order to produce Autonomous Vehicles (AV) showing an extended and safer operating envelope, these will be required to reproduce certain advanced driving patterns. This thesis has been elaborated with the aim to realise the previous statement. Due to the task complexity, this problem has been subdivided into two basic domains: vehicle perception and vehicle motion control.

Vehicle perception groups a wide range of research lines such as obstacle detection (e.g. traffic, pedestrian), road recognition (e.g. driveable surface), friction coefficient monitoring (e.g. slip-based friction potential identification), or vehicle motion state estimation (e.g. lateral velocity estimation). Following a bottom-up design strategy, the focus in this thesis has been placed on low-level perception subsystems critical for vehicle motion control. These are vehicle motion state estimation, tyre force virtual sensing and road friction monitoring. Specifically, different solutions employing model-based Kalman filtering techniques (EKF, UKF) have been proposed to infer the vehicle motion states from an inexpensive set of onboard measurements. Due to the uncertainty and complexity associated with the tyre friction modelling problem, an effort has been placed in offering tyre-model-less solutions based on "random-walk" and data-based tyre force modelling approaches. The combination of these solutions with machine-learning-based fitting techniques has lead to the elaboration of novel tyre-road friction learning functions. These functions are aimed at providing not only the maximum tyre-road friction factor but also the complete tyre friction curve. It is expected that the introduction of intelligent subsystems capable of learning the friction characteristics of unknown surfaces will be very relevant for developing autonomous vehicles with surface-based adaptation skills. These low-level subsystems may be combined with other high-level perception modules (e.g. machine vision-based terrain classification) giving as a result more robust and accurate vehicle adaptation skills. In essence, the major aim of the vehicle perception subsystems is to provide the motion state feedback and tyre-friction information required by the vehicle motion control layer. Therefore, the introduction of enhanced perception modules will permit the development of more sophisticated motion controllers. As an example, a rough terrain classification (e.g. wet tarmac) provided by a machine vision layer may be used to initialise the references of a certain vehicle motion controller, thus warning the system from a potentially hazardous situation. Once the system intervention has been triggered, the references can be re-adjusted with a more precise friction feature vector provided by a low-level slip-based friction learning module.

Following the previous bottom-up design methodology, the motion control problem has been approached in this thesis in two steps. In the first place, the vehicle motion controllers have been studied without considering the road geometry. The high body slip stabilisation case has been emphasised in this thesis due to its relevance for vehicle stability control on slippery surfaces and minimum-time-cornering on loose surfaces. Due to the strong tyre slip coupling exhibited at high body slip angles, centralised MIMO control architectures (LQR, MPC) have been proposed to optimally combine the powertrain and steering actuators offered by modern MAGV platforms. In addition, a machine-learning-based approach has been presented in combination with the traditional model-based reference derivation process. In brief, the former approach is proposed as an alternative way to extract the motion control references directly from field tests when the absence of a suitable tyre-friction model does not permit the execution of a model-based reference optimisation. On the other hand, this tyre-model-less advantage is limited by the necessity of converting the MAGV into a “driveable” configuration (find a suitable torque - pedal function) to manually drift and generate the training dataset. This limits the possibility of exploiting the full chassis potential by means of model-based optimisation for maximum centripetal acceleration, which is of particular interest for minimum-time cornering on loose surfaces. A possible solution to extract the maximum out of both perspectives may be to substitute the tyre model by a machine-learning-based friction model (e.g. Neural Network) and integrate it into the model-based reference optimisation loop. A rallycross case study adopting this methodology has been proposed in this thesis.

Secondly, a novel two-level structure has been proposed to achieve simultaneous high body slip control and path-following. A trajectory control block has been placed in a high-level layer to “correct” the low-level vehicle dynamics references based on the vehicle position and orientation error with respect to the reference path. The control action of the high-level layer has been realised adopting a PID-based control law. This preliminary system resembles highly-skilled drivers, who are able to sustain a high body slip angle along changing road geometries like spirals or clothoids. Moreover, as these drivers are able to adapt their behaviour to a wide range of road terrains, a friction compensation feature was added to the proposed structure. Different solutions were particularised for the model-based and data-based reference derivation approaches described in the previous paragraph. In particular, friction variations along rigid surfaces (e.g. dry tarmac, wet tarmac) are handled by means of a model-based friction scaling factor determined using RLS. For scenarios where a model-based reference derivation is not possible, a data-based approach relying on a braking-based road terrain classifier is proposed. Once again, the major limitation of the former approach lies in the necessity of generating a suitable training dataset on different road terrains with a constrained MAGV platform. As the last step, the preliminary path-following drifting system was enhanced, giving, as a result, a Highly-Skilled Autonomous Vehicle (HSAV) model capable of exhibiting a more sophisticated driving behaviour. Essentially, the proposed HSAV is able to drive along a race track combining racing-line path-following and drift path-following modes, as professional Drift or Rallycross drivers do. Moreover, the hybrid friction adaptation loop described in the previous paragraph (Neural Network friction model embedded in a model-based reference optimisation) was implemented in the HSAV to adapt the high body slip references in the presence of progressive friction changes.

All the solutions described in this thesis have been developed using high-fidelity vehicle dynamics simulation software. Specifically, during early development stages, the commercial package IPG-CarMaker was employed for the system SiL verification. A comprehensive virtual testing program formed by standardised open loop and closed loop driving manoeuvres was followed to test the virtual sensors. Moreover, additional experiments were performed with a DiL setup in order to subject the virtual sensors to a set of non-standardised manoeuvres (e.g. drift driving). During this process, special care was taken to build a realistic virtual testing environment. Thus, details like feedback noise addition, actuator constraints or vertical road profiling were considered to increase the simulation fidelity. Overall, this SiL process was aimed at implementing, debugging and benchmarking relevant conceptual ideas. After the SiL stage, the systems were subjected to a HiL verification process using the ROBORACE HiL setup. Specifically, this HiL setup uses the RT target machine mounted on the experimental MAGV. The vehicle behaviour is simulated using the real-time high-fidelity RFPro environment. The proposed systems were implemented in Simulink Real-Time and verified in a wide range of drifting test cases executed in a virtual wide open platform. This process was necessary to pre-calibrate the systems considering specific details of the final target vehicle. Some of these are the actuator constraints imposed by the target vehicle fail-safe strategies or the ECU communication latencies. Moreover, due to the costs associated with the experimental MAGV, this process was completed with a relevant number of sign-off sessions supervised by the ROBORACE software team.

Finally, in order to evidence the validity of the proposed solutions in real situations not captured by the SiL or HiL environments, additional experimental activities were executed with the fully instrumented JLR VBOTT and the ROBORACE DevBOT platform. These activities were completed during the course of this thesis as part of a PhD secondment hosted at the Tyre-CAE and Modelling group of Jaguar Land Rover (Gaydon, UK) and the professional research activities carried out at ARRIVAL Software (Banbury, UK). In the first place, the tyre force virtual sensing and friction learning tools introduced earlier were revisited and applied to the in-vehicle tyre characterisation problem. In essence, tyre-model-less virtual sensors were proposed as a cost-effective alternative to Wheel Force Transducers and the friction learning tools as an alternative to the time-consuming tyre fitting procedure. These activities lead to the elaboration of a virtual sensor for inexpensive tyre-friction characterisation, which was verified in a complete tyre characterisation program performed in dry tarmac (IDIADA, Spain) and snow (REVI, Sweden) with the JLR VBOTT. With regards to the professional activities carried out at ARRIVAL Software, a comprehensive testing program was defined to implement and verify the HSAV driver model in the ROBORACE DevBOT platform. Specifically, the complete model implementation was subdivided into three stages: high body slip stabilisation, simple path-following and advanced path-following. Several testing sessions were performed at Millbrook proving ground (UK) in dry and wet tarmac with the support of the ROBORACE crew.

Overall, the results obtained during the course of this research have evidenced that it is possible to design autonomous systems exhibiting advanced driving skills using current MAGV platforms. In addition to this, the virtual testing methodology (SiL, HiL) adopted during the course of this research has led to successful results on the track, reducing significantly the development cost and implementation time of the proposed systems. Despite the fact that further developments are still needed before these solutions can be standardised and implemented cost-effectively in future commercially available MAGV platforms, the author of this thesis expects that this research will significantly contribute to the development of a new generation of HSAVs. Additional guidelines to facilitate the realisation of this goal are provided in the following paragraphs.

6.1 On the road to highly-skilled autonomous vehicles: guidelines for the future

Due to technical limitations on the available MAGV platform, it has been not possible to perform additional experiments with the HSAV model on extreme off-road terrains. These are proposed here as part of potential future research activities once a more convenient off-road MAGV platform is available. Such research platform may be seen as an off-road DevBOT version and could be based on a compact-class rally chassis incorporating individual torque control, steer control and electro-hydraulic braking system. Current research trends indicate that experiments on loose surfaces will be of particular interest to approach the minimum-time cornering problem on gravel or snow, where professional drivers drift to increase the vehicle centripetal acceleration. These activities could eventually lead to the development of enhanced Autonomous Driving Assistance Functions (ADAS) for lane-departure avoidance on low-manoeuvrability loose surfaces.

Data-based approaches have been proposed in this thesis to facilitate the implementation of the high body slip controllers on loose surfaces. It is expected that in order to apply these solutions cost-effectively in the long term, it will be necessary to adopt virtual sensing techniques to generate the training datasets necessary to capture the tyre-friction characteristics. Still, tyre-model-less virtual sensing of individual lateral forces is a challenge that needs to be carefully treated. Despite the fact that solutions based on the vertical load proportionality principle are suitable for conventional vehicle platforms, this may lead to inaccuracies during severe torque vectoring intervention in modern MAGV architectures. In these conditions, the inner and outer tyres may be subjected to drastically different longitudinal forces, which will alter the even longitudinal slip assumption considered on the previous principle. The author of this thesis expects that the incorporation of additional strain-based measurements could help to sense the lateral force asymmetry and facilitate the resolution of this problem.

Despite the fact that relevant low-level virtual sensors have been already integrated into the feedback loop of the systems proposed in this thesis, there are still several perception subsystems that need to be progressively tested and integrated into future HSAV models. From bottom to top, current research lines indicate that steering effort measurements provided by modern Electric Power Steering (EPS) systems can be used to sense friction changes on the road friction potential with reduced lateral excitation. These may be combined with current slip-based friction monitoring approaches and at a higher level, with terrain classification based on machine vision. The latter solution could be utilised in the future to provide a rough estimate of the friction coefficient needed to initialise the low-level motion control functions. These systems may be supported by the information derived from vehicle-to-vehicle (V2V) or vehicle-to-infrastructure (V2I) communication technologies. As an ultimate goal, future autonomous vehicles should be able to upload the friction characteristics corresponding to different route locations to a centralised friction monitoring server, thus facilitating an efficient live identification of the friction changes along a predefined route. In addition to this, machine-vision techniques based on high-resolution cameras could be employed to support the estimation of the vehicle motion states (currently carried out using model-based or kinematic-based state estimation approaches).

Finally, during the elaboration of the HSAV described in this thesis, it has been assumed that a high-level perception layer exists to provide relevant information regarding the vehicle location and road geometry. It is expected that future vehicles equipped with LiDARS and cameras will be able to apply sensor fusion strategies to facilitate this task. The current advances on this topic were materialised during the 2018 GOODWOOD Festival of Speed in which the driver-less platform ROBOCAR was able to complete a high-demanding road layout in fully GPS-less configuration. Future research activities will be oriented towards the implementation of the HSAV functions relying on GPS-less perception strategies and the completion of the previous research points.

Figure 6.1: ROBOCAR being assembled at the ROBORACE factory in Banbury, United Kingdom, (*Oxlep, driving economic growth, oxfordshirelep.com*).

Funding Acknowledgement

This thesis is part of the Interdisciplinary Training Network in Multi-Actuated Ground Vehicles (ITEAM) European program and has received funding from the European Unions Horizon 2020 research and innovation program under the Marie Sklodowska-Curie grant agreement No 675999.

Peer-reviewed contributions

- M. Acosta and S. Kanarachos. Tire lateral force estimation and grip potential identification using neural networks, extended kalman filter and recursive least squares. *Neural Computing and Applications, Springer*, 2017:1–21, 2017
- M. Acosta, S. Kanarachos, and M. Blundell. Virtual tyre force sensors: An overview of tyre model-based and tyre model-less state estimation techniques. *IMEChE part D: Journal of Automobile Engineering*, 232:1883–1930, 2018
- M. Acosta, S. Kanarachos, and M. E. Fitzpatrick. Robust virtual sensing for vehicle agile manoeuvring: A tyre-model-less approach. *IEEE Transactions on Vehicular Technology*, 67:1894 – 1908, 2018
- M. Acosta, S. Kanarachos, and M. Blundell. Road friction virtual sensing: A review of estimation techniques with emphasis on low excitation approaches. *MDPI Applied Sciences*, 7(12), 2017
- M. Acosta and S. Kanarachos. Teaching a vehicle to autonomously drift: A data-based approach using neural networks. *Knowledge-based Systems*, 153:12–28, 2018
- M. Acosta, M. Gladstone, J. Prins, C. Rayo, M. Furlan, J. Gutierrez, and A. O'Neill. On tyre force virtual sensing for future automated vehicle-based objective tyre testing (avbott). *Vehicle System Dynamics, Taylor and Francis*, In press., 2019
- M. Acosta, S. Kanarachos, and M. Blundell. Vehicle agile maneuvering: From rally drivers to a finite state machine approach. In *IEEE Symposium Series on Computational Intelligence, Athens (Greece)*, 2016. doi:10.1109/SSCI.2016.7850095
- M. Acosta, A. Alatorre, S. Kanarachos, A. Victorino, and A. Charara. Estimation of tire forces, road grade, and road bank angle using tire model-less approaches and fuzzy logic. In *IFAC World Congress, Toulouse (France)*, pages 15401–15407, 2017
- M. Acosta, S. Kanarachos, and M.E. Fitzpatrick. A hybrid hierarchical rally driver model for autonomous vehicle agile maneuvering in loose surfaces. In *International Conference on Informatics in Control, Automation and Robotics (ICINCO), Madrid (Spain)*, volume 2, pages 216–225, 2017

- M. Acosta, S. Kanarachos, and M.E. Fitzpatrick. A virtual sensor for integral tire force estimation using tire model-less approaches and adaptive unscented kalman filter. In *International Conference on Informatics in Control, Automation and Robotics (ICINCO), Madrid (Spain)*, volume 1, pages 386–397, 2017
- M. Acosta and S. Kanarachos. Optimized vehicle dynamics virtual sensing using metaheuristic optimization and unscented kalman filter. In *International Conference on Evolutionary and Deterministic Methods for Design Optimization and Control with Applications to Industrial and Societal Problems, EUROGEN, Madrid (Spain)*, 2017
- M. Acosta, S. Kanarachos, and M.E. Fitzpatrick. Accurate virtual sensing of vertical tire forces for enhanced handling dynamics. In *43rd Annual Conference of the IEEE Industrial Electronics Society, Beijing (China)*, 2017
- M. Acosta, S. Kanarachos, and M.E. Fitzpatrick. Optimized tire force estimation using extended kalman filter and fruit fly optimization. In *43rd Annual Conference of the IEEE Industrial Electronics Society, Beijing (China)*, 2017
- M. Acosta, S. Kanarachos, and M.E. Fitzpatrick. On full magv lateral dynamics exploitation: Autonomous drift control. In *IEEE Advanced Motion Control, Tokyo (Japan)*, 2018
- M. Acosta, V. Ivanov, and S. Malygin. On highly-skilled autonomous competition vehicles: An fsm for autonomous rallycross. In *IEEE International Conference on Mechatronics, Ilmenau (Germany)*, 2019
- V. Ricciardi, M. Acosta, K. Augsburg, V. Ivanov, and S. Kanarachos. Robust brake linings friction coefficient estimation for enhancement of ehb control. In *IEEE International Conference on Advanced Technologies (ICAT), Sarajevo (Bosnia and Herzegovina)*, 2017
- M. Acosta, S. Kanarachos, and M.E. Fitzpatrick. *Vehicle Dynamics Virtual Sensing Using Unscented Kalman Filter: Simulations and Experiments in a Driver-in-the-loop setup*, chapter Lecture Notes in Electrical Engineering, ICINCO. Springer (In press), 2017
- M. Acosta and S. Kanarachos. *Optimized Vehicle Dynamics Virtual Sensing using Metaheuristic Optimisation and Unscented Kalman Filter*, volume 49, chapter Advances in Evolutionary and Deterministic Methods for Design, Optimization and Control in Engineering and Sciences, EUROGEN. Springer, 2018
- V. Ricciardi, C. Sandu, M. Acosta, V. Ivanov, and B. Shyrokau. Torque vectoring control on ice for electric vehicles with individually actuated wheels. In *26th Symposium on Dynamics of Vehicles on Roads and Tracks (IAVSD), Gothenburg (Sweden)*, 2019

Appendix A

Vehicle models

A.1 Vehicle model summary

Table A.1: Summary of vehicle models used during this research (SiL).

Software-in-the-loop stage		
Model	Thesis Section	Description
Ford Fiesta Zetec	Chapter 3, S-3.2	IPG CarMaker model used during the data-based virtual sensing SiL stage (NN-based EKF and NN-based UKF).
Compact-class RWD	Chapter 3, S-3.3	IPG CarMaker model used during the random-walk virtual sensing SiL stage (RW-EKF).
Compact-class MAGV	Chapter 4, S-4.2.2 and S-4.3.1	IPG CarMaker model used during the model-based high body slip stabilisation and model-based Autonomous Drift Control.
Sport-class MAGV	Chapter 4, S-4.2.3 and S-4.3.1	IPG CarMaker model used during the data-based high body slip stabilisation and data-based Autonomous Drift Control.
ROBORACE DevBOT	Chapter 4, S-4.3.1.3 and S-4.3.2	IPG CarMaker model used during the SiL stage of the Arrival and Roborace drifting project.

TABLE A.2: Summary of vehicle models used during this research (HiL and vehicle experiments).

Hardware-in-the-loop stage		
Model	Thesis Section	Description
ROBORACE DevBOT	Chapter 4, S-4.2.4 and S-4.3.1.3	RFPro model used during the HiL stage of the Arrival and Roborace drifting project.
Experimental validation		
Model	Thesis Section	Description
Ford Fiesta Zetec	Chapter 3, S-3.2.1	Experimental vehicle used to correlate the Ford Fiesta Zetec IPG-CarMaker model.
JLR VBOTT	Chapter 5, S-5.1	Instrumented research vehicle used to test experimentally the virtual sensing algorithms.
ROBORACE DevBOT	Chapter 5, S-5.2	MAGV autonomous racing vehicle used during the Arrival and Roborace drifting project.

A.2 Experimental vehicles: Technical specifications.

A.2.1 Ford Fiesta Zetec

TABLE A.3: Technical specifications of the Ford Fiesta Zetec.

Parameter	Symbol	Value
Vehicle mass	m	1260 $[kg]$
Front semi-wheelbase	l_f	0.95 $[m]$
Rear semi-wheelbase	l_r	1.60 $[m]$
Front track width	tw_f	1.50 $[m]$
Rear track width	tw_r	1.50 $[m]$
Steering ratio	SR	16 $[-]$
Yaw inertia	I_ψ	2150 $[kgm^2]$
Power	P	55 $[kW]$

A.2.2 Jaguar Land Rover VBOTT

TABLE A.4: JLR VBOTT technical specifications.

Parameter	Symbol	Value
Vehicle mass	m	2720 $[kg]$
Front semi-wheelbase	l_f	1.45 $[m]$
Rear semi-wheelbase	l_r	1.45 $[m]$
Front track width	tw_f	1.6 $[m]$
Rear track width	tw_r	1.6 $[m]$
Steering ratio	SR	17 $[-]$
Yaw inertia	I_ψ	3700 $[kgm^2]$
Power	P	190 $[kW]$

A.2.3 ROBORACE DevBOT

TABLE A.5: ROBORACE DevBOT technical specifications [42].

Parameter	Symbol	Value
Vehicle mass	m	1250 $[kg]$
Front semi-wheelbase	l_f	1.6 $[m]$
Rear semi-wheelbase	l_r	1.3 $[m]$
Front track width	tw_f	1.55 $[m]$
Rear track width	tw_r	1.55 $[m]$
Front tyres	-	295/30 ZR18 Michelin Pilot Sport Cup 2
Rear tyres	-	345/30 ZR20 Michelin Pilot Sport Cup 2
Power	P	450 $[kW]$
Transmission gear ratio	6.25:1	[-]

Bibliography

[1] M. Abe. Trends of intelligent vehicle dynamics controls and their future. *NTN Technical Review*, 81, 2013.

[2] M. Acosta, A. Alatorre, S. Kanarachos, A. Victorino, and A. Charara. Estimation of tire forces, road grade, and road bank angle using tire model-less approaches and fuzzy logic. In *IFAC World Congress, Toulouse (France)*, pages 15401–15407, 2017.

[3] M. Acosta, M. Gladstone, J. Prins, C. Rayo, M. Furlan, J. Gutierrez, and A. O'Neill. On tyre force virtual sensing for future automated vehicle-based objective tyre testing (avbott). *Vehicle System Dynamics, Taylor and Francis*, In press., 2019.

[4] M. Acosta, V. Ivanov, and S. Malygin. On highly-skilled autonomous competition vehicles: An fsm for autonomous rallycross. In *IEEE International Conference on Mechatronics, Ilmenau (Germany)*, 2019.

[5] M. Acosta and S. Kanarachos. Optimized vehicle dynamics virtual sensing using metaheuristic optimization and unscented kalman filter. In *International Conference on Evolutionary and Deterministic Methods for Design Optimization and Control with Applications to Industrial and Societal Problems, EUROGEN, Madrid (Spain)*, 2017.

[6] M. Acosta and S. Kanarachos. Tire lateral force estimation and grip potential identification using neural networks, extended kalman filter and recursive least squares. *Neural Computing and Applications, Springer*, 2017:1–21, 2017.

[7] M. Acosta and S. Kanarachos. *Optimized Vehicle Dynamics Virtual Sensing using Metaheuristic Optimisation and Unscented Kalman Filter*, volume 49, chapter Advances in Evolutionary and Deterministic Methods for Design, Optimization and Control in Engineering and Sciences, EUROGEN. Springer, 2018.

[8] M. Acosta and S. Kanarachos. Teaching a vehicle to autonomously drift: A data-based approach using neural networks. *Knowledge-based Systems*, 153:12–28, 2018.

[9] M. Acosta, S. Kanarachos, and M. Blundell. Vehicle agile maneuvering: From rally drivers to a finite state machine approach. In *IEEE Symposium Series on Computational Intelligence, Athens (Greece)*, 2016. doi:10.1109/SSCI.2016.7850095.

[10] M. Acosta, S. Kanarachos, and M. Blundell. Road friction virtual sensing: A review of estimation techniques with emphasis on low excitation approaches. *MDPI Applied Sciences*, 7(12), 2017.

[11] M. Acosta, S. Kanarachos, and M. Blundell. Virtual tyre force sensors: An overview of tyre model-based and tyre model-less state estimation techniques. *IMEChE part D: Journal of Automobile Engineering*, 232:1883–1930, 2018.

[12] M. Acosta, S. Kanarachos, and M. E. Fitzpatrick. Robust virtual sensing for vehicle agile manoeuvring: A tyre-model-less approach. *IEEE Transactions on Vehicular Technology*, 67:1894 – 1908, 2018.

[13] M. Acosta, S. Kanarachos, and M.E. Fitzpatrick. Accurate virtual sensing of vertical tire forces for enhanced handling dynamics. In *43rd Annual Conference of the IEEE Industrial Electronics Society, Beijing (China)*, 2017.

[14] M. Acosta, S. Kanarachos, and M.E. Fitzpatrick. A hybrid hierarchical rally driver model for autonomous vehicle agile maneuvering in loose surfaces. In *International Conference on Informatics in Control, Automation and Robotics (ICINCO), Madrid (Spain)*, volume 2, pages 216–225, 2017.

[15] M. Acosta, S. Kanarachos, and M.E. Fitzpatrick. Optimized tire force estimation using extended kalman filter and fruit fly optimization. In *43rd Annual Conference of the IEEE Industrial Electronics Society, Beijing (China)*, 2017.

[16] M. Acosta, S. Kanarachos, and M.E. Fitzpatrick. *Vehicle Dynamics Virtual Sensing Using Unscented Kalman Filter: Simulations and Experiments in a Driver-in-the-loop setup*, chapter Lecture Notes in Electrical Engineering, ICINCO. Springer (In press), 2017.

[17] M. Acosta, S. Kanarachos, and M.E. Fitzpatrick. A virtual sensor for integral tire force estimation using tire model-less approaches and adaptive unscented kalman filter. In *International Conference on Informatics in Control, Automation and Robotics (ICINCO), Madrid (Spain)*, volume 1, pages 386–397, 2017.

[18] M. Acosta, S. Kanarachos, and M.E. Fitzpatrick. On full magv lateral dynamics exploitation: Autonomous drift control. In *IEEE Advanced Motion Control, Tokyo (Japan)*, 2018.

[19] C. Ahn. *Robust Estimation of road friction Coefficient, PhD Thessis.* University of Michigan, USA, 2011.

[20] A. Albinsson, F. Bruzelius, B Jacobson, and J. Fredriksson. Design of tyre force excitation for tyre road friction estimation. *Vehicle System Dynamics*, 55:208–230, 2017.

[21] A. Albinsson, F. Bruzelius, M. Jonasson, and B. Jacobson. Tire force estimation utilizing wheel torque measurements and validation in simulations and experiments. In *Proceedings of the 12th International Symposium on Advanced Vehicle Control*, pages 294–299, 2014.

[22] R. Allen, J. Rosenthal, and J.P. Chrstos. A vehicle dynamics tire model for both pavement and off-road conditions. *SAE Technical Papers*, 1997. doi:10.4271/970559.

[23] M. Andersson, F. Bruzelius, M. Casselgren, M. Gafvert, M. Hjort, J. Hulten, F. Habring, M. Klomp, G. Olsson, M. Sjodahl, J. Svendenius, S. Woxneryd, and B. Walivaara. *Road Friction Estimation.* Intelligent Vehicle Safety Systems, 2007.

[24] M. Andersson, F. Bruzelius, M. Casselgren, M. Gafvert, M. Hjort, S. Lofving, G. Olsson, J. Ronnberg, M. Sjodahl, S. Solyom, J. Svendenius, and S. Yngve. *Road Friction Estimation, part II.* Intelligent Vehicle Safety Systems, 2010.

[25] S Antonov, A Fehn, and A Kugi. Unscented Kalman filter for vehicle state estimation. *Vehicle System Dynamics*, 49(9):1497–1520, 2011.

[26] M. A. Arat and S. Taheri. Identification of road surface friction for vehicle safety systems. *SAE Technical paper 2014-01-0885*, 2014. doi:10.4271/2014-01-0885.

[27] R. Attia, R. Orjuela, and M. Basset. Coupled longitudinal and lateral control strategy improving lateral stability for autonomous vehicle. In *American Control conference (ACC)*, 2012.

[28] R. Attia, R. Orjuela, and M. Basset. Combined longitudinal and lateral control for automated vehicle guidance. *Vehicle System Dynamics: International Journal of Vehicle Mechanics and Mobility*, 52:261–279, 2014.

[29] IPG Automotive. IPG automotive Gmbh, Bannwaldallee 60, Karlsruhe, Germany. `https://ipg-automotive.com/products-services/simulation-software/carmaker/`, 2019. [Online; accessed 14-January-2019].

[30] I. Belic. Neural networks and static modeling. *Recurrent Neural Networks and Soft Computing, Dr. Mahmoud ElHefnawi*, 2012.

[31] K. Bengler, K. Dietmayer, B. Färber, M. Maurer, C. Stiller, and H. Winner. Three decades of driver assistance systems. *IEEE Intelligent Transportation Systems Magazine*, 6(4):6–22, 2014.

[32] A. Benine-Neto, S. Scalzi, S. Mammar, and M. Netto. Dynamic controller for lane keeping and obstacle avoidance assistance system. In *13th International IEEE Annual Conference on Intelligent Transportation Systems*, 2010.

[33] K. Berntorp, B. Olofsson, B. Bernhardsson, K. Lundhal, and L. Nielsen. Models and methodology for optimal vehicle maneuvers applied to a hairpin turn. In *American Control Conference (ACC)*, 2013.

[34] K. Berntorp, B. Olofsson, K. Lundahl, and L. Nielsen. Models and methodology for optimal trajectory generation in safety-critical road-vehicle manoeuvres. *Vehicle System Dynamics: International Journal of Vehicle Mechanics and Mobility*, 52:1304–1332, 2014.

[35] P. N. Bhujbal and S. P. Narote. Lane departure warning system based on hough transform and euclidean distance. In *2015 Third International Conference on Image Information Processing*, 2015.

[36] M. Blundell and D. Harty. *The Multibody Systems Approach to Vehicle Dynamics*. El Sevier, 2004.

[37] F. Braghin, F. Cheli, and E. Sabbioni. Environmental effects on pacejka's scaling factors. *Vehicle System Dynamics: International Journal of Vehicle Mechanics and Mobility*, 44(7):547–568, 2006.

[38] B. Breuer, U. Eichhorn, and J. Roth. Measurement of tyre/road friction ahead of the car and inside the tyre. In *Proceedings of the International Symposium on Advanced Vehicle Control*, 1992.

[39] M. Cannon. *C21 Model Predictive Control, 4 Lectures Hilary Term, Oxford University*. mark.cannon@eng.ox.ac.uk, 2016.

[40] D. Casanova. *On Minimum Time Vehicle Manoeuvring: The Theoretical Optimal Lap, PhD Thesis*. Cranfield University, 2000.

[41] V. Cerone, M. Milanese, and D. Regruto. Combined automatic lane-keeping and driver's steering through a 2-dof control strategy. *IEEE Transactions on Control Systems Technology*, 17(1):135–142, 2009.

[42] C. Chatzikomis, A. Sorniotti, P. Gruber, M. Zanchetta, D. Willans, and B. Balcome. Comparison of path tracking and torque-vectoring controllers for autonomous electric vehicles. *IEEE Transactions on Intelligent Vehicles*, 3, 2018.

[43] F. Cheli, E. Leo, S. Melzi, and E. Sabbioni. On the impact of 'smart tyres' on existing abs/ebd control systems. *Vehicle System Dynamics*, 48:255–270, 2010.

[44] F. Cheli, E. Sabbioni, M. Sbrosi, Brusarosco, S. Melzi, and V. d'alessandro. Enhancement of abs performance through on-board estimation of the tires' response by means of smart tires. *SAE Technical Papers 2011-01-0991*, 2011. doi:10.4271/2011-01-0991.

[45] W. Chen, H. Xiao, Q. Wang, L. Zhao, and M. Zhu. *Integrated Vehicle Dynamics and Control*. John Wiley and Sons, Singapore Pte.Ltd, 2016.

[46] M. Cutler and J.P.How. Autonomous drifting using simulation-aided reinforcement learning. In *IEEE International Conference on Robotics and Automation*, 2016.

[47] J. Deur, V. Ivanovic, D. Pavkovic, J. Asgari, D. Hrovat, M. Troulis, and C. Miano. On low-slip tire friction behavior and modeling for different road conditions. In *IAVSD Symposium*, 2005. Milan, Italy.

[48] M. Doumiati, A. Charara, A. Victorino, and D. Lechner. *Vehicle Dynamics Estimation using Kalman Filtering*. Wiley-ISTE, 2012.

[49] M. Doumiati, A. Victorino, A. Charara, and D. Lechner. Estimation of vehicle lateral tire-road forces: A comparison between extended and unscented kalman filtering. In *European Control Conference (ECC)*, pages 4804–4809, 2009.

[50] J. Edelmann and M. Plöchl. Handling characteristics and stability of the steady-state powerslide motion of an automobile. *Regular and Chaotic Dynamics*, 14:682–692, 2009.

[51] C. M. Filho, D. F. Wolf, V. Grassi, and S. Osório. Longitudinal and lateral control for autonomous ground vehicles. In *IEEE Intelligent Vehicle Symposium*, 2014.

[52] International Organization for Standardization. *BS ISO 8608:2016 Mechanical vibration - Road surface profiles - Reporting of measured data.* BSI Standards publication, 2016.

[53] Audi France. Walter Röhrl, champion du monde des rallyes 1980 et 1982, au volant de l'audi quattro s1. `https://www.youtube.com/watch?v=wqREtbLe4sY`, 2010. [Online; accessed 10-January-2019].

[54] Y. Gao. *Longitudinal Velocity and Road Slope Estimation in Hybrid/Electric Vehicles. Development and evaluation of an adaptive Kalman filter. Master thesis.* Chalmers University, 2013.

[55] J. Gonzales, F. Zhang, K. Li, and F. Borrelli. Autonomous drifting with onboard sensors. In *Advanced Vehicle Control (AVEC)*, 2016.

[56] A. Gray, Y. Gao, T. Lin, K. Hedrick, H. Tseng, and F. Borrelli. Predictive control for agile semi-autonomous ground vehicles using motion primitives. In *American Control Conference*, 2012.

[57] J.-O. Hahn, R. Rajamani, and L. Alexander. Gps-based real-time identification of tire–road friction coefficient. *IEEE Transactions on Control Systems Technology*, 10:331–343, 2002.

[58] H. Hamann, J. Hedrick, S. Rhode, and F. Gauterin. Tire force estimation for a passenger vehicle with the unscented kalman filter. In *IEEE Intelligent Vehicles Symposium*, 2014. doi:10.1109/IVS.2014.6856391.

[59] I.C. Han, B.C. Luan, and F.C. Hsieh. Development of autonomous emergency braking control system based on road friction. In *IEEE International Conference on Automation Science and Engineering (CASE, Taipei, Taiwan)*, 2014.

[60] K. Han, Y. Hwang, E. Lee, and S. Choi. Robust estimation of maximum tire-road friction coefficient considering road surface irregularity. *International Journal of Automotive Technology*, 17:415–425, 2016.

[61] Y. Hattori. Optimum vehicle dynamics control based on tire driving and braking forces. toyota RCDL. `https://www.tytlabs.com/english/review/rev384epdf/e384_023hattori.pdf`, 2003. [Online; accessed 10-September-2018].

[62] R.L. Haupt and S.H. Haupt. *Practical Genetic Algorithms, Second Edition.* John Wiley, 2004.

[63] J. He, H. Rong, J. Gong, and W. Huang. A lane detection method for lane departure warning system. In *2010 International Conference on Optoelectronics and Image Processing*, 2010.

[64] B. Heißing and M. Ersoy. *Chassis handbook. Fundamentals, Driving dynamics, Components, Mechatronics, Perspectives.* Springer Verlag, 2011.

[65] C. Hewitt, I. Politis, T. Amanatidis, and A. Sarkar. Assessing public perception of self-driving cars: the autonomous vehicle acceptance model. In *24th International Conference on Intelligent User Interfaces*, 2019.

[66] R. Hindiyeh. *Dynamics and Control of Drifting in Automobiles, Ph.D Thesis.* Stanford University, 2013.

[67] Y. Hirano. Model based development of an integrated control of front steering and torque vectoring differential gear system. In *Proceedings of the SICE Annual Conference*, 2016.

[68] Y. Hirano. Development of an integrated control of front steering and torque vectoring differential gear system using modelica. In *Proceedings of the 12th International Modelica Conference*, 2017.

[69] R. G. Hoogendoorn, H. J. Breukink, and B. van Arem. A context aware intelligent speed adaptation system: A field operational test. In *IEEE 15th International Conference on Intelligent Transportation Systems*, 2012.

[70] M. Hrgetic, J. Deur, V. Ivanovic, and E. Tseng. Vehicle sideslip angle ekf estimator based on nonlinear vehicle dynamics model and stochastic tire forces modeling. *SAE International Journal of Passenger Cars - Mechanical Systems*, 7:86–95, 2014.

[71] C. Ifedi. *A High Torque Density, Direct Drive In-wheel Motor for Electric Vehicles, PhD thesis.* Newcastle University, 2013.

[72] ISO. *ISO 4138. Road vehicles, Steady State circular driving behavior.* International Standard Organisation, ISO, 2012.

[73] V. Ivanov. *Advanced automotive active safety systems: Focus on integrated chassis control for conventional and electric vehicles with identification of road conditions. Thesis for Dr.-Ing. habil.* TU-Ilmenau, 2017.

[74] V. Ivanov and D. Savitski. Systematization of integrated motion control of ground vehicles. *IEEE Access*, 3:1–20, 2015.

[75] J. Jang. Ieee transactions on systems, man, and cybernetics. *Anfis: Adaptive-network-based fuzzy inference system*, 23:665–685, 1993.

[76] A. Jayashankar. *Experimental and Modeling Study of the Influence of Support Stiffness on Load Sensing Bearings, Msc Thesis.* Delft University of Technology, 2011.

[77] F. Jimenéz, J. E. Naranjo, and O. Gómez. Autonomous manoeuvring systems for collision avoidance on single carriageway roads. *Sensors*, 12:16498–16521, 2012.

[78] U. Kiencke and L. Nielsen. *Automotive Control Systems: For engine, driveline, and Vehicle.* Springer, 2005.

[79] I. Kiliç, A. Yazici, O. Yildiz, M. Özçelikors, and A. Ondogan. Intelligent adaptive cruise control system design and implementation. In *10th System of Systems Engineering Conference (SoSE)*, 2015.

[80] H. Kopetz and S. Poledna. Autonomous emergency braking: A system-of-systems perspective. In *IEEE/IFIP Conference on Dependable Systems and Networks Workshop*, 2013.

[81] W. Kortüm and P. Lugner. *Systemdynamik und Regelung von Fahrzeugen.* Berlin: Springer-Verlag, 1994.

[82] S. Koskinen. *Sensor Data Fusion Based Estimation of Tyre-Road Friction to Enhance Collision Avoidance, PhD dissertation.* VTT, 2010.

[83] Y. Kou, H. Peng, and D. Jung. Worst-case evaluation for integrated chassis control systems. *Vehicle System Dynamics*, 46:329–340, 2008.

[84] F. L. Lewis, D. Vrabie, and V. L. Syrmos. *Optimal Control, Third edition.* John Wiley and Sons, 2012.

[85] J. Li, J. Yi, Y. Zhang, and Z. Liu. Understanding agile-maneuver driving strategies using coupled longitudinal / lateral vehicle dynamics. In *ASME Dynamics and Control Conference*, 2011.

[86] K. Li, J. A. Misener, and K. Hedrick. On-board road condition monitoring system using slip-based tyre–road friction estimation and wheel speed signal analysis. *Proceedings of the Institution of Mechanical Engineers, Part K: Journal of Multi-body Dynamics*, 221:129–146, 2007.

[87] L. Li, K. Yang, G. Jia, X. Ran, J. Song, and Z.-Q. Han. Comprehensive tire–road friction coefficient estimation based on signal fusion method under complex maneuvering operations. *Mechanical Systems and Signal Processing*, 2015:259–276, 2015.

[88] C.Y. Liang, R. Allen, J. Rosenthal, and J.P. Chrstos. Tire modeling for off-road vehicle simulation. *SAE Technical Papers*, 2004. doi:10.4271/2004-01-2058.

[89] L. Liu, X. Ran, and L. Li. Hybrid vehicle road loads simulation and correlation. *Sae Technical Paper 2007-01-1202*, 2007. doi:10.4271/2007-01-1202.

[90] LMC. *Autonomous Vehicles: The outlook for Autonomous Vehicle sales and their impact to 2050.* LMC automotive, 2018.

[91] K. Lundahl and B. Olofsson. *Optimal Vehicle Maneuvers for Different Road Conditions.* Linköping University and Lund University, 2014.

[92] S. Melzi and E. Sabbioni. On the vehicle sideslip angle estimation through neural networks: Numerical and experimental results. *Mechanical Systems and Signal Processing*, 25:2005–2019, 2011.

[93] V. Milanés, J. Pérez, J. Godoy, and E. Onieva. A fuzzy aid rear-end collision warning/avoidance system. *Expert Systems with Applications*, 39:9097–9107, 2012.

[94] W.F. Milliken and D.L. Milliken. *Race Car Vehicle Dynamics.* SAE International, 1995.

[95] S. Miyata, T. Nakagami, S. Kobayashi, T. Izumi, H. Naito, A. Yanou, H. Nakamura, and S. Takehara. Improvement of adaptive cruise control performance. *EURASIP Journal on Advances in Signal Processing*, 2010, 2010.

[96] Cathy Morrow. Automotive manufacturers invest in digitization, autonomous and electric vehicles, forbes. `https://www.forbes.com/sites/cathymorrowroberson/2019/03/24/automotive-manufacturers-invest-with-a-focus-on-digitization-autonomous/and-electric-vehicles/`, 2019. [Online; accessed 14-April-2019].

[97] MEMA. The motor and equipment Manufacturers Association. A roadmap to safer driving through advanced driver assistance systems. `http://image-src.bcg.com/Images/MEMA-BCG-A-Roadmap-to-Safer-Driving-Sep-2015_tcm9-63787.pdf`, 2015. [Online; accessed 06-January-2018].

[98] S. Müller, M. Uchanski, and K. Hedrick. Estimation of the maximum tire-road friction coefficient. *Journal of Dynamic Systems, Measurement, and Control*, 125(4):607–617, 2003.

[99] P. J. Narula, A. Heitmann, V. Held, and A. Kulms. Chassis control system based on the concept of moding. In *SAE 2011 World Congress and Exhibition*, 2011.

[100] J. Nilsson, J. Silvin, M. Brannstrom, E. Coelingh, and J. Fredriksson. If, when, and how to perform lane change maneuvers on highways. *IEEE Intelligent Transportation Systems Magazine.*, 8:68–78, 2016.

[101] C. Nuthong. *Estimation of tire-road friction forces using extended and unscented kalman filtering for advanced vehicle control, PhD Thesis.* Universität der Bundeswehr München, Germany, 2009.

[102] K. Ogata. *Modern Control Engineering.* Prentice Hall, 2010.

[103] G. Ostermeyer. On the dynamics of the friction coefficient. *Wear*, 254:852–858, 2003.

[104] H.B. Pacejka. *Tire and Vehicle Dynamics.* Butterworth-Heinemann, 2012.

[105] W. Pananurak, S. Thanok, and M. Parnichkun. Adaptive cruise control for an intelligent vehicle. In *IEEE International Conference on Robotics and Biomimetics*, 2008.

[106] A. Paul, R. Chauhan, R. Srivastava, and M. Baruah. Advanced driver assistance systems. *SAE Technical Papers*, 2016.

[107] R. Rajamani. *Vehicle Dynamics and Control.* Springer, 2012.

[108] L. Ray. Nonlinear state and tire force estimation for advanced vehicle control. *IEEE Transactions on Control Systems Technology*, 3(1):117–124, 1995.

[109] L. Ray. Nonlinear tire force estimation and road friction identification: Simulation and experiments. *Automatica*, 33(97):1819–1833, 1997.

[110] M. Rhudy and Y. Gu. *Understanding Nonlinear Kalman Filters, Part II: An implementation Guide.* Interactive Robotics Letters, Tutorial, 2013.

[111] V. Ricciardi, M. Acosta, K. Augsburg, V. Ivanov, and S. Kanarachos. Robust brake linings friction coefficient estimation for enhancement of ehb control. In *IEEE International Conference on Advanced Technologies (ICAT), Sarajevo (Bosnia and Herzegovina)*, 2017.

[112] V. Ricciardi, C. Sandu, M. Acosta, V. Ivanov, and B. Shyrokau. Torque vectoring control on ice for electric vehicles with individually actuated wheels. In *26th Symposium on Dynamics of Vehicles on Roads and Tracks (IAVSD), Gothenburg (Sweden)*, 2019.

[113] V. Ricciardi, D. Savitski, K. Augsburg, and V. Ivanov. Estimation of brake friction coefficient for blending function of base braking control. *SAE International Journal of Passenger Cars and Mechanical Systems.*, 10:774–785, 2017.

[114] SAE. *SAE J3016 Standard: Taxonomy and Definitions for Terms Related to On-Road Motor Vehicle Automated Driving Systems.* SAE, 2014.

[115] D. Savitski, V. Ivanov, K. Augsburg, M. Dhaens, S. Els, and C. Sandu. State-of-the-art and future developments in integrated chassis control for ground vehicles. In *13th European Conference of the ISTVS*, 2015.

[116] D. Savitski, D. Schleinin, V. Ivanov, and K. Augsburg. Individual wheel slip control using decoupled electro-hydraulic brake system. In *43rd Annual Conference of the IEEE Industrial Electronics Society*, 2017.

[117] D. Savitski, D. Schleinin, V. Ivanov, and K. Augsburg. Robust continuous wheel slip control with reference adaptation: Application to brake system with decoupled architecture. *IEEE Transactions on Industrial Informatics*, Early access, 2018.

[118] M.W. Sayers and S.M. Karamihas. *The little Book of Profiling (Basic information about Measuring and Interpreting Road Profiles).* University of Michigan, 1998.

[119] J. Segers. *Analysis Techniques for Racecar Data Acquisition, second edition.* SAE International, 2014.

[120] Y. Shibahata, K. Shimada, and T. Tomari. Improvement of vehicle maneuverability by direct yaw moment control. *Vehicle System Dynamics*, 22:465–481, 1993.

[121] Mechanical Simulation Corporation. CARSIM, Mechanical Simulation Corporation, USA. `https://www.carsim.com/`, 2019. [Online; accessed 14-January-2019].

[122] K. Singh and S. Taheri. Estimation of tire-road friction coefficient and its application in chassis control systems. *Systems Science and Control Engineering*, 3(1):39–61, 2014.

[123] MSC Software. *ADAMS/Tire.* MSC Software, 2009.

[124] MSC Software. Adams, MSC Software, Newport Beach, CA, USA. `https://www.mscsoftware.com/product/adams-car`, 2019. [Online; accessed 14-January-2019].

[125] T. Sun, H. Guo, J. Cao, L. Chai, and Y. Sun. Study on integrated control of active front steering and direct yaw moment based on vehicle lateral velocity estimation. *Mathematical Problems in Engineering, Hindawi*, 2013, 2013.

[126] J. Svendenius. *Tire Modeling and Friction Estimation, PhD Thesis.* Department of Automatic Control, Lund University, Sweden, 2007.

[127] Dassault Systemes. Simpack, Dassault Systemes, Gilching, Germany. `http://www.simpack.com/`, 2019. [Online; accessed 14-January-2019].

[128] D. Tavernini, M. Massaro, E. Velenis, D. Katzourakis, and R. Lot. Minimum time cornering: the effect of road surface and car transmission layout. *Vehicle System Dynamics: International Journal of Vehicle Mechanics and Mobility*, 51(10):1533–1547, 2013.

[129] Volvo Trucks. *Volvo Trucks Safety Report 2017, Volvo Trucks Accident Research Team.* Volvo, 2017.

[130] A. Van Zanten. Evolution of electronic control systems for improving the vehicle dynamic behavior. In *Proceedings of the 6th International Symposium on Advanced Vehicle Control (AVEC)*, 2002.

[131] E. Velenis. Expert driving techniques at the limit of handling. In *Vehicle Dynamics and Control Conference (VDC). Fitzwilliam College, Cambridge, UK*, 2011.

[132] E. Velenis, E. Frazzoli, and P. Tsiotras. On steady-state cornering equilibria for wheeled vehicles with drift. In *IEEE Decision and Control Conference*, 2009.

[133] E. Velenis, E. Frazzoli, and P. Tsiotras. Steady-state cornering equilibria and stabilisation for a vehicle during extreme operating conditions. *International Journal of Vehicle Autonomous Systems*, 8(2-3):217–241, 2010.

[134] E. Velenis, D. Katzourakis, E. Frazzoli, P. Tsiotras, and R. Happee. Steady-state drifting stabilization of rwd vehicles. *Control Engineering Practice*, 19(11):1363–1376, 2011.

[135] E. Velenis, P. Tsiotras, and J. Lu. Modeling aggressive maneuvers on loose surfaces: The cases of trail-braking and pendulum-turn. In *IEEE European Control Conference.*, 2007.

[136] E. Velenis, P. Tsiotras, and J. Lu. Optimality properties and driver input parameterization for trail-braking cornering. *European Journal of Control*, 2008(4), 2008.

[137] C. Vivas-Lopez, D. Hernandez-Alcantara, J.C. Tudon-Martinez, and R. Morales-Menendez. Review on global chassis control. In *5th IFAC Symposium on System Structure and Control*, 2013.

[138] E. A. Wan and R. Van Der Merwe. The unscented kalman filter for nonlinear estimation. In *Adaptive Systems for Signal Processing, Communications, and Control Symposium*, 2000.

[139] L. Wang. *Model Predictive Control System Design and Implementation Using Matlab*. Springer, 2009.

[140] J. Wei, Y. Zhuoping, and L. Zhang. Integrated chassis control system for improving vehicle stability. In *IEEE International Conference on Vehicular Electronics and Safety*, 2006.

[141] M. Wilkin, W. Manning, D. Crolla, and M.C. Levesley. Use of an extended kalman filter as a robust tire force estimator. *Vehicle Systems Dynamics*, 44(sup1):50–59, 2006.

[142] I.R. Wilmink, G.A. Klunder, and B. van Arem. Traffic flow effects of integrated full-range speed assistance (IRSA). In *IEEE Intelligent Vehicles Symposium, Istanbul, Turkey*, 2007.

[143] J. Yi. On hybrid physical/dynamic tire-road friction model. In *ASME Dyn. Syst. Control Conf.*, 2009.

[144] J. Yi, J. Li, J. Lu, and Z. Liu. On the stability and agility of aggressive vehicle maneuvers: A pendulum-turn maneuver example. *IEEE Transactions on Control Systems Technology*, 20:663–676, 2012.

[145] S. Yim and K. Yi. Design of active roll control system and integrated chassis control for hybrid 4wd vehicles. In *14th International IEEE Conference on Intelligent Transportation Systems*, 2011.

[146] P. Young. *Recursive Estimation and Time-Series Analysis*. Springer, 2011.

[147] J. Zhao and A. El Kamel. Integrated longitudinal and lateral control system design for autonomous vehicles. *IFAC Proceeding Volumes*, 42:496–501, 2009.

[148] J. Zhao, J. Zhang, and B. Zhu. Development and verification of the tire/road friction estimation algorithm for antilock braking system. *Mathematical Problems in Engineering, Hindawi Publishing Corporation*, 2014. doi:10.1155/2014/786492.

[149] M. Zhao. *Advanced Driver Assistant System: Threats, Requirements, Security Solutions. Technical White Paper*. Intel, 2015.

[150] B. Zhu, Y. Chen, J. Zhao, and Y. Su. Design of an integrated vehicle chassis control system with driver behavior identification. *Hindawi Publishing Corporation*, 2015, 2015.

List of Figures

List of Tables

Symbols

a_x	Long. acceleration	$[m/s^2]$
a_y	Lat. acceleration	$[m/s^2]$
V	Velocity module	$[m/s]$
μ	Tyre friction	[-]
$\mu_{\max}$	Road friction potential	[-]
λ	Tyre long. slip	[-]
m	Vehicle mass	$[kg]$
$\dot{\psi}$	Yaw rate	$[rad/s]$
v_x	Long. velocity	$[m/s]$
v_y	Lat. velocity	$[m/s]$
F_x	Long. tyre force	$[N]$
F_y	Lat. tyre force	$[N]$
δ	Front wheel angle	$[rad]$
g	Gravity constant	$[m/s^2]$
θ_r	Road slope	$[rad]$
ϕ_r	Road banking	$[rad]$
l_f	Front axle to CoG distance	$[m]$
l_r	Rear axle to CoG distance	$[m]$
tw_f	Front track width	$[m]$
tw_r	Rear track width	$[m]$
I_ψ	Yaw inertia	$[kgm^2]$
ω	Wheel rotational velocity	$[rad/s]$
r_e	Effective radius	$[m]$
η	Rolling resistance	[-]
F_z	Vertical force	$[N]$
γ	Wheel inclination	$[rad]$
T_{drv}	Driving torque	$[Nm]$
T_{brk}	Braking torque	$[Nm]$
α	Tyre lat. slip	$[rad]$

V_{xc}	Wheel centre long. velocity	$[m/s]$
$\Delta F_{z,x}$	Long. weight transfer	$[N]$
$\Delta F_{z,y}$	Lat. weight transfer	$[N]$
F_{st}	Static vert. force	$[N]$
h_{CoG}	CoG height	$[m]$
h_s	CoG to roll axis distance	$[m]$
h_{rc}	Roll centre height	$[m]$
K_ϕ	Roll stiffness	$[Nm/rad]$
WB	Wheelbase	$[m]$
$\mathbf{X_k}$	System state	[-]
$\mathbf{U_k}$	System input	[-]
$\mathbf{Y_k}$	System measurement	[-]
$\mathbf{w_k}$	System uncertainty	[-]
$\mathbf{v_k}$	measurement uncertainty	[-]
$\mathbf{Q_k}$	Process covariance matrix	[-]
α_{ukf}	Scaling param. UKF	[-]
κ_{ukf}	Scaling param. UKF	[-]
L_{ukf}	State vector length UKF	[-]
λ_{ukf}	Scaling param. UKF	[-]
χ	Sigma point matrix	[-]
Θ	Scaling factor UKF	[-]
η^c	Weighting factor UKF	[-]
η^m	Weighting factor UKF	[-]
β_{ukf}	Secondary scal. factor UKF	[-]
P_k^{yy}	Output covariance matrix UKF	[-]
P_k^{xy}	Output cross-covariance matrix	[-]
Z_k	System parameters	[-]
S_j	Output from a *j-th* neuron	[-]
μ_A	ANFIS memb. function	[-]
w_{anfis}	ANFIS *firing strength*	[-]
$\bar{w}_{anfis}$	ANFIS norm. *firing strength*	[-]
C_α	Tyre cornering stiffness	$[kN/rad]$
$F_{yf,meas}$	Measured front axle lat. force	$[N]$
μ_{est}	Est. friction potential	[-]
y_σ	Noise-corrupted signal	[-]
σ	Noise variance	[-]
P_{brk}	Brake pressure	$[bar]$
K_{brk}	Brake constant	$[Nm/bar]$

F_{res}	Rolling resistance force	$[N]$
Ω_{bias}	Tyre lat. bias	$[N]$
ω_{avg}	Average wheel speed	$[rad/s]$
$\mathbf{W}$	Decision variables	[-]
Γ_k	Random walk noise	$[N]$
a_1	Regression factor	[-]
a_{ycomp}	Compensated lat. acceleration	$[m/s^2]$
v_y^*	Lat. velocity pseudo meas.	$[m/s]$
$a_{y,m}$	Measured lat. acceleration	$[m/s^2]$
θ	Pitch orientation angle	$[rad]$
ϕ	Roll orientation angle	$[rad]$
ξ_k	Weighting factor RW-EKF	$[-]$
C	Max. admissible error RW-EKF	$[N]$
λ_{anfis}	Forgetting factor RW-EKF	$[-]$
n_{int}	Num. of slip intervals RW-EKF	$[-]$
n_s	Num. of samples on slip interval RW-EKF	$[-]$
c_{fill}	Filling factor RW-EKF	$[-]$
α_{lim}	Slip interval limit RW-EKF	$[rad]$
V	Training samples number RW-EKF	$[-]$
ξ_{thres}	Weighting factor threshold RW-EKF	$[-]$
n_{min}	Min. number of samples RW-EKF	$[-]$
$\mathbf{A_{ss}}$	Steady state lin. plant matrix	$[-]$
$\mathbf{B_{ss}}$	Steady state lin. input matrix	$[-]$
$\mathbf{x_{ss}}$	Equilibrium states	$[-]$
$\mathbf{u_{ss}}$	Equilibrium inputs	$[-]$
$\mathbf{\Delta x}(k)$	State error	$[-]$
$\mathbf{\Delta u}(k)$	Input correction	$[-]$
N_p	MPC state horizon	$[-]$
N_c	MPC input horizon	$[-]$
$\mathbf{F_{ss}}$	Augmented MPC plant matrix	$[-]$
$\mathbf{\Phi_{ss}}$	Augmented MPC input matrix	$[-]$
$\mathbf{A_c}$	Input amplitude matrix MPC	$[-]$
$\mathbf{b}(k)$	Slew rate matrix MPC	$[-]$
U_{min}	Minimum actuator amplitude MPC	$[-]$
U_{max}	Maximum actuator amplitude MPC	$[-]$
$U_{SR,min}$	Minimum actuator slew rate MPC	$[-]$
$U_{SR,max}$	Maximum actuator slew rate MPC	$[-]$
$T_{s,MPC}$	Discretisation time MPC	$[s]$

C_λ	Tyre long. stiffness	$[N]$
T	On-board motor torque	$[Nm]$
$I\omega$	Wheel inertia	$[kgm^2]$
$\mathbf{p_{ss}}$	Steady-state parameters	$[-]$
$\mathbf{\Omega}$	DES design variables	$[-]$
SR	Steering ratio	$[-]$
$\bar{\mathbf{Q}}$	MPC terminal cost matrix	$[-]$
$\mathbf{K_{lqr}}$	LQR gain	$[-]$
δ'	Steering wheel angle	$[rad]$
T_{output}	MAGV proportional torque	$[Nm]$
T_{max}	Maximum available torque	$[Nm]$
P_{pos}	Pedal command	$[-]$
$\tilde{\mathbf{x}}_{ss}$	NN-based drift ref. states	$[-]$
$F_{y,up}$	High slip NN output	$[N]$
$F_{y,down}$	Low slip NN output	$[N]$
$\Delta\alpha_{up}$	High slip increment	$[rad]$
$\Delta\alpha_{down}$	Low slip increment	$[rad]$
κ	Road curvature	$[1/m]$
$\tilde{\kappa}$	Corrected road curvature	$[1/m]$
$\Delta\kappa$	Road curvature correction	$[1/m]$
$k_{p,e_{lat}}$	Proportional curvature gain, e_{lat}	$[1/m^2]$
$k_{d,e_{lat}}$	Derivative curvature gain, e_{lat}	$[s/m^2]$
$k_{i,e_{lat}}$	Integral curvature gain, e_{lat}	$[1/m^2s]$
e_{lat}	Lat. deviation error	$[m]$
$a_{y,cent}$	Centripetal acceleration	$[m/s^2]$
MC_{press}	Master cylinder pressure	$[Bar]$
μ_x	Tyre long. friction	$[-]$
μ_y	Tyre lat. friction	$[-]$
D	Max. tyre friction	$[-]$
d	Road curvature prev. distance	$[m]$
θ_{pf}	Path-following heading error	$[rad]$
$K_{p,pf}$	Prop. heading error gain	$[1/mrad]$
$K_{d,pf}$	Der. heading error gain	$[s/mrad]$
F^*_{xf}	Front axle force pseudo meas.	$[N]$
t_{stab}	Stabilisation time	$[s]$

Abbreviations

HSAV	Highly-Skilled Autonomous Vehicle
VBOTT	Vehicle-Based Objective Tyre Testing
ITEAM	Horizon 2020 Marie-Curie Interdisciplinary Training Network
CAE	Computed-Aided Engineering
AV	Autonomous Vehicle
VD	Vehicle Dynamics
YSC	Yaw Stability Control
EM	Electric Motor
EHB	Electro-Hydraulic Braking
HSA	Highly-Skilled Autonomous
ADAS	Advanced Driver Assistance Systems
UGV	Unmanned Ground Vehicle
LKAS	Lane Keeping Assistance System
ESP	Electronic Stability Program
MAGV	Multi-Actuated Ground Vehicle
AFS	Active Front Steering
DGPS	Differential Global Positioning System
CAN	Controller Area Network
AI	Artificial Intelligence
ANN	Artificial Neural Networks
GPS	Global Positioning System
SiL	Software in the Loop
HiL	Hardware in the Loop
JLR	Jaguar Land Rover
DevBOT	ROBORACE development vehicle
DAS	Driving Assistance Systems
ABS	Anti-lock Braking System
TCS	Traction Control System
ESC	Electronic Stability Control
LIDAR	Light Detection and Ranging
LDW	Lane Departure Warning

ACC	Adaptive Cruise Control
OEM	Original Equipment Manufacturer
ISA	Intelligent Speed Assistance
V2V	Vehicle to vehicle
V2I	Vehicle to Infrastructure
AEB	Autonomous Emergency Braking
RCAS	Rear-end Collision Avoidance System
SAE	Society of Automotive Engineers
SISO	Single-Input Single-Output
OC	Optimal Control
FE	Friction Ellipse
WF	Weighting Function
ST	Single Track
RWD	Rear Wheel Drive
LSD	Limited Slip Differential
AWD	All Wheel Drive
SMC	Sliding Mode Control
LQR	Linear Quadratic Regulator
RL	Reinforcement Learning
WFT	Wheel Force Transducers
LSB	Load Sensing Bearings
UKF	Unscented Kalman Filter
EKF	Extended Kalman Filter
ANFIS	Adaptive Neuro-Fuzzy Inference Systems
ICC	Integrated Chassis Control
ARCS	Active Roll Control System
MIMO	Multi-Input Multi-Output
ECU	Electronic Control Unit
CDC	Continuous Damping Control
HVDM	Hierarchical Vehicle Dynamics Management
VDC	Vehicle Dynamics Control
SQP	Sequential Quadratic Programming
4WD	Four Wheel Drive
H4V	Hybrid Four Wheel Drive
WLS	Weighted Least Square
QP	Quadratic Programming
TVD	Torque Vectoring Differential
MPC	Model Predictive Control
DYC	Direct Yaw moment Control
UT	Unscented Transformation
LSE	Least Squares Estimate

MF	Magic Formula
RLS	Recursive Least Squares
IMU	Inertial Motion Unit
PID	Proportional Integral Derivative
NRMS	Normalised Root Mean Square
ST-EKF	Single Track Extended Kalman Filter
ICE	Internal Combustion Engine
LKF	Linear Kalman Filter
DIL	Driver In the Loop
NRMSE	Normalised Root Mean Square Error
GA	Genetic Algorithms
ECCS	Electronic Chassis Control Systems
NN-UKF	Neural Network-based UKF
RW-EKF	Random Walk EKF
AR	Auto Regressive
MFs	Membership Functions
PSD	Power Spectral Density
RW-LKF	Random Walk LKF
NN-EKF	Neural Network-based EKF
MF-EKF	Magic Formula-based EKF
LTI	Linear Time-Invariant
DCU	Drive Control Unit
DES	Drift Equilibrium Solutions
UDP	User Datagram Protocol
LMP	Le Mans Prototype
ADC	Autonomous Drift Control
FSM	Finite State Machine
CWS	Continuous Wheel Slip
ISMC	Integral Sliding Mode Control
LM	Levenberg Marquardt
RMS	Root Mean Square
DEHB	Decoupled Electro-Hydraulic Brake
SMC	Sliding Mode Control
PF	Path Following
EPS	Electric Power Steering
SAT	Self-Alignment Torque